Universidad de Oviedo

Departamento de Biología Funcional

Programa de doctorado en Biología Molecular y Celular

TESIS DOCTORAL

Implantable device for Aβ immunoselective nanopheresis in the cerebrospinal fluid to treat Alzheimer's disease

Nanoféresis inmunoselectiva de Aβ en el líquido cefalorraquídeo como tratamiento de la enfermedad de Alzheimer

María Almudena Coto Vilcapoma

Oviedo

- 2024 -

Universidad de Oviedo

RESUMEN DEL CONTENIDO DE TESIS DOCTORAL

1.- Título de la Tesis	
Español/Otro Idioma: Nanoféresis inmunoselectiva de Aβ en el líquido cefalorraquídeo como tratamiento de la enfermedad de Alzheimer	Inglés: Implantable device for Aβ immunoselective nanopheresis in the cerebrospinal fluid to treat Alzheimer's Disease

2.- Autor	
Nombre: María Almudena Coto Vilcapoma	
Programa de Doctorado: Programa de Doctorado en Biología Molecular y Celular	
Órgano responsable: Centro Internacional de Postgrado	

RESUMEN (en español)

La prevalencia de las enfermedades neurodegenerativas (EN) ha ido en aumento en las últimas décadas, afectando a millones de personas en todo el mundo. En muchos casos las EN son de origen desconocido, esporádicas, pero muchas de ellas comparten una característica: la acumulación de una o más proteínas patogénicas. Por ello, numerosas terapias se han centrado en eliminar estas proteínas, aunque ninguna ha llegado a ser modificadora de la progresión de estas enfermedades.

Dentro de estas patologías, la enfermedad de Alzheimer (EA) es una de las más comunes. La EA se caracteriza por una agregación temprana de una proteína llamada péptido beta amiloide (Aβ) y muchas de las terapias se centran en ella. De hecho, se ha aprobado el uso de inmunoterapias para su eliminación, ya que dos anticuerpos anti-Aβ han mostrado resultados esperanzadores en fases tempranas de la EA. Sin embargo, estas inmunoterapias no están exentas de efectos secundarios muy graves, por lo que es necesario buscar alternativas para un tratamiento más seguro.

El Aβ se encuentra en equilibrio dinámico entre el fluido intersticial (FIS) cerebral, el líquido cefalorraquídeo (LCR) y el sistema periférico, por lo que actuar sobre estos dos últimos desplazaría al equilibrio, disminuyendo la presencia de Aβ en el FIS. Las terapias actuales se aplican desde el sistema periférico, pero la relación entre el FIS y el LCR es más estrecha. Por ello, las terapias que actúan sobre el LCR tendrían un mayor efecto, definiendo así una nueva estrategia terapéutica donde el LCR actúa como sumidero. Basándose en esto, la hipótesis que se plantea en esta Tesis Doctoral es que el efecto terapéutico de esta estrategia se puede demostrar con un dispositivo implantable equipado con una membrana nanoporosa (MBNP) que permite la aféresis selectiva y continua del LCR. Esto permite administrar inmunoterapias anti-Aβ, sin liberarlas al cerebro, disminuyendo con ello la carga de Aβ en el cerebro. Esta *pseudoliberación* intratecal (IT) podría minimizar los efectos secundarios del tratamiento.

Por lo tanto, el objetivo general de esta Tesis se ha centrado en proporcionar: a) una prueba del principio del mecanismo de acción de la aféresis selectiva y b) una prueba de concepto de la *pseudoliberación* IT para mostrar los efectos de esta nueva estrategia terapéutica. Para ello, los objetivos específicos fueron: 1) Testar la permeabilidad selectiva de las MBNP *in vitro*; 2) Evaluar la factibilidad de la implantación del dispositivo de *pseudoliberación* IT en el modelo murino de EA APP/PS1 en fase sintomática temprana; 3) Evaluar los efectos de la *pseudoliberación* IT a largo plazo de anticuerpos anti-Aβ mediante sustitución percutánea de la solución terapéutica en el modelo murino de EA APP/PS1 en fase sintomática temprana.

Los resultados certificaron que las MBNP son permeables a moléculas de pequeño tamaño, como Aβ, e impermeables a moléculas más grandes, como la albúmina, *in vitro*. Asimismo, se comprobó la factibilidad de la implantación de un prototipo del dispositivo, especial para animales de pequeño tamaño, en un estudio de tres semanas, donde se verificó la selectividad de las MBNPs *in vivo* y los efectos positivos de la *pseudoliberación* IT sobre la agregación de Aβ en la corteza cerebral. No obstante, fueron necesarios realizar ajustes tanto en el dispositivo como en el proceso quirúrgico, para mejorar el bienestar de los ratones. Estas mejoras

permitieron realizar otro estudio *in vivo* más largo, donde se pudo confirmar que la implantación del dispositivo no supuso una alteración en el comportamiento normal de los ratones. Además, se demostró la factibilidad de realizar el recambio de la solución terapéutica, lo cual abre la puerta a tratamientos de larga duración.
Los estudios histopatológicos realizados en los estudios *in vivo* han permitido evaluar tanto el nivel de agregación de Aβ, como la neuroinflamación y el estado de los sistemas de aclaramiento de proteínas intracelulares y extracelulares.
La conclusión principal de esta Tesis doctoral es que la *pseudoliberación* IT durante al menos ocho semanas produce ligeras mejorías en la neuroinflamación y la proteostasis en este modelo animal de EA, resultando en la primera prueba de concepto de una nueva estrategia terapéutica aplicable a múltiples EN.

RESUMEN (en Inglés)

The prevalence of neurodegenerative diseases (ND) has been increasing in recent decades, affecting millions of people worldwide. In many cases, NDs are of unknown origin, sporadic, but many of them share one characteristic: the accumulation of one or more pathogenic proteins. As a result, numerous therapies have focused on eliminating these proteins, although none have been able to modify the progression of these diseases.
Among these pathologies, Alzheimer's disease (AD) is one of the most common. AD is characterized by an early aggregation of a protein called amyloid beta peptide (Aβ) and many therapies focus on it. In fact, immunotherapies have been approved for its elimination, as two anti-Aβ antibodies have shown encouraging results in early stages of AD. However, these immunotherapies are not exempt from very serious side effects, so it is necessary to look for alternatives for a safer treatment.
Aβ is in dynamic equilibrium between the cerebral interstitial fluid (IF), cerebrospinal fluid (CSF), and the peripheral system, so acting on the latter two would shift the equilibrium, decreasing the presence of Aβ in the IF. Current therapies are applied from the peripheral system, but the relationship between the IF and CSF is closer. Therefore, therapies acting on the CSF would have a greater effect, thus defining a new therapeutic strategy where the CSF acts as a sink. Based on this, the hypothesis put forward in this PhD Thesis is that the therapeutic effect of this strategy can be demonstrated with an implantable device equipped with a nanoporous membrane (NPMB) that allows for selective and continuous apheresis of CSF. This allows anti-Aβ immunotherapies to be administered, without releasing them into the brain, thereby decreasing the Aβ load in the brain. This intrathecal (IT) *pseudodelivery* could minimize the side effects of the treatment.
Therefore, the general objective of this Thesis focused on providing: a) a proof of principle of the mechanism of action of selective apheresis and b) a proof-of-concept of IT *pseudolibery* to show the effects of this new therapeutic strategy. To this end, the specific objectives were: 1) Test the selective permeability of the NPMBs *in vitro*; 2) Evaluate the feasibility of implanting a device for IT *pseudodelivery* in the AD murine model APP/PS1 in early symptomatic stage; 3) Assess the effects of long-term IT *pseudodelivery* of Aβ-mAbs by percutaneously replacement of therapeutic solution in the AD murine model APP/PS1 in early symptomatic stage.
The results certified that NPMBs are permeable to small molecules, such as Aβ, and impermeable to larger molecules, such as albumin, *in vitro*. In addition, the feasibility of implanting a prototype of the device, special for small animals, was tested in a three-week study, where the selectivity of NPMBs *in vivo* and the positive effects of IT *pseudodelivery* on the Aβ aggregation in the cerebral cortex were verified. However, adjustments to both the device and the surgical procedure were necessary to improve the welfare of the mice. These improvements allowed another longer *in vivo* study to be performed, where it was possible to confirm that the implantation of the device did not lead to an alteration in the normal behavior of the mice. In addition, the feasibility of replacing the therapeutic solution was demonstrated, which opens the doors to long-term treatments.
Histopathological studies performed in the *in vivo* studies have allowed us to evaluate the level of Aβ aggregation, neuroinflammation and the status of intracellular and extracellular protein clearance systems.
The main conclusion of this PhD Thesis is that IT *pseudolibery* for at least eight weeks produces slight improvements in neuroinflammation and proteostasis in this animal model of

Universidad de Oviedo

AD, resulting in the first proof-of-concept of a new therapeutic strategy applicable to multiple NDs.

SR. PRESIDENTE DE LA COMISIÓN ACADÉMICA DEL PROGRAMA DE DOCTORADO EN _Oviedo, a 14 de junio de 2024

A mi familia,

por el apoyo incondicional

AGRADECIMIENTOS

Me gustaría comenzar dedicando este trabajo a las personas que han hecho posible que llegue hasta aquí. En primer lugar, quiero agradecer a mis directores de tesis, los Dres. Cristina Tomás Zapico y Manuel Menéndez González, el haber confiado en mí y haberme dado la oportunidad de realizar este trabajo de investigación. Por enseñarme tanto en estos años, no sólo de laboratorio.

Mi agradecimiento también a los Dres. Eduardo Iglesias Gutiérrez y Benjamín Fernández García, por su colaboración y por recibirme en el gran grupo que es Intervenciones Traslacionales para la Salud. Porque este grupo no es sólo un grupo de investigación, sino una gran familia que se ayuda y acompaña en todo momento. Comenzar en un nuevo laboratorio siempre da algo de miedo, y más si es en una ciudad desconocida, pero no pude tener más suerte. Por ello, también gracias a todos y cada uno de mis compañeros de laboratorio. A Juan y Paola, con los que comencé esta aventura y con los que nos hemos ido enfrentando a todos los pasos de esta etapa. A Manu, también presente desde el inicio, con sus consejos. Y a los que se han ido incorporando en este tiempo, María, Ester, Alex y Paula, de los que también me llevo un aprendizaje. Seguid haciendo grande este grupo.

Al grupo de becarios, por hacer más llevadera esta etapa.

Al personal del Bioterio, por su gran trabajo y colaboración en el cuidado de los protagonistas de esta Tesis, los ratones, por los que también hay que agradecer a los Drs. José María Pérez Freije y Olaya Santiago Fernández por cedérnoslos, y a Marta, de la Unidad de Microscopía Fotónica y Procesamiento de Imágenes, por su gran ayuda. Sin sus aportaciones, este trabajo no habría sido posible.

Thanks also to all the people I had the pleasure of meeting at my stay in CTN. To Maiken, for giving me the opportunity to stay in your lab. To Virginia and Søren, for your help and advice that have improved this Thesis. To my office and lab partners, for your help and support in and out of CTN during this time. Good luck with everything you set out to do.

Y no menos importante, gracias a mi familia, por su apoyo, sin el cual no sé si habría dado este paso. Sin olvidar la paciencia más que necesaria en esta etapa pretésica.

Como dijo Isaac Newton: "Si yo he visto más allá, es porque logré pararme sobre hombros de gigantes". Gracias a todos.

La investigación recogida en la presente Tesis Doctoral ha sido financiada por:

- El Instituto de Salud Carlos III, en el marco de los proyectos de Desarrollo Tecnológico DTS19-00071 y DTS2022 y la red EuroNanoMed III (AC20/00017; subvención 20-0084). IP: Manuel Menéndez González.

- La Fundación para el Fomento en Asturias de la Investigación Científica Aplicada y la Tecnología (FICYT), dentro del Plan Ciencia, Tecnología e Innovación 2018-2022 del Principado de Asturias, cofinanciado con por el Fondo Europeo de Desarrollo Regional (FEDER) bajo el proyecto AYUD/2021/57540. IP: Cristina Tomás Zapico.

La contratación durante el período predoctoral ha sido apoyada económicamente por la Universidad de Oviedo, gracias a la convocatoria "Ayudas para la realización de tesis doctorales-modalidad A" (PAPI-21-PF-20), por FICYT, y gracias al contrato asociado al proyecto AYUD/2021/57540.

INDEX

AAO	Anodic aluminum oxide
ALD	Atomic layer deposition
Aβ	Beta amyloid
Aβos	Beta amyloid oligomers
aCSF	Artificial cerebrospinal fluid
AD	Alzheimer's Disease
AICD	APP intracellular domain
ALS	Amyotrophic lateral sclerosis
AMBAR	Alzheimer management by albumin replacement
AP	Anteroposterior
APOE	Apolipoprotein E
APP	Amyloid Precursor Protein
AQP4	Aquaporin 4
ARIA	Amyloid-related imaging abnormalities
α-syn	Alpha synuclein
BACE 1	β-secretase
BBB	Blood-brain barrier
BCSFB	Blood-cerebrospinal fluid barrier
BSA	Bovine serum albumin
CAA	Cerebral amyloid angiopathy
CBD	Corticobasal degeneration
CNS	Central Nervous System
CSF	Cerebrospinal fluid
D	Dorsal
DAM	Disease-associated microglia
DLB	Dementia with Lewy bodies
DMEM	Dulbecco's Modified Eagle Medium
DMF	Dimethyl fumarate
DMSO	Dimethyl sulfoxide
DNA	Deoxyribonucleic acid
DV	Dorsoventral
ELISA	Enzyme-linked immunosorbent assay
FBS	Fetal bovine serum
FDA	Food Drug Administration
FTD	Frontotemporal dementia
GFAP	Glial fibrillary acidic protein
GSM	γ-secretase modulators
HD	Huntington's disease
HFIP	1,1,1,3,3,3-Hexafluoro-2-propanol
IDE	Insulin-degrading enzyme
Iba1	Ionized calcium binding adaptor molecule 1
IgG	Immunoglobulin G
IP	Intraperitoneal
ISF	Interstitial fluid
IT	Intrathecal
L	Left
LANDO	LC3-associated endocytosis
LRP1	Low density lipoprotein receptor-related protein 1
mAb	Monoclonal antibody
mAb 488	Alexa-488-conjugated monoclonal antibody
MCI	Mild cognitive impairment
MGnD	Neurodegenerative microglia
ML	Mediolateral
MSA	Multiple system atrophy
MW	Molecular weight
MWM	Morris water maze
ND	Neurodegenerative disease
NfL	Neurofilament-light chain
NPMB	Nanoporous membrane
NSAIDs	Nonsteroidal anti-inflammatory drugs
NVU	Neurovascular unit
PAM	Plaque-associated microglia
PB	Monobasic phosphate buffer
PBS	Phosphate-Buffered Saline
PCM	Plaque-distant microglia
PCR	Polymerase chain reaction
PD	Parkinson's disease
PFA	Paraformaldehyde
PP	Polypropylene
PSP	Progressive supranuclear palsy

ABBREVIATIONS

PS-1	Presenilin 1
RA	Reactive astrocytes
RAGE	Receptor for Advanced Gly-cation end products
ROS	Reactive oxygen species
RT	Room temperature
SC	Subcutaneous
SEM	Scanning electron microscopy
Simoa	Single-molecule array
SOD1	Superoxide dismutase 1
TDP-43	Transactive response DNA-binding protein 43 kDa
TREM2	Triggering receptor expressed on myeloid cells 2
UPS	Ubiquitin-proteasome system
WHO	World Health Organization
WT	Wild type
W-1	One week before surgery
W2	2 weeks after surgery
W3	3 weeks after surgery
W4	4 weeks after surgery
W5	5 weeks after surgery
W8	8 weeks after surgery

KEY DEFINITIONS

Autophagy — Natural degradation process in the cell that removes unnecessary or dysfunctional components through a lysosome-dependent regulated mechanism.

Drug delivery systems — Devices or systems that can assist in the administration of drugs.

Glymphatic system — System for waste clearance in the central nervous system of vertebrates, in which cerebrospinal fluid flows into the paravascular space around cerebral arteries, combining with interstitial fluid and parenchymal solutes, and exiting down venous paravascular spaces.

Immunoselective apheresis — Process of clearing target molecules from a fluid by means of a filter or membrane in combination with antibodies that provide molecular selectivity.

Immunotherapy — Therapy based on the immune system, most typically monoclonal antibodies.

Intrathecal — Within the intrathecal space, either spinal intrathecal space, ventricular cavity or subarachnoid space, which contains the cerebrospinal fluid.

Liquorpheresis — Technique by which target molecules from the cerebrospinal fluid are removed using physical methods.

Nanopheresis — Filtration of particles with filters or membranes whose pores size are measured in the nanometric scale. Filtration of particles 1 to 10 nanometers.

Proteostasis — Dynamic regulation of a balanced, functional proteome. It involves a complex interconnection of pathways that influence the fate of a protein from synthesis to degradation.

Proteinopathies — Family of diseases caused by misfolded proteins and featured by the presence of aberrant protein aggregates in cells or tissues.

Pseudodelivery — Administration of a drug without releasing it to the organism.

Selective apheresis — Process of clearing target molecules selectively from a fluid by means of a filter or membrane.

Selective permeability — Property of membranes by which certain classes of molecules can pass through a membrane due to their physical-chemical properties such as size, electromagnetic charge, or others, while other classes of molecules cannot.

INTRODUCTION

1. Neurodegenerative diseases as proteinopathies

Neurodegenerative diseases (NDs) have a great impact on millions of people worldwide. They are caused by progressive dysfunction and neuronal loss. Currently, the specific etiologies behind the sporadic form of these conditions remain unknown; however, many of them share a common characteristic: the accumulation of one or more proteins. Therefore, they are often referred to as proteinopathies. This is the case of the most common NDs (Table 1), such as Alzheimer's disease (AD), Parkinson's disease (PD), frontotemporal dementia (FTD) and its variants, amyotrophic lateral sclerosis (ALS), progressive supranuclear palsy (PSP), corticobasal degeneration (CBD), dementia with Lewy bodies (DLB), multiple system atrophy (MSA), and Huntington's disease (HD) (1, 2). Nevertheless, it has been observed protein aggregates classically associated to a specific ND in a different one, resulting in the emergence of co-pathologies (2, 3). Therefore, the complexity of these diseases is increased as a result. Additionally, this could imply that they potentially share the underlying cause.

Table 1. List of the most common neurodegenerative diseases and their associated main aggregate proteins used as disease-specific biomakers.

Neurodegenerative disease	Proteins accumulated
Alzheimer's disease (AD)	Beta amyloid (Aβ) Tau
Parkinson's disease (PD)	Alpha synuclein (α-syn)
Frontotemporal dementia (FTD)	Tau Transactive response DNA-binding protein 43 KDa (TDP-43) FUS
Amyotrophic lateral sclerosis (ALS)	Transactive response DNA-binding protein 43 KDa (TDP-43) Superoxide dismutase 1 (SOD1) FUS
Progressive supranuclear palsy (PSP)	Tau
Corticobasal degeneration (CBD)	Tau
Dementia with Lewy bodies (DLB)	Alpha synuclein (α-syn) Ubiquitin
Multiple system atrophy (MSA)	Alpha synuclein (α-syn)
Huntington's disease (HD)	Huntingtin

In a healthy brain, these proteins are typically present as monomers, performing their regular function to ensure the proper operation of the Central Nervous System (CNS).

Because of genetic mutations or changes in their processing, their normal folding is disrupted, leading to sticky proteins that tend to aggregate and form extracellular plaques and/or intracellular inclusions. In this manner, not only do these proteins lose their functionality, but they also give rise to toxicity (4, 5). In normal conditions, neurons and other cells in the neural tissue can handle these proteins and degrade them through autophagy and ubiquitin-proteasome system (6). However, there seems to be a point where all these mechanisms become overwhelmed, so they begin to accumulate, increasing toxicity and giving rise to the pathological processes (7) that lead to neurodegeneration. This can be detected by measuring the biomarker of axonal injury, the Neurofilament-light chain (NfL)(8). One of the reasons for this overload could be the loss of efficiency of these systems with age, which would explain why these diseases are associated with relatively advanced ages (9).
Beta amyloid (Aβ) peptide is one of these key proteins and, due to the prevalence of AD, one of the most studied.

2. Alzheimer's Disease: The role of beta amyloid as a pathogenic protein

According to reports from the World Health Organization (WHO), dementia is the seventh leading cause of death in the world (10). It is estimated that 152 million people will be affected by 2050 (11). This group of conditions is characterized by symptoms of memory, language, problem solving and other mental abilities. Various diseases affecting the CNS can lead to dementia, among which AD is the most frequent, accounting for 60-80% of cases (12).

AD was described in 1906 by Alois Alzheimer, after whom it is named (13). He did so based on the case of a 51-year-old patient with symptoms that had not been classified to date (memory loss, disorientation, and personality disorders). After the patient's death, Alzheimer studied her brain and described the lesions that characterize this disease: extracellular amyloid plaques and intracellular neurofibrillary tangles, with their consequent neurodegeneration (14). Nowadays, it is known that these amyloid plaques are associated with the Aβ and the neurofibrillary tangles with hyperphosphorylated tau protein. The progression of the deposition of these proteins marks the evolution of the disease, where Thal stages describe the progression of Aβ, and Braak stages characterize that of Tau. Aβ deposits begin in the neocortex, followed by the entorhinal cortex, the hippocampus, and eventually spreads to subcortical regions, the brainstem, and concludes in the cerebellum. On the other hand, the progression of Tau tangles follows a different pattern, initially manifesting in the entorhinal cortex, then advancing through hippocampus, and finally covering the neocortex (15, 16).
Aβ is produced as a consequence of enzymatic processing on the amyloid precursor protein (APP). This protein is encoded on chromosome 21 (17). Individuals with Down

Syndrome, who possess an extra copy of this specific chromosome, exhibit the formation of plaques at a premature stage, typically starting around 50 years prior to the general population (18). This, in addition with the discovery of autosomal dominant forms of AD, in which there are changes in the *APP* gene sequence, led Hardy and Higgins to propose Aβ deposition as the onset of this disease (19). Recently, a new *APP* mutation, known as A673T, has been found to be protective, as it reduces the production of Aβ. Actually, homozygous carriers of this mutation have not shown any history of dementia, supporting the amyloid hypothesis (20, 21).

Over the years, researchers have observed several factors that play a role in the progression of the disease, such as neuroinflammation, acetylcholine deficiency, oxidative stress, glucose hypometabolism, vascular impairments, and metal ion accumulation, among others, leading to the emergence of different hypotheses (22-25). Nevertheless, the focus of most therapeutic strategies continues to be Aβ.

2.1. Aβ production

APP is synthesized in the endoplasmic reticulum and transported to the Golgi apparatus. After reaching maturity, it is transported to the plasma membrane, where it will be processed by different enzymes in two distinct routes, resulting in the production of smaller fragments with distinct compositions (26) (Figure 1).

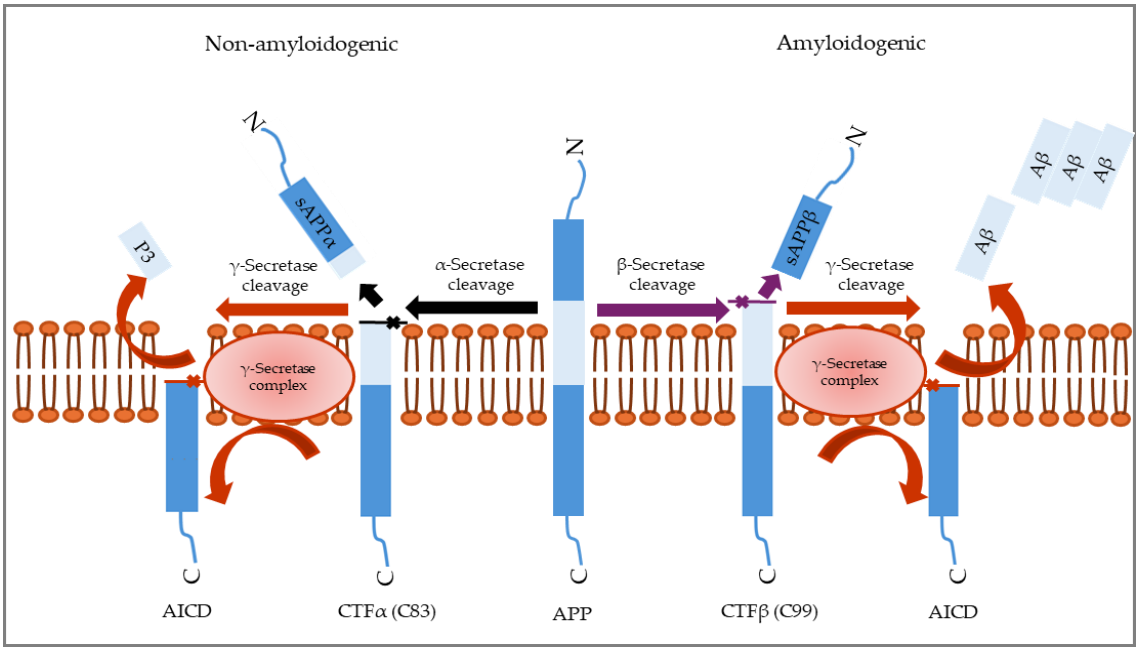

Figure 1. APP proteolytic pathways. Non-amyloidogenic processing of APP involves α-secretases cleaving within the Aβ domain to produce CTFα (C83) and sAPPα. CTFα is then processed by γ-secretases to generate P3 and the APP intracellular domain (AICD). Amyloidogenic processing is carried out by β- and γ-secretases, resulting in CTFβ (C99) and sAPPβ. CTFβ is further cleaved by γ-secretases to produce Aβ and AICD. Scheme modified from (26).

By the non-amyloidogenic pathway, APP is processed by α-secretase, which produces sAPPα and CTF83 fragments. When γ-secretase cleaves the latter, it generates the P3

peptide and the APP intracellular domain (AICD). In contrast, through the amyloidogenic route, β-secretase (BACE 1) cleaves APP into a soluble fragment known as sAPPβ and fragments of the C-terminal region 89 and 99 (CTF89, CTF99). These fragments are then processed by γ-secretase, resulting in soluble Aβ and the AICD (27-29). $A\beta_{1-40}$ (<80%), $A\beta_{1-38}$ (<20%), and $A\beta_{1-42}$ (10%) are the predominant soluble monomeric isoforms of Aβ. Among these, $A\beta_{1-42}$ is the most hydrophobic, thus it can form insoluble aggregates (30). Interestingly, these shorter forms of Aβ have been found to inhibit $A\beta_{1-42}$ aggregation (31). This process occurs mostly inside endosomes and its release is regulated by synaptic activity, encompassing both the presynaptic and postsynaptic levels (27, 29). In fact, under typical physiological conditions, Aβ plays a role in modulating synaptic activity and may also have antibacterial properties (32). Studies have also indicated that it could play a role in promoting neuronal differentiation, aiding in injury recovery, reducing oxidative stress, and suppressing tumors (33). However, under pathological conditions, Aβ begins to accumulate and aggregate in conformations rich in folded β-sheets.

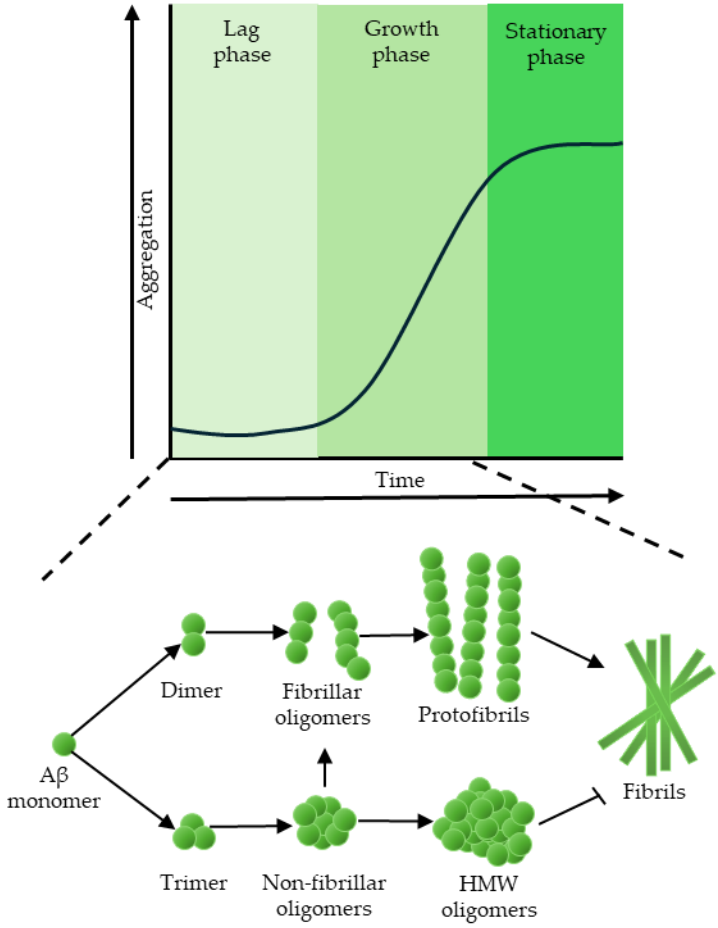

Figure 2. Schematic representation of Aβ aggregation. Aβ undergoes three phases in its transformation from monomers to mature fibrils: an initial lag phase, a growth phase and a stationary phase. Aβ oligomers are primarily found in the lag and growth phases. Some of them, known as fibrillar oligomers, rapidly advance to protofibrils and mature fibrils starting with Aβ dimers. Others, like Aβ trimers or globulomers, called non-fibrillar oligomers, have a different structure and must first convert into fibrillar oligomers before progressing to fibrils. Scheme modified from (32).

This process *in vitro* is usually segmented into three stages: an initial latent phase, followed by a growth phase, and ultimately the stationary phase, in which fibers form insoluble plaques (Figure 2). During the first two stages, individual monomers start to assemble, either through primary nucleation (aggregation fiber independent) or secondary nucleation (aggregation dependent on existing fibers) (32). The various forms of Aβ are in a dynamic equilibrium, where compact amyloid

plaques can shed soluble $A\beta_{1-42}$ monomers, which subsequently reassemble into clusters (30). In this process, a wide range of intermediate products with different sizes, morphology and conformation are produced, known as oligomers (Aβos)(26). Aβos levels increase in early AD stages but decrease as tau levels rise (34). These Aβos have been shown to have neurotoxic potential through several mechanisms. For instance, Aβos can bind to receptors located on the surface of neurons, hindering their normal activity, and ultimately leading to their death (26).

De Strooper and Karran (35) proposed an extension of the amyloid hypothesis called "the cellular phase" of AD. According to this extension, the accumulation of Aβ and tau occurs gradually over time and is initially tolerated by cells in the CNS (the "biochemical phase"). However, the disease only becomes clinically apparent when cellular homeostatic mechanisms fail. This failure leads to a breakdown in the clearance of aggregated pathological Aβ, increased stress on cells, and a disruption of normal intercellular functions. Ultimately, this cascade of events results in neurodegeneration. Then, the cellular phase is characterized by dysfunction in the neurovascular unit (NVU), abnormalities in the neuronal network activity, and impaired functions of astrocytes and microglia, which are responsible for maintaining a healthy cellular environment. There is also a possibility of these cells gaining toxic functions during this phase (35). These homeostatic mechanisms in the brain include autophagy, the functions of microglia and astrocytes, and the glymphatic system.

2.2. Aβ and autophagy

Under normal conditions, approximately 30% of newly synthesized proteins are misfolded, thus, there are systems to maintain cellular proteostasis. These are the ubiquitin-proteasome system (UPS) and autophagy, and they work together for this objective (Figure 2). In fact, there are proteins that can interact with ubiquitin marked proteins, like p62, that link both systems.

The UPS is responsible for the breakdown of short-lived, misfolded, and damaged proteins. Through this system, ubiquitinated proteins are degraded by the proteasome, which is a protease complex (Figure 3B)(36).

Autophagy is the cellular mechanism for eliminating altered proteins and organelles in lysosomes when it is not possible to carry out repairs. Furthermore, in the CNS it has great importance due to its role in synapse plasticity. Thus, when autophagy is suppressed, it results in notable atrophy characterized by severe axonal swelling, ultimately leading to neurodegeneration (37). There are three types of autophagy, based on the mechanism of delivery of cargo to the lysosomes. First, in macroautophagy, the cytosolic cargo becomes initially enclosed within autophagosomes, which are double membrane vesicles. Then, these autophagosomes subsequently merge with lysosomes to

ensure complete degradation of the cargo (Figure 3A). In chaperone-mediated autophagy, a chaperone identifies the proteins and takes them to the lysosomal surface. Lastly, in microautophagy and endosomal microautophagy, internalization of cargo occurs through its invagination in the lysosomal and endosomal membrane. Chaperone-mediated autophagy targets individual proteins for degradation. However, if these proteins form abnormal oligomeric complexes, they cannot be degraded through this pathway anymore. Instead, small aggregates and oligomers can be degraded via endosomal microautophagy. The only autophagy mechanism to eliminate irreversible aggregates is macroautophagy, which can occur in bulk or selectively through a mechanism known as aggrephagy (38).

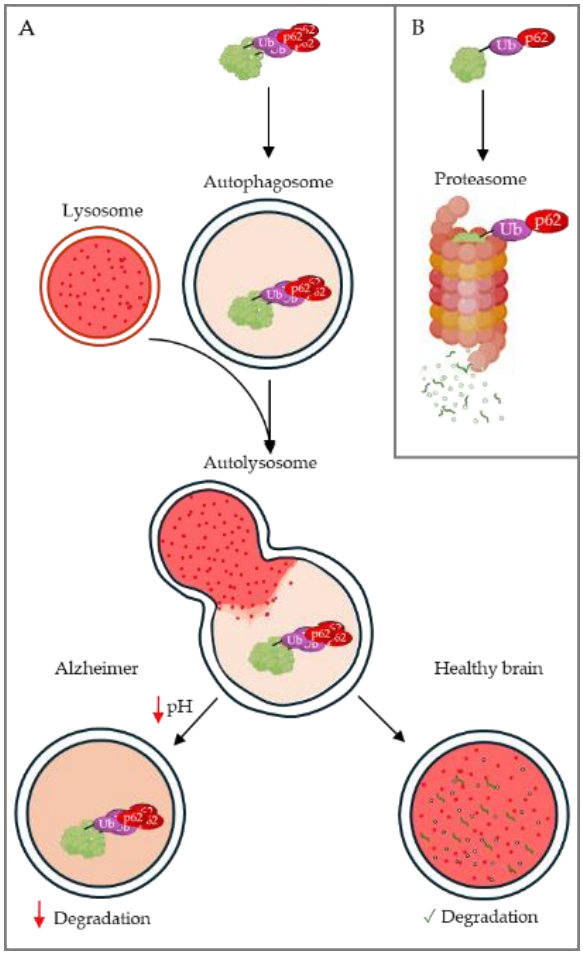

Figure 3. Overview of autophagy and the ubiquitin proteasome system (UPS) in a healthy brain and AD. In the UPS pathway (**B**), ubiquitin binds to short-lived, misfolded, and damaged proteins, which are then recognized by adapters like p62 and targeted for degradation by the proteasome. In the autophagy pathway (**A**), cargo is enclosed within autophagosomes, which then fuse with lysosomes for complete degradation. In AD, lysosome acidification is reduced, impairing the degradation process.

In NDs, it has been observed that autophagy effectors and regulators are trapped in aggregates, which leads to a reduction in autophagy. Furthermore, Aβos can bind to dynein, a cytoskeletal motor protein, hindering the mobility of autophagosomes and, thus, promoting their accumulation in the distal part of the axons (38).

Besides that, impaired autophagy can lead to overactivation of γ-secretase, by stimulating the expression of the presenilin 1 (*PS-1*), one subunit of γ-secretase (39). In addition, mutations in *PS-1* in some genetic forms of AD reduce lysosomal acidification, impairing its ability to degrade (Figure 3A)(38). This leads to the accumulation of other waste products, like lipofuscin (40, 41). This accumulation increases lipid peroxidation and ferroptosis, worsening and speeding up the disease progression (42).

2.3. Aβ and immune system

2.3.1. Microglia

Microglia are the cells of the innate immune system of the CNS, with a crucial role in maintaining homeostasis. They contribute to various essential functions, such as neurogenesis, neuronal migration, axonal growth, modulation of synapses (43), and clearance of cellular debris, dead cells or misfolded proteins, among which Aβ is included (44).

Dani et al. (45) observed correlation between microglia activation and the progression of the load of Aβ, even in the early stages. Thus, there are phenotypic changes in microglia since the beginning of the disease (43). The state of microglial activation is ever-changing during AD progression, with two distinct peaks of microglial activation proposed: an initial anti-inflammatory peak during the preclinical stage, followed by a later pro-inflammatory peak as the disease progresses and Aβ clearance fails. Thus, microglia play a dual role in the development of AD (46).
Active microglia can be classified as either neurotoxic (M1), promoting inflammation, or neuroprotective (M2), stimulating anti-inflammatory responses and aiding in healing, with a range of diverse intermediate phenotypes between both. M2 microglia have the responsibility of uptake and eliminate insoluble Aβ deposits, as well as sequestering and encapsulating them as a protective barrier against Aβ toxicity (46). It is important to note that the interaction between microglia and Aβ depends on its conformation or aggregation state. Soluble Aβ increases microglial proliferation (43), and the NLRP3 inflammasome facilitates microglial recognition and recruitment to exogenous Aβ plaques (47). Aβ is internalized and rapidly released with minimal degradation, while Aβos are degraded through the release of cathepsin B into the cytoplasm (43).
Furthermore, M2 microglia contributes to Aβ degradation through the secretion of enzymes, such as neprilysin and insulin-degrading enzyme (IDE) (47). Overactivated microglia exhibit increased proliferation, stimulate chemotaxis, and elevate the presence of inflammatory M1 markers. Thus, M1 microglia release cytokines that are harmful to neurons, either directly or by triggering the activation of astrocytes with neurotoxic effects. Additionally, microglia assist in the engulfment of synapses with the aid of complement, facilitating the spread of tau pathology (46). In fact, axonal distress can impede microglial clearance of Aβ by shifting their focus to myelin dysfunction (48). Microglia may also contribute to the spread of Aβ, as all remaining Aβ is released upon their death (43).

This classification is a useful concept for understanding microglia polarization, inspired by the macrophage polarization paradigm. However, recent research suggests that this

model does not accurately represent the diverse polarization states observed *in vivo* (49). Recent single-cell RNA sequencing has identified several microglial phenotypes related to aging and AD (50). These include "disease-associated microglia" (DAM), which may be involved in protective phagocytosis, and "neurodegenerative microglia" (MGnD), a dysfunctional microglia phenotype (51), among others with unclear roles (50).

Apolipoprotein E (APOE) and the triggering receptor expressed on myeloid cells 2 (TREM2) are crucial factors for these two phenotypes. These proteins hold such importance that mutations in them occur in familial forms of AD. TREM2 is involved in the microglial clearance of damaged neurons and Aβ by interacting with various types of membrane lipids and oligomeric Aβ (43). Microglia deploys a process called LC3-associated endocytosis (LANDO) to efficiently remove Aβ and restore Aβ receptors to the cell surface, including TREM2 (29). This process also suppresses the release of inflammatory cytokines (47). If TREM2 is genetically deleted in an AD mice model, like the 5XFAD model, microglia do not work properly, leading to an increased accumulation of Aβ and microgliosis, accompanied by the release of proinflammatory cytokines, ultimately resulting in damage to neurons (29). Lately, it has been noted that TREM2 is involved in the formation of the protective microglial barrier around Aβ plaques (Figure 4). Microglia distribution around plaques differs between dense core and diffuse plaques. It is unknown whether it is the plaque changes its structure because of the microglial barrier or whether it is the other way around, because it is important to consider that dense core fibrillar plaques can harbor other Aβ conformations due to their tendency to accumulate Aβos (43, 52). Microglial morphology and genetic profile differ between plaque-associated microglia (PAM) and plaque-distant microglia (PCM), with PCM resembling control microglia. However, PCM are also reactive and may play a role in detecting Aβos and initiating Aβ-plaque formation (50).

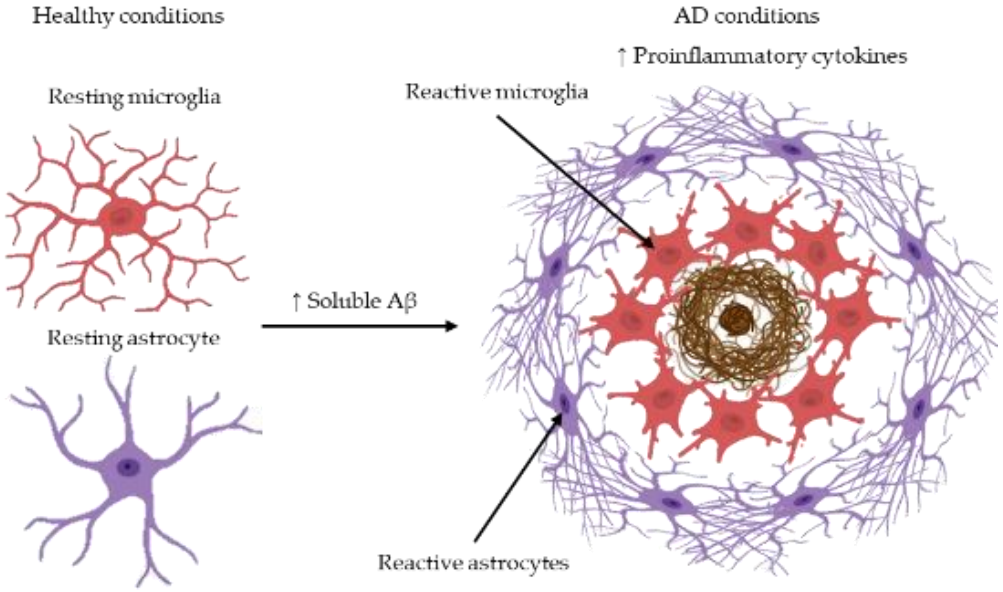

Figure 4. Overview of microglia and astrocytes in healthy conditions and in AD. In healthy conditions, microglia and astrocytes are in resting state. Once the levels of soluble Aβ increase, both become reactive, producing proinflammatory cytokines, leading to neuroinflammation.

Another important receptor that interacts with Aβ is the receptor for Advanced Glycation end products (RAGE). This cell surface receptor is expressed on microglia and astrocytes, and functions as an inflammatory pattern recognition receptor. When it interacts with Aβ, it activates microglia, leading to an increase in pro-inflammatory cytokines, cell stress, reactive oxygen species (ROS) generation, and intraneuronal transport of Aβ. Additionally, it facilitates the transportation of Aβ across the BBB and increases the activities of β-secretase and γ-secretase, ultimately resulting in an increase of the amyloidopathy (53).

Lastly, under the electron microscope, another microglia phenotype known as dark microglia has been discovered. These dark microglia also express TREM2. It earns its name from its dark appearance resulting from the condensation of its cytoplasm and nucleoplasm. Dark microglia possess highly branched and exceptionally thin processes that enwrap different synaptic components such as synaptic clefts, pre-synaptic axon terminals, and post-synaptic dendritic branches, suggesting a role in synaptic remodeling (54). Its distribution seems to be restricted to some areas where there are large blood vessels, so they could be involved in the maintenance of the integrity of the BBB. It is uncommon to find in healthy young mice, but under aging and chronic stress, like in AD, the amount of dark microglia significantly increases. Thus, it seems that they may be a group of microglial cells that experience stress due to their excessive engagement in the maintenance of brain functions (43).

2.3.2. Astrocytes

Astrocytes play an important role in the CNS as the main homeostatic regulators. They are involved in the maintenance of supply of metabolic substrates to neurons and other glial cells, the regulation of ions and neurotransmitters in the extracellular space, and the modulation of synaptic activity, among others. Furthermore, astrocytes also play a role in the BBB, the NVU, and the glymphatic system (55).
Research has shown that astrocytes can migrate to Aβ plaques, internalize, and degrade them. When exposed to Aβ, astrocytes increase the expression of glial fibrillary acidic protein (GFAP), becoming reactive astrocytes (RA; Figure 4) (55). Moreover, microglia also trigger the activation of astrocytes (47). Similar to microglia, there are two phenotypes of RA: A1, which possess primarily neurotoxic characteristics, whereas A2 is primarily associated with neuroprotective functions. However, there is a broader spectrum between them (55).
Several mechanisms can be utilized by RA to clear Aβ, including cholesterol signaling, through APOE, as well as receptor-mediated clearance via receptors such as RAGE and LRP1 (Low density lipoprotein receptor-related protein 1) (56). However, astrocytes have limited efficiency in degrading Aβ (57). Then, it is worth mentioning the clearance

through the glymphatic system via the aquaporin 4 (AQP4), a protein usually expressed in astrocyte endfeet processes (58).

2.4.Aβ and the glymphatic system

The glymphatic system is a network of fluid pathways in the brain that involves the exchange of CSF and interstitial fluid (ISF) and is facilitated by astrocytes (Figure 5). In this system, CSF is driven from the subarachnoid space into the spaces around penetrating arteries, and then flows along these spaces in the same direction as the blood flow. CSF flows from perivascular space and moves through the glial basement membrane and the astroglial endfoot processes, which surround the cerebral vasculature. Within these endfeet, there is a high concentration of the water channel AQP4, which aids in the movement of CSF into the brain tissue where it mixes with the ISF. This fluid then diffuses throughout the interstitium, with a specific fluid movement towards the venous perivascular and perineuronal spaces (59). Changes in the shape of these spaces influence fluid movement (60).

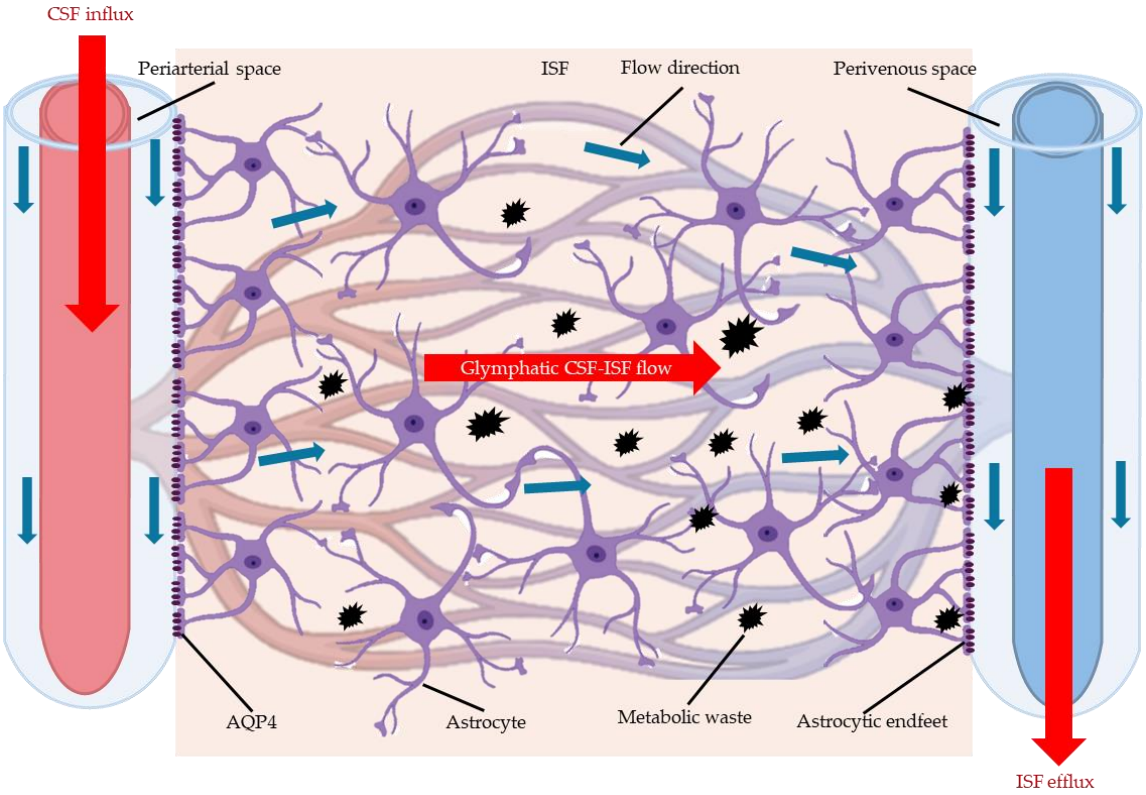

Figure 5. Overview of the glymphatic system. CSF flows from the subarachnoid space into the spaces around penetrating arteries, and then flows along these spaces following the same direction of the blood flow. It moves through the glial basement membrane and the astroglial endfoot processes surrounding the cerebral vasculature. Within these endfeet, the aquaporin 4 (AQP4) aids in its movement into the brain tissue where it mixes with the interstitial fluid (ISF). This fluid then diffuses throughout the ISF, with a specific fluid movement towards the perivenous space. In the end, the CSF is released via the perineural sheaths of cranial and spinal nerves, meningeal lymphatic vessels, and arachnoid granulations, effectively removing the metabolic waste from the CNS. Modified from (59).

Recent studies have revealed that neurons also play a role in regulating the paravascular flow (61). In the end, the CSF is released via the perineural sheaths of cranial and spinal nerves, meningeal lymphatic vessels, and arachnoid granulations. This way, the system effectively eliminates the protein waste and metabolic byproducts from the CNS, including Aβ. In addition, AQP4 could have a protective effect by modulating the inflammatory response to Aβ (59).

In aging, it has been observed a reduction in the clearance rate due to an alteration in the AQP4 expression, as well as a reduction in CSF flow. This alteration means that the AQP4 is being relocated from the endfeet of the astrocyte to the soma. This is also known as a loss of polarization of the AQP4 (59). Prolonged mislocalization of AQP4 hinders glial scar formation by impairing astroglial migration (62).

There is evidence to suggest that reduced glymphatic function not only leads to a decrease in the clearance of Aβ, but also that Aβ by itself can disrupt the flow in the glymphatic pathway, indicating a potential feedback mechanism (59).

3. Therapies targeting Aβ

The primary objective of most treatments developed to decelerate the advancement of AD is to directly counteract the Aβ peptide using various approaches. The most studied modifiers have been γ- and β-secretase inhibitors, along with inhibitors that target the aggregation of Aβ itself (63).

3.1.Gamma- and beta-secretase inhibitors

One effective approach for diminishing Aβ levels is by directly targeting its production, specifically by inhibiting the enzymes responsible for cleaving APP and releasing the peptide, BACE1 and the γ-secretase.

In animal models of AD, the inhibition of BACE1 has led to a decrease in the initiation of new plaques, but it did not limit the growth of established plaques. Several BACE1 inhibitors have been tested on clinical trials, but all have failed, either because of lack of efficacy or the severity of side effects (64). Worsening of cognitive function and weight loss are some of the common side effects of these inhibitors. The possible reason behind could be that BACE1 also plays a role in neurodevelopment (29).

Regarding γ-secretase inhibitors, they all have failed for similar reasons to those of BACE1 inhibitors, so now γ-secretase modulators (GSM) are being studied instead (29, 31). Currently, only a few GSM programs are active, with three drugs in clinical trials (31). Among them, Roche's GSM RG6289 is the most advanced, in a Phase IIa study (GABriella; (65)), while the others are still in Phase I (31).

As a result of the issues arising from these therapies, other therapies based on the clearance of Aβ have been developed.

3.2.Therapies to promote autophagy

There is growing evidence suggesting that promoting autophagy induction, and therefore, promoting the degradation of misfolded proteins and dysfunctional organelles, could be beneficial for AD treatment. Most induce autophagy through inhibiting mTOR and/or activating AMPK. One of them is rapamycin, that is an mTOR inhibitor. Both in animal models and clinical trials, improvements in cognitive functions have been noted. Thus, despite some side effects, it is still considered as a potential treatment for AD (66). Other mTOR inhibitors, like Everolimus and Temsirolimus, have been developed to minimize side effects. These inhibitors did inhibit autophagy, while they still reduced Aβ levels and improved cognition. Then, further studies are needed to better understand the mechanisms of these compounds (39). Additionally, enhancing lysosomal activity has also been shown to effectively clear Aβ (67). Natural compounds, such as curcumin, resveratrol and oleuropein, have shown some protective effects in AD patients, including an increase in autophagy and a reduction in inflammation (66).
In 2003, the U. S. Food Drug Administration (FDA) has approved memantine, an NMDA receptor blocker, for AD treatment. Memantine also enhances autophagy, either through mTOR-dependent or independent pathways (66). Conversely, the FDA approved antiepileptic drug carbamazepine, which also possesses the ability to induce autophagy in mTOR dependent or -independent way (66), though it is not specifically approved for AD.

3.3.Modulation of immune response

Excessive activation of microglia, and therefore a significant amount of neuroinflammation, plays an important role in the progress of AD. For this reason, neuroinflammatory therapies are under study.
Several substances have shown inhibitory effects on NLPR3 inflammasome, reducing microgliosis and Aβ deposits. Besides that, certain nonsteroidal anti-inflammatory drugs (NSAIDs) such as ibuprofen and indomethacin were found to have a direct impact on Aβ deposition by modifying γ-secretase activity. Other anti-inflammatory drugs, like dimethyl fumarate (DMF), reduce Aβ load by promoting its autophagy through the up regulation of LC3.

AL002c is a monoclonal antibody (mAb) that acts as an anti-hTREM2 agonist. In animal models, systemic administration of AL002c has been shown to decrease Aβ load, reduce neurite dystrophy, and regulate the inflammatory response of microglial cells. In addition, in a phase I clinical trial, no serious adverse effects were reported (47). Inhibition of RAGE has also been suggested as a therapeutic target for reducing inflammation in AD (47, 55).

Some scavenger molecules have been tested to treat AD with positive results. Edavarone has been found to have protective mechanisms that involve reducing Aβ deposits, astrogliosis, and, therefore, neuroinflammation and mitigation of the endothelium/astrocyte unit dysfunction. It also modulates AQP4 expression (55).

Nowadays, the stimulation of Aβ-degrading molecules offers a novel therapeutic approach in the treatment of AD. Lovastatin and somatostatin, drugs used as a treatment for hypercholesterolemia, stimulate the secretion of IDE, as well as metformin, a type 2 diabetes treatment (47).
Electroacupuncture, among other non-pharmacological therapies, can effectively reduce Aβ deposits by enhancing the levels of Aβ-degrading molecules, promoting microglia activity, and improving the function of Aβ-transporters on the BBB. Additionally, it results in a reduction in astrocytes reactivity and enhances AQP4 polarization, subsequently leading to an improvement in the glymphatic system (68).
Finally, another potential strategy for treatment of AD would be increasing the M2 polarization with molecules like resveratrol (47).

3.4. Modulation of the glymphatic system

Besides the therapies that enhance astrocyte function, certain anesthetics that induce slow-wave sleep can increase the clearance through the glymphatic system (55). Additionally, drugs that enhance cardiac contractility and arterial pulsatility have also been shown to improve CSF-ISF exchange. Treatment with TGN-073, an AQP4 facilitator, can induce changes in AQP4 conformation, increasing flux (62).
Sensory manipulations can affect waste buildup in the brain. Studies have found that inducing synchronous gamma oscillations through 40 Hz light flickers or tones can reduce amyloid deposition (60). Photobiomodulation therapy, also known as low-level light/laser therapy, involves using visible and/or neared-infrared light to stimulate biological processes without increasing temperature. Research suggests it can enhance the lymphatic contractility, improving waste clearance (69). In addition, a recent study demonstrated that light could restore mitochondrial metabolism and cellular function of meningeal lymphatic endothelial cells, thereby restoring its function (70).

3.5.Strategies for clearing Aβ from the periphery

The BBB not only acts as a physical barrier but also controls the movement of substances between the blood and the brain. It helps maintain the balance of molecules like glucose, insulin, leptin, and cytokines, which are important for brain function and immune activity. LRP1 and RAGE are important proteins involved in the transport of Aβ across the BBB. LRP1 is thought to facilitate the removal of Aβ from the brain to the peripheral

system, while RAGE helps Aβ enter to the brain. Thus, there is an equilibrium of Aβ levels between brain and periphery blood. The "peripheral sink hypothesis" suggests that clearing Aβ in the periphery would improve Aβ clearance in the CNS. Therefore, several strategies have been developed based on this (71).

3.5.1. Plasmapheresis

The process of plasmapheresis involves the separation of plasma from the other constituents of blood, after which the plasma is returned to the patient. In plasma exchange, the removed plasma is substituted with an equal amount of plasma or colloid solutions. For instance, in the treatment of AD, procedures such as plasmapheresis and plasma albumin replacement have been conducted (Alzheimer management by albumin replacement, AMBAR study) (72-77).

The aim of this therapeutic plasmapheresis is to remove the disease-causing elements (Aβ) from the plasma by introducing albumin, which has the ability to bind to Aβ at the plasma level. By replacing the albumin, a significant portion of Aβ will attach to the fresh albumin, reducing the amount of free Aβ. This technique is based on the hypothesis that albumin replacement can alter the balance of Aβ between the CNS and blood plasma, causing a shift of Aβ forms from CSF to plasma. This shift promotes natural degradation of Aβ at the systemic level. A reduction in plasma Aβ has been observed in clinical trials involving patients with mild and moderate AD (75, 76). However, it is estimated that most of the Aβ cleared at the plasma level would not be of cerebral origin, but mostly peripheral (78). Nevertheless, it is noteworthy that there was also a reduction in cognitive decline, particularly noticeable in moderate AD patients. In addition, plasma exchange also reduces proinflammatory elements and other detrimental substances that may contribute to the development of AD (73, 74). While regulatory agencies have not granted approval for this procedure in AD, it has gained some support from the American Society of Apheresis and today is being used in some centers (79, 80).

3.5.2. Dialysis

Dialysis, which includes hemodialysis and peritoneal dialysis, is an effective way to remove waste products and metabolites from the blood to maintain a balanced state in the brain. Some clinical studies have suggested that dialysis can reduce levels of Aβ. One study conducted by Jin et al. (81) found that peritoneal dialysis specifically led to a decrease in soluble Aβ levels in both blood and brain ISF. This could be due to the dialysis process facilitating the movement of Aβ from the brain to the blood. It appears that peritoneal dialysis may achieve this by increasing the levels of LRP1 and decreasing the levels of RAGE. This reduction in neuroinflammation may then lead to a decrease in pro-

inflammatory cytokines and an increase in anti-inflammatory ones, further supporting the benefits of peritoneal dialysis in reducing Aβ levels (81).
Regarding hemodialysis, both short-term and long-term studies have shown that hemodialysis can lead to a decrease in both plasma and brain Aβ levels. This reduction in blood Aβ levels is believed to promote the excretion of Aβ from the brain, resulting in decreased levels of Aβ in the brain (82, 83).

3.5.3 Immunotherapy

Immunotherapy has emerged as one of the most sophisticated and effective strategies in combating Aβ peptide thus far. This approach encompasses two main types: active immunotherapy, which stimulates the immune system to generate antibodies, and passive immunotherapy, involving the introduction of externally derived monoclonal antibodies specifically targeting the protein of interest (29, 63, 84).

3.5.3.1 Active immunotherapy

Active immunization involves the combination of an immunogen, specifically Aβ in this situation, with an adjuvant to induce an immune response. In animal models, it has been observed a decrease in Aβ deposits and cognitive decline. Conversely, in clinical trials, there have been severe side effects (i.e., meningoencephalitis). After 4.6 years, in the antibody-responder patients that did not have side effects, it was found mitigated cognitive decline without encephalitis. Currently, there are at least three phase 1 trials and two phase 2 trials investigating active anti-amyloid immunotherapy, including the use of innovative DNA-based vaccine technologies, in individuals with mild cognitive impairment (MCI) or mild dementia. Moreover, there is also potential for preventive trials utilizing active anti-amyloid immunotherapy in middle-aged cognitively healthy individuals, to be conducted before the accumulation of amyloid in the brain (85).

3.5.3.2 Passive immunotherapy

Passive immunotherapy has been administered directly to the brain or peripherally (85). In several animal studies, it has been observed a reduction in Aβ load after the direct injection of anti-Aβ antibodies in the brain (86-88). Nonetheless, the effectiveness of this system is limited (89, 90), and it can also have side effects (91). To circumvent these side effects, alternative therapies are being developed to transport drugs, such as antibodies, through the BBB (92, 93). Furthermore, these methods could prove beneficial for peripheral administration too, considering that BBB disruption has been observed following administration (94).

Several antibodies have been developed against different Aβ species (95, 96). Initially, a first-generation approach (Bapineuzumab) targeted the N-terminus of the aggregated Aβ. Subsequent advancements led to the creation of second-generation agents, such as Crenezumab, Gantenerumab, and Solanezumab, which were designed to specifically target Aβ species that are not in plaque form. Moving forward, third generation agents were developed as high affinity antibodies directed towards either Aβ protofibrils (Lecanemab) or plaque Aβ (Aducanumab and Donanemab; Table 2) (85).

Table 2. List of monoclonal antibodies targeting Aβ, including their target region, and their outcomes in clinical trials.

Antibody	Generation	Target	Clinical trials	State
Bapineuzumab	First	Residues 1-5 Unprocessed APP	↓ Aβ load = Cognitive decline	Failure
Crenezumab	Second	Residues 13-24	= Cognitive decline	Failure
Gantenerumab	Second	Residues 3-11 and 18-27	↑ ARIA = Cognitive decline	An improved version (Trontinemab) is under study
Solanezumab	Second	Residues 16-26	= Cognitive decline	Failure
Lecanemab	Third	Residues 1-16	↓ Aβ load ↓ Cognitive decline ↑ ARIA APOε4 carriers	Approved by FDA on January 6, 2023. More clinical trials in progress
Aducanumab	Third	Residues 3-7	↓ Aβ load ↑ ARIA	Approved by FDA on June 7, 2021. More clinical trials in progress
Donanemab	Third	Pyroglutamyl E3 Aβ peptide (Aβp3-42)	↓ Aβ load ↑ ARIA	An improved version (Remternetug) is under study

The first one, Bapineuzumab, is a humanized murine antibody that specifically targets residues 1-5 at the N-terminus of Aβ protein. This antibody, also known as anti-3D6 humanized antibody, has a distinct specificity that prevents it from recognizing unprocessed APP. Additionally, this epitope can be detected in various forms of Aβ, including compacted Aβ plaques and soluble oligomeric species. However, in human studies, even if there was a reduction in Aβ accumulation, there was no improvement in cognitive functions (85).

Regarding second generation antibodies, Crenezumab possesses the capacity to bind to different forms of Aβ, with a higher affinity for oligomers than monomers. In contrast, Gantenerumab only attaches to a specific conformational region found in insoluble fibrillar Aβ, while Solanezumab targets soluble monomeric Aβ by recognizing the mid-domain of Aβ. Clinical trials did not show any improvement in cognitive function with

these antibodies, and Gantenerumab was associated with amyloid-related imaging abnormalities (ARIA). However, an improved version of Gantenerumab, Trontinemab, with higher BBB penetrance, is currently being studied (85).

So far, the antibodies Lecanemab, Donanemab and Aducanumab have demonstrated the most significant reduction in Aβ deposition, with over a 60% decrease after 18 months of treatment (97). These antibodies target Aβ aggregates. Lecanemab targets soluble Aβ aggregates, like oligomers and protofibrils. Aducanumab binds to residues 3-7 in the Aβ N-terminus, requiring multiple copies of this epitope to bind. Donanemab (N3pG) is a humanized IgG1 antibody that specifically targets the pyroglutamyl E3 Aβ peptide (Aβp3-42), a variant of the N-terminal truncated Aβ, found exclusively in stable Aβ plaques and highly prone to aggregation. All these drugs have been shown to cause ARIAs in clinical trials, especially in *APOE ε4* carriers in the case of Lecanemab. There is also controversy about the effectiveness of Aducanumab due to differing results between the two phase 3 clinical trials, EMERGE and ENGAGE. Despite this, the FDA approved Aducanumab on June 7, 2021, and Lecanemab on January 6, 2023, for the treatment of MCI or mild dementia. More clinical trials are ongoing to validate the effectiveness and gather extensive data on its long-term impact (85). Actually, a recent study by Cadiz et al. (98) suggested that Aducanumab may impact microglia function, since microglia are unable to prevent plaque reaccumulation after discontinuation of the treatment. Then, Biogen recently announced the discontinuation of Aducanumab development and commercialization to focus on Lecanemab, citing reasons unrelated to safety or efficacy concerns (Biogen communication).

Donanemab is still being tested on early symptomatic AD and in dose determination. Additionally, Remternetug, an improved version of Donanemab, that also specifically targets N-terminal pyroglutamated Aβ, is under study (85).

Regarding safety, immunotherapies have several side effects. The most common are allergic reactions, which are generally manageable. However, more dangerous and difficult to manage are ARIAs. As previously mentioned, in the clinical trials testing these immunotherapies there have been patients that have developed ARIAs (95). The mechanisms underlying ARIAs are not fully understood but appear to be linked to the development of cerebral amyloid angiopathy (CAA) and its associated changes. This might explain the higher occurrence of ARIAs in *APOE ε4* carriers, which have a higher risk of CAA (99). Since immunotherapy is administered intravenously, anti-Aβ antibodies bind first to the Aβ present in the vasculature, compromising their integrity and increasing vascular permeability by triggering an immune response against the vessels (100, 101). Additionally, parenchymal Aβ shifts to the vascular wall, increasing the risk of molecular diffusion through the broken BBB (ARIA-E) and vessel rupture (ARIA-H) (99, 101). Therefore, initiating immunotherapy before widespread CAA development or exploring alternative administration routes is crucial to mitigate ARIA risk. Notably, ARIA occurrence is more common with anti-Aβ antibodies targeting aggregated Aβ, as

this binding can increase local inflammation, worsening CAA, and then, promoting the development of ARIAs (102). Then, targeting soluble Aβ may be a safer approach.

3.5.4 Liquorpheresis

Currently, only a few studies have attempted to decrease target molecules from the CSF using physical methods (liquorpheresis). Proteins from the ISF, such as soluble Aβ, can be removed into the CSF, which includes the ventricles and subarachnoid space (30). As Aβ is in constant equilibrium between the ISF and the CSF, several research studies have suggested a method to address the neuropathology of AD by directly eliminating Aβ from CSF, known as the CSF-sink therapeutic strategy. Such interventions could prove beneficial not only for AD, but also for any other condition involving the accumulation of proteins in the CNS (103, 104).

Similar to the hypothesis of the AMBAR study (72-77), studies have been developed using the replacement techniques and infusion of Aβ-binding molecules, such as albumin or transthyretin, with positive results (105-107). However, this infusion carries a potential risk of elevated intracranial pressure due to albumin's osmotic properties, for instance (78).

Liquorpheresis involves using implantable systems to filter CSF and remove protein from it. The filtered fluid is then returned to the ventricular system or the subarachnoid space. This method has been previously used for treating autoimmune and NDs (108). Additionally, it has also been explored as a potential treatment for CNS infections and subarachnoid hemorrhages (109, 110). As the CSF-ISF barrier is much laxer than the BBB, liquorpheresis is expected to have a stronger effect on clearing CNS deposits compared to plasmapheresis.

This strategy can be performed by different methodologies, some of which have already been clinically tested while others have not. In fact, our research group has proposed a new approach that can be considered a particular method for liquorpheresis (103, 108, 11), which, like any new product or technology needs proof-of-principle and proof-of-concept. The terms proof-of-principle and proof-of-concept are often used interchangeably in industries, such as technology and research, but they have distinct meanings and purposes. While both aim to validate ideas or hypotheses, their approaches and scopes differ significantly, making it crucial to understand these differences for effective project management and successful innovation. A proof-of-principle demonstrates that a particular concept or theory can be successfully implemented, focusing on the feasibility of an idea rather than its practical application. The goal of a proof-of-principle is to validate the underlying principles or theories behind the product idea without necessarily proving its commercial viability or scalability. It is often the initial step in the research and development process, providing a foundation upon which a proof-of-concept template or further development can be built. Thus, a proof-of-concept

is a more advanced stage than a proof-of- principle, since it aims to demonstrate the practicality and potential value of implementing that idea in a real-world scenario.

HYPOTHESIS AND OBJECTIVES

The Aβ peptide is still one of the main targets in the treatment of AD. However, the various therapeutic approaches that have been put forward to try to decrease the levels of this pathogenic protein present important limitations, in addition to significant side effects, as we have highlighted in the previous section.

In this PhD Thesis, we propose a new therapeutic strategy based on the following **HYPOTHESIS**:

Since Aβ peptide is in equilibrium between the brain ISF and the CSF, its removal from the CSF leads to a decrease in the ISF. Therefore, acting from the CSF is more efficient than peripheral administered therapies, due to the closer relationship between ISF and CSF. This is what defines the CSF-sink therapeutic strategy. Moreover, the CSF-sink therapeutic effect is demonstrated by an implantable device equipped with a nanoporous membrane (NPMB) that allows both continuous and selective apheresis of CSF by administering anti-Aβ immunotherapies – while preventing the passage of such drugs- thus decreasing Aβ load in the brain (Intrathecal (IT) pseudodelivery).

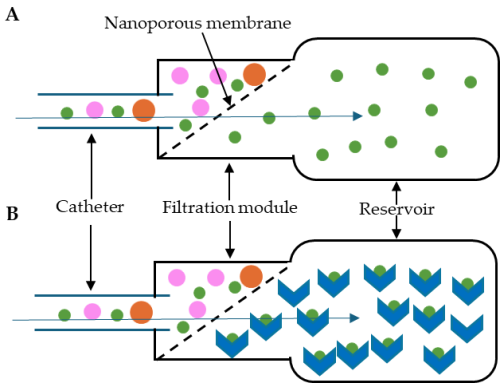

Figure 6. Therapeutic approaches with the NPMBs. CSF reach the device (blue arrow), where it is size based filtered by the NPMB (Selective apheresis, **A**). Then, Aβ (green dots) would be captured by the therapeutic agent (thick blue arrow) in the reservoir (Intrathecal *pseudodelivery*, **B**). Modified from (182).

The CSF-sink strategy can be achieved by means of NPMBs with selective molecular permeability to remove target-molecules from a fluid through a process called selective apheresis (Figure 6A). Selectivity is provided by the selective binding of drugs -in our case it is *immunoselectivity*, because we use antibodies as therapeutic agents-. Thus, membranes allow the passage of small circulating molecules of interest -in our case Aβ- in our fluid of interest -in our case the CSF-, but prevent large therapeutic agents from crossing them, because of their size -in our case mAb-. Precisely to prevent the passage of therapeutic agents into the CSF, selective apheresis is performed inside a closed-loop device. The device can be surgically implanted to connect the IT space -in our case the ventricular system- to a reservoir with the therapeutic solution to filter the CSF and capture the Aβ protein. Since the drug is not released to the organism, we have termed this therapy IT *pseudodelivery* (Figure 6B). Thanks to this new strategy, the filtered CSF can return to the CNS, leading to a reduction in soluble Aβ and subsequently decreasing Aβ deposits in the brain (104, 111).

Therefore, the **GENERAL OBJECTIVE** of this PhD Thesis has been set to provide a proof-of-principle of the selective apheresis mechanism of action and a proof-of-concept of the IT *pseudodelivery* to show the effects of this therapeutic strategy in a murine model of AD.

To achieve this, we propose the following **SPECIFIC OBJECTIVES**:

OBJECTIVE 1: Test the selective permeability of the NPMBs *in vitro*.

a. Study the selective permeability of the NPMBs for small molecules.
b. Study the selective impermeability of the NPMBs for large molecules.

OBJECTIVE 2: Evaluate the feasibility of implanting a device for IT *pseudodelivery* in the AD murine model APP/PS1 in early symptomatic stage.

a. Analyze the effects of implantation surgery on mouse welfare.
b. Determine the permeability/impermeability of the apheresis module *in vivo*.

OBJECTIVE 3: Assess the effects of long-term IT *pseudodelivery* of Aβ–mAbs by percutaneously replacement of therapeutic solution in the AD murine model APP/PS1 in early symptomatic stage.

a. Analyze the effects of long-term implantation of an IT *pseudodelivery* device on mouse welfare.
b. Study the effect of IT *pseudodelivery* of Aβ–mAbs at functional level, evaluating anxiety-like behavior and spatial memory.
c. Assess the effect of IT *pseudodelivery* of Aβ–mAbs on the levels of Aβ in brain parenchyma/CSF/plasma.
d. Perform a comprehensive evaluation of the status of the intracellular and extracellular protein clearance systems.

EXPERIMENTAL DESIGN AND MATERIAL AND METHODS

1. Experimental design for *in vitro* studies

Selective permeability was tested using homemade permeation cameras, where a nanoporous membrane (NPMB) separates 2 cells (Figure 7). Permeation cameras were prepared in 24-well commercial cell cultures insert plates (Figure 7A; VWR; ref.: 734-2737). Thus, plate wells act as donor cells, and culture inserts, as receptors cells (Figure 7B). Since the inserts have polycarbonate membranes attached to them, they were replaced with our NPMBs.

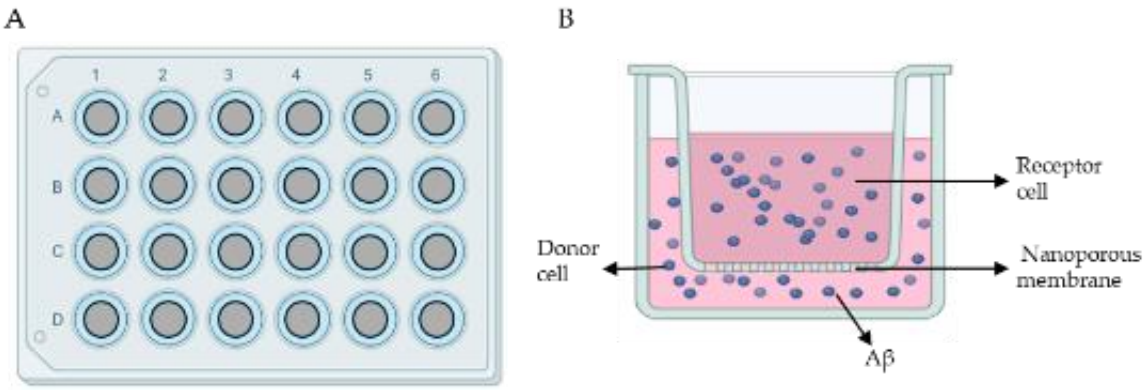

Figure 7. A. Top view of a 24-well plate with transwell inserts (inner circles). **B.** Plate wells act as donor cells, where Aβ peptide will be added. Transwell inserts have the nanoporous membrane attached at its bottom. This design allows the free movement of the peptide from the donor to the receptor cell.

Using this system, a time course was developed to evaluate system efficacy over time. For this purpose, the following test was performed to ensure the correct performance of the NPMBs and permeation cameras. All tests were be developed in a humidified chamber with 5% CO_2, at 37 °C (Memmert™ ICO50med, Fisher Scientific).

1.1. Evaluation of $A\beta_{1-42}$ peptide binding and permeability

To evaluate $A\beta_{1-42}$ peptide binding over time (0, 6, 24 and 48 hours), an initial experiment was performed in triplicate. For each condition, enough volume for triplicates were prepared. From this stock, a 0.5 ml sample was taken (time 0). Then, the stock was distributed in the wells for each time point: 6-, 24-, and 48-hours samples. Donor cells were filled with 0.5 ml of the specified solution, while the receptor cells were filled with 0.16 ml. Tested solutions were artificial cerebrospinal fluid (aCSF; ACSF Cat. No. 3525, Tocris), as control, or a dose of 2 ng/ml of $A\beta_{1-42}$ peptide diluted in aCSF. A higher dose of $A\beta_{1-42}$ (20 µg/ml) was also tested in a subsequent study, but only for 48 hours (Table 3).

Each solution was placed in opposite cells within the same well. Control permeation chambers were also used, where only $A\beta_{1-42}$ solution was added and no NPMB was present. Samples from the donor and receptor cells were collected at the specified time points from the different wells. $A\beta_{1-42}$ peptide concentration was determined in both donor and receptor cells to assess the $A\beta_{1-42}$ peptide binding and the permeability of the NPMBs. This was done

using the Human Aβ_42 ELISA kit (Invitrogen, Waltham, MA, USA, ref.: KHB3441) following the manufacturer's instructions.

Additionally, an ELISA for $A\beta_{1-42}$ aggregates (Invitrogen™ Amyloid beta (Aggregated) Human ELISA Kit, ref.: 10766743) was used to measure them in the 20 µg/ml permeability assay.

Table 3. Summary of conditions for the evaluation of $A\beta_{1-42}$ binding and permeability

	Control	Low dose	High dose
No membrane	0 ng/ml	2 ng/ml	20,000 ng/ml
Membrane	0 ng/ml	2 ng/ml	20,000 ng/ml

Each condition was done in triplicate for each time point.

1.2 Evaluation of albumin impermeability

This experiment was conducted with a design similar to 1.1. In this case, cells were filled with aCSF, as control, or 2 mg/ml of albumin diluted in aCSF. Each solution was placed in opposite cells within the same well. Samples from the donor and receptor cells were collected at the specified time points from the different wells. Control permeation chambers were also used, where only albumin solution was added and no NPMB was present. Samples from the donor and receptor cells were taken after 72-hours incubation. Albumin concentration from the donor and receptor cells from the same well were determined using the Pierce BCA Protein Assay (Thermo Scientific, ref.: 10678484). The resulting concentrations were compared to establishing the impermeability of the nanoporous membrane to albumin.

2. Materials and methods for *in vitro* studies

2.1. Nanoporous membranes (NPMBs)

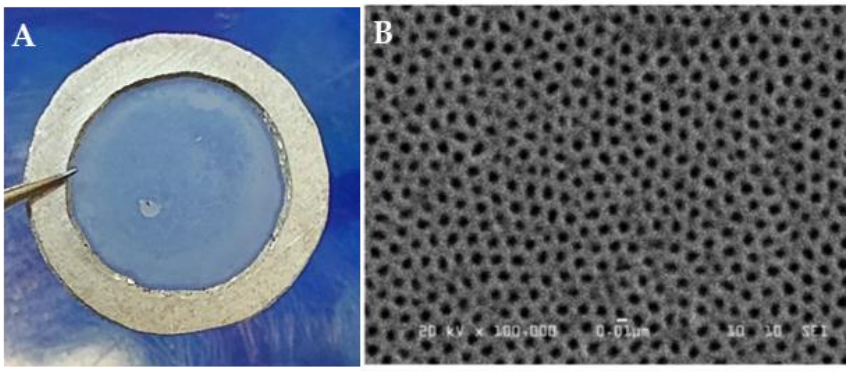

Figure 8. Anodic aluminum oxide nanoporous membrane (AAO-NPMB) employed in the studies. Photograph of a NPMB (**A**) and its high-resolution electron microscopy photograph (**B**).

Anodic aluminum oxide (AAO) NPMBs were manufactured by the Magnetism of Materials and Nanomaterial Group (MAGMATNANO, University of Oviedo). Briefly, they were

obtained by electrochemical anodization of aluminum foils using a two-step anodization method, followed by atomic layer deposition (ALD) with SiO_2 coating, as previously described (112). The membranes (Figure 8) were approximately 50 µm thick and had a pore size of 9 ± 2 nm and porosity of 7 ± 2%, as confirmed by scanning electron microscopy (SEM) and transmission spectra analysis (112, 113). This design allows NPMBs to act as a filter, as they enable the passage of small molecules and prevent the passage of molecules larger than their pore size.

2.2. Human recombinant Aβ1-42 solution

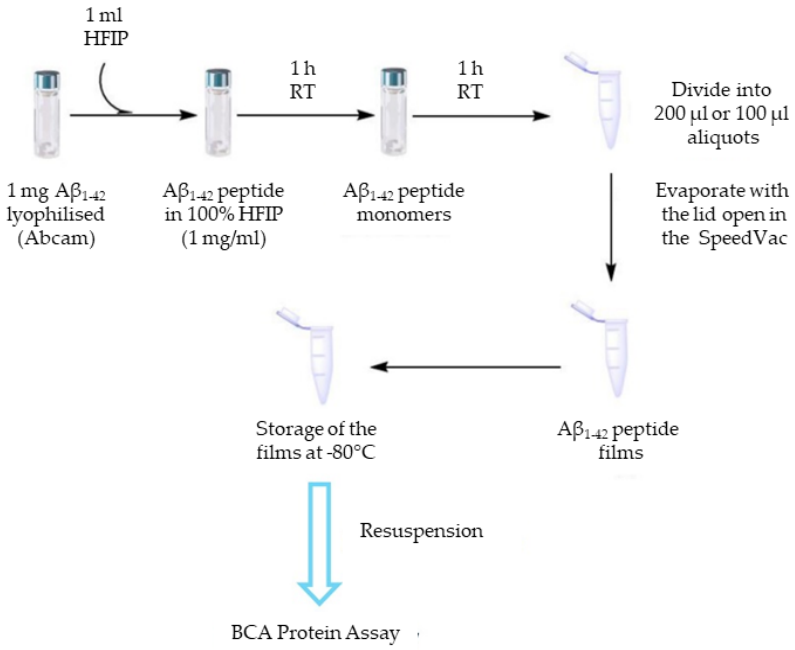

Figure 9. Schematic of the procedure used for the preparation of Aβ1-42 films.

To assess the permeability of Aβ through NPMBs, human recombinant Aβ1-42 (beta-Amyloid Peptide (1-42) (human); Abcam, ref.: ab120301) was used. Aβ1-42 solution was prepared from films, which were first generated from 1 mg vials of recombinant protein dissolved in 1,1,1,3,3,3-Hexafluoro-2-propanol (HFIP, Merck, ref.: 8045150100) (114, 115). The preparation of the films is summarized in Figure 9.

Various resuspension methods were tested to find the optimal method for the Aβ1-42 films with the lowest probability of generating aggregated forms:

1) DMSO/DMEM-F12 solution (1:1);

2) 100% DMSO;

3) HEPES/NaCl (115).

After the resuspension, Aβ1-42 concentration on the films was determined using the BCA Assay, and Western blot analysis was conducted to assess oligomer formation. The first solvent tested was DMSO/DMEM-F12 (DMSO, Molecular Probes, ref.: D12345; DMEM-F12, Gibco, ref.: 11580376), with a film concentration of 469 µg/ml. Positive controls for aggregated Aβ1-42 forms were prepared by resuspending Aβ1-42 stock directly in phosphate buffer saline (PBS; Corning Incorporated, Corning, NY, USA, ref.: 21-040-CM; 50 µg/ml) and

leaving it incubating (aging) in a humidity chamber at 37 °C, and 5% CO_2 for different times (0, 24, 48, 72, and 96 hours). For the other two solvents, modifications were made to the preparation protocol (Figure 10). For both protocols, every 15 minutes the $A\beta_{1-42}$ HFIP solution was vortexed. Then, in the case of 100% DMSO protocol, 10 minutes of sonication were done before the 10 minutes in SpeedVac (CentriVap concentrator; Labconco, Kansas, MO, USA) drying. It was then resuspended with 100% DMSO and stored at -80 °C until use.

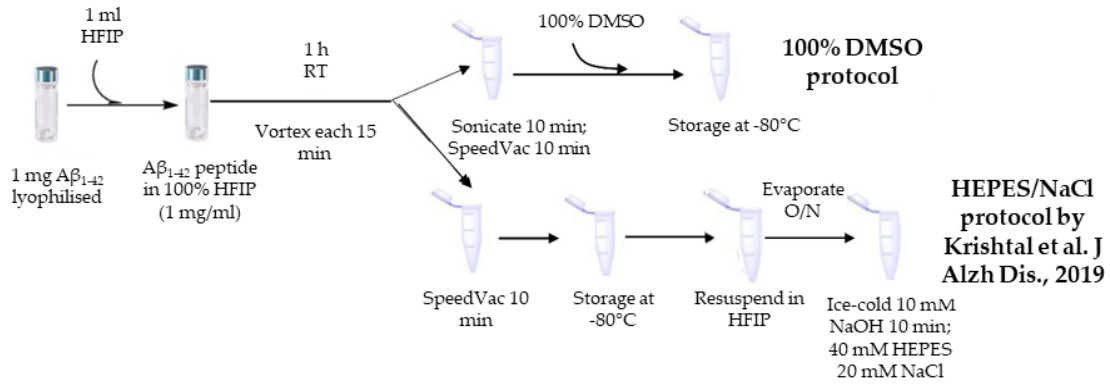

Figure 10. Schematic of the 100% DMSO and HEPES/NaCl protocols for the resuspension of $A\beta_{1-42}$ films.

For the HEPES/NaCl protocol, the film was resuspended again in HFIP, left to dry overnight, diluted in ice-cold 10 mM NaOH for 10 minutes, and then resuspended in a buffer containing 40 mM HEPES and 200 mM NaCl (115).

For these two protocols, Western-blot analysis was conducted using $A\beta_{1-42}$ samples resuspended in PBS and aged $A\beta_{1-42}$ samples for 72 hours as controls. Three known peptide concentrations (10 µg/ml, 25 µg/ml and 50 µg/ml) were loaded based on previous cell culture experiments (115).

Thus, 15 µl from each sample were run in an SDS-PAGE homemade acrylamide/bisacrylamide (Acrylamide solution (30%) – Mix 37.5: 1; Applichem, ref.: A3626). Gel was composed by an upper stacking 4% and a resolving 15% gels. Then, proteins were transferred to PVDF membrane (PVDF Amersham Hybond P 0,2 µm; Cytiva, ref.: 10600021). The membrane was then blocked in 5% bovine serum albumin (BSA) TBS-T (Tris buffered saline and 1% Tween-20). Next, membrane was incubated with human Anti-Aβ antibody [MOAB-2] (Abcam; ref.: ab126649), which detects Aβos, diluted in TBS-T (1:100). This incubation was performed overnight at 4 °C. After washing in TBS-T, the membrane was further incubated with anti-mouse secondary antibody conjugated with horseradish peroxidase (1:25,000; Goat Anti-Mouse IgG H&L (HRP) preadsorbed; Abcam, ref.: ab97040) for 1 hour at room temperature (RT). Detection was developed with ECL (ECL™ Prime Western Blotting System; Cytiva, RPN2232). Images were acquired using the software VisionWorksLs (UVP).

2.3. Albumin solution

To study the selective permeability of NPMBs, BSA fraction V (~ 68 KDa; BSA; PanReac AppliChem, ref.: A1391) was used. BSA was dissolved in aCSF with gentle agitation to achieve a final concentration of 2 mg/ml.

3. Experimental design for the feasibility *in vivo* study

The *in vivo* study was performed using the murine model of AD APPswe/PS1dE9 mice (hereafter referred to as "APP"), that co-express a chimeric mouse/human APP carrying the Swedish mutation (Mo/HuAPP695swe) with the human presenilin-1 gene containing the exon 9 deletion variant (PSEN1dE9) (116-118), in 129Sv background (parents kindly provided by Drs. José María Pérez Freije and Olaya Santiago Fernández, University of Oviedo).

For the experiments, seventeen seven-month-old and eight non-transgenic littermates (WT) male mice were used (Figure 11).

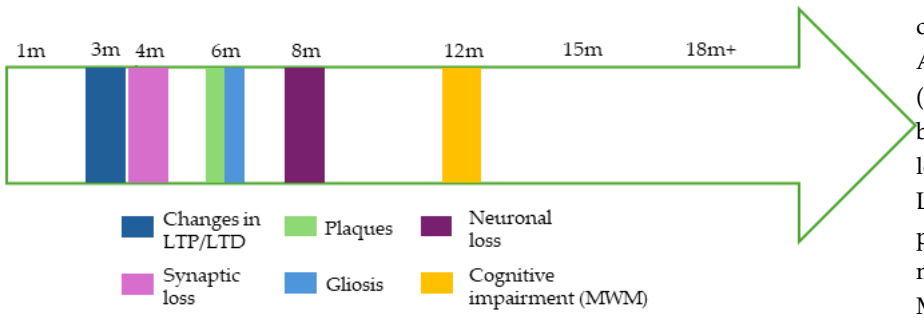

Figure 11. Phenotype characterization of APPswe/PS1dE9 mice (C57BL6; C3H background). LTD, long-term depression; LTP, long-term potentiation; m, month (s); MWM, Morris water maze. Modified from https://www.alzforum.org/research-models/appswepsen1de9-c57bl6

All these mice underwent surgery to implant the device for IT *pseudodelivery* with different solutions in their reservoirs. The mice were randomly distributed as follows:

- Verification of the correct cannula implantation: one WT mouse (see *In vivo dye infusion and visualization* section).
- Verification of the system impermeability to antibody diffusion: Two APP and two WT mice (see *In vivo impermeability and permeability test* section).
- Proof-of-concept for IT *pseudodelivery* strategy feasibility (Figure 12): eight APP and two WT mice had the mAb-filled reservoir; seven APP and three WT mice had the vehicle-filled reservoir.

Additionally, eight APP and one WT male mice of the same age were used as control (Naïve), with no intervention. The mice were housed under a 12/12 light/dark cycles (with lights on at 8:00 a.m.) at both constant temperature (22 ± 2 °C) and relative humidity (55 ± 7%), and provided with *ad libitum* access to water and rodent global diet chow (A40; SAFE®, Rosenberg, Germany) at the Animal Facilities of University of Oviedo (Spain).

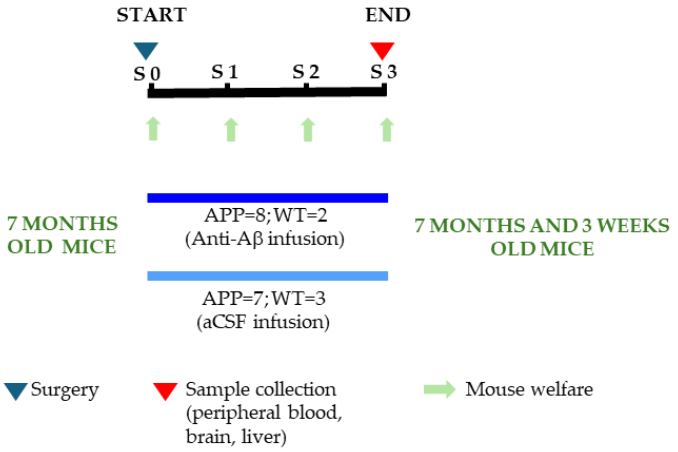

Figure 12. Experimental design for the proof-of-concept for IT *pseudodelivery* strategy feasibility.

All animal procedures were performed during the light period (8:30-15:00 a.m.) and were approved by the Research Ethics Committee of University of Oviedo (PROAE ID 32/2020) in compliance with European (Directive 2010/63/UE) and Spanish (RD118/2021, Law 32/2007) legislation.

4. Materials and methods for the feasibility *in vivo* study

4.1. Implantable device

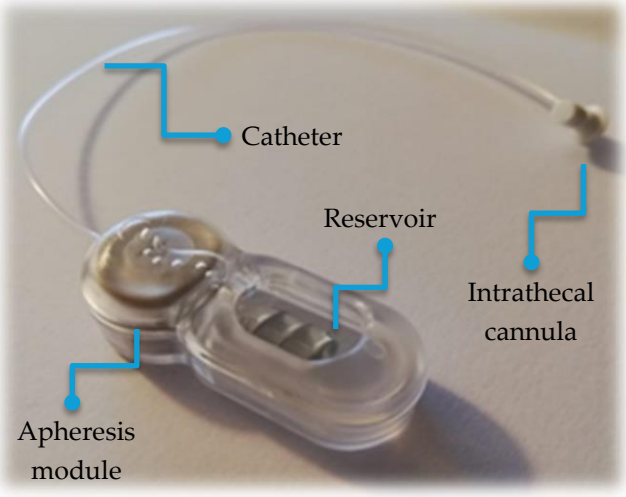

Figure 12. Device used in the feasibility study. The device includes an apheresis module housing the NPMBs, connected to a reservoir containing the therapeutic agent, both enclosed in a protective capsule. A catheter links the apheresis module to the intrathecal cannula that is implanted in the brain.

The device was designed and manufactured by Neuroscience Innovative Technologies S.L. for continuous and selective apheresis of CSF. An initial prototype of the device for IT *pseudodelivery* (119) was used for this study.

It consists of a subcutaneous reservoir and an apheresis module with selective AAO NPMBs connected to an IT brain infusion cannula (Brain Infusion Kit 3; ALZET®, Cupertino, CA, USA; ref.: 0008851) (Figure 12). The reservoir has a volume of 100 µL, with a self-sealing port, which allows filling using a 50 µL syringe (800 series microliter syringes;

Hamilton, Reno, NV, USA; ref.: 84857). Due to its size (3.5 x 1 x 1 cm), this device could only be implanted in large mice, weighing at least 30 g.

4.2. Filling the reservoir with anti-Aβ mAb or Vehicle

The reservoir was filled, under sterile conditions, with a solution of anti- $A\beta_{1-42}$ mAb, which recognizes human but not murine $A\beta_{1-42}$ (clone 6E10; Biolegend, San Diego, CA, USA, ref.: 803003). To determine the most appropriate dose of the antibody, we referred to previous studies that used a single intracerebroventricular injection of 10 μg of antibody and evaluated Aβ clearance (86, 88). Since the effect of the 10 μg lasted up to seven days but not up to thirty days, we decided to use a dose of 50 μg of antibody and a study duration of three weeks of treatment in this first approach. Thus, ten devices were loaded with a solution of non-conjugated anti-Aβ mAb diluted in aCSF, while four devices contained fluorophore-conjugated anti-Aβ antibody (Alexa Fluor® 488 anti-Aβ antibody, clone 6E10; Biolegend, ref.: 803013) for the impermeability *in vivo* test. The final mAb concentration within the device was 500 μg/ml. Eleven devices were used as controls and filled with the same volume of aCSF.

4.3. PCR genotyping

For mice genotyping, genomic DNA was extracted from small tail samples. The samples were digested in a lysis buffer (1M Tris-HCl (pH 8), 0.5 M EDTA, 10% SDS, 5 M NaCl and 80 μg/ml proteinase K) for 1 hour at 60 °C, with agitation of 1400 rpm using a thermo-shaker (TS-100; Biosan). After this, 6 M NaCl solution was added and centrifuged for 10 minutes at 13000 rpm. The resultant supernatant was transferred to a new tube, isopropanol was added, and the mixture was centrifuged for 10 minutes at 13000 rpm. The pellet was then resuspended in 70% ethanol, followed by resuspension in sterile distilled water using a thermos-shaker with a max agitation of 1400 rpm at 60 °C. DNA concentration was determined using a NanoDrop One 2000c, Spectrophotometers (Thermo Scientific, Waltham, MA, USA).

Subsequently, genotyping was carried out with a polymerase chain reaction (PCR). This was done using the AmpliTaq Gold 360 Master Mix following manufacture instructions (Thermo Scientific, Waltham, MA, USA, ref.: 10219584) and the primers for transgene detection (Table 4). Fragments were visualized by electrophoresis on 2% agarose gels.

Table 4. List of primers used for mouse genotyping

Primer type	Sequence 5′→3′
Wild type forward	GTG TGA TCC ATT CCA TCA GC
Common	GGA TCT CTG AGG GGT CCA GT
Mutant Forward	ATG GTA GAG TAA GCG AGA ACA CG

4.4. Surgery and mice welfare for the feasibility study

First, "clean" and "dirty" areas were prepared to keep asepsis and a sterile surgical field throughout the surgical process. The working area was cleaned with soap and water, dried, and wiped with 70% ethanol. Protective paper (Nalgene ™ Super Versi-Dry™ Surface Protectors, Thermo Scientific™, Waltman, MA, USA; ref.: 74000-00) was then placed on the surface. Before each procedure, and between surgeries on different mice, all instruments were cleaned thoroughly with an enzymatic detergent (Helizyme, B. Braun, ref.: 18767) and sterilized using both 70% ethanol and heating at 230 °C for 1 minute, in a microbead sterilizer (B1305-E-FIS, Fisherbrand, Waltman, MA, USA). In addition, the larger equipment, such as the isoflurane delivery system, surface of the induction chamber, the stereotaxic frame and its digital controller, and the stereo microscope, as well as other products used during surgery, were cleaned with 70% ethanol.

Prior to the surgery, analgesia and antibiotics were administered to all mice 15-20 minutes before the beginning of the surgery. For this purpose, buprenorphine (0.05 mg/kg, subcutaneous injection (SC), Bupaq; Richter Pharma, Wels, Austria), and enrofloxacin (10 mg/kg, SC, Syvaquinol; Syva Laboratories, Leon, Spain) were used. In addition, warm sterile saline solution (1 ml of 0.9% NaCl) was given intraperitoneally (IP) or SC to prevent dehydration during the surgical procedure.

The surgical procedure was performed on anesthetized mice (2% isoflurane and 0.4 L/min O_2) according to the protocol described in (119, 120). The mice were placed in a digital stereotaxic frame (Digital Compact Mouse Stereotaxic Instrument; Harvard Apparatus, Holliston, MA, USA; ref.: 75-1823) and the surgery area was shaved. After confirming the absence of pedal withdrawal reflex, Lubrithal ocular ointment (Dechra Pharmaceuticals, Northwick, UK) was applied. Then, a linear incision was made to expose the skull, and a subcutaneous pocket was opened to insert the device. A 0.5 mm diameter craniotomy was drilled in the skull at the coordinates AP -1.26 mm, ML -0.7 mm, with respect to Bregma, and a cannula was then implanted into the right lateral ventricle, at -2.5 mm to the skull. The cannula was secured with cyanoacrylate (Cicastick Suturvet; Chemical Iberica, Salamanca, Spain), and the incision was sutured using 5-0 monofilament non-resorbable polypropylene suture thread (Sterile Surgical Suture; Lorca Marín, Murcia, Spain).

After surgery, the mice were placed, for the first 24 hours, in an intensive care cage with temperature control (28-30 °C; S50 Advance Series II Model; Vetario, Western-Super-Mare, UK) for 24 hours to ensure proper recovery. They received meloxicam (2mg/kg, SC, Metacam; Boehringer Ingelheim, Rhein, Germany) as anti-inflammatory treatment and 1 ml of sterile saline solution (SC). The mice were then housed individually to prevent damage to the sutures. For the next 3 days, they received buprenorphine (SC), every 12 hours, and meloxicam (SC), every 24 hours, with a progressive reduction in the dose, and 1 ml of sterile saline solution. The two weeks following surgery, enrofloxacin was injected SC every day, with a progressive reduction in the dose, and 0.5 ml of sterile saline solution.

This study was scheduled to terminate at 21 days, and throughout the study, the mice were monitored daily for weight, cage behavior (nest formation), food, and water consumption. Body weight was measured between 9:00 a.m. and 1:00 p.m. using a portable balance (CB 501; Adam Equipment, Milton Keynes, UK).

4.5. *In vivo* dye infusion and visualization

The correct placement of the catheter in the right lateral ventricle was confirmed by means of a dye *in vivo*. A 5% (w/v) solution of blue dextran dye (5 kDa; TdB Labs, Ultuna, Arlanda, ref.: 87915-38-6) in aCSF was infused into a WT mouse implanted with vehicle-filled device through the reservoir. A total of 200 µL of tracer solution was infused in two sessions, 24 hours apart, at a flow rate of 5 µL/min using a programmable syringe pump (Remote Infuse/Withdraw Pump 11 Elite Nanomite Programmable Syringe Pump; Harvard Apparatus; ref.: 70-4507). After infusing the CSF tracer, while the mouse was anesthetized with 1.5-2% isoflurane and 2.5% O_2, the cisterna magna was exposed as previously described (121) (more details in the *Fluids and Tissues Collection and Processing* section of the long-term study). A stereomicroscope with an integrated camera (S9i; Leica Microsystems, Wetzlar, Germany) was used to observe the CSF color in the mouse ventricular system *in vivo*. The mouse was then euthanized by decapitation, and the brain was immediately removed and frozen at 80 °C after embedding in Tissue-Tek® O.C.T. (Sakura Finetek Europe, Alphen aan den Rijn, The Netherlands, ref.: 12351753). The brain was sliced into 80 µm thick transversal sections using a cryostat (CM1900; Leica Microsystems). Images were captured with a digital camera to visualize the blue/dark color tracer in the mouse ventricular system.

4.6. Fluids and Tissues Collection and Processing

Three weeks after surgery, or sooner in case of severe complications, mice were deeply anaesthetized with a combination of ketamine (100 mg/kg) and xylazine (10 mg/kg) in a saline solution. The device was carefully removed and thoroughly cleaned externally with 70% ethanol. Subsequently, the fluid was removed from the reservoir and stored at −80 °C for further analysis.

Peripheral blood samples (~0.5–1 ml) were collected from the inferior vena cava using EDTA (as anticoagulant; 1.5 mg/ml blood) pretreated 1 ml syringes (BD, Franklin Lakes, NJ, USA) and intravenous catheters (BD Insyte-W, 21 GA, BD). The blood was immediately centrifuged at 2000 g, and the plasma was stored at −80 °C until use.

After blood collection, the abdominal aorta was cut at the same level of the vena cava, and sterile ice-cold PBS (pH 7.4; ~30 mL) was perfused to clean the tissues. The brain was carefully dissected, and the cortex and hippocampus were isolated and stored at −80 °C until use. The liver was also collected and stored at −80 °C for later use.

4.6.1. Tissue Processing for Biochemical Analysis

In mice used for biochemical analysis, the brains were dissected sagittally, and the cerebral cortexes and hippocampi were extracted from the right hemispheres and subsequently frozen at −80 °C. In addition, liver samples (200 mg) were also taken and divided into two halves, with one half frozen until use at −80 °C.

The cerebral cortexes, hippocampi and liver samples (100 mg) were homogenized in lysis buffer (20 mM HEPES pH 7.4, NaCl 100 mM, NaF 50 mM, EDTA 5 mM, Triton X-100 1%) with protease inhibitors (Complete™, Mini Protease Inhibitor Cocktail; Roche, Basel, Switzerland, ref.: 11836153001) using a glass potter homogenizer on ice. The homogenates were then centrifuged for 10 min at 12,000 × g at 4 °C, and the supernatants were collected for analysis. Total protein concentration was determined using a NanoDrop One 2000c, Spectrophotometers (Thermo Scientific, Waltham, MA, USA).

4.6.2. Tissue Processing for Histological Analysis

The left hemisphere and liver tissues were fixed with 4% paraformaldehyde (PFA; pH 7.4), freshly prepared from 16% PFA (Electron Microscopy Science, Hatfield, PA, USA, ref.: 50-980-487) diluted in Sorensen's phosphate buffer overnight at 4 °C for histology processing. Then, they were washed in PBS and immersed in 30% sucrose (Panreac AppliChem, Darmstadt, Germany, ref.: A2211) in PBS for 24 h for cryoprotection. Samples were then frozen in O.C.T. and stored at −80 °C until use. Coronal sections (40 µm) were cut on a cryostat and preserved in a solution containing 30% glycerol (VWR Chemicals, Radnor, PA, USA, ref.: 24386.298) and 30% ethylene glycol (Sigma-Aldrich, St. Louis, MO, USA, ref.: 324558) in 0.02 M monobasic phosphate buffer (PB) with pH 7.2 at −20 °C until further use.

For the validation of the catheter placement (see *In vivo dye infusion and visualization* section), the brain was sectioned into 30 µm coronal slices using the cryostat. Three non-consecutive coronal sections were washed in PBS 3 times for 10 minutes, and then stained with 0.5% Toluidine blue O (Sigma Aldrich, ref.: T3260) in distilled water for 1 minute at RT. After staining, the sections were washed again in PBS 3 x 10 minutes, dried overnight at RT, and mounted on gelatin-coated slides (VWR). Aqueous mounting medium (Aquatex®, Merck, Rhaway, NJ, USA, ref.: 108562) was used to cover the sections. Visualization and image

acquisition were done using the integrated camera of a stereomicroscope and compared with Paxinos and Franklin's Mouse Atlas (122) and the Allen Brain Mouse Atlas (http://mouse.brain-map.org/ ; accessed on 31 May 2024) for reference.

4.7. *In vivo* impermeability and permeability test

To evaluate the selective permeability of the NPMBs *in vivo*, impermeability for mAb was evaluated using mice samples through immunofluorescence and fluorescence quantification. Permeability for Aβ was determined by analyzing the solutions from the reservoirs.

4.7.1. Immunofluorescence for mAb impermeability test

To test the impermeability of NPMBs to the antibody, free-floating immunofluorescence was performed with consecutive coronal sections of hemibrains and liver sections for each mouse. After washing with PB, sections were washed with PBS and incubated with 1% Triton X-100 and 1% BSA. For Aβ staining, samples were incubated with anti-Aβ amyloid antibody [MOAB-2] (Table 5) or anti-β-amyloid (clone 6E10; Table 5) under gentle shaking at 4 °C for four days. Slices were then incubated with the secondary antibody conjugated with Alexa 488 (Donkey anti-Mouse IgG (H + L) Alexa Fluor Plus 488; Invitrogen, Hong Kong, China, ref.: A32766; Table 5). Controls included sections incubated only with the secondary antibody or without primary or secondary antibodies. DAPI was used for nuclear staining, and sections were mounted on slides with polyvinyl alcohol mounting medium with DABCO (Supelco, Bellefonte, PA, USA, ref.: 10981). Then, they were observed with an Olympus BX61 fluorescence microscope.

Table 5. List of antibodies used in the feasibility study

Primary antibody	Clone/Catalogue	Dilution	Host	Manufacturer
Aβ	MOAB-2	1:200	Mouse	Abcam
Aβ	6E10	1:1000	Mouse	Biolegend
Secondary antibody	**Clone/Catalogue**	**Dilution**	**Host**	**Manufacturer**
Alexa 488 Anti-Mouse IgG	10424752	1:1000	Donkey	Invitrogen

Abbreviations: Aβ, beta amyloid; IgG, immunoglobulin G

4.7.2. Fluorescence Levels

Levels of fluorescence were measured at 488 nm excitation and 530 nm emission in whole blood, plasma, and liver homogenates. Samples (50 µL) were aliquoted into a black 96-well optical bottom plate (Fisher Scientific, Hampton, NH, USA, ref.: 10281092). The plate was scanned on an Odyssey XF Imaging System (LI-COR Biosciences, Lincoln, NE, USA) and the results were expressed as mean fluorescence (signal).

4.7.3. $A\beta_{1-42}$ immunoassays

To test the permeability of the NPMBs, $A\beta_{1-42}$ levels in the reservoir fluid were measured on the ultra-sensitive single-molecule array (Simoa) HD-X analyzer platform (Platform for Biomarkers, Achucarro Basque Center for Neuroscience, Leioa, Spain) following the manufacturer's instructions. $A\beta_{1-42}$ levels in plasma were also measured. The $A\beta_{1-42}$ Simoa 2.0 assay (Cat. N° 101664) was purchased from Quanterix (Billerica, MA, USA). These assays detect levels of $A\beta_{1-42}$ in human plasma with a detection limit of 0.044 pg/mL (range 0.0017–0.108 pg/mL). Two quality control samples were included with the samples, and calibrators were tested in duplicates. The average of the two measurements (pg/mL) was used for statistical analysis.

$A\beta_{1-42}$ levels in brain cortex and hippocampus homogenates were quantified using the Human Aβ_42 ELISA Kit (Invitrogen) following the manufacturer's instructions.

4.8 Quantification of Aβ plaques

Aβ plaques were quantified using immunofluorescence labeling. Three non-consecutive coronal sections were used for each mouse. After washing PBS, the sections were then blocked with a solution containing 10% normal donkey serum, 0.1% Triton X-100 (Sigma-Aldrich, MO, USA, ref.: T8787) and 40 µg/ml Fab fragments (AffiniPure Fab Fragment Goat Anti-Mouse IgG (H+L), Jackson Immunoresearch, PA, USA, ref.: 115-007-003) for 1 hour at RT. Next, after washing with PBS, incubation overnight at 4 °C with anti-Aβ amyloid antibody [MOAB-2] (Table 5) diluted in the blocking solution, without the Fab fragments, was done under gentle shaking. After this, slices were incubated with the secondary antibody conjugated with Alexa 488 (Donkey anti-Mouse IgG (H + L) Alexa Fluor Plus 488; Table 5), in the same solution than primaries, for 1 hour at RT. Sections were mounted on glass slides using mounting medium with DAPI (Fluoroshield™ with DAPI, Sigma, ref.: F6057). Images were obtained with the Leica TCS-SP8X Spectral Confocal Laser Microscope (Leica Microsystems, Germany).

Aβ plaques were analyzed in the cortex and hippocampus using ImageJ software (123). To obtain the percentage of area occupied by Aβ plaques in each area, we applied the following formula for each slice: [area covered with Aβ plaques in the brain region]/ [total area of the brain region]. The mean percentage for each mouse was then calculated, and the average for each treatment group was determined. The number of Aβ plaques per mm^2 was determined with a similar formula: [number of Aβ plaques in the brain region]/ [total area of the brain region]. For further analysis, Aβ plaques were classified based on size using a classification similar to that described by Trujillo-Estrada et al. (124): <100 μm^2, 500-1000 μm^2, 1000-2000 μm^2 and >2000 μm^2.

4.9. Statistical Analysis

Statistical analysis and graphical representation were performed using GraphPad Prism 10.2.3 (GraphPad Software, Dotmatics, Bishop's Stortford, U.K.). Normality of the variables were assessed using the Shapiro–Wilk test. Kruskal-Walli's test, followed by Dunn's post hoc test, was used for comparisons among groups. A significance level of $p < 0.05$ was considered for all analyses.

5. Experimental design for the long-term *in vivo* study

Fourteen seven-month-old male mice, ten APP and four WT mice, were used for this experiment. Mice were randomly distributed between treatment groups: five APP and two WT mice had the reservoir filled with vehicle, while five APP and one WT mice had the reservoir filled with mAb (Figure 13). Additionally, five APP and six WT mice of the same age were used as control (Naïve), with no intervention.

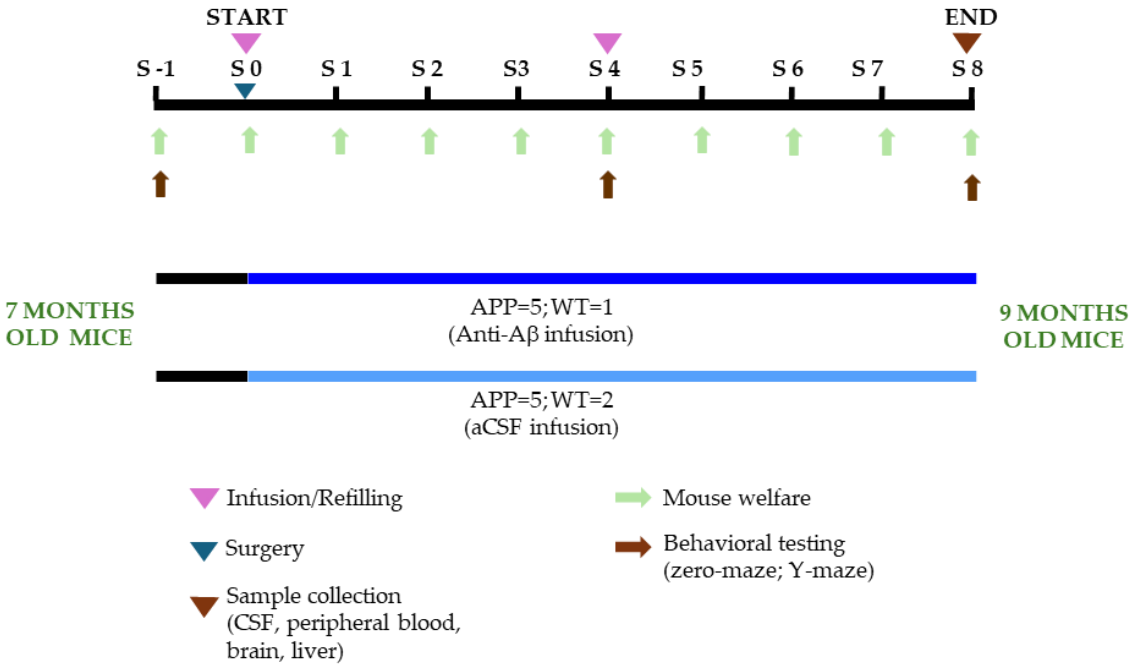

Figure 13. Experimental design of the long-term *in vivo* study.

The mice were housed under a 12/12 light/dark cycles (with lights on at 8:00 a.m.) at both constant room temperature (22 ± 2 °C) and relative humidity (55 ± 7%), and provided with *ad libitum* access to water and rodent global diet chow (A40; SAFE®, Rosenberg, Germany) at the Animal Facilities of University of Oviedo. All animal procedures were performed during the light period (8:30-15:00 a.m.) and were approved by the Research Ethics

Committee of University of Oviedo (PROAE ID 06/2022) in compliance with European (Directive 2010/63/UE) and Spanish (RD118/2021, Law 32/2007) legislation.

6. Materials and methods for the long-term *in vivo* study

6.1. Implantable device

The device used in the feasibility proof-of-concept study underwent modifications before this experiment. Mainly, the protective capsule was removed, and a silicone coating (LOCTITE® SI 5248 silicone, Henkel, Düsseldorf, Germany) was applied, reducing the device's size (125).

6.2. Surgery and mice welfare for the long-term study

To improve the welfare of mice and decrease some side effects of the surgery (126-128), mice were housed individually one week before the surgery with a diverse range of cage enrichments. In particular, a red polycarbonate arch (Bio-Serv, Flemington, NJ, USA, ref.: K3357), sizzle-nest (Datesand, Bredbury, UK), disposable cardboard tunnels, cocoon (Datesand), or paper wool (Datesand) were simultaneously provided. In addition, palatable gel diet energy and transport food (SAFE®, Rosenberg, Germany) was placed in a Petri dish on the cage bedding.

On the day of the surgery, as pre-anesthetic warming has been shown to help to maintain normothermia during surgery (129), mice were placed in the veterinary intensive care unit and kept at a controlled temperature of 33-36 °C for 30 minutes prior to surgery. In the meantime, the surgical area and all the material was prepared as previously described (see *surgery and mice welfare* section of the feasibility study). After this, drugs were injected (see details in *surgery and mice welfare* section of the feasibility study) and anesthesia was induced. Following the shaving, a topical anesthetic ointment (lidocaine 25 mg/g, EMLA; AstraZeneca, Cambridge, UK) was applied around the ear canal. The mouse was then carefully positioned in the stereotaxic frame with a heating pad underneath to maintain body temperature and prevent hypothermia. After confirming the absence of pedal withdrawal reflex and applying ocular ointment, a U-shaped incision was made. To aid in locating the craniometric points bregma and lambda on the cranial surface and improve the fixation of the posterior cannula, the periosteum was gently scraped using a microcurette (Model 10080-05; Fine Surgical Tools F.S.T., Chandler, AZ, USA) and dried with a cotton swab soaked in 70% ethanol. The coordinates of the bregma and lambda landmarks were measured, and the head position was adjusted to align them within a 0.5 mm difference ("flat-skull" position). As well as in the previous feasibility study, a craniotomy was drilled in the skull and the cannula was carefully inserted at the coordinates AP -1.26 mm, ML -0.7

mm, with respect to Bregma, and at -2.5 mm to the skull. In this case, a cannula holder (Stoelting Co., Wood Dale, IL, USA, ref.: 51636-1) was used to maintain the cannula while it is glued to the skull surface with cyanoacrylate. To ensure the cannula is in place, a thin annular layer of UV light-curing resin (Transbond XT 4; 3M, Saint Paul, MN, USA) was applied around the base of the brain cannula and cured in three 20-second cycles with a portable UV lamp (Lux E; Bestdent, Gansu, China). After letting the resin harden for 1 minute, the top of the cannula was removed with a bone nipper (Model 16102-11, F.S.T.). Then, the incision was sutured using 5-0 monofilament suture thread.

After the surgery, while the mice were still under anesthesia, their front and back nails were trimmed closely to prevent scratching that could hinder healing or reopen wounds. Thereafter, meloxicam and sterile saline solution were injected, before leaving them in a clean and enriched cage inside the veterinary intensive care unit. Postoperative care and treatments were as previously explained for the first study. Throughout the study, the mice were monitored daily for weight, cage behavior (nest formation), food, and water intake. Body weight was measured between 9:00 a.m. and 1:00 p.m. using a portable balance.

6.3. Re-fill

The device is designed so that the solution in the reservoir can be replaced with fresh therapeutic solution at certain intervals. In the case of this study, four weeks post-surgery, a re-fill of the device was performed.

A programmable syringe pump was used to extract 50 µl from the reservoir and to inject the same volume of a fresh solution, with or without the antibody, depending on the experimental group, at a rate of 2 µl/min. All this procedure was done under inhaled anesthesia (isoflurane), controlling the temperature of the mice with a heating pad underneath to prevent hypothermia during the procedure.

6.4. Behavioral analysis

Mice were assessed for general and anxiety-like behaviors and memory performance at three time points: before surgery (W-1), 4 weeks after surgery (W4), and just before the end of the experiment (W8), all between 9:00 am and 2:00 pm. Mice were acclimatized to the environment and staff a week before testing.

The elevated zero maze test was used to evaluate general and anxiety-like behaviors. The test apparatus (UGO Basile, Gemonio, Italy; ref.: 40163) consisted of a 60 cm diameter annular gray platform elevated 60 cm above the floor, with two 15 cm closed corridors (Figure 14A). A single mouse was placed in the center of one corridor, and its behavior was recorded for 5 minutes using a Basler ace acA1300-60gm GigE camera (Basler, Ahrensburg, Germany). The analysis included measuring the total distance traveled and the percentage of time spent in the open area.

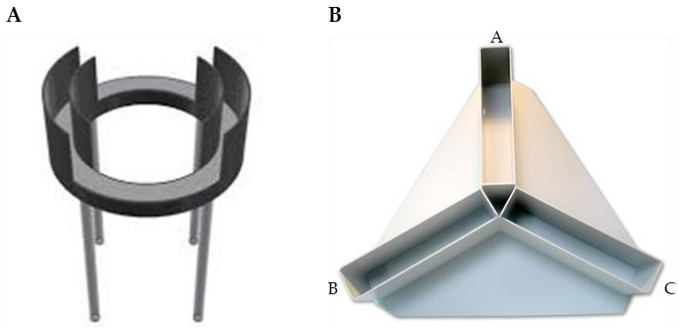

Figure 14. Photographs of the mazes employed. A. Zero maze. Image taken from https://www.noldus.com/applications/zero-maze. **B.** Y-maze with an example of the labeling of the arms. Image taken from https://www.harvardapparatus.com/compact-y-maze-panlab.html.

Y-maze tests were conducted to assess cognitive changes in short-term spatial working memory (measured by spontaneous alternation and percentage of novel arm entries) and exploratory activity (measured by total arm entries). The Y-maze (Harvard Apparatus, ref.: 76-0079) consists of three symmetrical arms at a 120° angle from each other, which were labeled with A, B, and C before the test (Figure 14B). As previously described (130), each mouse was placed into the distal part of the arm labelled A, facing towards the center of the maze, and allowed to freely explore the maze for 8 minutes. The number of arm entries and alternations were recorded to calculate the alternation percentage applying the formula described by Prieur and Jadavji (131). Additionally, the number of entries and time spent in arms B and C were noted to identify the preferred arm. An entry of a mouse was considered when all four limbs were within the arm, passing the middle circle region. The following day, the non-preferred arm (B or C) was closed, and the mouse was placed at the end of arm A. Mouse was allowed to explore the open arms during 15-minute training session. Then, the mouse was returned to its home cage. After one hour, the closed arm was reopened, and the mouse was placed at the end of A arm again. Mouse was allowed to explore for 5-minute test session. The total number of entries in each arm was recorded to determine the percentage of entries into the novel arm.

All videos were analyzed using Ethovision XT version 16 software for Windows (Noldus, Wageningen, The Netherlands).

6.5. Fluids and Tissues Collection and Processing

Eight weeks after surgery, or sooner if necessary, mice were anaesthetized with isoflurane and CSF was collected as previously described (121). Briefly, the cephalic area was shaved and cleaned with 70% ethanol. The mouse was placed in the intervention area, and once the reflexes were absent, a sagittal incision was made in the skin. Then, the subcutaneous tissue and cervical muscles were dissected using micropincers under a stereotactic microscope S9i (Leica), avoiding damaging vessels and causing bleeding. If bleeding occurred, sterile swabs were used to clean and stop the bleeding. Once the cisterna magna, located as an inverted triangle posterior to the cerebellum and over the spinal cord, was identified, the mouse head was positioned at a 135° angle to the back. The working area was cleaned to prevent blood contamination of the CSF. A sterile beveled glass capillary was used to perforate the dura

mater, with slight pressure until a change in resistance was felt. CSF was collected through the capillary by passive flow, transferred to microcentrifuge tubes and stored at -80°C until analysis.

The device was then carefully removed and thoroughly cleaned externally with 70% ethanol. Subsequently, the fluid was removed from the reservoir and stored at −80 °C for further study.

Peripheral blood samples were collected from the inferior vena cava using EDTA pretreated 1 mL syringes and intravenous catheters. Blood was immediately centrifuged at 2000 g, and plasma was stored at −80 °C until use.

After blood extraction, the abdominal aorta was cut at the same level of the vena cava, and sterile ice-cold PBS was perfused to clean tissues. The brain was carefully dissected, and the cortex and hippocampus were isolated and stored at −80 °C until use. The liver was also collected and stored at −80 °C for later use.

6.5.1. Tissue Processing for Biochemical Analysis

Brains were dissected sagittally, and the cerebral cortexes and hippocampi were extracted from the right hemispheres and subsequently frozen at −80 °C. In addition, liver samples (200 mg) were also taken and divided into two halves, with one half frozen until use at −80 °C.

The cerebral cortexes, hippocampi, and liver samples (100 mg) were homogenized in lysis buffer (20 mM HEPES pH 7.4, NaCl 100 mM, NaF 50 mM, EDTA 5 mM, Triton X-100 1%) with protease inhibitors using a glass potter homogenizer on ice. The homogenates were then centrifuged for 10 min at 12,000 × g at 4 °C, and the supernatants were collected for analysis. Total protein concentration was determined using a NanoDrop One 2000c, Spectrophotometers.

6.5.2. Tissue Processing for Histological Analysis

The left hemisphere and liver tissues were fixed with 4% PFA, freshly prepared from 16% PFA diluted in Sorensen's phosphate buffer overnight at 4 °C for histology processing. Then, they were washed in PBS and immersed in 30% sucrose in PBS for 24 h for cryoprotection. Samples were then frozen in O.C.T. and stored at −80 °C until use. Sagittal sections (40 µm) were cut on a cryostat and preserved in a solution containing 30% glycerol and 30% ethylene glycol in 0.02 M monobasic phosphate buffer of pH 7.2 at −20 °C until further use.

6.6. Immunohistochemistry for Aβ plaques analysis

Aβ plaques were quantified using immunohistochemistry labeling. Ten non-consecutive coronal sections (spaced 300 µm) were used for each mouse. After washing with 0.1 M PB (pH 7.4), a heat-mediated citrate buffer pH 6.0 antigen reveal step was performed. Next, the

slices were washed with PB, and the peroxidase endogenous activity was quenched for 45 min with 1% H_2O_2. After washing with PBS, the sections were incubated with 1% Triton X-100, 1% BSA, and 0.5% fetal bovine serum (FBS). Samples were then incubated with anti-Aβ antibody [MOAB-2] under gentle shaking at 4 °C for four days. Peroxidase activity was developed with the Vectastain Elite ABC-HRP kit (Rabbit IgG; Vector Laboratories, ref.: PK-6101) using diaminobenzidine (DAB; Abcam, Cambridge, UK, ref: ab64238). Images were obtained with an Olympus BX61 microscope (4× objective) equipped with a digital camera (Olympus D70).

Aβ plaques analysis was as previously described in *Quantification of Aβ plaques* section.

6.7. Immunofluorescence

Immunofluorescences for Aβ, AQP4, GFAP, Iba-1 and p62 were performed as previously described in *Quantification of Aβ plaques* section with the corresponding primary and secondary antibodies (Table 6). Immunolabeled sections were imaged using different microscopes: whole slice images were captured with the Montage Microscope Nikon Eclipse Ni-E with the Camera Nikon DS-Fi3 (Nikon Instruments Inc., Tokio), 10X images with the Leica TCS-SP8X Spectral Confocal Laser Microscope (Leica Microsystems, Germany) and 40X images with the Nikon Eclipse Ti Confocal Microscope with Spectral detector C2Si (Aβ, Iba-1, GFAP and AQP4 labeling), and the Leica TCS-SP8X Spectral Confocal Laser Microscope (p62 labeling). These immunofluorescences were repeated in brain sections from the feasibility study to further understand.

Table 6. List of antibodies used in the long-term study

Primary antibody	Clone/Catalogue	Dilution	Host	Manufacturer
Aβ	MOAB-2	1:200	Mouse	Abcam
AQP4	AB3594	1:500	Rabbit	Sigma
GFAP	Z0334	1:500	Rabbit	Dako
Iba-1	ab5076	1:400	Goat	Abcam
p62	2C11	1:100	Mouse	Sigma
Secondary antibody	**Clone/Catalogue**	**Dilution**	**Host**	**Manufacturer**
Alexa 488 Anti-Mouse IgG	10424752	1:1000	Donkey	Invitrogen
Cy2 Anti-Mouse IgG	715-225-151	1:500	Donkey	Jackson ImmunoResearch
Cy3 Anti-Goat IgG	705-165-147	1:500	Donkey	Jackson ImmunoResearch
Cy5 Anti-Rabbit IgG	711-175-152	1:500	Donkey	Jackson ImmunoResearch

Abbreviations: Aβ, beta amyloid; AQP4, aquaporin 4; GFAP, glial fibrillary acidic protein; Iba-1, ionized calcium binding adaptor molecule 1; IgG, immunoglobulin G

6.7.1. Immunofluorescences analysis

To analyze p62 expression through immunofluorescence, mean fluorescence intensity was measured using ImageJ software. Rectangular areas of 387.5 µm x 387.5 µm were selected, with three in the cortex and two in the hippocampus per sagittal slice, and two in the cortex and two in the hippocampus per coronal slice. This resulted in a total of six areas in the cortex and four in the hippocampus for each mouse. Autofluorescence from lipofuscin was assessed in the same areas in images captured using a Hyd3 detector after a 590 nm excitation.

Global microglial (Iba1) and astrocytic (GFAP) activation was evaluated by measuring the mean fluorescence intensity in rectangular areas in the cortex and hippocampus. In the feasibility study, samples from mice were analyzed using areas of 1025 µm x 1025 µm in the cortex and hippocampus. This resulted in six areas in the cortex and two in the hippocampus for each mouse. In the subsequent study, the areas measured 1500 µm x 700 µm, with a total of nine areas in the cortex and three in the hippocampus per mouse. In these same areas, astrocytic proliferation was measured as the percentage of area occupied by GFAP immunostaining. Microglial and astrocytic activation around plaques was analyzed in 40X images (290.91 µm x 290.91 µm in the feasibility study; 314.91 µm x 314.91 µm in the long-term study samples). Aβ plaques were categorized based on their radius: 10 µm, 15 µm, 20 µm and 30 µm. Mean fluorescence intensity was determined within a 15 µm radius of Aβ plaques, and the percentage of area covered by GFAP immunostaining was also quantified in this area. The number of microglia cells was also quantified in these images. Microglia cells were classified based on morphology: ramified (longer ramifications than the soma, thin, with only nucleus in the soma) and ameboid (shorter ramifications than the soma, thick and/or presence of cytoplasm in the soma) (Figure 15). In addition, the number of microglia within a 15 µm radius of Aβ plaques was determined with the following formula (Figure 15):

$$\sqrt{(x_2 - x_1)^2 + (y_2 - y_1)^2} - \frac{Feret_{plaque} + minFeret_{plaque}/_2}{2} - \frac{Feret_{microglia} + minFeret_{microglia}/_2}{2} \leq 15\ \mu m$$

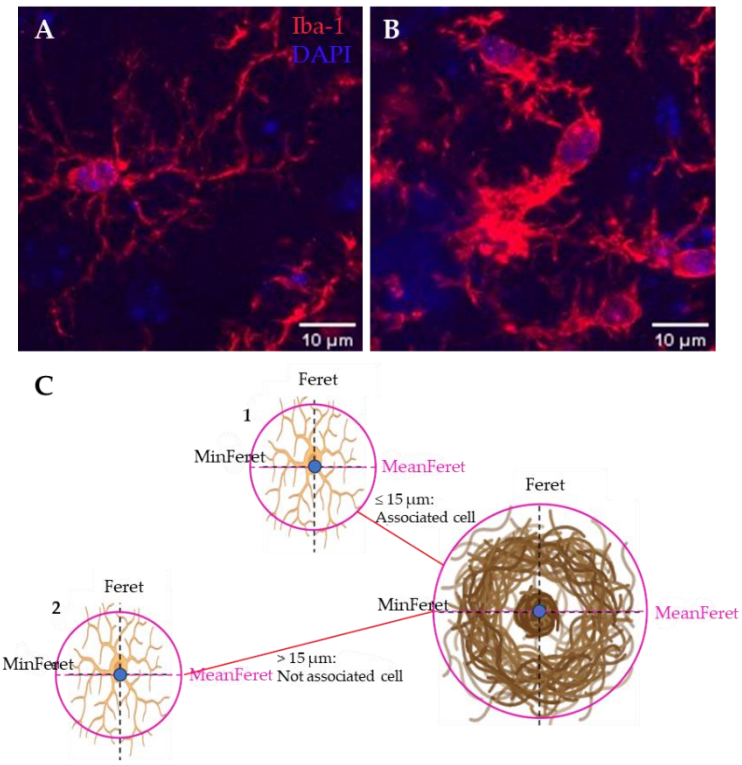

Figure 15. Analysis of microglia. A, B. Representative images of ramified (**A**) and ameboid (**B**) microglia labeled with Iba-1 antibody. Scale bar: 10 µm. **C.** Scheme of the analysis of microglia distribution. First, the distance between the plaque centroid (x_1, y_1) and the microglia centroid (x_2, y_2) (blue dots) was calculated. Half of the mean of Feret and minFeret of plaque and half of the mean of Feret and minFeret of microglia (Means in magenta) was then subtracted. If the distance was less than or equal to 15 µm, like it is microglia 1, it was considered associated with the plaque. If the distance is higher than 15 µm, like microglia 2, it was not associated with the plaque.

AQP4 analysis was conducted on 40X images with dimensions of 290.91 µm x 290.91 µm in the feasibility study and 314.91 µm x 314.91 µm in the long-term study samples. AQP4 expression was evaluated by measuring the mean intensity fluorescence in one cortex and one hippocampus image per mouse. To quantify AQP4 polarization, the fluorescence intensity of a 50 µm segment centered around a blood vessel was measured. Five vessels with similar diameter (~20 µm) per image were analyzed. The AQP4 polarization index of each mouse was calculated by normalizing the peak and baseline values and dividing the normalized peak value by the normalized baseline value.

6.8. Aβ$_{1–42}$ immunoassays

Aβ$_{1–42}$ levels in CSF, plasma, and the reservoir fluid at 4 and 8 weeks of IT *pseudodelivery*, were measured on the ultra-sensitive single-molecule array (Simoa) HD-X analyzer platform (Billerica, MA, USA) following the manufacturer's instructions. The Neurology 4-PlexE assay (Cat. Nº 103670; Quanterix) was used, which includes Aβ$_{1–42}$, Aβ$_{1–40}$, GFAP and NfL. Two quality control samples were included with the samples, and calibrators were tested in duplicates. The average of the two measurements (pg/ml) was used for statistical analysis.

Aβ$_{1–42}$ levels in brain cortex and hippocampus homogenates were quantified using the Human Aβ_42 ELISA Kit (Invitrogen) following the manufacturer's instructions.

6.9. Statistical Analysis

Statistical analysis and graphical representation were performed using GraphPad Prism 10.2.3 (GraphPad Software, Dotmatics, Bishop's Stortford, U.K.). Normality of the variables was assessed using the Shapiro–Wilk test. For parametric variables, Student's t-test for independent samples was used to compare WT and APP mice. For non-parametric variables, Kruskal-Walli's test, followed by Dunn's post hoc test, was used for comparisons among groups at each time point, and Friedman's test, followed by Dunn's post hoc test, was used to assess changes within each group over time. A significance level of $p < 0.05$ was considered for all analyses.

RESULTS

1. Optimizing Aβ$_{1-42}$ solution preparation protocol for *in vitro* studies

Aβ$_{1-42}$ peptide has a strong tendency to aggregate under *in vitro* conditions. Therefore, we first examined different protocols for preparing Aβ$_{1-42}$ solutions, to determine the optimal method with the lowest probability of generating aggregated forms.

1.1. HEPES/NaCl protocol was effective in preserving the oligomeric forms of Aβ

Three distinct protocols were evaluated: 1) DMSO/DMEM-F12 solution (1:1); 2) 100% DMSO; 3) HEPES/NaCl (115).

To assess which of the three was most suitable, we performed a western blot for Aβ. Samples incubated in PBS, without performing a previous HFIP film, at different incubation times served as aggregation control. Figure 16 shows that these PBS control samples were mainly monomeric Aβ$_{1-42}$ and insoluble aggregates at all time points. Interestingly, the DMSO/DMEM-F12 resuspension exhibited both monomers and high molecular weight oligomers, resulting in a smearing pattern in the lanes, indicating varying levels of aggregation, without large insoluble fibers in the stacking gel.

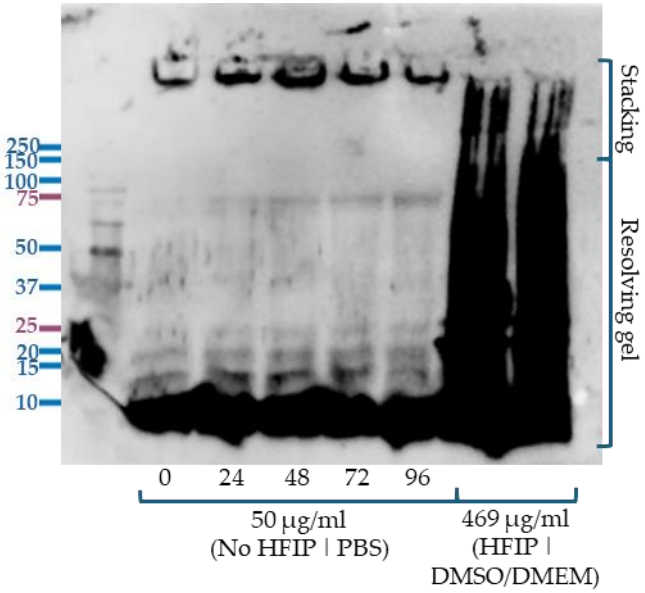

Figure 16. Western blot for PBS and DMSO/DMEM Aβ$_{1-42}$ preparations. Aβ$_{1-42}$ samples resuspended directly in PBS and aged for 0, 24, 48, 72 and 96 hours formed highly aggregated structures that did not enter in the resolving gel. Despite this, significant amounts of monomeric Aβ$_{1-42}$ and some oligomeric forms were present. Conversely, Aβ$_{1-42}$ samples prepared from resuspension in HFIP and then resuspended in DMSO/DMEM-F12 did not form large structures. Instead, a high abundance of oligomers of various sizes, along with a substantial amount of monomeric Aβ$_{1-42}$, were observed.

When the 100% DMSO and HEPES/NaCl protocols were evaluated by western blot, we observed abundant Aβ$_{1-42}$ monomers, with increasing insoluble aggregate formation as Aβ$_{1-42}$ concentration rose (Figure 17). Moreover, oligomeric forms below 50 kDa were also seen. Therefore, although both protocols appeared to preserve oligomeric forms, HEPES/NaCl protocol maintained slightly better the different oligomeric forms. Then, we selected this protocol used for the next experiments.

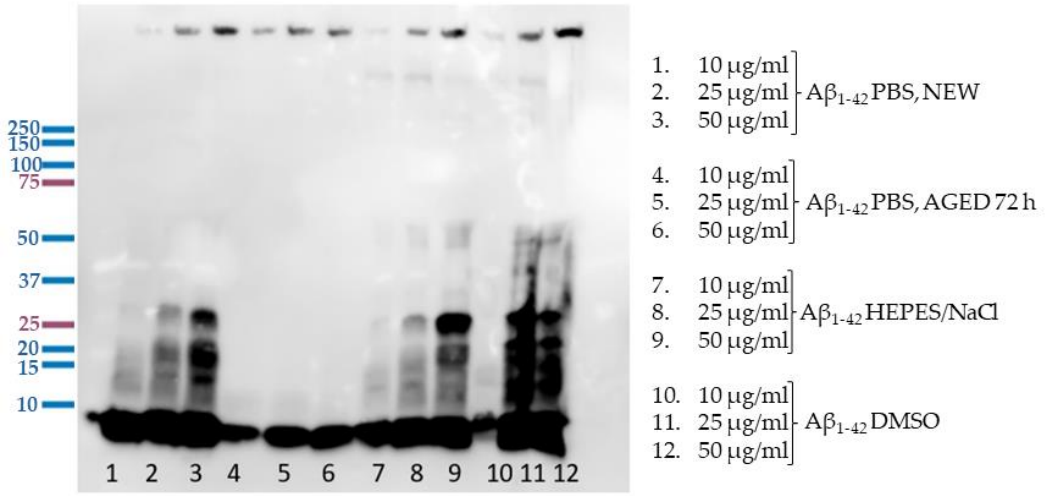

Figure 17. Western blot showing different Aβ1-42 resuspension protocols at three peptide concentrations. Lanes 1-6 show Aβ1-42 prepared under prone-to-aggregate conditions (PBS). Lanes 7-12 show Aβ1-42 prepared from HFIP films further reconstituted in HEPES/NaCl (lanes 7-9) or in DMSO (lanes 10-12).

1.2. Higher than expected Aβ1-42 concentrations were needed for the *in vitro* studies

After selecting the resuspension protocol, the permeability of the manufactured AAO NPMBs was tested using permeation chambers, with separated donor and receptor cells.

We were aware that it would be difficult to have the desired peptide concentration in the permeation chambers, since the material they are made of, polystyrene, does not have low adhesion properties and Aβ is very sticky. Since Aβ1-42 concentration in CSF samples in AD is ~ 735 pg/ml (132), we considered starting with a higher working Aβ1-42 solution concentration of 2000 pg/ml.

Due to the small size of the Aβ1-42 peptide in its monomeric form (~ 4 kDa), we expect it to have the ability to diffuse through the NPMB in both directions: from the donor cell to the receptor cell and the other way around. Thus, we added Aβ1-42 peptide solution in some cases to the donor cell and in other cases to the receptor cell. This Aβ1-42 was reconstituted in HEPES/NaCl, as indicated in the previous section. Reconstituted stock Aβ1-42 concentration was 267 µg/ml, previously determined using BCA. Thus, the desired working Aβ1-42 concentrations were achieved diluting Aβ1-42 stock in aCSF. Cells with no Aβ1-42 peptide at time 0 are filled with aCSF, as vehicle solution. Table 7 summarizes the contents of each permeation chamber.

Table 7. Summary of the content of the permeation chambers

Condition Receptor | Donor	Content (final volumen)	
	Receptor (160 µl)	Donor (500 µl)
aCSF | aCSF	aCSF	aCSF
aCSF | Aβ	aCSF	2.64 ng/ml
Aβ | aCSF	8.25 ng/ml	aCSF
No membrane (660 µl)		
aCSF	aCSF	
Aβ	2 ng/ml	

Thus, to determine the Aβ1-42 permeability over time, its levels were measured at 6, 24 and 48 hours by ELISA. We obtained much lower values than expected, since results in all cells, including control wells without NPMBs, were similar to those in aCSF, suggesting that all Aβ1-42 may have bound to the wells (Table 8).

Table 6. $A\beta_{1-42}$ ELISA results from the permeability assay using 2000 pg/ml

Receptor | Donor	6 hours (pg/ml)		24 hours (pg/ml)		48 hours (pg/ml)	
	Receptor	Donor	Receptor	Donor	Receptor	Donor
aCSF | aCSF	38.5	57.5	-	-	-	-
aCSF | aCSF	38	-	-	-	-	-
Aβ | aCSF	120	33.5	37	32.5	53.5	47
Aβ | aCSF	117	27.5	34.5	38.5	44.5	78
aCSF | Aβ	34.5	32	47.5	42.5	53	-
aCSF | Aβ	48	39	58.5	36	-	-
Aβ	51.5		51		-	
Aβ	41.5		42		-	

Therefore, to carry out *in vitro* studies as we have proposed, it is necessary to work at much higher Aβ1-42 concentrations than those initially established.

2. Testing the selective permeability of AAO nanoporous membranes *in vitro*

As we did not obtain good results working with 2000 pg/ml of Aβ1-42, we performed a study with an Aβ1-42 concentration close to the toxic range for SH-SY5Y cells, 20 µg/ml (115). Aβ1-42 stock concentration was estimated with a BCA assay, as indicated previously, and the concentration was 267 µg/ml.

2.1. AAO NPMBs are permeable to Aβ1-42 and impermeable to albumin *in vitro*

Table 9. Summary of the content of the permeation chambers

Condition Receptor | Donor	Content (final volumen)	
	Receptor (160 µl)	Donor (500 µl)
aCSF | aCSF	aCSF	aCSF
aCSF | Aβ	aCSF	26.4 µg/ml
Aβ | aCSF	82.5 µg/ml	aCSF
No membrane (660 µl)		
aCSF	aCSF	
Aβ	20 µg/ml	

The design of this experiment was similar to the previous one. Table 9 summarizes how permeation chambers were prepared.

Only 48 hours samples were analyzed by ELISA. Permeation chambers incubated for 48 hours with aCSF in both cells (aCSF \| aCSF) presented very low signal

Table 10. $A\beta_{1-42}$ ELISA results. Expected concentrations at equilibrium: 20 µg/ml

Receptor | Donor	µg/ml	
	Receptor	Donor
aCSF | aCSF	0.0001	0.0001
aCSF | aCSF	0.0001	0.0001
Aβ | aCSF	16.11	13.99
Aβ | aCSF	13.40	13.26
aCSF | Aβ	11.93	10.93
aCSF | Aβ	11.20	11.54
Aβ	11.54	
Aβ	12.00	

levels. However, in those permeation chambers were $A\beta_{1-42}$ solution was added in either of the two cells ($A\beta_{1-42}$ \|aCSF or aCSF \| $A\beta_{1-42}$), the concentration of $A\beta_{1-42}$ detected (when corrected for the dilution factor) was very similar at both sides of the NPMBs (Table 10).

Thus, these results suggest that, after 48 hours of incubation, the system would be at equilibrium, which is what we were looking for. However, although we expected higher concentrations (20 µg/ml) at equilibrium from the estimation made, $A\beta_{1-42}$ levels in the permeation chambers without NPMBs (Aβ), which had a starting concentration of 20 µg/ml, were equal to those observed in the permeation chambers with NPMBs.

Therefore, this indicates that either we are losing peptide, or we are indeed adding a lower amount of peptide from the starting point.

Possible reasons for the loss of peptide could be that it is sticking to the walls of the permeation chambers or that the high concentration of $A\beta_{1-42}$ that we are working with is prone to form aggregates. And these aggregates cannot be determined with this ELISA kit. Therefore, we tested a specific ELISA for $A\beta_{1-42}$ aggregates. The results indicated that at 20 µg/ml, aggregates were not detected in the samples from the permeation chambers, but they were detected in the stock, which was 10 times more concentrated (267 µg/ml; Table 11).

Table 11. $A\beta_{1-42}$ aggregates ELISA results

Receptor | Donor	µg/ml	
	Receptor	Donor
aCSF | aCSF	0.00	0.00
aCSF | aCSF	0.00	0.00
Aβ | aCSF	-0.54	-0.48
Aβ | aCSF	-0.58	-0.28
aCSF | Aβ	-0.63	-0.22
aCSF | Aβ	-0.46	-0.29
Aβ	-0.55	
Aβ	-0.42	
Aβ stock	1.67	

Once we have established that the NPMBs allowed the passage of small substances, such as $A\beta_{1-42}$, in both directions, we evaluated albumin (~ 68kDa), a much larger molecule than the pore size, to assess the selective permeability. Thus, a solution containing 2 mg/ml albumin was added to either the receptor or donor cell and its concentration was measured in both cells after 72 hours of incubation. The results demonstrated that NPMBs do not allow the passage of larger substances than their pore size, as albumin was only detected in the cells where it was initially placed (Figure 18).

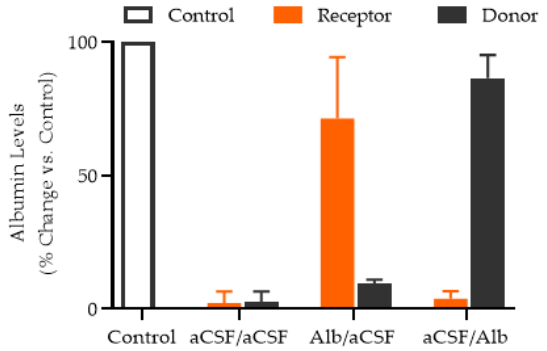

Figure 18. In vitro testing of nanoporous membranes selective impermeability. Albumin levels expressed as a percentage relative to the control permeation chamber, without a nanoporous membrane, after 72 hours of incubation. Receptor cell/Donor cell. Alb (albumin). Data shown as mean ± SEM (n = 6 replicates). Modified from (119).

In conclusion, the designed NPMBs selectively allow the passage of small molecules like $A\beta_{1\text{-}42}$, while effectively blocking larger molecules such as albumin.

3. Proof of concept of the feasibility of the implantation of IT *pseudodelivery* device in a murine model of Alzheimer's disease

3.1. The intraventricular cannula implantation and its connection to the device were validated

The implantation surgery involved two steps: first, placement of the IT *pseudodelivery* device in a subcutaneous pocket located in the lumbar region of the mouse; second, insertion a cannula at the intracerebroventricular level, connected to the *pseudodelivery* device. The specific stereotaxic coordinates (AP -1.26 mm, ML -0.7 mm and DV -2.5 mm) were taken from the commonly used mouse brain atlases, Paxinos and Franklin (99) and Allen Brain Mouse Atlas (Figure 19A, B).

To confirm the connection between the device and intrathecal cannula, a dextran blue dye solution (5 kDa) was added to the device reservoir of one of the mice (Figure 19C). After 24 hours, the flow of the dye solution through the whole system was visualized. Figure 17D shows how the dextran blue reaches the catheter connecting the device to the IT cannula. Moreover, cisterna magna has a bluish color (Figure 19E), confirming correct flow. Cannula insertion at the stereotaxic coordinates was further confirmed by toluidine blue staining of coronal sections (Figure 19F).

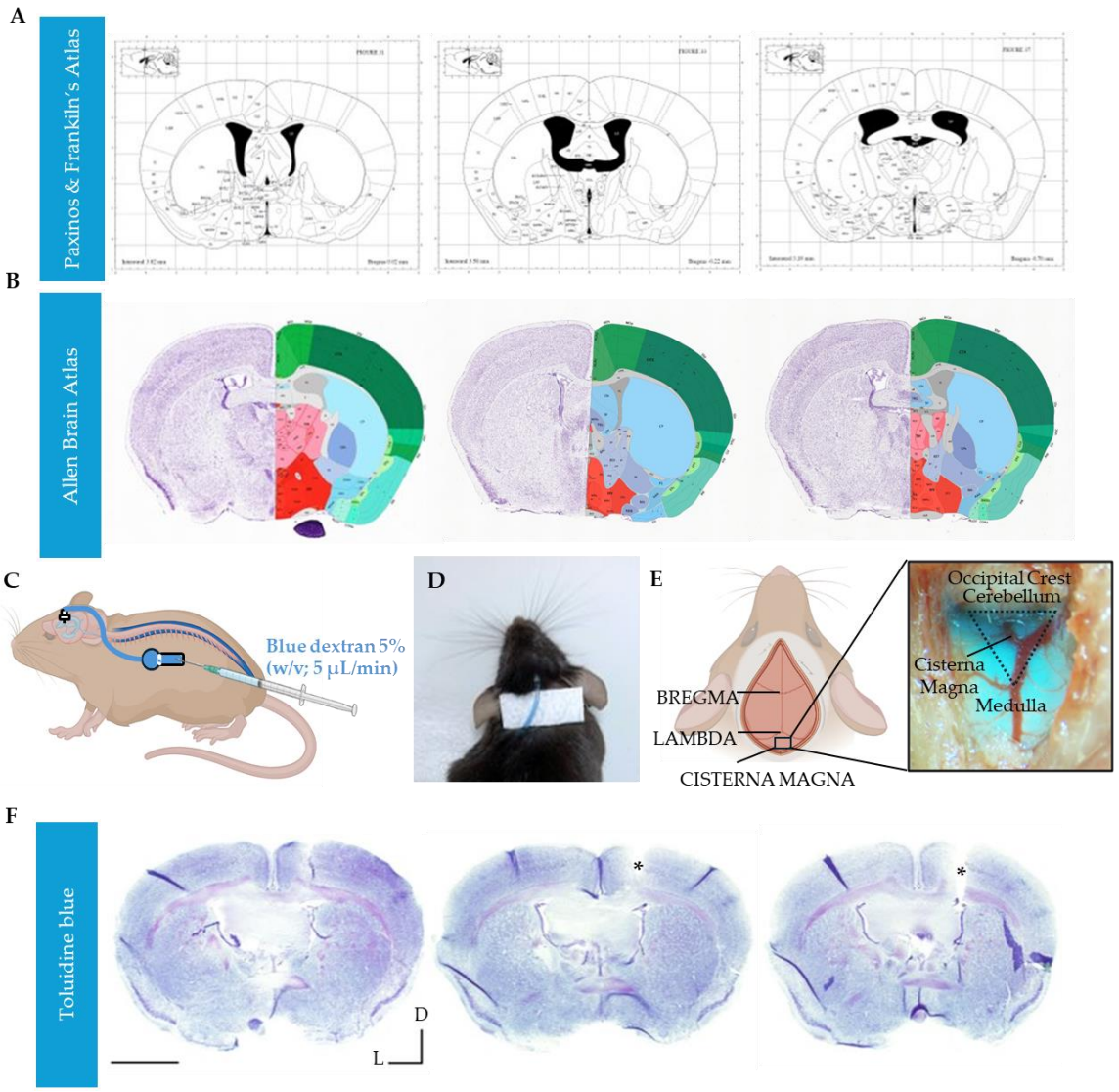

Figure 19. Confirmation of the correct placement of the cannula. A, B. Mouse brain sections close to the stereotaxic coordinates chosen for the cannula insertion from the Paxinos & Franklin (**A**) and Allen Brain (**B**) atlases. **C.** Representative scheme of blue dextran (5%, v/v in aCSF) infusion. **D.** Dorsal view of the connecting tube between the cannula and the device filled with blue dextran. **E.** Scheme of a mouse skull (left) and the cisterna magna of the mouse dyed with blue dextran (right). **F.** Histological validation with toluidine blue staining, referencing mouse brain atlases. Scale bar: 2mm. D, dorsal; L, left; *, cannula placement. Images taken from (125).

3.2. The complexity of the surgery and/or the size of the device may result in mouse welfare complications

The selection of mice for the feasibility study was based on several factors. The primary consideration was the weight (4.29 ± 0.41 g) and the size (3.5x1x1 cm) of the device. In fact, the device weight accounted for 12.86 ± 0.44% of seven-month-old APP mice's weight and 14.92 ± 0.38% of WT mice of the same age. Moreover, the length of the device, which is 66.51 ± 1.77% of the back length in APP mice and 69.56 ± 1.86% in WT mice, was found to be the most limiting factor. As a result, only male mice weighing at least 30 g were used.

Thus, a total of twenty-five male mice, consisting of seventeen APP and eight WT mice, were successfully operated on. Among them, eight APP and two WT mice had the mAb-filled reservoir, while seven APP and three WT mice had the vehicle-filled reservoir. However, after surgery a series of events were observed that led us to stop the study in some of the intervened mice. Therefore, lethargy was one of the events that appeared most frequently in these mice throughout the study. Hence, three mice were euthanized due to severe lethargy within 48-72 hours post-surgery, another mouse one week later, and another three after two weeks. Additionally, one mouse experienced significant weight loss and was euthanized two weeks after surgery. The remaining sixteen mice (64% of the total) completed the three-week infusion study without complications, exhibiting normal cage behavior, such as nest formation and grooming (Table 12).

Table 12. Summary of the mice used in the feasibility study and the complications observed

Animal ID	Genotype	Content Infused	Time implanted	Complications
7	APP	mAb	48 h	Lethargy
20	WT	mAb	48 h	Lethargy
21	WT	aCSF	72 h	Lethargy
5	APP	mAb	1 week	Lethargy
11	APP	mAb	2 weeks	Weight loss
26	APP	mAb	2 weeks	Lethargy
27	APP	aCSF	2 weeks	Lethargy
28	APP	aCSF	2 weeks	Lethargy
2	APP	aCSF	3 weeks	None
8	APP	aCSF	3 weeks	None
9	APP	aCSF	3 weeks	None
12	APP	aCSF	3 weeks	None
4	APP	aCSF	3 weeks	None
17	WT	aCSF	3 weeks	None
19	WT	aCSF	3 weeks	None
3	APP	mAb	3 weeks	None
6	APP	mAb	3 weeks	None
10	APP	mAb	3 weeks	None
1	APP	mAb	3 weeks	None
18	WT	mAb	3 weeks	None
13	APP	mAb 488	3 weeks	None
14	APP	mAb 488	3 weeks	None
15	WT	mAb 488	3 weeks	None
16	WT	mAb 488	3 weeks	None
38	WT	aCSF-Blue dextran	3 weeks	None
29	APP	Naïve	-	None
30	APP	Naïve	-	None
31	APP	Naïve	-	None
32	APP	Naïve	-	None
33	APP	Naïve	-	None
34	APP	Naïve	-	None
35	APP	Naïve	-	None
36	WT	Naïve	-	None
37	APP	Naïve	-	None

Abbreviations: aCSF, artificial cerebrospinal fluid; APP, APPswe/PS1dE9; mAb, monoclonal antibody; mAb 488, Alexa 488-conjugated monoclonal antibody; WT, wild type.

3.3. The nanoporous membranes are permeable to Aβ and impermeable to the Anti-Aβ Antibody *in vivo*

To evaluate the effectiveness of IT *pseudodelivery*, it was first determined if the CSF-soluble Aβ peptide could reach, through the catheter, the apheresis module, where the NPMB is located, and reach the reservoir, where the therapeutic solution is stored.

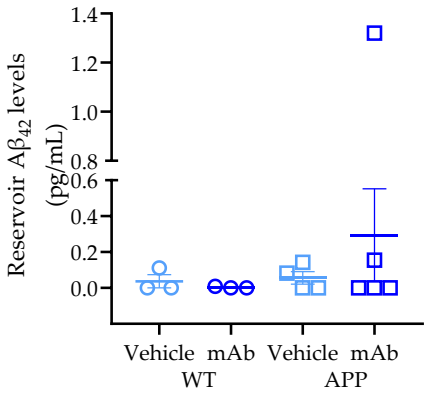

Figure 20. In vivo validation of NPMBs permeability to Aβ. Aβ levels detected (pg/mL) in the reservoir of WT and APP mice, which could be loaded with vehicle or with anti-Aβ mAb (mAb). Data are presented as mean ± SEM. Each dot represents one mouse. Modified from (119).

Thus, at the end of the 3-week study, devices were explanted, and fluid was extracted from the reservoir to measure $A\beta_{1\text{-}42}$ levels. As the volume of the reservoir is relatively large compared to the total CSF volume, it is assumed that its levels will be very low. Therefore, the determination of $A\beta_{1\text{-}42}$ levels was performed using an ultrasensitive system such as Simoa. Thus, at the end of the study, $A\beta_{1\text{-}42}$ was detected in one-third of the analyzed reservoirs (Figure 20).

On the other hand, to study the impermeability of the NPMBs to the antibody, four mice (two APP and two WT) had a therapeutic solution with the Alexa 488-conjugated version of the same mAb. This allows us to determine the fluorescence levels emitted by the Alexa 488-mAb both in the reservoir and various peripheral tissues of the mice (whole blood, plasma, and liver). Table 13 displays the fluorescence levels (emission: 600 nm) found in these samples. 1:200 dilution of the mAb was used as a control for mAb fluorescence. Reservoir samples showed higher fluorescence levels compared to undiluted peripheral samples. The emissions were similar to those in naïve mice, which served as a control for basal autofluorescence.

Table 13. Emitted fluorescence data at 600 nm

	Treated		Naïve	
Sample	**Mouse 13**	**Mouse 14**	**Mouse 30**	**Mouse 31**
Reservoir	5266	25,314		
Blood	34	110	13	33
Plasma	1067	1442	951	1004
Liver	5825	5809	5956	5883
6E10-Alexa488 conjugated	29,950			
Blank (aCSF)	55			
Blank (Liver Buffer)	59			

Furthermore, immunofluorescence analysis was conducted on cryopreserved brain and liver sections in APP/PS1 mice (Figure 21). First, typical immunofluorescence was performed, using a primary antibody targeting oligomeric Aβ1-42 (clone 6C3), and a secondary antibody labeled with Alexa 488. The results revealed abundant Aβ plaques in the cerebral cortex, as expected, but no signal in the liver. In consecutive sections, another classical immunofluorescence was performed, with the same primary antibody used as therapeutic solution (clone 6E10), with higher affinity for soluble and intracellular forms of Aβ (86). In this case, there was slight labeling in the cerebral cortex and no signal in the liver. Two control samples were developed in the same type of section, one using only the secondary antibody and the other with no antibody. None of them yield any signal in either tissue. These findings suggest that the mAb in the reservoir cannot pass through the apheresis module and, thus, reach brain or peripheral tissues.

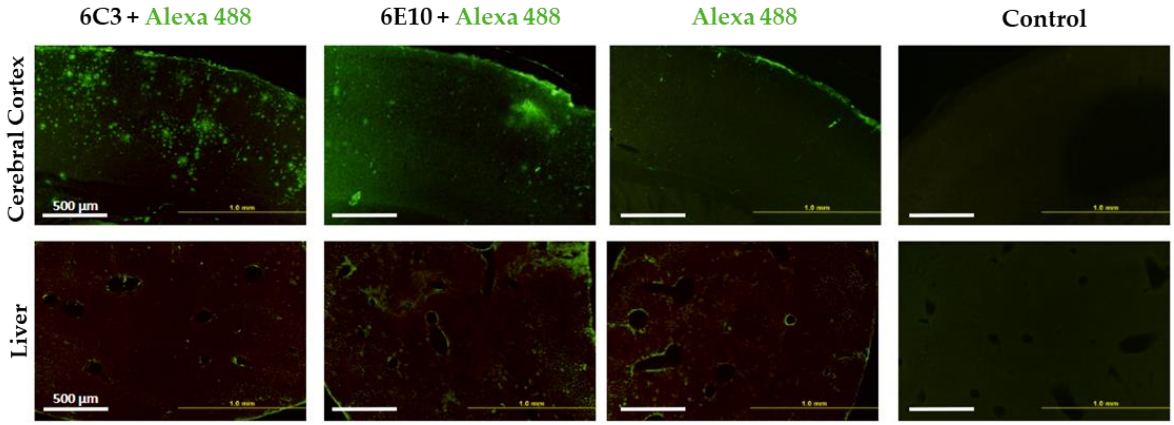

Figure 21. In vivo validation of NPMBs impermeability to mAb. Representative images of cerebral cortex and liver sections from APP mice treated with Alexa 488-conjugated mAb (clone 6E10). From left to right, the immunofluorescence was performed using a primary antibody for Aβ plaque detection (clone 6C3), a primary antibody specific for soluble Aβ (clone 6E10), only the Alexa 488-conjugated secondary antibody, or no antibody (control). Modified from (119).

This study has shown two key findings for subsequent experiments. Firstly, NPMBs allow small molecules like Aβ to pass through but block larger molecules, like immunoglobulins *in vivo*. Secondly, implanting the device in mice was found to be feasible. However, although it was globally safe, complications were present in the immediate and deferred post-operatory. These complications, such as weight loss and lethargy, appeared to be related to the surgical procedure or side effects of the post-surgical medication rather than the device or the therapeutic agent. However, it is worth noting that the device size is at the upper limit of what is feasible for an implantable subcutaneous device in mice, potentially causing animal distress.

Therefore, a number of modifications to the device were necessary to enhance safety, improve animal welfare, and then, enable longer studies and conducting behavioral tests.

4. Long-term IT *pseudodelivery* with replacement of the therapeutic solution in the AD murine model APP/PS1 in early symptomatic stage

4.1. Improvements made to the surgery and device enhanced mouse welfare

Before conducting another study *in vivo*, the device underwent some modifications to reduce its size, while maintaining the same functionality (125). These modifications mainly concern the replacement of the protective plastic capsule with a biocompatible silicone coating. Thus, the weight, volume and height have been reduced by approximately half (47.55%, 57.09% and 40% respectively). Additionally, the length and width of the device have been significantly reduced (17.44% and 13.33% respectively). In addition, modifications to the surgery were performed to avoid wound reopening and other side effects of the procedure (Figure 22).

Figure 22. Diagrams and photographs of mice from the feasibility (left) and long-term (right) studies. Comparison of the original (left) and modified (right) devices, their placement, and the sutures used in each study. Mice with each device are depicted on both sides, with both devices displayed in the center. Note the difference in size between the implantable devices. Scale bar: 1 cm. Images taken from (125).

This modified device was implanted in fourteen male mice, including ten APP and three WT mice (Table 14). Among these, five APP and two WT mice had the reservoir filled with vehicle, while five APP and one WT mice had the reservoir filled with mAb.

In this study, we have encountered some problems related to the disconnection of the catheter from the IT cannula (Table 14). In one, this event could not be solved, and the mouse was euthanized for tissue and fluid collection. However, on three other occasions, this event was observed, but was successfully resolved by a quick intervention for repositioning.

Table 14. Summary of the mice used in the long-term study and the complications observed

Animal ID	Genotype	Content Infused	Time implanted	Complications
38	APP	aCSF	8 weeks	None
39	APP	aCSF	8 weeks	None
40	APP	aCSF	8 weeks	None
41	APP	aCSF	8 weeks	None
42	APP	aCSF	8 weeks	None
43	WT	aCSF	8 weeks	None
44	WT	aCSF	8 weeks	Disconnected (W3, W8)
45	APP	mAb	8 weeks	None
46	APP	mAb	8 weeks	None
47	APP	mAb	8 weeks	None
48	APP	mAb	3 weeks	Cannula detached (W3)
49	APP	mAb	8 weeks	Disconnected (W2, W8)
50	WT	mAb	8 weeks	Disconnected (W5, W8)
51	APP	Naïve	-	None
52	APP	Naïve	-	None
53	APP	Naïve	-	None
54	APP	Naïve	-	None
55	APP	Naïve	-	None
56	WT	Naïve	-	None
57	WT	Naïve	-	None
58	WT	Naïve	-	None
59	WT	Naïve	-	None
60	WT	Naïve	-	None
61	WT	Naïve	-	None

Abbreviations: aCSF, artificial cerebrospinal fluid; APP, APPswe/PS1dE9; mAb, monoclonal antibody; W, week; WT, wild type.

Apart from working to improve device-related issues, we invested a lot of effort in improving the mouse welfare.

One way of assessing the outcome of surgery was by determining the recovery time, which we had recorded in both the feasibility study and this long-term study. Recovery time was defined as the period from the end of the stereotaxic surgery (i.e., cessation of inhaled anesthesia) to the mouse's full recovery (*i.e.*, engaging with food or enrichment objects). It was categorized into three ranges: under 5 minutes, 5-10 minutes, and over 20 minutes, based on the collected data.

The results show that in the long-term study, most mice recovered in less than 5 minutes. This contrasts with the feasibility study, where it took over 20 min to fully recover (Figure 23A). Additionally, implanted mice lost less weight after surgery with the modified protocol, indicating improved welfare (Figure 23B).

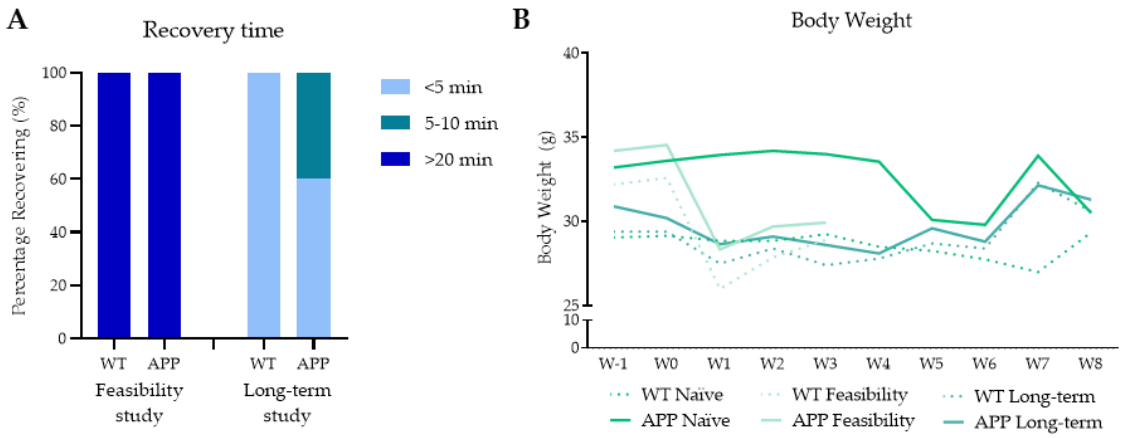

Figure 23. Effect of the changes in the device and the surgery protocol in the recovery time and the body weight throughout the studies. A. Quantification of the percentage of WT and APP mice of both studies in each range of recovery time. **B.** Representation of the median body weight throughout the duration of the experiments. W, week. Modified from (125).

4.2. The implantation of the device did not seem to affect anxiety-like behaviors and spatial memory

As a consequence of the improvements throughout the surgical procedure and post-operative care in the long-term study, we were able to perform a functional assessment by studying the mouse behavior. To do this, it was first determined if wearing the device altered their general behavior and their anxiety state.

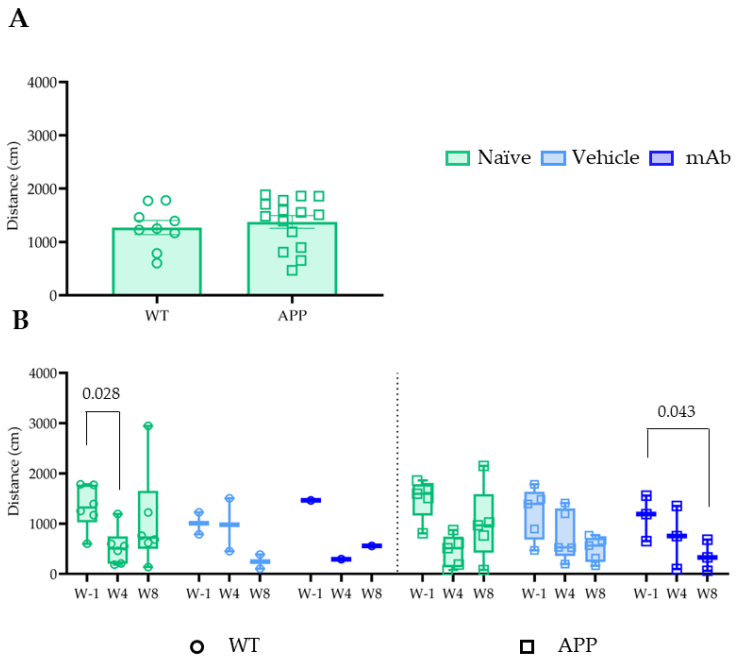

Figure 24. Total distance traveled in the elevated zero maze test. A. Distance traveled by WT and APP in the maze before surgery (W-1). Data are presented as mean ± SEM. Unpaired t-Student´s test. **B.** Changes along time (W-1, W4, and W8) for each experimental group. Data are presented as median. Friedman test. Each dot represents one mouse. W, week.

Thus, the elevated zero maze test was used to evaluate general and anxiety-like behavior at different time points: one week before surgery (W-1), before the re-fill at week 4 (W4), and at the end of the infusion (W8). Measurements included the total distance traveled (Figure 24) and the time spent in the open area of the maze (Figure 25).

The distance travelled in the mazed assess the mouse´s exploratory behavior and anxiety level. The test performed in all mice one

week before surgery indicated that there were no statistical differences between genotypes (Figure 24A). This suggests that all of them start from the same conditions at this level.

When this test was repeated throughout the study, we observed that the distance travelled decreased over the weeks (Figure 24B). In fact, this decrease was significant in the naïve WT group between W-1 and W4 (p-value = 0.028) and in the APP group with the mAb filled-device between W-1 and W8 (p-value = 0.043). This decline in the distance travelled suggests a certain level of anxiety. It is probably actually present in all groups of mice, but the low number of individuals in some cases impedes significance.

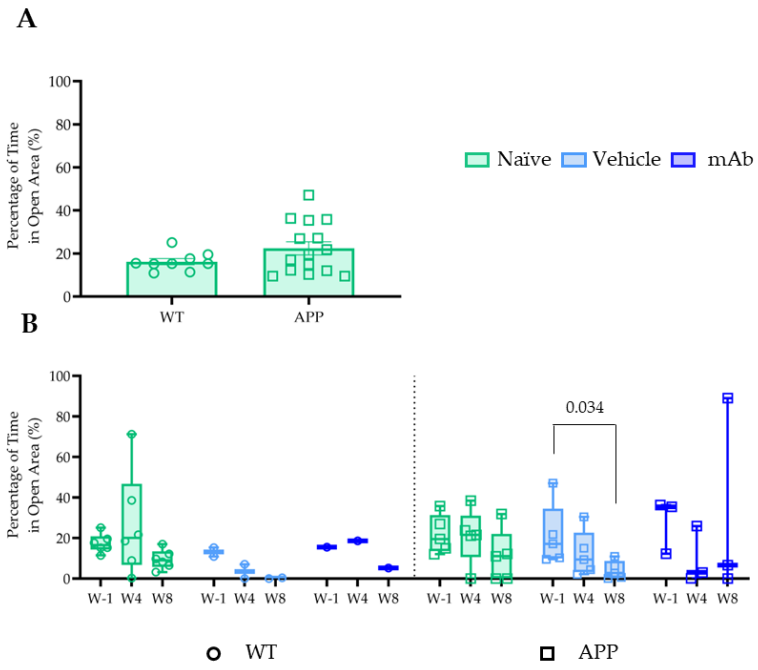

Figure 25. Percentage of time in the open area in the elevated zero maze. A. Percentage of time spent in open arena in WT and APP mice before surgery (W-1). **B.** Changes of the percentage of time in open arena (W-1 to W8) within each group. Statistical comparison between time points was performed using paired Friedman's test. Data are presented as mean ± SEM. Each dot represents one mouse. W, week.

When analyzing the percentage of time spent in the more aversive open area, there was also no difference between the two genotypes one week before surgery (Figure 25A). As we saw in the case of distance travelled, over time it appears that in all groups the time spent in the open arena is lower, which is also a symptom of anxiety. This parameter was only significant in the APP group with vehicle between W-1 and W8 (p-value = 0.034) (Figure 25B).

This decrease in movement and time spent in the open area appeared independent of the implantation of the device, as we found no differences compared to naïve mice of both genotypes. However, the response observed in naïve WT mice is striking, as they are the reference controls in this test.

To investigate whether the treatment administered by IT *pseudodelivery* can influence memory, one of the main changes associated with AD, Y-maze tests were conducted at the three time points (W-1, W4 and W8) (Figures 26, 27). This test assesses both spatial and working memory. Measurements included the percentage of alternations, novel arm entries, and total arm entries.

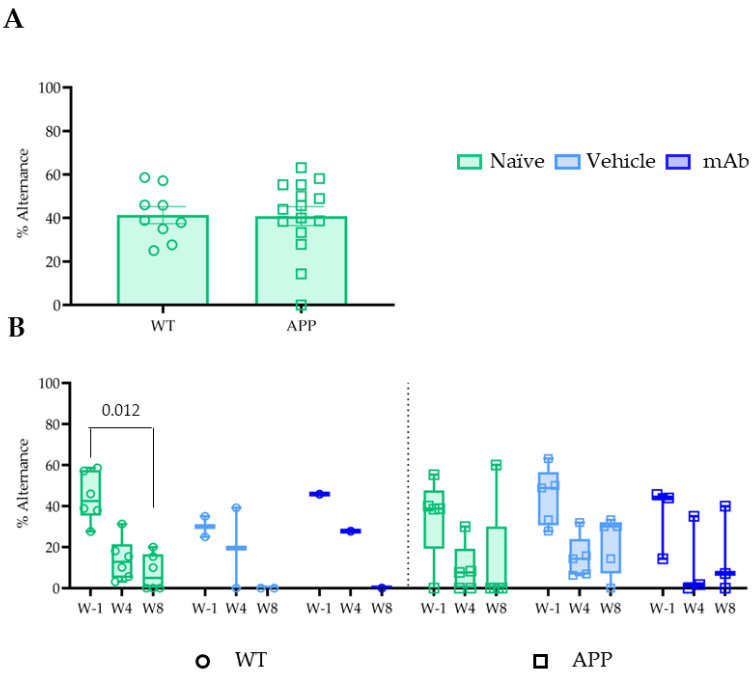

Figure 26. Percentage of alternance in the Y-maze. A. Percentage of alternance in WT and APP mice before surgery (W-1). **B.** Changes of the percentage of alternance over time (W-1 to W8) within each group. Statistical comparison among time points was performed using paired Friedman's test. Data are presented as mean ± SEM. Each dot represents one mouse. W, week.

First, spontaneous alternation was determined in all mice one week before surgery, with no differences between genotypes (Figure 26A). Although there were no differences in the percentage of alternance between groups over time, there was a general decline, particularly significant in the WT naïve group between W-1 and W8 (p-value = 0.012; Figure 26B).

A similar trend was observed in the total arm entries (Figures 27A, 27B), indicating a decrease in activity over time, consistent with findings from the Zero Maze test.

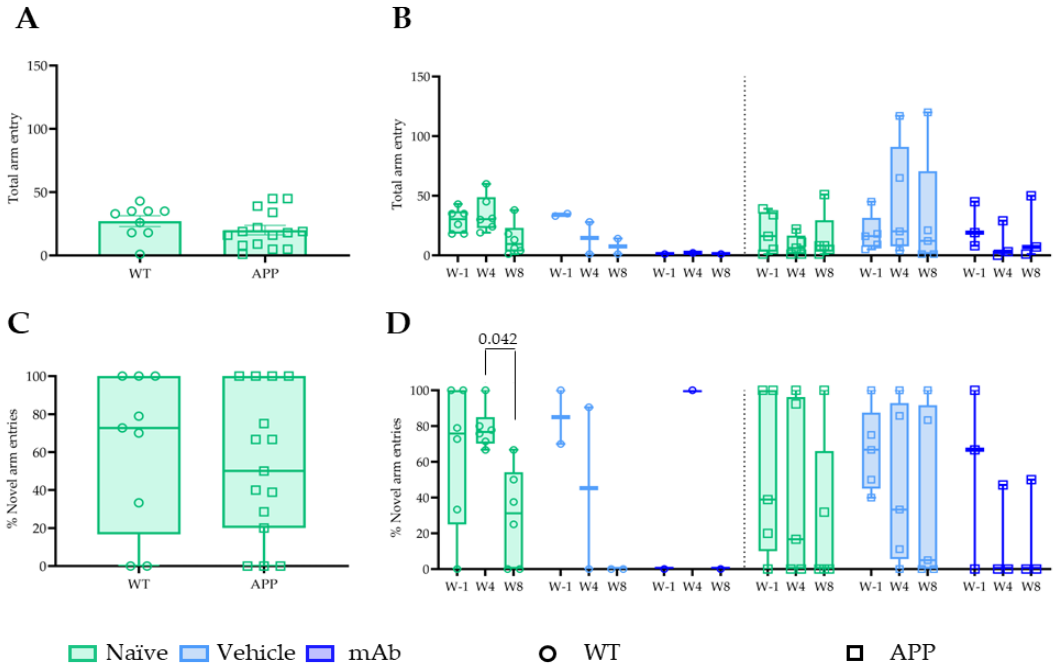

Figure 27. Effect of the implantation of the devices, filled with vehicle or mAb on memory. A. Total arm entries in WT and APP mice before surgery (W-1). **B.** Changes in total arm entries over time (W-1 to W8) within each group. **C.** Percentage of novel arm entries in WT and APP mice before surgery. D. Changes in novel arm entries over time (W-1 to W8) within each group. Data are presented as mean ± SEM. Each dot represents one mouse. W, week.

Finally, entries in the novel arm, which determine the mouse´s ability to remember and recognize the less explores arm, also showed no differences between the two genotypes at baseline (Figure 27C). However, changes in the percentage of new arm entries were observed within groups over time, albeit with a very heterogenous distribution (Figure 27D). Again, it was striking naïve WT mice results, since they presented a significant decrease in new arm entries between W4 and W8 (p-value = 0.042), suggesting a decrease in new arm recognition in the reference group.

Once again, results in spatial memory appeared independent of the implantation of the device, as we found no differences compared to naïve mice of both genotypes. However, the in this test the naïve WT mice again have shown results not expected for a control group. This could lead us to think that there may be external causes that could be affecting the mice at this level.

4.3. Determination of molecules in the biofluids obtained of implanted mice

To assess the impact of the device on soluble proteins associated with AD ($A\beta_{1-42}$, $A\beta_{1-40}$, GFAP and NfL), their concentrations were measured in the reservoir, plasma, and CSF.

4.3.1. It is possible to detect proteins associated with neurodegeneration in the reservoir of implanted mice

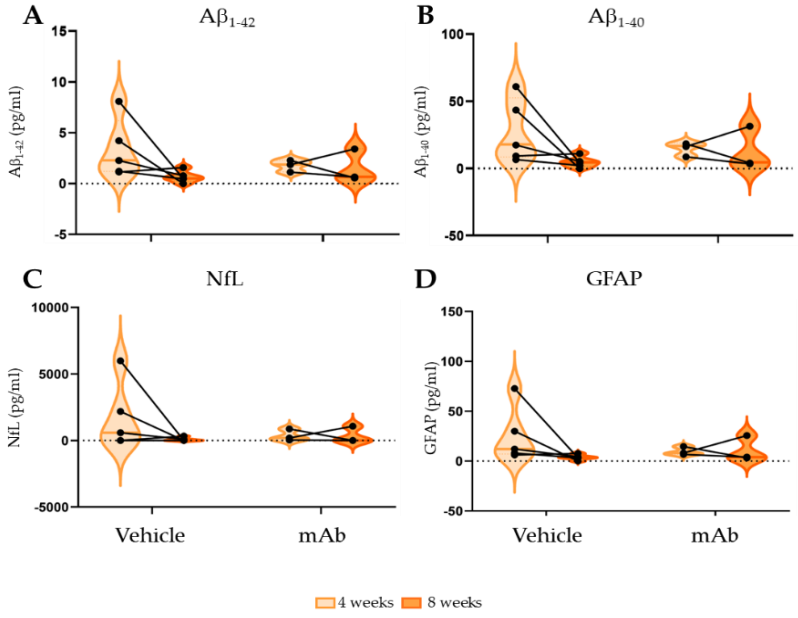

Figure 28. Quantification of soluble proteins in the reservoir at two points of the long-term study. Violin plots for quantification of $A\beta_{1-42}$ (**A**), $A\beta_{1-40}$ (**B**), NfL (C) and GFAP (**D**) for each of the evaluation times, at the middle of the study, 4 weeks, and at the end of the study, 8 weeks. Changes in reservoir solution during this period are also represented by before-after lines. Data are presented as median and interquartile ranges. Each point represents one reservoir. Statistical analyses were developed using the nonparametric Wilcoxon test for comparison of two paired samples.

The possibility of being able to access the contents of the reservoirs during the *in vivo* study, enabled us to compare the solutions at the middle (4 weeks after surgery) and at the end (8 weeks after surgery) of the long-term study. For this purpose, we used a multiplex Simoa kit that allows the detection of $A\beta_{1-42}$, $A\beta_{1-40}$, NfL and GFAP. Figure 28 shows that it was possible to detect levels of the four proteins at both time points in most of the reservoirs. Only one reservoir from a mouse treated with vehicle did not present any protein at the

end of the study. For all markers, there seems to be a clear downwards in mice treated with vehicle while trajectories in the few treated with mAb are variable, but in no case were significant differences found between the levels of each marker at the two time points considered. Usually, the levels of $A\beta_{1-42}$ are lower than those of $A\beta_{1-40}$ in the CSF. The results show that, in the reservoirs, the amount of $A\beta_{1-40}$ is also higher in this case (Figure 28A, B), thus, the diffusion of both peptides through the apheresis module seems to be in accordance with their concentration in CSF.

This implies that the apheresis module allows the passage of molecules such as the various forms of Aβ, as well as filamentous proteins such as NfL and GFAP, both of which have a molecular weight of ~60 kDa.

4.3.2. No changes were observed in Aβ isoforms in either CSF or plasma after eight weeks of IT *pseudodelivery*

In this study, we were able to extract CSF samples and therefore to determine the concentration of these four proteins in this compartment. It should be noted that the kit is specific for proteins of human origin. Nevertheless, $A\beta_{1-42}$ and $A\beta_{1-40}$ proteins present in APP mice are indeed human forms, since this murine model carries a chimeric APP protein with the human-specific Aβ sequence (116). In this case, naïve WT mice were used as control, since they only have Aβ of murine origin.

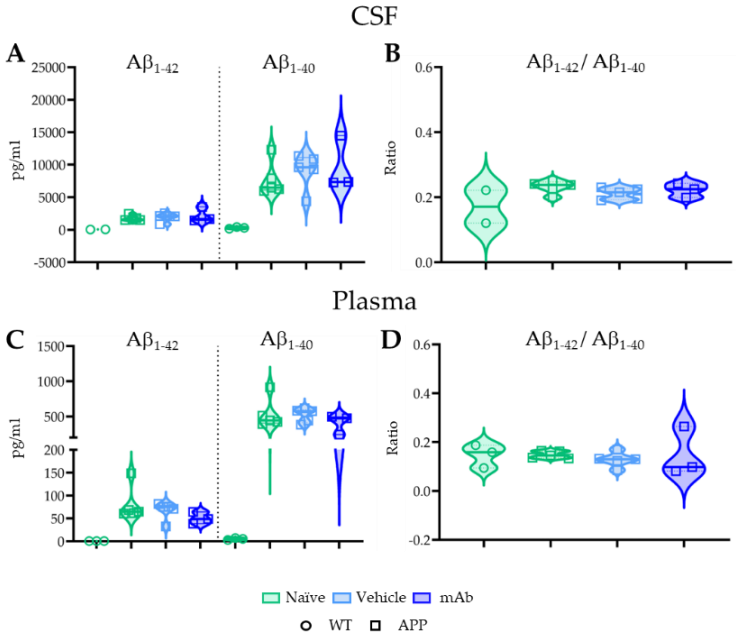

Figure 29. Quantification of soluble $A\beta_{1-42}$ and $A\beta_{1-40}$ in CSF and plasma at the end of long-term study. Violin plots for quantification of $A\beta_{1-42}$ and $A\beta_{1-40}$, and $A\beta_{1-42}$/ $A\beta_{1-40}$ in CSF (**A**, **B**) and plasma (**C**, **D**). Data are presented as median and interquartile ranges. Each point represents one mouse. Statistical analyses were developed using the nonparametric Kruskal-Wallis's test followed by Dunn's test for multiple comparisons across groups.

As expected, neither form of Aβ could be detected in naïve WT mice for both CSF and plasma. Usually, the levels of $A\beta_{1-42}$ are lower than those of $A\beta_{1-40}$ in the CSF. The results show that, in the reservoirs, the amount of $A\beta_{1-40}$ is also higher in this case (Figure 29A, B), thus, the diffusion of both peptides through the apheresis module seems to be in accordance with their concentration in CSF. CSF $A\beta_{1-40}$ levels were higher than $A\beta_{1-42}$ levels in APP mice, as expected, with no significant differences detected for each form of the peptide among

APP groups. The concentrations found were within the range described by other authors in other AD murine models for CSF, although the determination was performed by radioimmunoassay (133). When estimating the $A\beta_{1-42}$/ $A\beta_{1-40}$ ratio, no differences between the three groups of APP mice were found (Figures 29B, D). Similar results were obtained in the case of plasma samples, with no difference among APP groups. $A\beta_{1-42}$ and $A\beta_{1-40}$ detected levels were in the same range described for the APP/PS1 plasma samples, as measured by ELISA (81).

4.3.3. Plasma and CSF levels of NfL and GFAP were not significantly modified by IT *pseudodelivery*

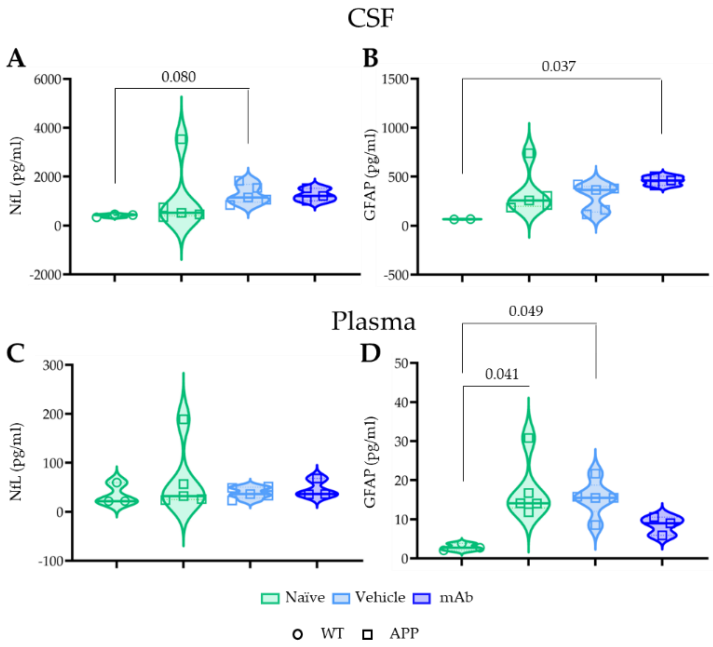

Figure 30. Quantification of soluble NfL and GFAP in CSF and plasma at the end of long-term study. Violin plots for quantification of NfL GFAP in CSF (**A**, **B**) and plasma (**C**, **D**). Data are presented as median and interquartile ranges. Each point represents one mouse. Statistical analyses were developed using the nonparametric Kruskal-Wallis's test followed by Dunn's test for multiple comparisons across groups.

In the case of both NfL and GFAP, although the manufacturer has informed about the possibility of their reactivity also in mice, the pertinent tests to verify this point were not done. Thus, the information set aside by the naïve WT mice may be interesting, since in all cases we are determining the levels of proteins of murine origin.

NfL levels (Figure 30A) were much higher than in plasma (Figure 30C). Considering that CSF was diluted 400 times more than plasma samples, this finding suggests that detection by antibodies against the human-derived forms have good reactivity for the murine forms. Interestingly, a tendency to increase was observed in both implanted groups in CSF (Figure 30A), with no differences in plasma (Figure 30C). We have no references on NfL levels in CSF or plasma for APP/PS1 mice. As an examples, MCI and AD patients' plasma levels are ~ 25 pg/ml. Although the expected NfL reactivity of this kit for murine proteins is higher than the human protein (Quanterix communication), a study in a murine model of ataxia indicates that NfL levels in plasma are below 100 pg/ml in WT mice, while they are above 200 pg/ml in ataxic mice (134). Thus, it is possible that plasma NfL levels are higher in mice, already in WT.

GFAP levels were higher in APP naïve compared to WT naïve in both CSF and plasma (Figures 30B and 30D), although significant differences were only found in plasma (naïve WT *vs.* naïve APP naïve, p-value = 0.041; Figure 30D). In CSF, GFAP levels were similar to naïve APP in both implanted groups, but in mAb-treated mice the levels were significantly higher than in WT mice (p-value = 0.037; Figure 30B). Plasma GFAP levels in vehicle-treated mice were also significantly higher than in naïve WT (p-value = 0.049). However, in mAb-treated mice, although the levels were still higher than in WT mice, there was a trend to decrease compared to APP naïve (Figure 30D). Once again, we do not have other studies to compare our results regarding GFAP levels in these fluids. In the murine model 5xFAD, GFAP plasma levels were estimated above 10,000 pg/ml (135), orders of magnitude higher than in our model. In the case of GFAP reactivity of the kit, it seems that it is dependent on mouse strain (Quanterix communication), therefore, we cannot be sure that the levels detected were as expected for our strain. Further analysis would be necessary, for example, using specific ELISA in plasma samples.

5. Comparison of IT *pseudodelivery* effects on Aβ levels and intracellular and extracellular protein clearance systems in both in *vivo* studies

Having two studies at different treatments times allowed us to have a better understanding of the effects of IT *pseudodelivery* over time.

5.1. Soluble $A\beta_{1-42}$ levels in the hippocampus decreased after eight weeks of IT *pseudodelivery*

The levels of soluble $A\beta_{1-42}$ were compared in brain tissue, plasma, and the reservoirs at the end of each study (Figure 31).

Determination of soluble $A\beta_{1-42}$ levels in brain tissue was performed using a specific ELISA kit, as we expect high levels of the peptide to fall within its detection range. In the case of cerebral cortex, no changes were observed between the three groups of mice in any of the studies (Figure 31A). Levels of this peptide tend to be much higher in naïve APP mice in the long-term study compared to the same group in the feasibility study (*p*-value = 0.054), as the pathology is more advanced. Interestingly, IT *pseudodelivery* for 8 weeks significantly reduced hippocampal soluble $A\beta_{1-42}$ levels in mAb APP with respect to naïve APP mice of the same study (*p*-value = 0.034; Figure 31B). It is tempting to speculate that this decrease may be associated with increased mobilization of soluble peptide in the ISF of the hippocampus to the lateral ventricle.

Concerning the determination of $A\beta_{1-42}$ levels in plasma, these were performed by the ultrasensitive Simoa technique (Figure 31C). $A\beta_{1-42}$ levels were very heterogeneous in vehicle and mAb APP groups in the feasibility study, but no differences were observed regarding their naïve counterparts. Plasma $A\beta_{1-42}$ in the long-term study mice exhibited similar levels

within each group, with no significant differences observed. A comparison of Aβ1-42 levels within reservoirs also showed no differences between studies (Figure 31D).

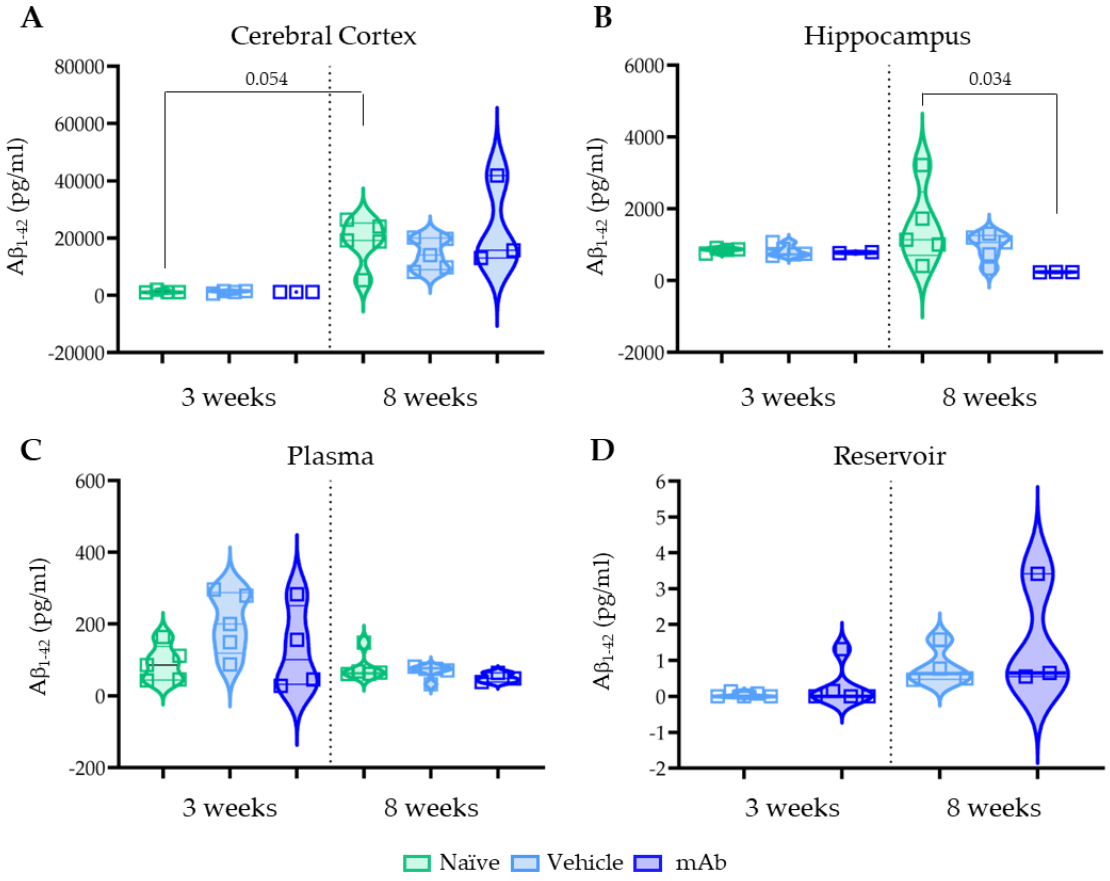

Figure 31. Levels of soluble Aβ1-42 in brain tissue, CSF, and plasma. A, B. Violin plots for the representation of Aβ1-42 quantification by ELISA in cerebral cortex (**A**) and hippocampus (**B**) of APP mice from both the feasibility study (3-week duration) and the long-term study (8-week duration). **C.** Violin plots for the representation of Aβ1-42 quantification by SIMOA in CSF. In this case it was only possible to perform the determination in the long-term study. **D.** Violin plots for the representation of Aβ1-42 quantification by Simoa in plasma. Data are presented as median and interquartile ranges. Each dot represents one mouse. Statistical analysis was performed using the non-parametric Kruskal-Wallis's test followed by Dunn's test for multiple comparisons across groups.

5.2. Implantable devices caused an initial increase in the Area Covered by Aβ plaques in the Cerebral Cortex, but it was markedly decreased after eight weeks

To evaluate the effect of this new therapeutic strategy at the histopathological level, the first step was to analyze the presence of amyloid plaques in brain sections (Figure 32A-F). The area and number of Aβ+ plaques were measured relative to the total area of the cerebral cortex in APP mice.

In the three-week feasibility study, the cerebral cortex area covered with Aβ+ plaques showed that the mice with the device presented higher medians than their naïve counterparts, although no significant differences were found (Figure 32G). Something similar was observed in the case of the number of plaques per area (Figure 32H). However,

in the long-term study, the results of the treated mice, regardless of the content of the reservoirs, were much more similar to those of their naïve mice, although their median values were lower (Figure 32G).

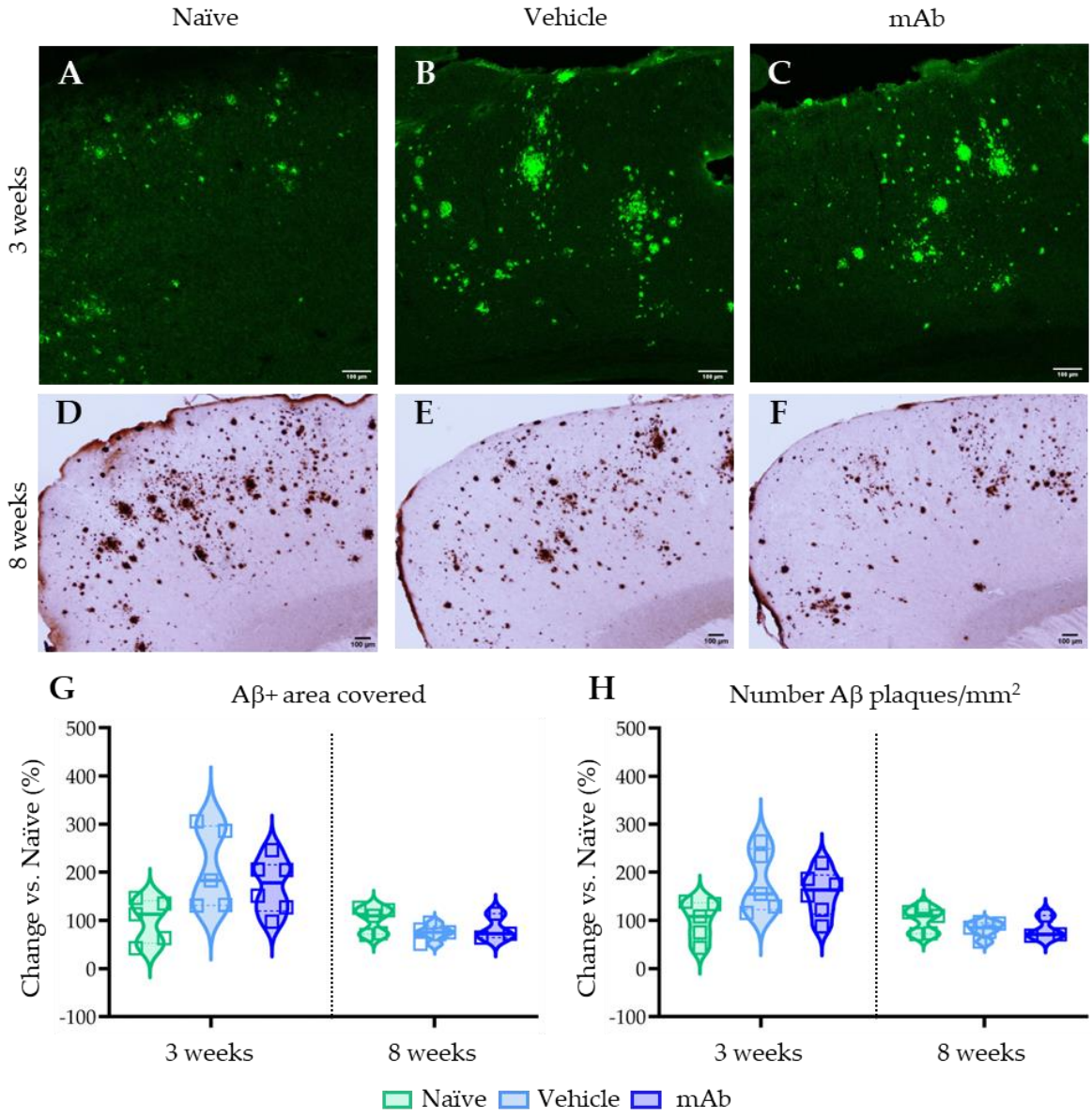

Figure 32. Effect of intrathecal *pseudodelivery* on amyloid plaques in cerebral cortex after 3- or 8-week interventions. (A-C) Representative images of Aβ immunofluorescence developed in APP mice, Naïve (**A**), Vehicle filled-device (**B**), or mAb filled-device (**C**), three weeks post-surgery (feasibility study). Scale bar: 100 μm. (**D-F**) Representative images of Aβ immunohistochemistry developed in APP mice, Naïve (**D**), Vehicle filled-device (**E**), or mAb filled-device (**F**), eight weeks post-surgery (long-term study). Scale bar: 100 μm. **G, H.** Violin plots for the quantification of the Aβ plaque area (**G**) and plaque count (**H**) with respect to the area of the cortex is represented as the percentage of change in relation to their respective Naïve group. Data are presented as median and interquartile ranges. Each dot represents one mouse. Statistical analysis was performed using the non-parametric Kruskal-Wallis's test followed by Dunn's test for multiple comparisons across groups.

5.3. In the hippocampus there was a similar trend in Aβ plaques as in the cortex

Hippocampus (Figure 33) mirrored the findings in the cerebral cortex. In this case, the area occupied by amyloid plaques was significantly higher in vehicle-treated mice compared to naïve APP mice in the feasibility study (3 weeks, *p*-value= 0.029; Figure 33G). However, no differences were found at this level in the long-term study.

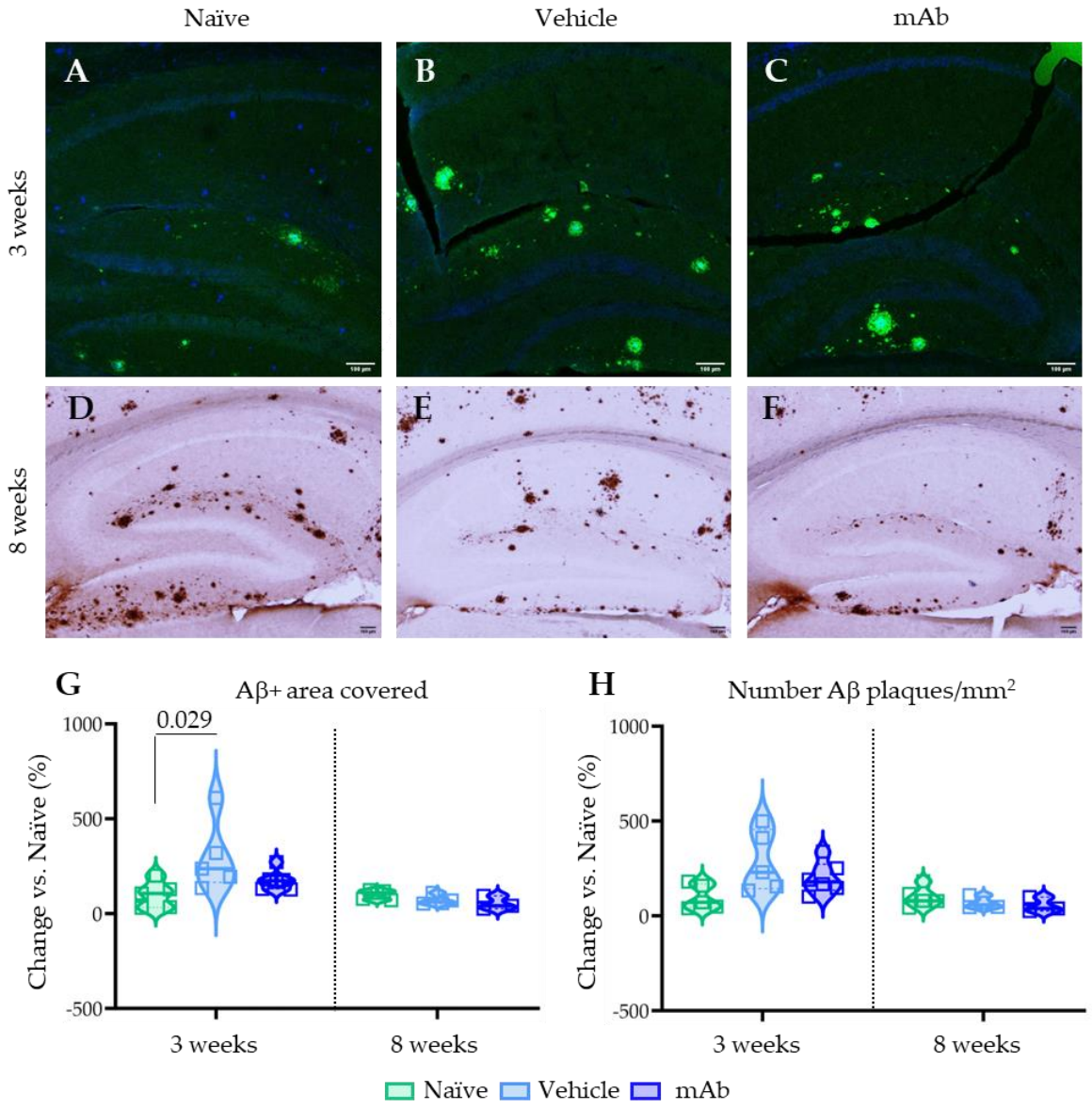

Figure 33. Effect of intrathecal *pseudodelivery* on amyloid plaques in hippocampus after 3- or 8-week interventions. (A-C) Representative images of Aβ immunofluorescence developed in APP mice, Naïve (**A**), Vehicle filled-device (**B**), or mAb filled-device (**C**), three weeks post-surgery (feasibility study). Scale bar: 100 µm. (**D-F**) Representative images of Aβ immunohistochemistry developed in APP mice, Naïve (**D**), Vehicle filled-device (**E**), or mAb filled-device (**F**), eight weeks post-surgery (long-term study). Scale bar: 100 µm. **G, H.** Violin plots for the quantification of the Aβ plaque area (**G**) and plaque count (**H**) with respect to the area of the hippocampus is represented as the percentage of change in relation to their respective Naïve group. Data are presented as median and interquartile ranges. Each dot represents one mouse. Statistical analysis was performed using the non-parametric Kruskal-Wallis's test followed by Dunn's test.

5.4. The distribution of all plaque sizes in both brain regions followed a similar trend to the Aβ Area Covered

Although no differences were seen in the accumulation of Aβ in the cerebral cortex and hippocampus, the possibility that IT *pseudodelivery* altered its level of aggregation was explored. Thus, Aβ+ plaques were classified based on their area, separated into four categories according to the surface area occupied: <500, 500-1000, 1000-2000, and >2000 μm². In the case of cerebral cortex, after 3 weeks of infusion, the number of amyloid plaques increased in both vehicle and mAb groups, but no differences were found (Figure 34A, C).

In contrast, after 8 weeks of infusion, both groups reduced the number of amyloid plaques regarding naïve mice (Figure 34B, C), but not significantly.

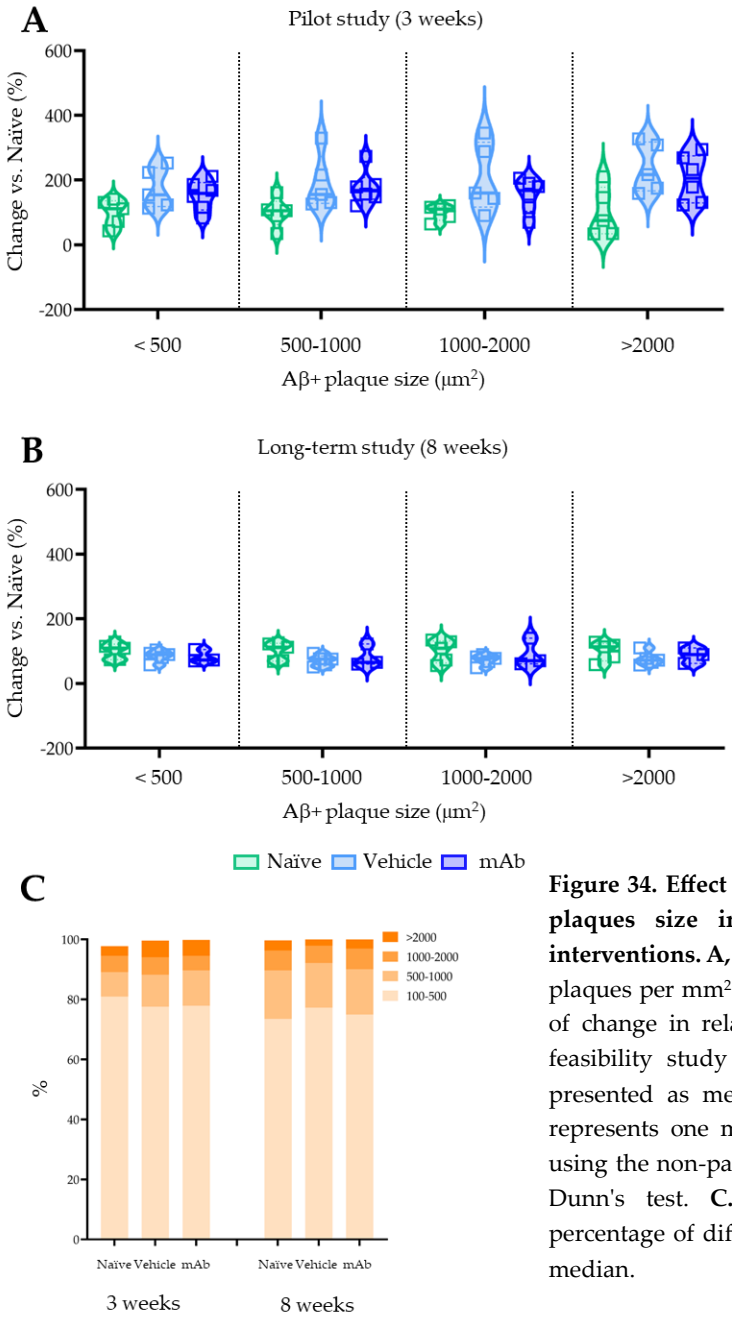

Figure 34. Effect of intrathecal *pseudodelivery* on amyloid plaques size in cerebral cortex after 3- or 8-week interventions. A, B. Violin plots showing the number of Aβ+ plaques per mm² classified per size (μm²) as the percentage of change in relation to their respective naïve group for feasibility study (**A**) and long-term study (**B**). Data are presented as median and interquartile ranges. Each dot represents one mouse. Statistical analysis was performed using the non-parametric Kruskal-Wallis's test followed by Dunn's test. **C.** Stacked bar graph representing the percentage of different plaque sizes. Data are presented as median.

Similarly, hippocampus showed higher median values for Aβ⁺ plaques in both feasibility study vehicle and mAb mice, particularly for the smaller plaque size. Notably, the number of >2000 μm² Aβ⁺ plaques in the vehicle-treated mice displayed an increase regarding naïve mice (*p*-value = 0.049; Figure 35A, C). Interestingly, after eight weeks of infusion, there was a reduction in the total number of plaques in vehicle and mAb mice regarding to the naïve group, but no significant changes were found (Figure 35B, C).

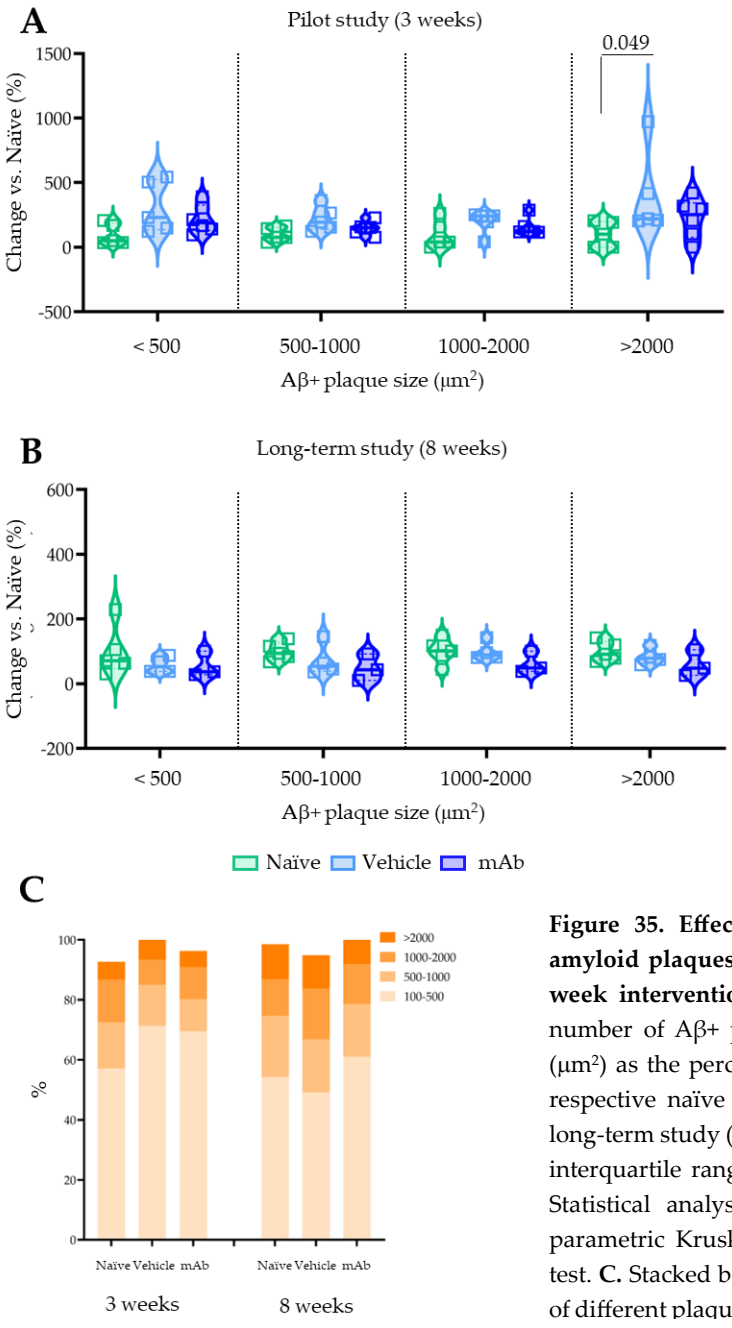

Figure 35. Effect of intrathecal *pseudodelivery* on amyloid plaques size in hippocampus after 3- or 8-week interventions. A, B. Violin plots showing the number of Aβ+ plaques per mm² classified per size (μm²) as the percentage of change in relation to their respective naïve group for feasibility study (**A**) and long-term study (**B**). Data are presented as median and interquartile ranges. Each dot represents one mouse. Statistical analysis was performed using the non-parametric Kruskal-Wallis's test followed by Dunn's test. **C.** Stacked bar graph representing the percentage of different plaque sizes. Data are presented as median.

5.5. IT *pseudodelivery* may prevent p62 accumulation after 8 weeks of infusion

As the purpose of IT *pseudodelivery* is to assist in clearing accumulated proteins -Aβ in this case-, we investigated its impact on the physiological clearance systems. First, the state of autophagy was analyzed by performing a p62 immunofluorescence, given the important role of this protein in this process (136). The mean fluorescence was measured.

In the cortex, the mean fluorescence was lower in naïve APP mice compared to naïve WT at the end of the feasibility study (7 months and 3 weeks-old mice; Figure 36B and 36A, respectively), but higher at the end of the long-term study (9-month-old mice; Figure 36F and 36E, respectively). Interestingly, both vehicle and mAb APP mice had a similar mean fluorescence than their naïve APP counterparts in the 3-week study (Figures 36C and 36D *vs.* Figure 36B). However, after the eight-week intervention, vehicle and mAb mice resembled naïve WT mice (Figures 36G and 36H *vs.* Figure 36E)).

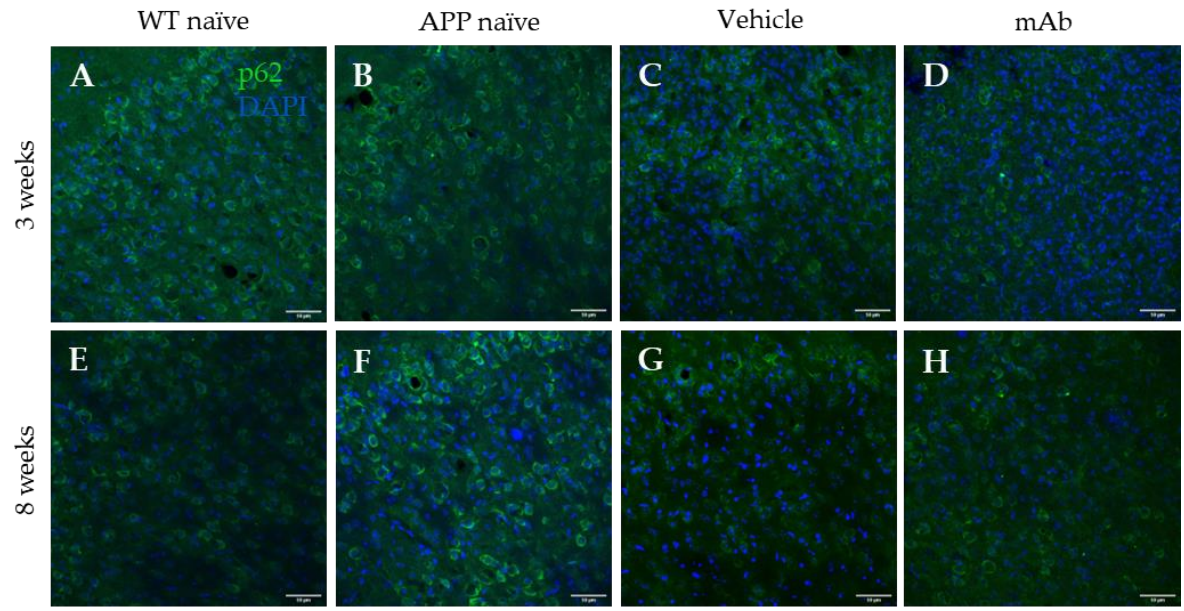

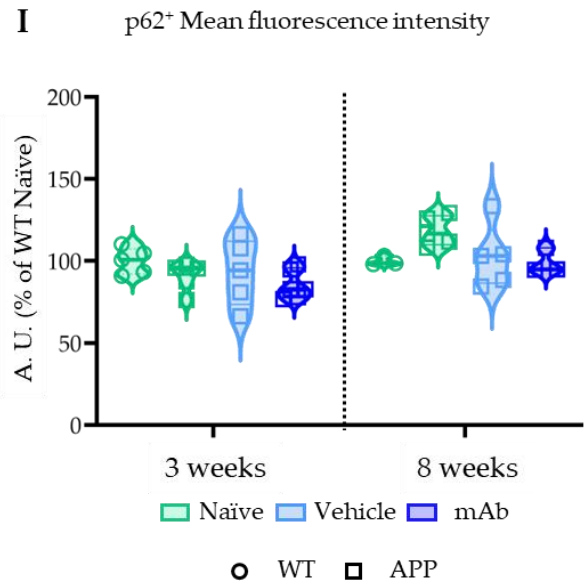

Figure 36. Evaluation of the autophagy state through p62 immunofluorescences in the cortex after 3- and 8-weeks infusion. (A-H) Representative images of p62 immunofluorescence in Naïve WT mice (**A, E**), Naïve APP mice (**B, F**), implanted with the vehicle filled-device (**C, G**) or with the mAb filled-device (**D, H**) for 3 or 8 weeks. Scale bar: 50 µm. **I.** Violin plots for the mean fluorescence intensity of p62 immunofluorescence in the expressed as the percentage of change in relation to their WT naïve group counterparts. Data are presented as median and interquartile ranges. Each dot represents one mouse.

Nevertheless, quantification of the mean fluorescence intensity of p62 indicated that there were no differences among the groups in either study (Figure 36I).

In the hippocampus (Figure 37), p62 mean fluorescence was consistent across all groups, being slightly lower in APP naïve mice compared to naïve WT mice in the 3-week study, although no significant differences were found (Figure 37I).

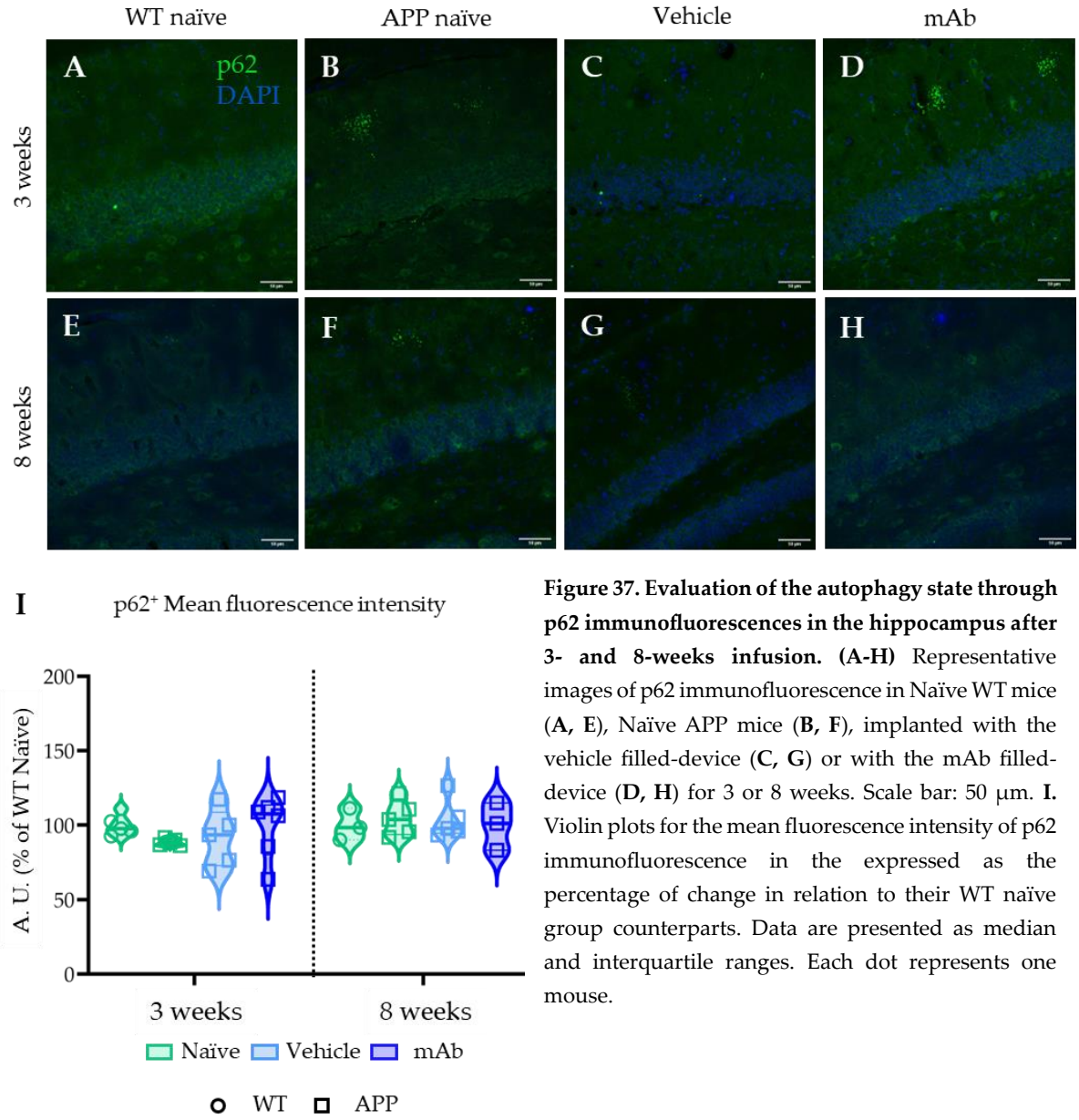

Figure 37. Evaluation of the autophagy state through p62 immunofluorescences in the hippocampus after 3- and 8-weeks infusion. (A-H) Representative images of p62 immunofluorescence in Naïve WT mice (**A, E**), Naïve APP mice (**B, F**), implanted with the vehicle filled-device (**C, G**) or with the mAb filled-device (**D, H**) for 3 or 8 weeks. Scale bar: 50 μm. **I.** Violin plots for the mean fluorescence intensity of p62 immunofluorescence in the expressed as the percentage of change in relation to their WT naïve group counterparts. Data are presented as median and interquartile ranges. Each dot represents one mouse.

5.5.1. Lipofuscin levels increased following the 3-weeks implantation, but showed no significant difference from naïve APP levels after 8 weeks of infusion

To further analyze the autophagic state, lipofuscin levels, a waste product linked to aging and impaired autophagy (40), were measured. As it is autofluorescent, its mean fluorescence

was measured from cerebral cortex and hippocampus images taken using a Hyd3 detector after a 590 nm excitation (Figures 38 and 39).

At the end of the three-week study, no differences were observed between WT and APP mice at this age, and the lipofuscin levels tended to be higher in all implanted mice compared to naïve APP mice in both brain regions (Figures 38I and 39I). At the end of the long-term study, higher lipofuscin levels were found in APP compared to WT mice, particularly in the hippocampus (Figure 39I). In their respective implanted mice, lipofuscin levels were similar to those in APP naïve mice, being slightly elevated in the hippocampus (Figure 39I).

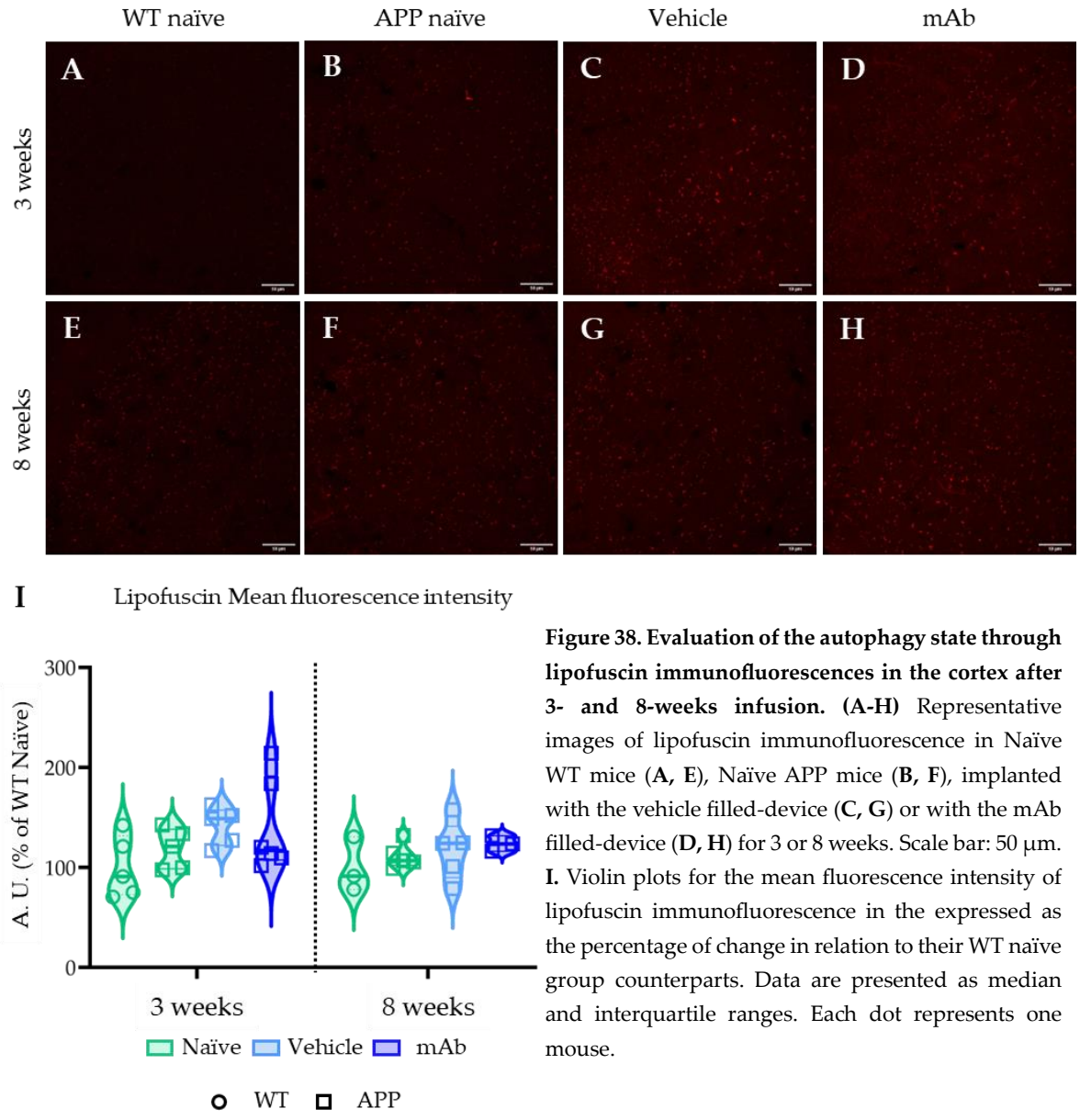

Figure 38. Evaluation of the autophagy state through lipofuscin immunofluorescences in the cortex after 3- and 8-weeks infusion. (A-H) Representative images of lipofuscin immunofluorescence in Naïve WT mice (**A, E**), Naïve APP mice (**B, F**), implanted with the vehicle filled-device (**C, G**) or with the mAb filled-device (**D, H**) for 3 or 8 weeks. Scale bar: 50 µm. **I.** Violin plots for the mean fluorescence intensity of lipofuscin immunofluorescence in the expressed as the percentage of change in relation to their WT naïve group counterparts. Data are presented as median and interquartile ranges. Each dot represents one mouse.

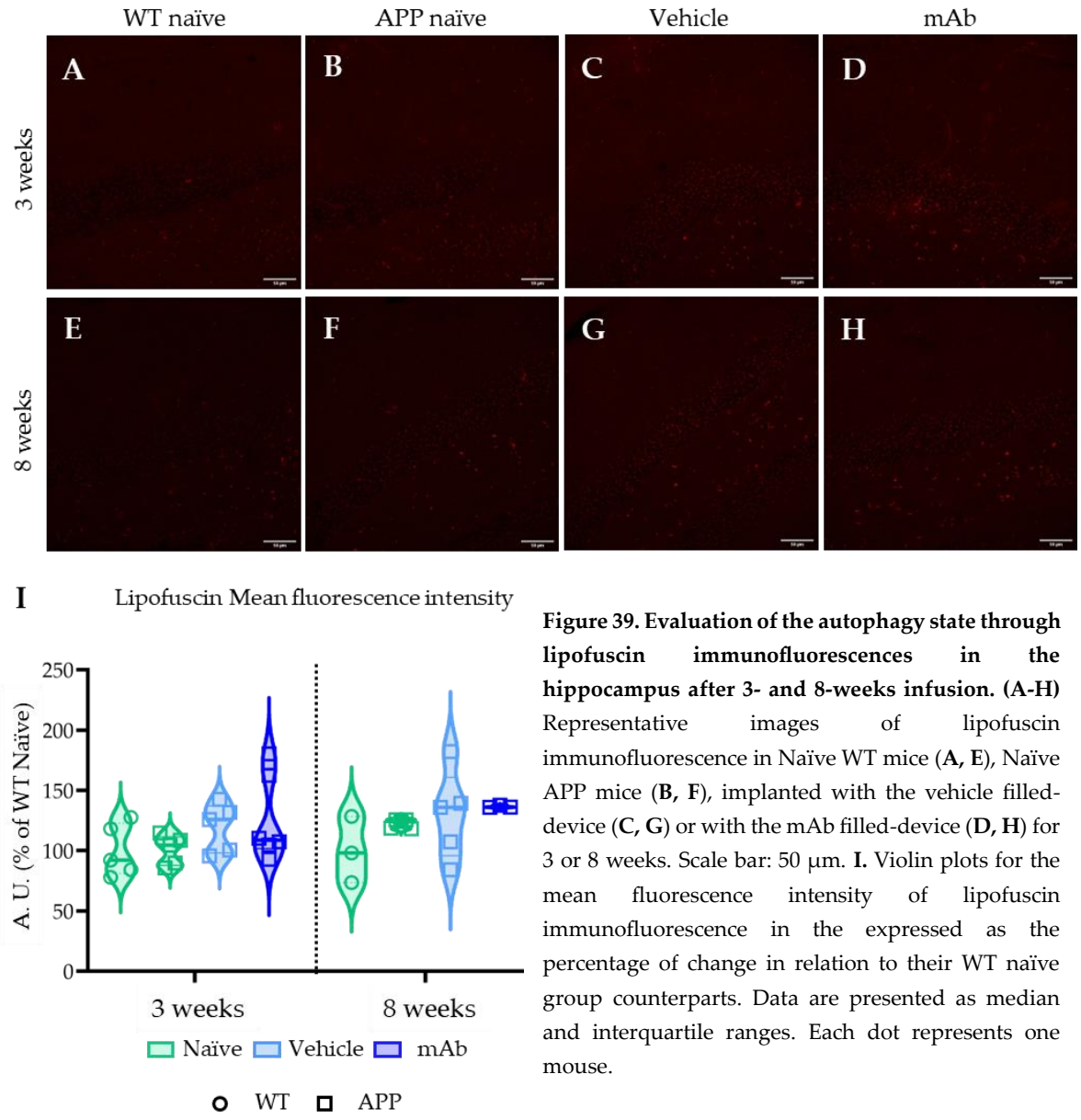

Figure 39. Evaluation of the autophagy state through lipofuscin immunofluorescences in the hippocampus after 3- and 8-weeks infusion. (A-H) Representative images of lipofuscin immunofluorescence in Naïve WT mice (**A, E**), Naïve APP mice (**B, F**), implanted with the vehicle filled-device (**C, G**) or with the mAb filled-device (**D, H**) for 3 or 8 weeks. Scale bar: 50 µm. **I.** Violin plots for the mean fluorescence intensity of lipofuscin immunofluorescence in the expressed as the percentage of change in relation to their WT naïve group counterparts. Data are presented as median and interquartile ranges. Each dot represents one mouse.

5.6. IT *pseudodelivery* induced microglia activation in the short-term, but it was normalized in the long-term study

Microglia are crucial for clearing aggregated proteins. Therefore, to assess microglial activation in the cortex and the hippocampus, the levels of Iba-1, a specific protein marker expressed on the surface of microglia, were measured by immunofluorescent staining (Figure 40 and 41). Three weeks post-surgery, both groups of implanted mice showed a significant increase in Iba-1 levels in both brain regions: Cortex naïve APP *vs.* vehicle, p-value = 0.057 and Cortex naïve APP *vs.* mAb, p-value = 0.020 (Figure 40I); Hippocampus naïve APP *vs.* vehicle, p-value = 0.035 and Hippocampus APP naïve *vs.* mAb, p-value = 0.003 (Figure 41I). No differences were observed among groups in any brain region after both studies.

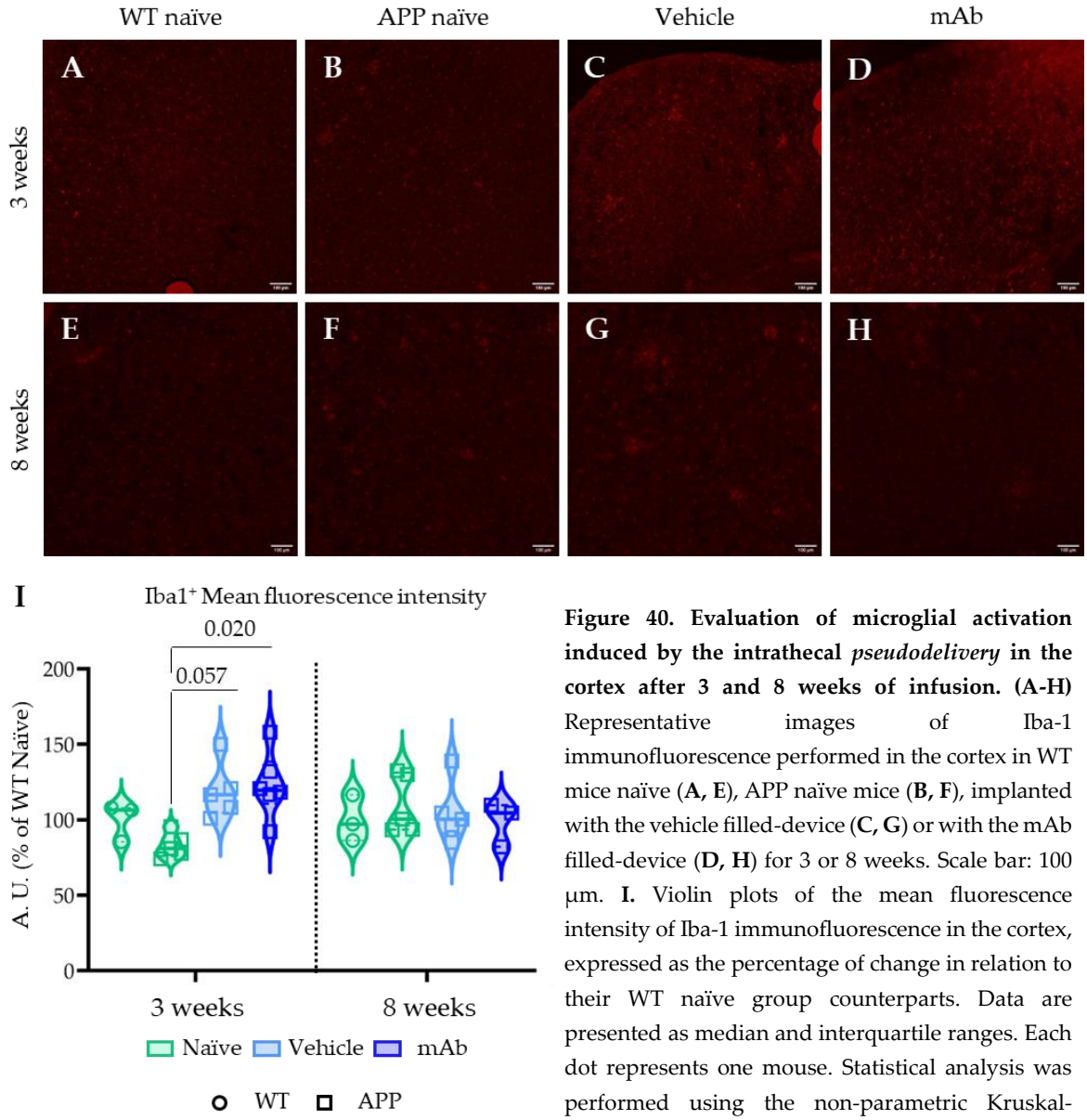

Figure 40. Evaluation of microglial activation induced by the intrathecal *pseudodelivery* in the cortex after 3 and 8 weeks of infusion. (A-H) Representative images of Iba-1 immunofluorescence performed in the cortex in WT mice naïve (**A, E**), APP naïve mice (**B, F**), implanted with the vehicle filled-device (**C, G**) or with the mAb filled-device (**D, H**) for 3 or 8 weeks. Scale bar: 100 µm. **I.** Violin plots of the mean fluorescence intensity of Iba-1 immunofluorescence in the cortex, expressed as the percentage of change in relation to their WT naïve group counterparts. Data are presented as median and interquartile ranges. Each dot represents one mouse. Statistical analysis was performed using the non-parametric Kruskal-Wallis's test followed by Dunn's test.

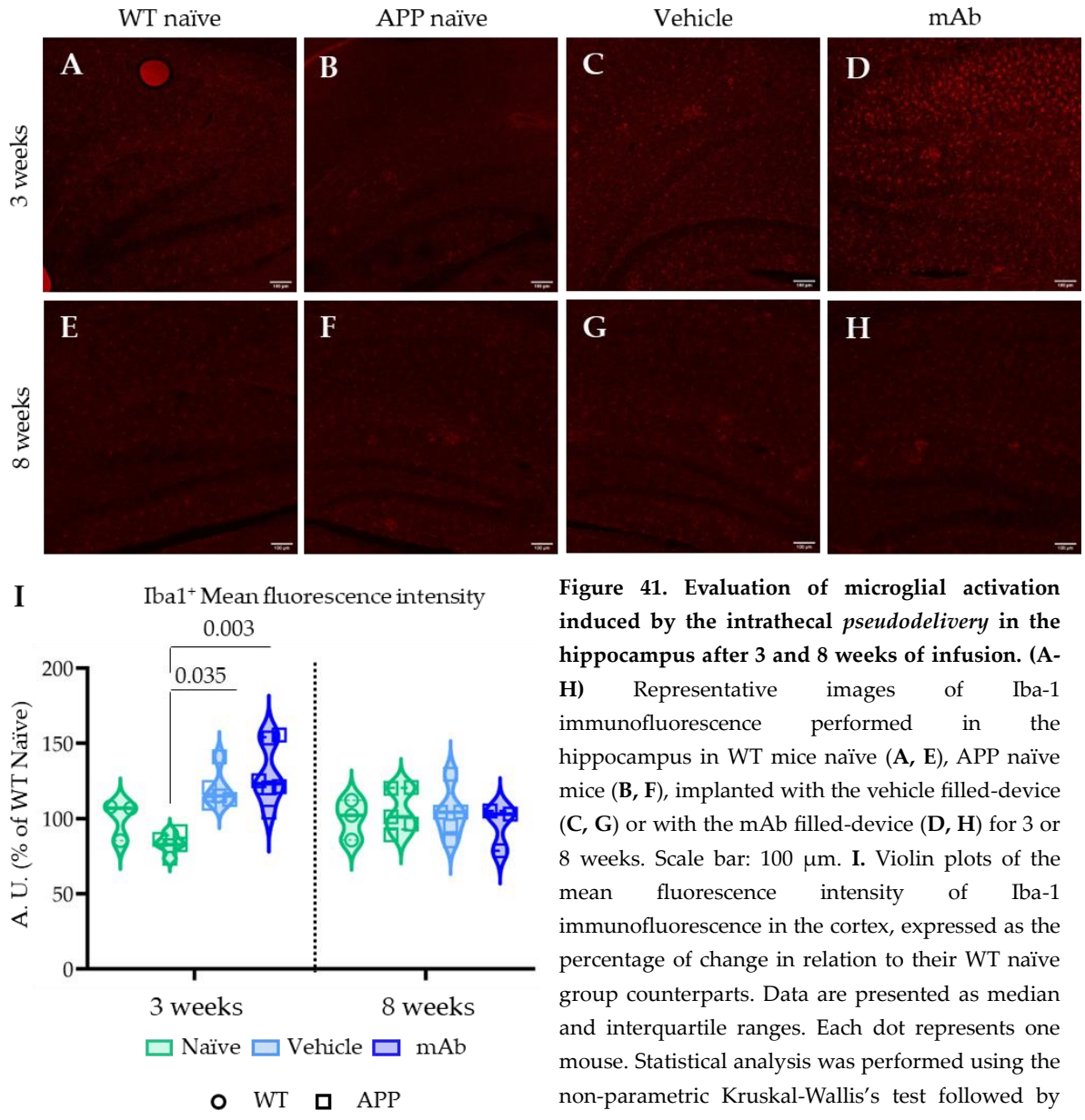

Figure 41. Evaluation of microglial activation induced by the intrathecal *pseudodelivery* in the hippocampus after 3 and 8 weeks of infusion. (A-H) Representative images of Iba-1 immunofluorescence performed in the hippocampus in WT mice naïve (**A, E**), APP naïve mice (**B, F**), implanted with the vehicle filled-device (**C, G**) or with the mAb filled-device (**D, H**) for 3 or 8 weeks. Scale bar: 100 µm. **I.** Violin plots of the mean fluorescence intensity of Iba-1 immunofluorescence in the cortex, expressed as the percentage of change in relation to their WT naïve group counterparts. Data are presented as median and interquartile ranges. Each dot represents one mouse. Statistical analysis was performed using the non-parametric Kruskal-Wallis's test followed by Dunn's test.

5.6.1. Activated microglia was around Aβ plaques

Microglial activation was assessed within a 15 µm radius around plaques of varying sizes (10, 15, 20 and 30 µm radius). After 3 weeks of infusion, there was a significant increase in microglial activation around all plaque sizes in the cortex, particularly in mAb-treated mice around small plaques (10 µm, naïve *vs.* mAb, p-value = 0.007; Figure 42A). After eight weeks of infusion, microglial activation around the smallest plaques remained higher in mAb-treated mice compared to vehicle-treated mice (10 µm, naïve *vs.* vehicle, p-value = 0.034). In hippocampus, there were no significant changes in activation around any plaque size at any infusion time (Figure 42B).

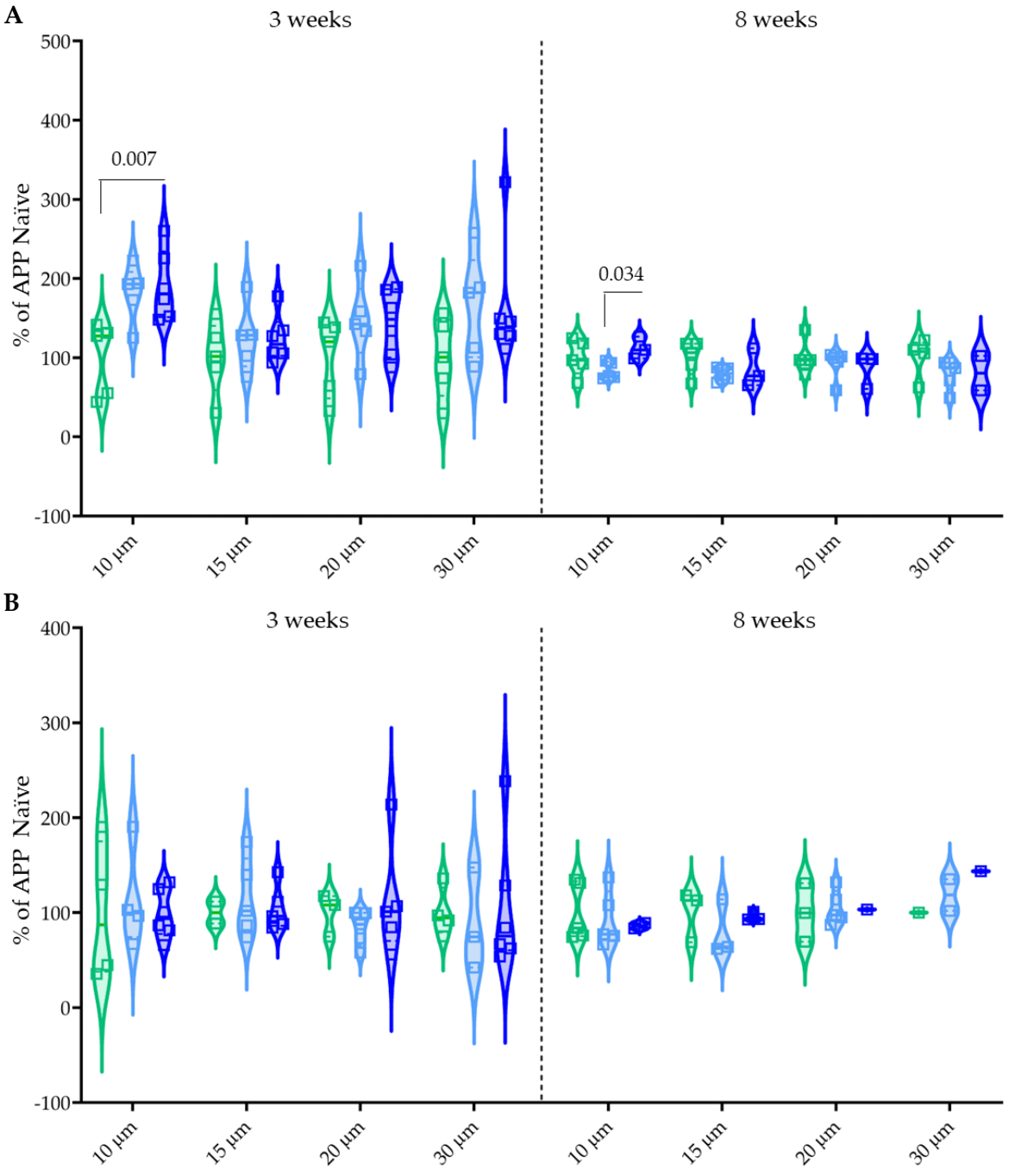

Figure 42. Evaluation of microglial activation around plaques induced by the intrathecal *pseudodelivery* in the cortex and hippocampus after 3 and 8 weeks of infusion. A, B. Graphical representation of the mean fluorescence intensity of Iba-1 immunofluorescence within 15 µm radius around 10, 15, 20 and 30 µm radius plaques in the cortex (**A**) and hippocampus (**B**) expressed as the percentage of change in relation to their respective naïve group. Data are presented as median and interquartile ranges. Each dot represents one mouse. Statistical analysis was performed using the non-parametric Kruskal-Wallis's test followed by Dunn's test.

5.6.2. IT *pseudodelivery* enhanced Aβ clearance by promoting microglial proliferation in the short-term and increasing its targeting of Aβ plaques in the cortex in the long-term

As expected for the results of the mean fluorescence, the number of Iba1$^+$ cells per mm^2 was higher in implanted mice compared to naïve mice in the cortex after 3 weeks of infusion, especially in vehicle-treated mice (p-value = 0.031; Figure 43G). Most of these cells exhibited an ameboid morphology (Figure 43H). It is worth noting that the increase in Iba1$^+$ cells at this point also included an increase in the number of Iba1$^+$ cells that are within a 15 μm radius from Aβ plaques, which were termed as plaque-associated microglia (Figure 43I). In addition, the mean number of plaques per microglia tended to be higher in implanted mice (Figure 43K). However, the percentage of plaques associated with microglia remained the same (Figure 43J), as well as the mean number of microglia per plaque, except for a slight decrease in mAb-treated mice (Figure 43L).

After eight weeks of infusion, there was no increase in the number of microglia per mm^2 in the cortex, but a slight rise in the percentage of ameboid Iba1$^+$ cells in mAb-treated mice (Figure 43G, H). The percentage of plaque-associated microglia was similar in all groups, with a slight increase in the percentage of plaques associated with microglia in mAb-treated mice (Figure 43I, J). In addition, the mean number of plaques per microglia was consistent across all groups, while the mean number of microglia per plaque tended to be higher in mAb-treated mice compared to the other groups (Figure 43K, L).

Figure 43. Evaluation of microglia changes and its relation to Aβ plaques in the cortex of 3- and 8-weeks implanted mice. (A-F) Representative images of Iba-1 (red) and Aβ (green) immunofluorescence performed in the cortex in APP naïve mice (**A, D**), implanted with the vehicle filled-device (**B, E**) or with the mAb filled-device (**C, F**) for 3 (**A-C**) or 8 weeks (**D-F**). Scale bar: 50 μm. **G.** Violin plots for the number of microglia per mm^2 found in the cortex of APP mice with the device filled with vehicle or mAb, and in its age-matched APP naïve mice, treated for 3 or 8 weeks. **H.** Violin plots for the percentage of ameboid microglia found in the cortex of APP mice with the device filled with vehicle or mAb, and in its age-matched APP naïve mice, treated for 3 or 8 weeks. **I.** Violin plots for the percentage of microglia associated to Aβ plaques found in the cortex of APP mice with the device filled with vehicle or mAb, and in its age-matched APP naïve mice, treated for 3 or 8 weeks. **J.** Violin plots for the percentage of Aβ plaques associated to microglia found in the cortex of APP mice with the device filled with vehicle or mAb, and in its age-matched APP naïve mice, treated for 3 or 8 weeks. **K.** Violin plots for the mean number of Aβ plaques per microglia found in the cortex of APP mice with the device filled with vehicle or mAb, and in its age-matched APP naïve mice, treated for 3 or 8 weeks. **L.** Violin plots for the mean number of microglia associated to an Aβ plaque found in the cortex of APP mice with the device filled with vehicle or mAb, and in its age-matched APP naïve mice, treated for 3 or 8 weeks. Data are presented as median and interquartile ranges. Each dot represents one mouse. Statistical analysis was performed using the non-parametric Kruskal-Wallis's test followed by Dunn's test.

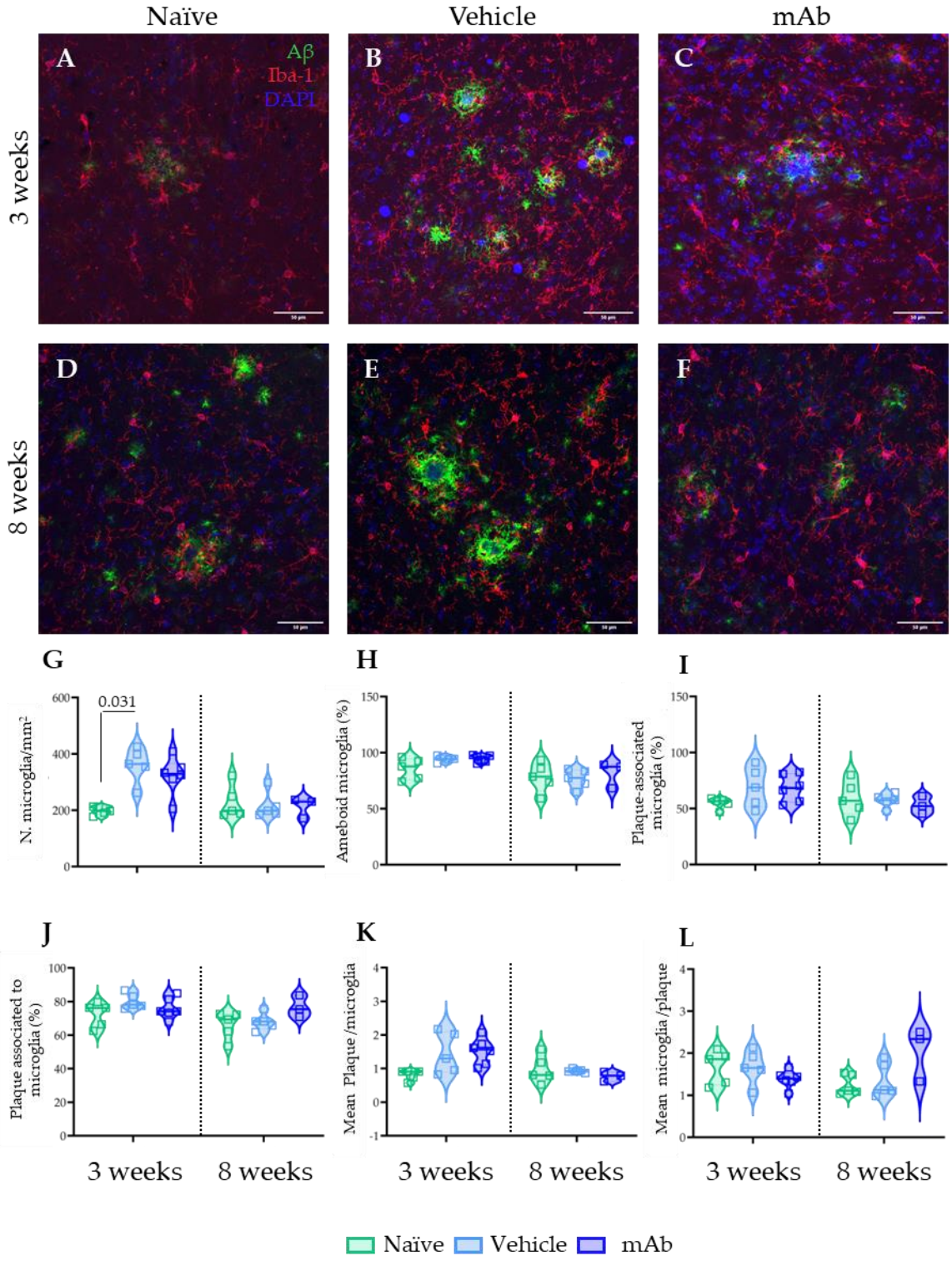

5.6.3. Initial microglia proliferation induced by IT *pseudodelivery* in the short-term was normalized in the long-term study in the hippocampus

As well as in cortex, in the hippocampus the number of Iba1⁺ cells per mm² was significantly higher in implanted mice compared to naïve mice after 3 weeks of infusion (Naïve *vs.* vehicle, p-value = 0.008; Naïve *vs.* mAb p-value = 0.002; Figure 44G). The percentage of

ameboid microglia was also higher in implanted mice (Figure 44H). There were no differences in the analysis of the relationship between microglia and Aβ plaques (Figure 44I-L).

In mice infused for eight weeks, the number of Iba1^{+} cells per mm^{2} was similar among groups in the hippocampus, with a slight decrease in mAb-treated mice (Figure 44G). This trend in mAb-treated mice was also observed in the percentage of plaque-associated

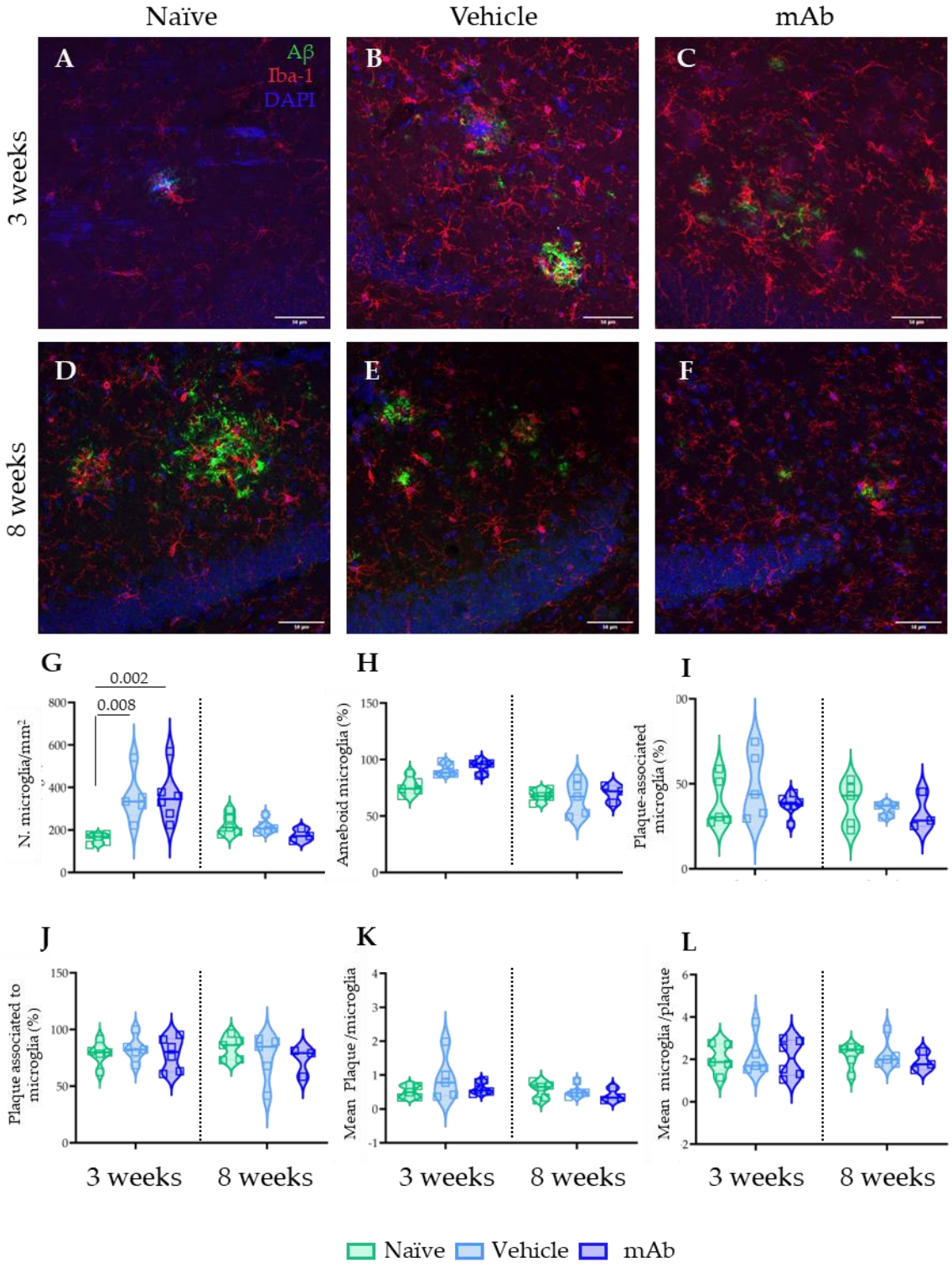

Figure 44. Evaluation of microglia changes and its relation to Aβ plaques in the hippocampus of 3- and 8-weeks implanted mice. (A-F) Representative images of Iba-1 (red) and Aβ (green) immunofluorescence performed in the cortex in APP naïve mice (**A, D**), implanted with the vehicle filled-device (**B, E**) or with the mAb filled-device (**C, F**) for 3 (**A-C**) or 8 weeks (**D-F**). Scale bar: 50 μm. **G.** Violin plots for the number of microglia per mm² found in the hippocampus of APP mice with the device filled with vehicle or mAb, and in its age-matched APP naïve mice, treated for 3 or 8 weeks. **H.** Violin plots for the percentage of ameboid microglia found in the hippocampus of APP mice with the device filled with vehicle or mAb, and in its age-matched APP naïve mice, treated for 3 or 8 weeks. **I.** Violin plots for the percentage of microglia associated to Aβ plaques found in the hippocampus of APP mice with the device filled with vehicle or mAb, and in its age-matched APP naïve mice, treated for 3 or 8 weeks. **J.** Violin plots for the percentage of Aβ plaques associated to microglia found in the hippocampus of APP mice with the device filled with vehicle or mAb, and in its age-matched APP naïve mice, treated for 3 or 8 weeks. **K.** Violin plots for the mean number of Aβ plaques per microglia found in the hippocampus of APP mice with the device filled with vehicle or mAb, and in its age-matched APP naïve mice, treated for 3 or 8 weeks. **L.** Violin plots for the mean number of microglia associated to an Aβ plaque found in the hippocampus of APP mice with the device filled with vehicle or mAb, and in its age-matched APP naïve mice, treated for 3 or 8 weeks. Data are presented as median and interquartile ranges. Each dot represents one mouse. Statistical analysis was performed using the non-parametric Kruskal-Wallis's test followed by Dunn's test.

microglia (Figure 44I), the percentage of plaques associated with microglia (Figure 44J), the mean number of plaques per microglia (Figure 44K) and the mean number of microglia per plaque (Figure 44L), despite the similar percentage of ameboid microglia in all groups (Figure 44H).

5.6.4. The device's significant impact on microglia interaction with Aβ plaques was observed in the cortex, but not in the hippocampus

A detailed analysis of the interaction between plaques and microglia revealed differences based on plaque sizes (Figure 45). After 3 weeks of treatment, there were more microglia per plaque in the case of the bigger plaques (>2000 μm²) in the cortex of implanted mice compared to naïve mice, being more noticeable in vehicle treated mice (p-value = 0.054), while there were no differences in the other plaque sizes (Figure 45A). A similar trend was observed in the hippocampus with smaller plaques (<500 μm²; Figure 45B).

After 8 weeks of treatment, in the cortex, the mean number of microglia associated with plaques smaller than 500 μm² and with sizes between 1000 and 2000 μm² tended to be higher with the device, especially in mice treated with mAb (1000-2000 μm², Naïve 8 w *vs.* mAb 8w, p-value = 0.048). However, for larger plaques, the trend was reversed (Figure 45A). In the hippocampus, more microglia were associated with plaques sized between 500 and 1000 μm² in mAb-treated mice, while fewer microglia were associated with larger plaques in both groups of implanted mice (Figure 45B).

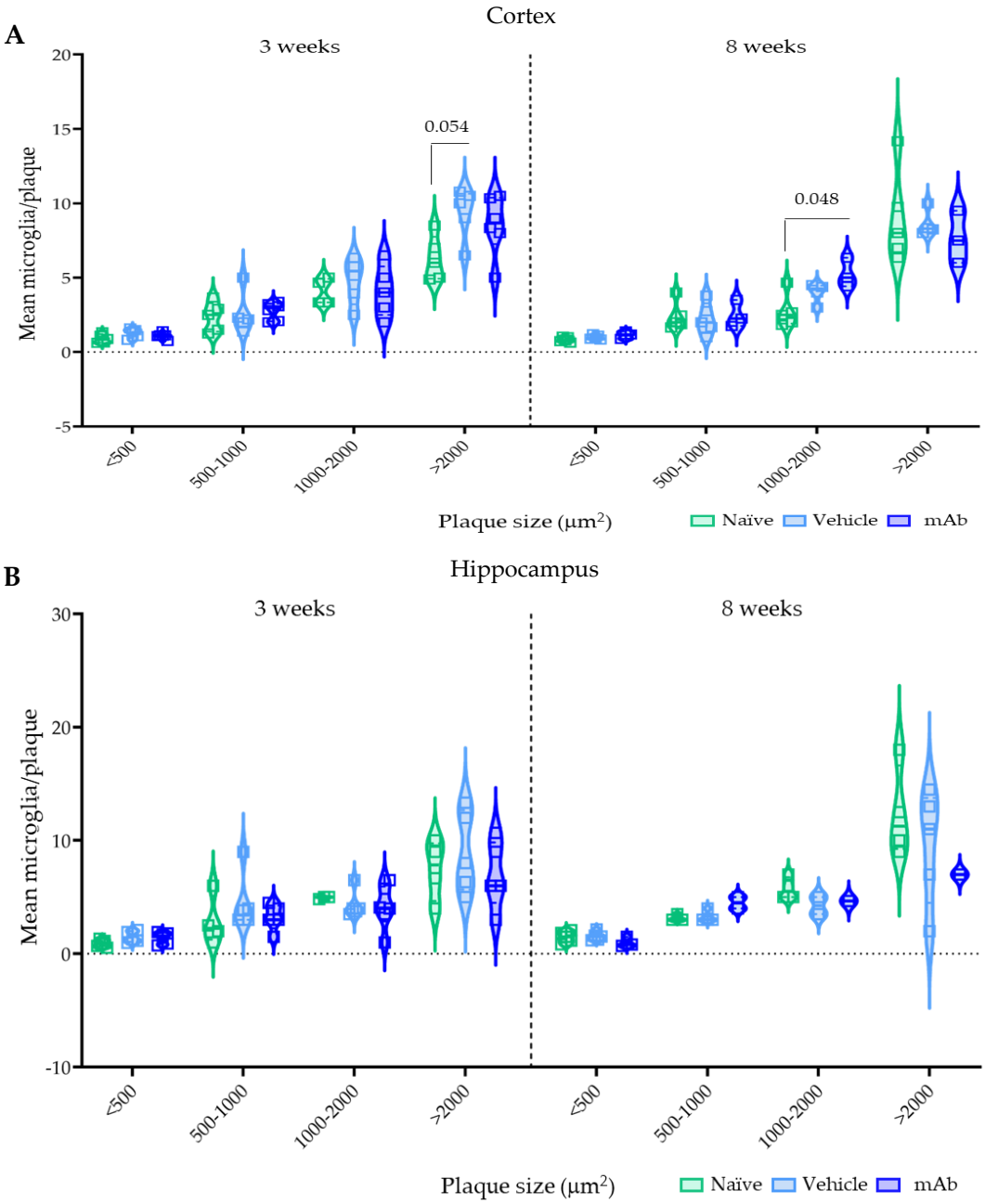

Figure 45. Evaluation of changes in the microglia interaction with plaques induced by the intrathecal *pseudodelivery* in the cortex and hippocampus after 3 and 8 weeks of infusion. Violin plots for the mean number of microglia associated to an Aβ plaque, grouped by the sizes of plaques, in the cortex (**A**) and hippocampus (**B**) of APP mice with the device filled with vehicle or mAb, and in its age-matched APP naïve mice, treated for 3 or 8 weeks. Data are presented as median and interquartile ranges. Each dot represents one mouse. Statistical analysis was performed using the non-parametric Kruskal-Wallis's test followed by Dunn's test.

5.7. IT *pseudodelivery* induced astrocytic activation at three weeks, but it was normalized after eight weeks

Astrocytes are also involved in clearing aggregated proteins. To evaluate astrocytic activation in the cortex and hippocampus, GFAP levels were measured using immunofluorescent staining.

Both 3-week study vehicle and mAb APP mice showed a significant increase in GFAP levels regarding naïve WT mice in cerebral cortex (Figure 46I): naïve WT *vs.* vehicle APP, p-value = 0.015 and naïve WT *vs.* mAb APP, p-value= 0.023. However, in the long-term study, GFAP levels tended to be higher in the cortex in all APP mouse groups regarding their naïve WT counterparts, although no significant differences were found (Figure 46I).

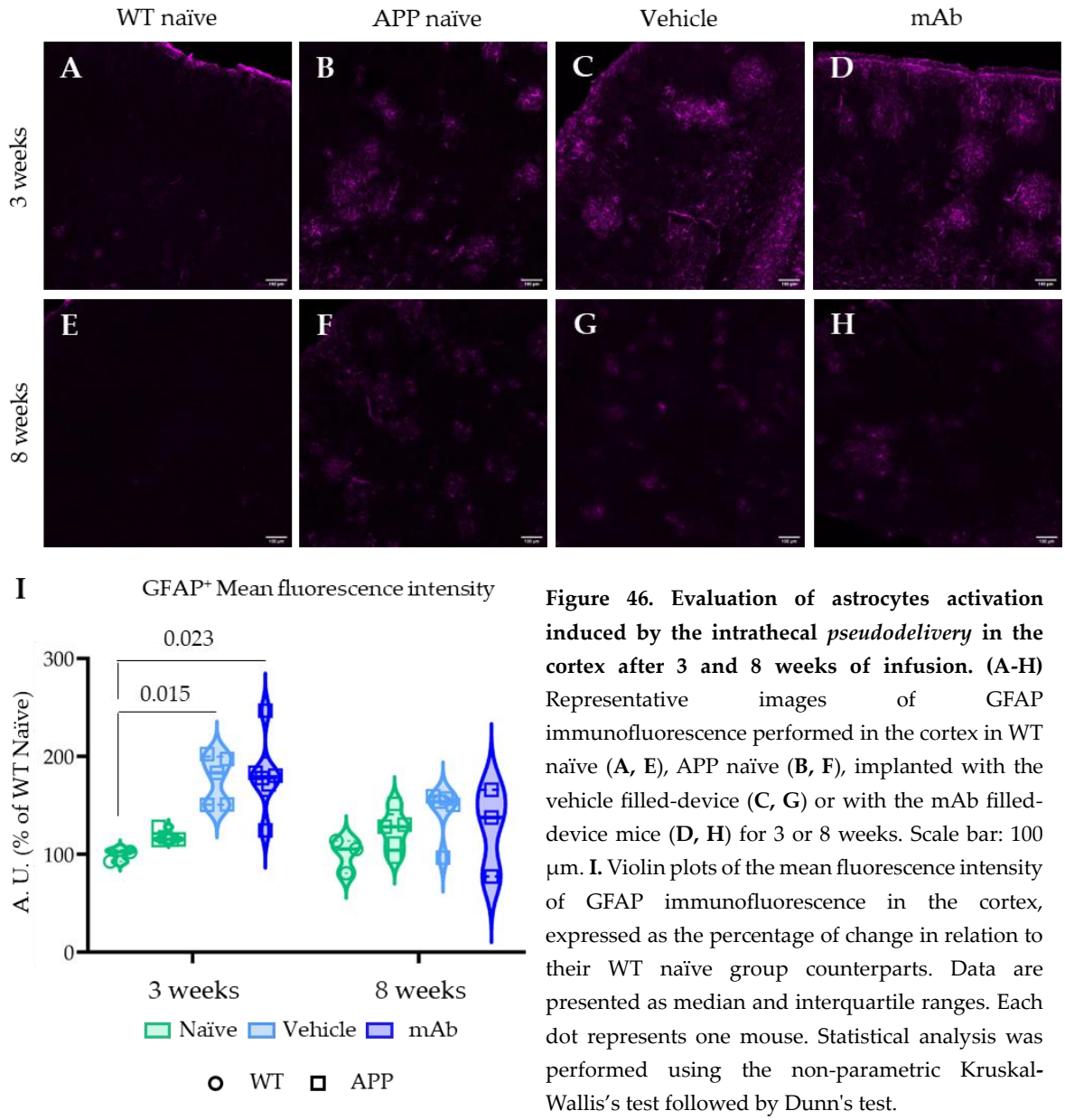

Figure 46. Evaluation of astrocytes activation induced by the intrathecal *pseudodelivery* in the cortex after 3 and 8 weeks of infusion. (A-H) Representative images of GFAP immunofluorescence performed in the cortex in WT naïve (**A, E**), APP naïve (**B, F**), implanted with the vehicle filled-device (**C, G**) or with the mAb filled-device mice (**D, H**) for 3 or 8 weeks. Scale bar: 100 µm. **I.** Violin plots of the mean fluorescence intensity of GFAP immunofluorescence in the cortex, expressed as the percentage of change in relation to their WT naïve group counterparts. Data are presented as median and interquartile ranges. Each dot represents one mouse. Statistical analysis was performed using the non-parametric Kruskal-Wallis's test followed by Dunn's test.

In the hippocampus, GFAP mean fluorescent intensity was higher in mAb APP mice after the short-term study regarding their naïve APP mice (naïve APP *vs.* mAb APP, p-value = 0.043), but there were no differences among groups in the long-term study (Figure, 47I).

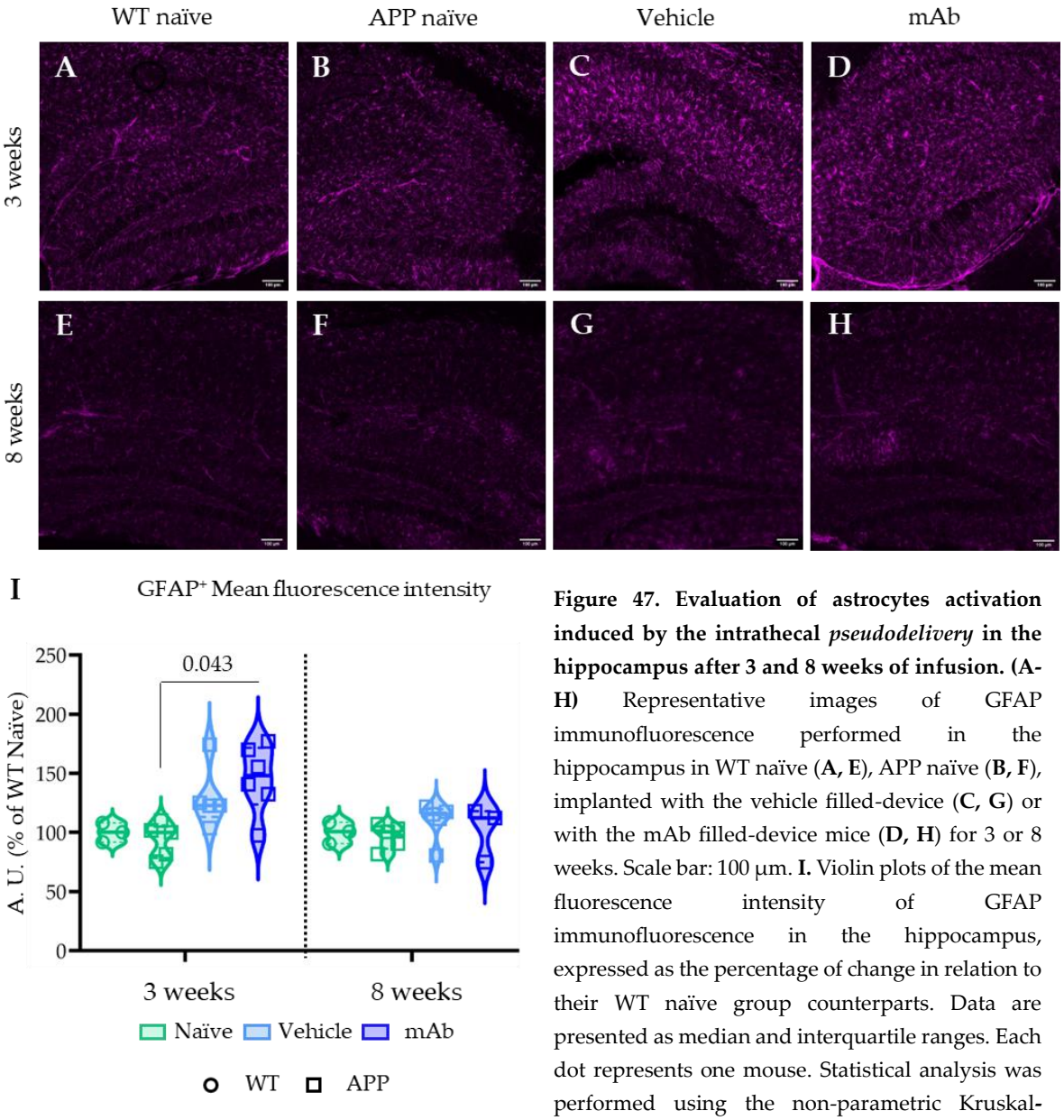

Figure 47. Evaluation of astrocytes activation induced by the intrathecal *pseudodelivery* in the hippocampus after 3 and 8 weeks of infusion. (A-H) Representative images of GFAP immunofluorescence performed in the hippocampus in WT naïve (**A, E**), APP naïve (**B, F**), implanted with the vehicle filled-device (**C, G**) or with the mAb filled-device mice (**D, H**) for 3 or 8 weeks. Scale bar: 100 µm. **I.** Violin plots of the mean fluorescence intensity of GFAP immunofluorescence in the hippocampus, expressed as the percentage of change in relation to their WT naïve group counterparts. Data are presented as median and interquartile ranges. Each dot represents one mouse. Statistical analysis was performed using the non-parametric Kruskal-Wallis's test followed by Dunn's test.

5.7.1. The percentage of Area Covered by astrocytes followed the same trend than its activation

As anticipated for the results of the mean fluorescence, the percentage of area covered by astrocytes was higher in APP mice compared to WT mice in both cortex and hippocampus (Figure 48). In fact, 3-week study implanted mice showed a greater coverage compared to naïve WT mice in the cortex (naïve WT *vs.* vehicle APP, p-value = 0.024; naïve WT *vs.* mAb APP, p-valu e= 0.013; 3 weeks, Figure 48A). The percentage was significantly higher compared to naïve WT at the end of the long-term study, particularly in vehicle-treated mice (naïve WT *vs.* vehicle APP, p-value = 0.024; 8 weeks, Figure 48A).

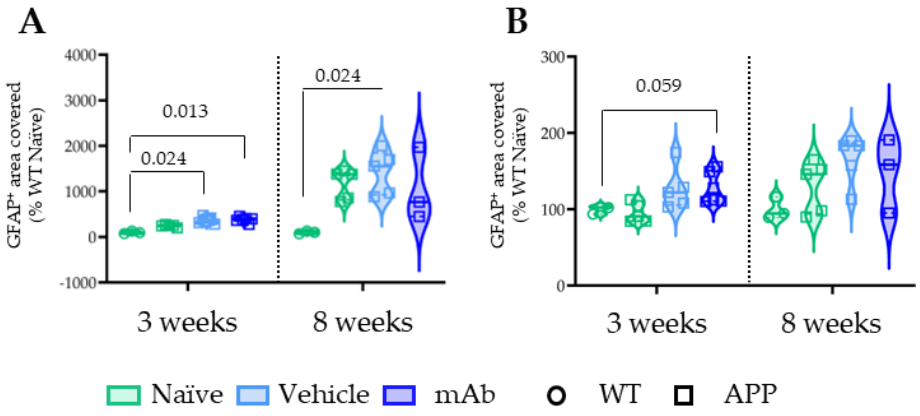

Figure 48. Evaluation of astrocytic proliferation induced by the IT *pseudodelivery* in the cortex and hippocampus after 3 and 8 weeks of infusion. Graphical representation of the percentage of GFAP staining in the cortex (**A**) and hippocampus (**B**) expressed as the percentage of change in relation to their respective WT naïve group. Data are presented as median and interquartile ranges. Each dot represents one mouse. Statistical analysis was performed using the non-parametric Kruskal-Wallis's test followed by Dunn's test.

In the hippocampus, there were no differences between naïve APP mice and naïve WT mice in the short-term study (Figure 48B). At this time, the area covered by astrocytes increased in all implanted mice, especially in mAb-treated mice (naïve WT *vs.* mAb APP, p-value = 0.059; Figure 48B). In the 8-week study, all APP mice, with or without the device, exhibited astrogliosis, since their medians were higher than their corresponding WT counterparts, although no significant differences were found (Figure 48B).

5.7.2. Astrocytic activation found after 3 weeks of infusion was around Aβ plaques in the cortex, but not in the hippocampus

Astrocytic proliferation and activation were also evaluated within a 15 μm radius around plaques of different sizes (Figures 49 and 50). In the cerebral cortex, after three weeks of infusion, the area covered by astrocytes around 10 μm radius plaques was higher in both implanted groups, although only mAb-treated mice showed significant differences with naïve APP mice (p-value = 0.007; Figure 49A). In the case of long-term study, astrocyte area was significantly higher in mAb APP mice regarding vehicle-treated mice (p-value = 0.034; Figure 49A). No differences were observed among experimental groups for other plaque

sizes. Moreover, no differences around any plaque size at any time-point were found in the hippocampus (Figure 49B).

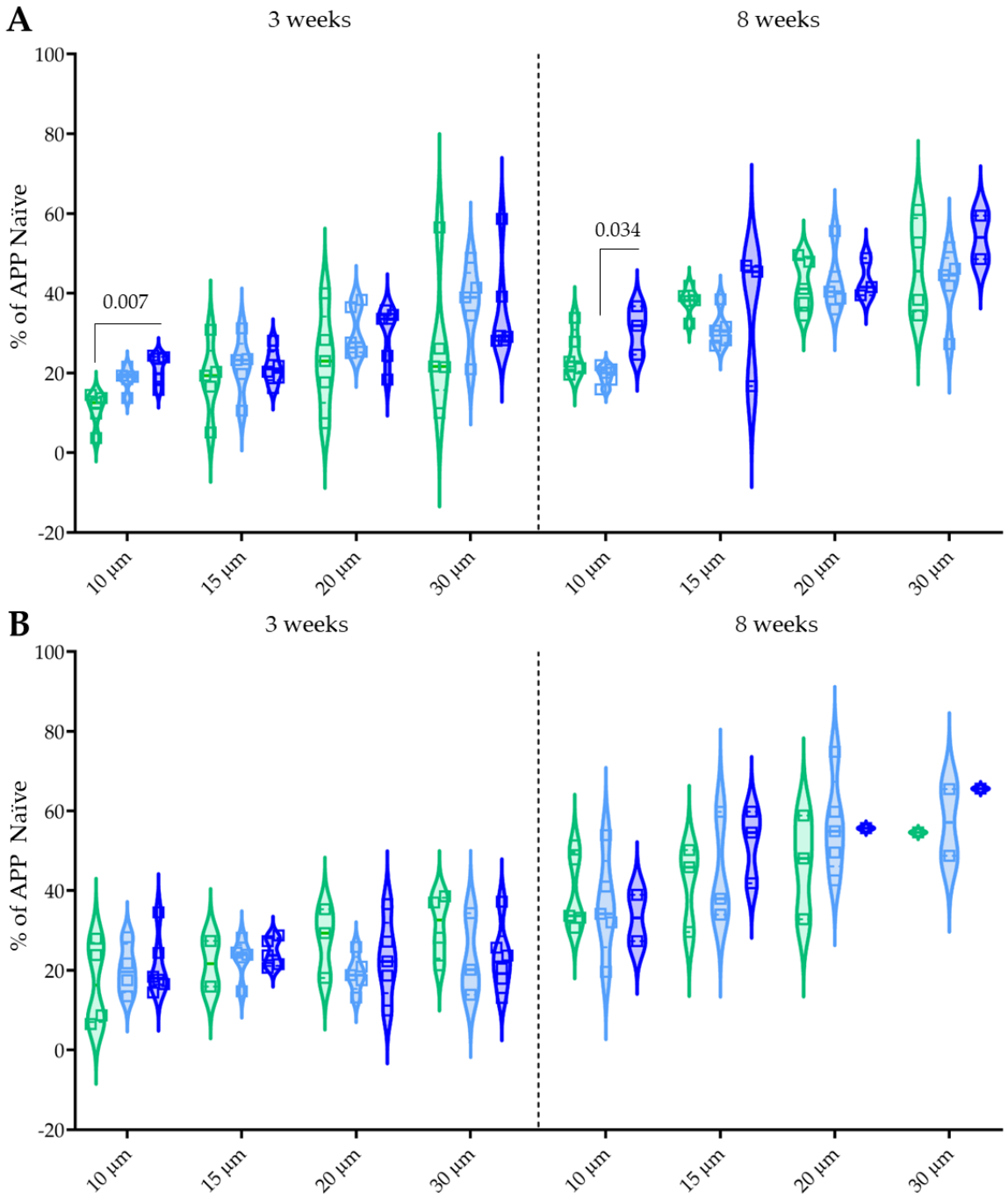

Figure 49. Astrocytic proliferation around plaques induced by the IT *pseudodelivery* in the cortex and hippocampus after 3 and 8 weeks of infusion. Violin plots for the percentage of area covered by GFAP staining within 15 µm radius around 10, 15, 20 and 30 µm radius plaques in the cortex (**A**) and hippocampus (**B**). Data are presented as median and interquartile ranges. Each dot represents one mouse. Statistical analysis was performed using the non-parametric Kruskal-Wallis's test followed by Dunn's test.

However, median astrocytic activation was significantly higher around all plaque sizes in the cortex after 3 weeks of infusion, although only in 10 µm radius plaques in mAb-treated

mice this increase is statistically significant regarding naïve APP mice (p-value= 0.026; Figure 50A). No changes were observed in the hippocampus of the short-term study (Figure 50B). In long-term study, astrocytic activation remained consistent across all groups and plaque sizes in both brain regions, with no differences among groups (Figures 50A and 50B).

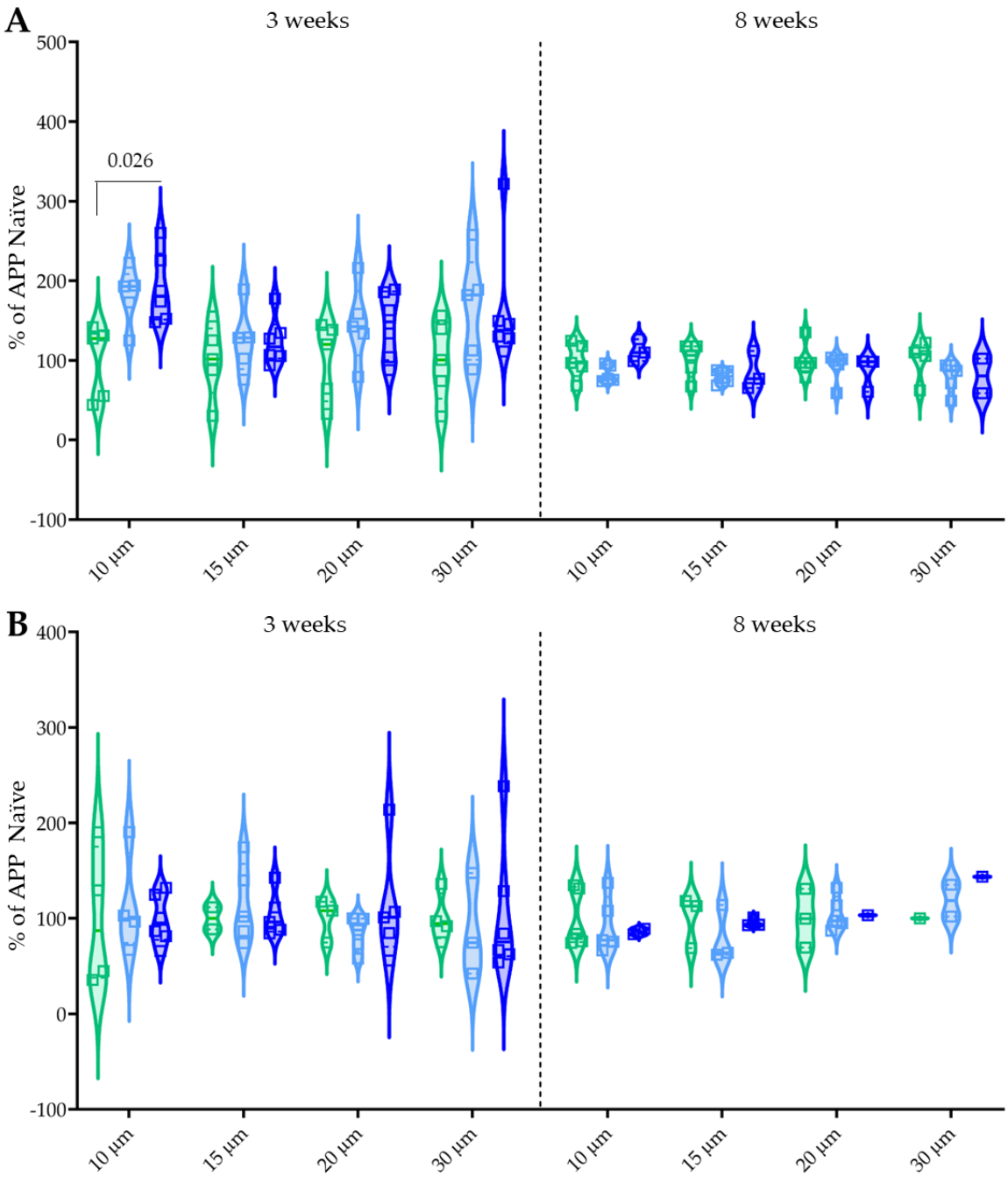

Figure 50. Astrocytic activation around plaques induced by the IT *pseudodelivery* in the cortex and hippocampus after 3 and 8 weeks of infusion. Violin plots for the mean fluorescence intensity of GFAP immunofluorescence within 15 µm radius around 10, 15, 20 and 30 µm radius plaques in the cortex (**A**) and hippocampus (**B**) expressed as the percentage of change in relation to their respective naïve group. Data are presented as median and interquartile ranges. Each dot represents one mouse. Statistical analysis was performed using the non-parametric Kruskal-Wallis's test followed by Dunn's test.

5.8. Eight weeks of CSF apheresis decreased AQP4 levels, while increasing its polarization

AQP4 levels and localization are commonly used to evaluate the glymphatic system. Therefore, AQP4 immunofluorescence was performed for this purpose (Figures 51 and 52). After three weeks of infusion, there were no differences in AQP4 expression, measured as mean intensity, in the cortex (Figure 51I). However, eight-week treatment shows a tendency to lower AQP4 expression in mAb- compared to vehicle-treated mice, though it is not statistically significant (p-value = 0.058; Figure 51I). No differences were observed in AQP4 polarization in the cerebral cortex after the short-term study (Figure 51J, 51K), although a tendency to increase was observed in implanted mice, particularly in mAb-treated mice, after the eight-week study (Figures 51J and 51L).

In the hippocampus, AQP4 expression after 3 weeks of infusion increased in both groups of implanted mice (Figure 52). This increase was significantly higher in vehicle-treated mice compared to naïve WT mice (p-value = 0.041; Figure 52I). However, after eight weeks of infusion, AQP4 levels tended to decrease in mAb-treated mice. Regarding AQP4 polarization, there were no differences among groups after either of the two studies, although in 8-week treated mAb mice, a tendency to increase was observed (Figure 52J-L).

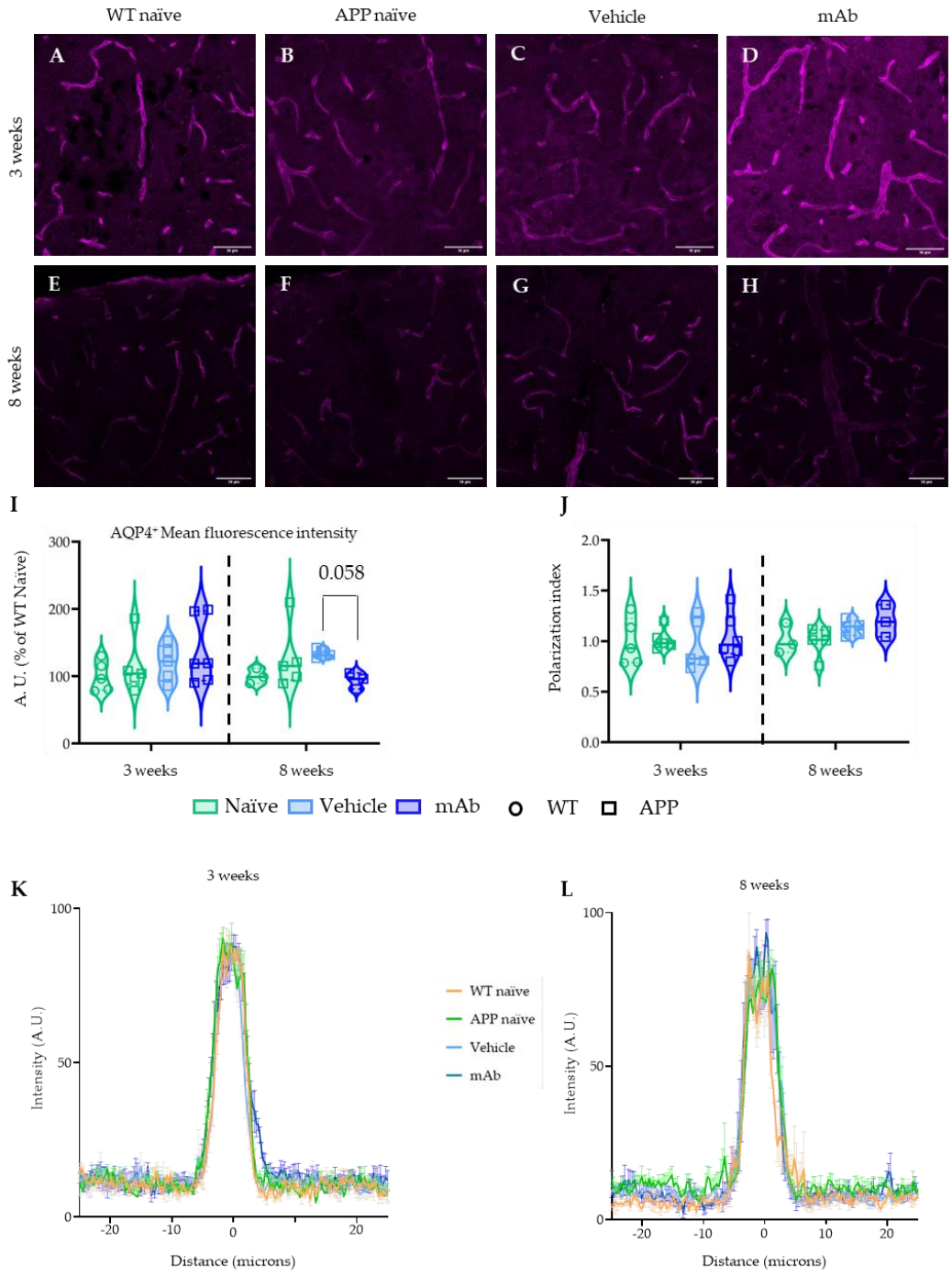

Figure 51. State of the glymphatic system in the cortex based on AQP4 expression and polarization after 3 and 8 weeks of infusion. (A-H) Representative images of AQP4 immunofluorescence performed in the cortex in WT naïve mice (**A, E**), APP naïve mice (**B, F**), implanted with the vehicle filled-device (**C, G**) or with the mAb filled-device (**D, H**) for 3 (**A-D**) or 8 weeks (**E-H**). Scale bar: 50 µm. **I.** Violin plots for the mean intensity fluorescence of AQP4 found in the cortex expressed as the percentage of change in relation to their respective WT naïve. **J.** Violin plots for the AQP4 polarization index found in the cortex expressed. **I-J**, Data are presented as median and interquartile ranges. Each dot represents one mouse. Statistical analysis was performed using the non-parametric Kruskal-Wallis's test followed by Dunn's test. **K, L.** Average intensity of AQP4 staining centered on vasculature in the cortex after 3 weeks (**K**) and 8 weeks of treatment (**L**). Data are represented as mean (line) ± SEM.

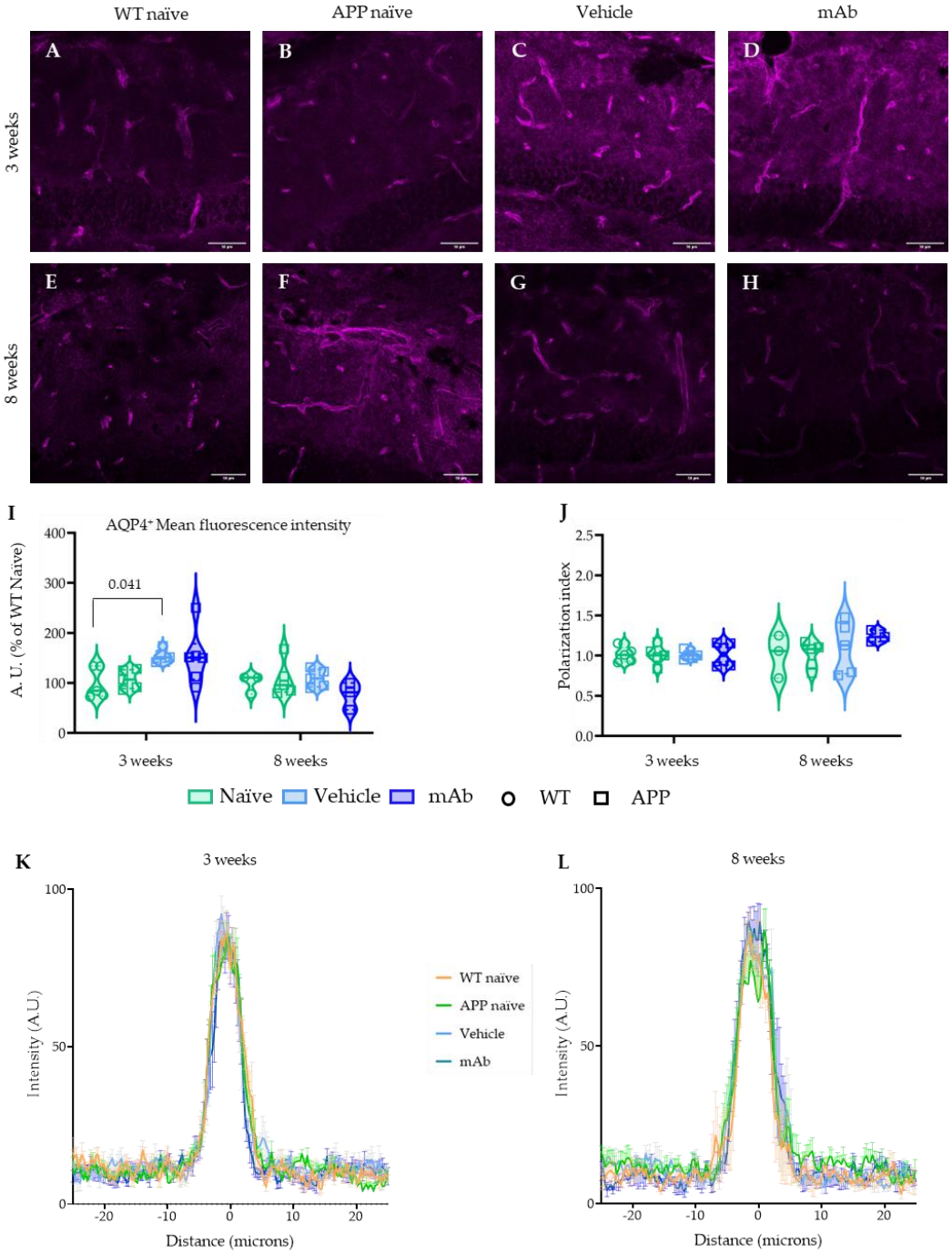

Figure 52. State of the glymphatic system in the hippocampus based on AQP4 expression and polarization after 3 and 8 weeks of infusion. (A-H) Representative images of AQP4 immunofluorescence performed in the hippocampus in WT naïve mice (**A, E**), APP naïve mice (**B, F**), implanted with the vehicle filled-device (**C, G**) or with the mAb filled-device (**D, H**) for 3 (**A-D**) or 8 weeks (**E-H**). Scale bar: 50 µm. **I.** Violin plots for the mean intensity fluorescence of AQP4 found in the hippocampus expressed as the percentage of change in relation to their respective WT naïve. **J.** Graphical representation of the AQP4 polarization index found in the hippocampus expressed. **I-J**, Data are presented as median and interquartile ranges. Each dot represents one mouse. Statistical analysis was performed using the non-parametric Kruskal-Wallis's test followed by Dunn's test. **K, L.** Average intensity of AQP4 staining centered on vasculature in the hippocampus after 3 weeks (**K**) and 8 weeks of treatment (**L**). Data are represented as mean (line) ± SEM. Data are represented as mean (line) ± SEM.

DISCUSSION

Aggregated proteins are one of the main characteristics of neurodegenerative diseases. Then, several therapeutic strategies were developed to clear them (5, 137-139). In the case of AD, immunotherapy has emerged as one of the most sophisticated and effective strategies in combating Aβ-peptide thus far (29, 63, 84, 85, 96). However, this therapy may have important limitations and complications when administered systemically, like poor efficacy and the development of ARIAs (95).

This Thesis presents the proof-of-concept of the CSF-sink therapeutic strategy. This new approach was tested by means of a new implantable device, designed to selectively clear targeted molecules directly from the CSF without delivering the therapeutic agent to the brain (*pseudodelivery*). As we are proposing not only a new therapeutic strategy but also a new mechanism of action, the roadmap to product development should start with *in vitro* proof-of-principle of the mechanism of action –the *selective apheresis*-. After that, a feasibility *in vivo* study is needed to show proof-of-concept of the therapeutic application. Given we are interested in AD and the best animal models for this disease are transgenic mice, we needed to use a miniaturized prototype of the device to test the therapeutic strategy *in vivo.* Moreover, as this is the first time such a device is implanted in mice, we further needed to perform a feasibility study before we could optimize the device for a long-term study.

1. Immunoselective nanopheresis

Membrane processes are commonly used for filtration, with different types of membranes having specific pore sizes tailored to their applications. Nanofiltration membranes typically have pore sizes ranging from 1 to 10 nanometers, smaller than those used in microfiltration and ultrafiltration, but slightly larger than those in reverse osmosis. Then, these membranes are effective for filtering particles in the 1–10 nanometers range, which would include some proteins, small molecules like sugar and salts (140). NPMBs come in a wide variety of types based on their material, pore geometry, and fabrication methods. Materials can be organic, like polymers, inorganic, like metals and ceramics, or composite materials. Most of the commercial filtration membranes are polymeric with Nafion, polycarbonate, polyethylene terephthalate and polysulfone being commonly used. Inorganic nanoporous materials with well-ordered pores, like nanoporous silica and anodic alumina, are increasingly popular for biomedical applications. This type of membrane offers good physical and chemical stability, with the possibility of smaller pore sizes compared to polymeric membranes (141). Nanoporous silica is not structurally strong enough to support weight, so it is typically used for nanoparticles or thin coatings, such as on implants (142). Conversely, anodic alumina can be tailored to different applications while maintaining its porous structure, making it versatile for a wide range of applications (143), including biomedical applications, like biosensors, cell growth, tissue engineering, and drug delivery (144). One of the main reasons for this is that anodic alumina membranes are characterized by a high density of uniform

pores in large areas of a chemically stable composite, which can easily be tailored (144). These membranes are obtained through electrochemical oxidation of the metal (anodization). By adjusting anodization conditions such as temperature, electrolyte composition, and time, pore size, interpore distance and thickness are controlled. A two-step protocol can be employed to achieve a highly ordered nanoporous structure. Additionally, to enhance their long-term chemical stability and resistance to leaching under physiological conditions, several coating treatments, with ALD being the most efficient method, have been used (144). This method does not alter the properties of anodic alumina membranes (112). Therefore, this process was used to obtain the 9 nm pore size alumina NPMBs for this study (112, 113).

First, the selective permeability of alumina NPMBs was evaluated *in vitro*. Since our aim is to remove soluble form of Aβ, different protocols for preparing $A\beta_{1-42}$ solutions were tested to minimize Aβ aggregation. Several protocols have been developed with this purpose (115, 145, 146), but in this study only three protocols were tested for its resuspension: 1) DMSO/DMEM-F12 (1:1); 2) 100% DMSO; 3) HEPES/NaCl. Among these protocols, the HEPES/NaCl method from Krishtal et al. (115) was found to better preserve Aβos, and was therefore chosen for the subsequent experiments.

In the first permeability assay, no changes in Aβ flow through the NPMB were observed as it was not detected in any cell. These results could be due to the material of the plates and inserts used as permeation chambers, polystyrene, possibly because Aβ may have adsorbed to their various surfaces. In fact, previous research has indicated that polypropylene (PP) has the highest Aβ recovery rate. In our case, whenever possible, we used this type of material (pippete tips, tubes, etc.) but not all PP labware showed the same level of recovery, and even pure PP not being the one with the best recovery rate (147). Moreover, suitable polypropylene cell culture plates were not found for our studies. Then, polystyrene plates used in this assay may explain the lack of Aβ detection. Therefore, to overcome this problem, a higher dose was used to saturate the cell surface. This way, there would still be enough Aβ to flow through the NPMB. Thus, using 20 μg/ml we confirmed the NPMBs' permeability to Aβ. The next step was to determine whether these NPMBs are impermeable to larger molecules, such as albumin. In this case, there were no detection problems, although its adsorption to this material has been previously described (148, 149). All in all, the impermeability of the NPMBs *in vitro* to large molecules was confirmed.

A major problem we have had to face has been the difficulty in handling alumina NPMBs. All these membranes have to be manipulated to place them at the base of the inserts, thus separating the receptor and donor cells. However, many of them broke in the process, due to their extreme fragility. This is a serious problem, not only for this type of in vitro studies, but also makes it difficult to adapt them to the devices, since, at present, their manufacture is homemade and has minimum and maximum size limits. In the framework of other projects, we have tested flat sheet polyethersulfone (PES) NPMBs, to avoid the fragility of

alumina NPMBs (150, 151). One of the advantages of these membranes is that they are much more flexible, son they can be adapted to different shapes and sizes. In addition, their high commercial availability and diversity and diversity of nanopore size allows the most appropriate selection for each molecule of interest under conditions of high homogeneity among the different batches. After performing a similar characterization to that carried out with alumina NPMBs, we observed that it was not possible to detect the flux of Aβ through these membranes. In fact, PES membranes require high pressure (> 100 kPa; https://www.sterlitech.com/microdyn-nadir-nadir-pm-up010-10kda-pes-uf-297x210mm-1-pk.html) for filtration. In our case, the intention is that the flows are given by the physiological CSF pressure, estimated around 1.1-2 kPa (152). Therefore, PES NPMBs were discarded because they do not meet our needs. Polycarbonate (PC) membranes have the same advantages as PES membranes - flexible (150) and commercially available – but without the limitation of the need to apply high pressures (153). These PC NPMBs are being tested with promising results. The first data from *in vitro* studies using permeation chambers with PC NPMBs indicate that not only they are permeable to soluble Aβ but also impermeable to larger molecules, such as albumin and immunoglobulins.

2. The challenge of implementing IT *pseudodelivery* in mice

The second objective of this Thesis was to assess the feasibility of implanting a device endowed with a module for immunoselective nanopheresis in mice. Due to its size, the device was not suitable for implantation in small mice. Therefore, for the feasibility study, only male mice weighing at least 30 g were used. However, the device was still challenging to implant in these animals as it weighted approximately the 15% of the animals´ weight and its length was close to the 70 % of their back length, regardless of genotype.

A key issue identified in this study was the reopening of the surgical wound, as nearly all mice required reoperation to ensure wound closure. It was noted that the mice tended to scratch around the wound area, likely due to the itchiness associated with healing wounds (154). While no infections were observed, this issue could impact the mice welfare and should be addressed in subsequent experiments. Additionally, some animals experienced major welfare issues, resulting in euthanasia in 30% of the cases. It is unclear whether these issues were caused by the device´s size or surgical complications, as half of the euthanized mice developed complications within the first three days, while the other half did so after weeks. The invasiveness of the procedure and the short time frame for complications in the first case suggest that surgical factors may have played a role. For the other half, the device´s size may have contributed more to the welfare issues. Therefore, modifications to both the surgical procedure and the device's size were necessary to improve mice welfare.

Despite the complications found in the feasibility study, it was possible to confirm the Aβ efflux through the NPMBs and their impermeability to molecules larger than their pore size,

like immunoglobulins. However, Aβ levels found in the reservoirs varied among samples, possibly due to implantation time and the type of treatment administered (mAb or aCSF).

Before continuing with the *in vivo* experiments, the device was modified to reduce its size, by removing the protective shell and replacing it with biocompatible silicone lining. Additionally, surgery modifications were also implemented to prevent wound reopening and other side effects of the procedure. One significant change was the increase in the cannula fixation. Various methods have been employed for this purpose, with dental cement and cyanoacrylate gel being the most common choices (155). In our feasibility study, cyanoacrylate was used due to its quicker preparation time and fewer side effects compared to dental cement (155). However, it was noted that cannula fixation was not entirely satisfactory, likely due to the mismatch between the large, flat cannula and the small, round shape of the mice skull (155). To address this issue, Sike et al. (155) developed an adapter made of a special soft and elastic silicon paper that mimics the shape of the mouse skull. While this could have been a helpful solution for our experiments, we lacked the required materials, such as a 3D printer. Groseclose et al. (156) found that UV light-curing resin creates a strong and long-lasting bond between the cannula and bone, lasting for at least 60 days. Furthermore, this compound offers benefits such as no side effects, easy shaping, and quick curing time (156). Then, a protocol that combined this compound with cyanoacrylate (125) was used for the long-term study. This protocol proved effective as the cannula remained securely attached to the skull throughout the experiment, consistent with previous observations (125). Additionally, although in the feasibility study the correct placement of the cannula was verified, in the long-term study, the "flat-skull" position of the brain was checked to completely ensure the vertical alignment of the cannula (157). Another significant change was the modification of the incision shape. The thin skin over the head, combined with the increased tension caused from the presence of the cannula, raised the risk of skin breakage, hindering the healing process. To promote healing, it was crucial to reduce tension in the wound. As the cannula's volume and skin fragility couldn't be altered, adjustments were made to the incision's shape and location. Then, following veterinary advice, the linear incision from the middle of the head to the end was replaced with a U-shaped incision at the back of the head. As it was noted in the feasibility study, scratching was a major issue in wound healing. In this sense, nail trimming has been shown to be effective in reducing the effects of scratching behavior (158), so this step was also incorporated into the surgical procedure. As a result, the amount and severity of wound reopening were significantly reduced, indicating the effectiveness of these modifications. These surgical changes significantly reduced the recovery time. Furthermore, these adjustments also minimized the initial drop in body weight. Only one mouse was euthanized due to connectivity issues, indicating that these changes enhanced the welfare of the mice (125, 159, 160). Actually, the enhanced welfare of the mice resulted in a more favorable assessment by the Research Ethics Committee, leading to a downgrade in the severity of the procedure from severe to moderate.

Furthermore, all the improvements associated with surgery and pre- and post-operation, allowed the development of behavioral tests at different times. In fact, anxiety-like behaviors were not found. These tests did not reveal differences among groups, but a decline in activity was noted over time. This decrease could be due to habituation to the mazes, although the mazes used are suitable for repeated testing with a 4-weeks test-interval (161). It is worth mentioning that 129Sv background mice are typically hypoactive (162-164), which could also explain the decrease in activity. Therefore, the device does not seem to affect mice behavior at this level.

Memory impairment was not detected in the APP mice at the end of the experiment (9 months old). Previous research has shown memory deficits in APP mice at different ages, ranging from 6 months old (165-169) to 9 months (170) or later (171, 172), which could also be the case for the mice used in our study. It is important to note that most studies on APPswe/PS1dE9 transgenic mice are conducted on C57BL6/J (166, 168, 170) or C57BL6;C3H (165, 171, 172) backgrounds, not on the 129Sv background like our mice. Additionally, it is important to mention that movement is essential for memory tasks (173), which may pose challenges in assessing memory impairments in a strain with low activity levels. However, it is still possible for this strain to perform well in memory tests (164, 174). The novel object recognition task has been suggested to be suitable for this kind of strains with low exploratory activity (164), so it is being considered to assess cognitive performance in these mice. Additionally, it is important to note that the minimum sample size of 10 mice per group is required for behavioral test (175), which was not achieved in this experiment.

3. Effects of IT *pseudodelivery* by replacement of therapeutic solution in the AD murine model APP/PS1 in early symptomatic stage

The long-term study also allowed to perform a mid-treatment refill of the therapeutic solution, i.e., four weeks after the device implantation surgery. During the refill, an equal volume of fresh solution was added while an equivalent amount was extracted from the device reservoir. Thus, the levels of $A\beta_{1-42}$, $A\beta_{1-40}$, NfL, and GFAP were measured using the ultrasensitive Simoa technique at the mid-treatment refill and at the end of the experiment. Given the molecular size of these last two peptides (GFAP: 49.88 kDa (176), NfL: 60 kDa (177)), it would not be expected to detect them in the reservoirs, but their filamentous structure allowed them to pass through the NPMB due to their small diameter (178, 179). No differences were found in the levels of each marker at the two times considered. However, it is worth noting that while most reservoirs contained detectable levels of these proteins, one reservoir had no proteins detected at the end of the study. Additionally, after eight weeks of infusion, the levels of all these proteins were lower compared to those found in the reservoir after four weeks of infusion, particularly in the reservoirs filled with vehicle. This decrease may be due to pore obstruction. Biofouling, which could impact NPMBs

permeability by obstructing pores with protein accumulation, was not investigated in this study. Previous research suggests that SiO_2 coating may help prevent biofouling (180, 181), but a recent study found significant protein accumulation in similar NPMBs after four weeks of *in vivo* use (182). Some studies have suggested that protein adsorption by materials may be dynamic and competitive, with protein concentration in the solution affecting its adsorption (183). Due to its stickiness (147), Aβ peptide may be one of the adsorbed proteins contributing to biofouling. If the mAb effectively removed some Aβ from the CSF, its concentration would have decreased. This could potentially reduce protein accumulation and pore obstruction, which may explain the different trend in protein concentration observed in the reservoirs filled with mAb. Further research may be needed to better understand NPMBs biofouling, its composition and potential treatments for its reduction (184, 185), as well as exploring NPMBs made from different materials (186).

These four proteins were also quantified in CSF and plasma. The levels of $A\beta_{1-42}$ observed in the reservoir were lower than those of $A\beta_{1-40}$ in the CSF. This matches what we expected, since $A\beta_{1-40}$ is the most predominant soluble monomeric isoform of Aβ (30), as well as for $A\beta_{1-42}$ deposition in the brain (187). However, it is unclear whether the levels of $A\beta_{1-40}$ in the CSF were as expected in this AD model due to the lack of comparative studies. This could be due because the mutation in PS1 is not expected to affect the levels of $A\beta_{1-40}$ (116). This, added to the challenges in collecting CSF samples and the limited volume obtained (188), may have led to a focus on $A\beta_{1-42}$ analysis. Regarding $A\beta_{1-42}$, a study by Liu et al. (189) reported about 3 times higher levels of $A\beta_{1-42}$ in APPswe/PS1dE9 mice compared to our study. It is important to note that they measured $A\beta_{1-42}$ levels using an ELISA kit, while we used the Simoa technique. Previous research has shown that the Simoa technique may yield lower $A\beta_{1-42}$ levels compared to ELISA, likely due to their different sensitivities(190). In other AD mice model, DeMattos et al. (133) found $A\beta_{1-42}$ levels more similar to ours using the radioimmunoassay method, which is also a technique with high sensitivity. Few studies have measured both Aβ isoforms in CSF in different AD mouse models (191-193), showing similar levels and ratios to our study, although the mutations of these transgenic mice were different (191, 192). Additionally, the diffusion of both peptides through the apheresis module seems to be in accordance with their concentration in CSF. In the case of plasma, more studies have been performed to study this in our AD mouse model (81, 169, 194), where they found similar levels of both Aβ isoforms than ours. There were no differences in both isoforms of Aβ among APP groups in plasma either, leading to similar $A\beta_{1-42}$/ $A\beta_{1-40}$ ratio among them. This lack of differences in the levels of soluble Aβ levels in these biofluids may support the idea that the NPMBs were obstructed after eight weeks of treatment, highlighting the importance of abording this problem.

Regarding GFAP, CSF GFAP levels were much higher than in plasma, where the levels were similar to those found in the reservoir, consistent with the known differences between these two biofluids in humans (195). It is unknown whether the levels found in the CSF were those

expected in this AD model, since there were no studies to compare. Despite this, they seem to distinguish between WT and APP mice, since in all APP groups the levels were higher than in the WT group. No differences were found among APP groups. Then, since CSF GFAP is associated more with neuroinflammatory changes rather than Aβ load (195), neuroinflammation would not be expected at this point with the device. Additionally, CSF GFAP has only been associated with cognitive impairment (196), which was not observed in our mice. With respect to GFAP levels in plasma, they were comparable to other APP/PS1 mouse models (197). The mAb-treated group showed a decrease in plasma GFAP levels after the 8 weeks of treatment, suggesting an improvement in Aβ pathology in the brain, since plasma GFAP levels correlate with cerebral Aβ pathology (196, 198, 199). However, it was found a positive association between plasma GFAP and both Aβ isoforms in plasma, which may seem contradictory with previous studies since they described that plasma GFAP increase with Aβ deposition, which would decrease Aβ levels in plasma (196, 198, 199). This could be explained by some studies that show that plasma Aβ may affect endothelial cell function, reducing blood flow, increasing the production of Aβ by these cells, increasing plasma levels (200). Additionally, plasma GFAP has also been associated with vascular disturbances (201, 202). This also correlates with the previously described vascular disturbances found in mice with this mutation (203). Furthermore, continuous *selective apheresis* may have beneficial effects on the BBB, as increased plasma GFAP levels are associated with acute neuronal injuries, possibly due to BBB dysfunction (195). It is worth noting that CSF GFAP is more sensitive to freeze-thaw cycles compared to plasma GFAP, making plasma GFAP a more reliable tool (204).

Lastly, no neural damage was found in the implanted mice, as indicated by similar levels of NfL, a biomarker for neurodegeneration (8, 177, 205), compared to APP naïve mice. However, there is uncertainty regarding the accuracy of the Simoa kit's antibody in detecting NfL in our murine samples. The levels detected in all mice in both biofluids were comparable to those found in other APP/PS1 mice (206), but it is not possible to differentiate between WT and APP/PS1 mice based on these levels. This differentiation should be possible when plaques are present or even in asymptomatic stages whether brain lesions are detected (206). If the NfL levels detected are accurate, they suggest that there is no significant injury caused by Aβ in our 9 months old mice, as CSF NfL levels have been associated with Aβ neuronal injury (207). Further studies are required to understand the longitudinal changes in neurodegeneration in our AD mouse model, in addition to measure NfL levels by a specific ELISA to corroborate our results. Plasma NfL levels were related to CSF GFAP levels. Since plasma NfL is associated with larger ventricle volumes (208) and CSF GFAP with neuroinflammation (195), it would be expected that in implanted mice, where the CSF from the device could result in an increase in ventricle volume, there were some neuroinflammation associated with it, although it was not significant given that none of these parameters have been shown significantly different among APP groups.

Having two *in vivo* studies at different treatments times allows us to compare soluble $A\beta_{1-42}$ levels in both brain tissue, plasma, and the reservoirs at the end of each study. Only this peptide was considered for comparison, as it was determined in both studies. In the cortex, the levels of $A\beta_{1-42}$ tended to be much higher in naïve APP mice in the long-term study compared to the same group in the feasibility study, since the pathology is more advanced (117). However, no changes were observed between the three groups of mice in any of the studies. In the hippocampus, soluble $A\beta_{1-42}$ levels were significantly reduced after 8 weeks of IT *pseudodelivery*, suggesting a higher clearance effect in this area, likely due to proximity to the lateral ventricle where the cannula is inserted. However, this reduction was not observed in either plasma or CSF, in the case of the long-term study, of the implanted mice. A positive correlation was found between $A\beta_{1-42}$ levels in plasma and the ones found in the hippocampus. Then, this could also be explained by the obstruction of the NPMBs. Before the obstruction of the NPMBs, the $A\beta_{1-42}$ levels could have been also reduced in the plasma. However, after the blockade, they may have returned to near-normal levels, as there was still a correlation between these two samples. Since in the hippocampus the effects were more pronounced, it was still noticeable at the end of the experiment.

Then, the histopathological effects of this therapeutic strategy were analyzed. Surprisingly, after three weeks of infusion, all implanted mice showed an increase in Aβ plaques in both brain regions. This could be due to two possible explanations. Firstly, anesthesia has been shown to induce Aβ accumulation (209-212), as it can lead to neuroinflammation (126, 213), and therefore oxidative stress (214), which in turn can increase Aβ production (215). However, the duration of anesthesia exposure is crucial (213, 216), since in these studies exposures were longer than ours and repeated. Alternatively, the brain injury resulting from surgery may be another explanation, as implanting devices has been found to harm brain tissue, triggering a series of reactions (217, 218). Research indicates that even minor traumatic brain injuries can lead to an increase in the production and accumulation of Aβ (219, 220). However, the effects may vary among different injuries (221, 222). Microbleeds may contribute to this increase (223), and a lack of changes in Aβ levels in some models could be due to insufficiently injured blood vessels. While evident bleedings were not observed in our study, the possibility of microbleeds cannot be ruled out, especially in these mice where the catheter was not as securely fixed as in the long-term study. Some studies suggest that the increased expression of Aβ after injuries may have beneficial effects by stimulating brain recovery (33). Despite these factors, mice treated with mAb showed fewer Aβ plaques in the hippocampus compared to those treated with vehicle, as the increase in plaque area was only significant in vehicle-treated mice. This suggests that the continuous IT *pseudodelivery* may have promoted Aβ clearance. After eight weeks, there were no differences in any brain area, indicating that the initial increase in Aβ levels may have been normalized due to the longer post-surgery time, improved surgical procedures, or the need for the therapy to take more time to show significant effects. Additionally, the presence of biofouling may have obscured the presence of the therapeutical agent, explaining the lack

of differences in Aβ plaques between implanted mice. Further research is required to better understand the effectiveness and timing of this approach, as well as to the efficiency of clearing. The 6E10 antibody dose was selected based on its proven efficacy in reducing Aβ plaques in a study by Oddo et al. (88), where a significant reduction was observed 3 days post- injection in the 3xTg-AD mice. While plaques reappeared after 30 days in their research, our continuous treatment approach was anticipated to yield a sustained response. However, our results indicates that in the subsequent experiments the antibody dose should be adjusted. Additionally, exploring different antibodies (224, 225) or other target-capturing molecules (226, 227), and combining different therapeutics for multiple targets, along with combining this strategy with interventions that enhance proteostasis like physical activity and dietary supplements (47, 66, 228), could boost the effectiveness of this strategy.

The purpose of IT *pseudodelivery* is to assist in clearing molecules from the CNS. When we apply this concept to proteins that accumulate in the brain it can contribute to rescuing unbalanced proteostasis. Autophagy is highly active in the brain, showing increased activity in the early stages of AD before Aβ deposition (229). However, disruptions in the autophagy flux occur in AD, leading to the accumulation of autophagic vesicles (230). The protein p62 serves as a marker of autophagic flux, as it accumulates when autophagy is inhibited, and decreases when autophagy is stimulated (231). Initially, autophagy appears to be functioning properly at the first time point (7 months and 3 weeks old), since p62 levels are lower in APP naïve mice compared to WT mice. However, by 9 months of age, p62 accumulation in the cortex becomes evident. In all implanted mice, p62 levels remained similar to those in WT mice, suggesting that our therapeutic strategy may help to restore proper autophagic function. However, the levels of waste products such as lipofuscin did not show a corresponding decrease. Our findings revealed higher levels of lipofuscin in APP naïve mice compared to WT mice, with even higher levels in implanted mice. This aligns with previous research showing elevated lipofuscin levels in AD and in cases of chronic electrode implantation (218).

Microglia and astrocytes also play an important role in Aβ clearance. Both were found activated after 3 weeks of treatment. Since this was found in all implanted mice, it seems unlikely that the antibody was the cause. Overall, when the mAb was not detected either in the brain tissue or peripheral tissues like the liver. Then, these changes in activation could have been induced by the surgery (126, 210, 232-235), the resulting accumulation of Aβ (55, 236, 237), or the rise in Aβos due to plaque disaggregation caused by the device (43, 238). However, the levels of soluble Aβ did not change in any brain region at this time, indicating that the latter may not be the cause. What is evident is that activation was focused on Aβ plaques. In the case of microglia, not only were they more active around all plaque sizes, but they also proliferated around the larger plaques, which facilitated Aβ removal (239). Since plaques are surrounded by a halo of Aβos (240-242), which are mobilized with the treatment, more Aβos may have been mobilized in larger plaques, attracting microglia's

attention to them. In line with this, Aβos in smaller plaques should have been captured faster, making them less toxic (243) and, therefore, less attractive to microglia. Microglia activation and number were similar in all mice after 8 weeks of treatment. Despite similar quantities of microglial cells, there were more microglia per plaque, suggesting that the treatment enhances the targeting of existing microglia towards amyloid plaques. Specifically, microglia were more concentrated around plaques smaller than 2000 μm^2, reducing their number around larger plaques. While microglia typically remain stable around plaques (244), this behavior may be attributed to the reduced toxicity of larger plaques at the beginning of the treatment (245) and the emergence of new deposits (236, 237). However, in hippocampus, there was a slight decrease in the number of microglia around the smallest plaques (< 500 μm^2). The variability in the microglial response to small plaques (237) may be a factor, but it is important to note that Aβ clearance by the treatment was still evident in this area. Therefore, the treatment's effect on these deposits may still be present, rendering them inert.

The rise in GFAP immunoreactivity in astrocytes observed after 3 weeks was accompanied by an increased proliferation of astrocytes, indicating a potential improvement in clearance mechanisms (246). The increase in immunoreactivity was mainly observed around smaller plaques and was sustained after 8 weeks. In contrast, astrocytes around other plaque sizes initially showed an increase in GFAP immunoreactivity at 3 weeks, which later decreased to levels lower than those in naïve mice. In addition, the area occupied by astrocytes did not change around the other plaque sizes at any time point. This response of the astrocytes could be explained by several theories. Since some studies have determined that astrocytes response is more dependent to plaque-associated neuritic damage than to plaque size (247), the sustained response around these plaques could be to the damage caused by them since accumulating Aβ, which first forms Aβos (26). Another explanation could be that these plaques could be caused by the main astrocyte's lysis (248). For larger plaques, the attenuation of astrocyte reaction after 8 weeks may be due to the increased microglia association observed (249). In addition, the decrease in Aβ load could also have led to the reduction of GFAP levels (250). Conversely, in the hippocampus there were no changes in GFAP immunoreactivity around any plaque size, possibly due to the treatment's effects.

Finally, the glymphatic system function was evaluated through the analysis of AQP4 expression and location, since they are linked to Aβ accumulation. Studies have shown conflicting results, with some indicating increased AQP4 levels with the increase in Aβ deposition (212, 251-253), while others have reported decreased AQP4 expression during AD (254). These discrepancies may be due to different disease stages (255). In our study, after 8 weeks of treatment, AQP4 expression increased in the hippocampus in both groups of implanted mice after 3 weeks of treatment but decreased in mAb-treated mice in the cortex and hippocampus after 8 weeks. The initial increase in AQP4 levels may be related to its role in astrocyte migration (251), which could be related to the increase in astrocytes

found in this area. However, if astrocyte increase were the sole cause, AQP4 levels would also be elevated in the cortex. The disparity may be attributed to the hippocampus being more responsive to the volume changes induced by the device (256). Despite changes in AQP4 expression, the polarization index remained consistent with WT mice and APP naïve mice, indicating no changes in glymphatic system function even in APP mice at this point. The latter decrease in AQP4 levels found in both brain areas with the mAb treatment could be attributed to changes in Aβ deposits. Although the decrease in Aβ plaques was not so evident in the cortex, there could be a decrease in the formation of insoluble Aβ aggregates, which appears to trigger AQP4 expression (257). However, there is still debate about the plaque stage that triggers AQP4 expression (251, 257-260). What is clear is that the polarization of AQP4 to the perivascular astrocytic endfeet is crucial for its functions. With the mAb treatment, the polarization of AQP4 increased in both brain regions after 8 weeks, suggesting that the continuous selective apheresis may enhance glymphatic clearance (261-264).

4. The contribution of IT *pseudodelivery* to the challenge of brain drug delivery

Administering drugs to the CNS presents significant challenges, primarily due to poor drug penetration through the BBB. Various *in vivo*, *in vitro*, and *in situ* studies have demonstrated this difficulty (265). Small molecule diffusion through the BBB is akin to solute-free diffusion through biological membranes. The likelihood of a small molecule passing through the BBB can be predicted based on its molecular weight (MW) and structure. Molecules with a MW exceeding 450 Daltons or those with polar functional groups forming more than seven hydrogen bonds exhibit low transport through the BBB unless facilitated by carrier-mediated transport (266). Conversely, molecules with a MW below 450 Daltons and forming seven or fewer hydrogen bonds with water may cross the BBB significantly, provided they are not substrates for active efflux transporters.

In certain pathological conditions, such as stroke or cancer, structural and functional alterations in the BBB can result in damage to the CNS. This BBB disruption increases the permeability for immune cells and substances, allowing greater passage into the ISF (267). Physical interventions, like hyperosmotic infusions or focused ultrasound, can also temporarily open the BBB, facilitating the delivery of drugs, including mAbs (268). In neurodegenerative diseases, BBB dysfunction is associated with chronic inflammation, oxidative stress, and the pathological accumulation of misfolded proteins, which further impede drug delivery to the CNS compared to acute conditions. Additionally, the blood-CSF barrier (BCSFB) may also undergo similar changes, affecting its permeability (266-269).

Overcoming the challenges posed by the BBB and other CNS barriers requires innovative drug delivery technologies. Continued advancements in this field hold promise for more effective treatments for CNS disorders. Recent years have seen the development of

numerous brain drug delivery technologies, including transcranial delivery, CSF delivery, BBB disruption, lipid carriers, prodrugs, stem cells, exosomes, nanoparticles, gene therapy, and endogenous BBB carrier-mediated and receptor-mediated transport systems (266).

Nanoparticle (NP)-based systems, such as liposomes, micelles, polymeric NPs, solid-lipid NPs, and inorganic NPs, have shown promising potential for precision medicine by effectively penetrating the BBB through various mechanisms (270, 271). Exosomes, extracellular vesicles secreted by a variety of cells, play key roles in intercellular communication, immune responses, human reproduction, and synaptic plasticity. Due to their natural origin and molecular similarity to most cell types, exosomes are emerging as promising therapeutic tools, particularly for NDs (272).

Invasive techniques for CNS drug delivery involve implantable devices that access the CSF through IT, intraventricular, or intraparenchymal delivery methods. Despite the extensive use of CSF for diagnostic purposes, it has not been frequently targeted for CNS therapies due to the invasiveness of the required procedures and systems. However, implantable devices such as Omaya reservoirs for intraventricular delivery, or electromechanical intrathecal pumps for delivery in the spinal intrathecal space have been in clinical use for many decades ago, but few developments have been made in the last years (104).

While various devices have been tested for treating symptoms or diseases intrathecally, such as pain (273), spasticity (62); CNS neoplasms (274, 275), and more recently, for neurodegenerative diseases (104, 276), with some promising results, they can lead to complications related to the direct effect of the drug released within the CNS such as overdose and immune reactions prompted by the drug, and other related to the device itself like the formation of granulomas, CSF flow obstruction, infections, loss of CSF (104, 273). Given IT *pseudodelivery* is designed for not releasing therapeutic agents, some of these side effects would be avoided. Therefore, since the focus of this study has been the Aβ peptide, the NPMBs inside the apheresis module were specifically designed to allow the passage of Aβ.

Some clues of our *in vivo* studies are: firstly, we used the anti-Aβ monoclonal antibody 6E10, which can bind to various amyloid forms (277), serving as therapeutic agent. This design reduces the risk of developing ARIAs, since the antibody will not interact directly with the plaques (99, 100, 102) or the Aβ in the vessels (101); secondly, given the size of the animal model, we accessed the CSF intraventricularly, as it is not possible to implant a catheter in the spine in rodents. This means that we had to use an intraventricular catheter that we implanted through brain parenchyma. This surgery may involve small brain injuries and activation of astrocytes and microglia that would be avoided if the catheter were implanted in the spinal IT space; and thirdly, the system does not actively promote the flow of CSF, something that would enhance the rate of target-molecule clearance.

Although Aβ peptide is still the main target in the treatment of AD and has been the one of interest for the proof-of-concept in this Thesis, IT *pseudodelivery* could be used for other targets beyond Aβ in AD or for other targets in other CNS conditions; just by changing the therapeutic agent. If needed, the NPMBs can also be tailored to fit better the needs of other target-therapeutics depending on their size.

The flexibility of the selective nanopheresis mechanism of action, with the possibility of targeting NPMBs in terms of pore size and geometry provides multiple possibilities to have drugs administered via IT *pseudodelivery*. In order to be suitable for this strategy, the target molecule must be soluble in the CSF and involved directly (i.e aggregating proteins) or indirectly (i.e. mediators) in the physiopathology of the disease. As this is a combinational therapy, a drug acting or binding specifically the target molecule is needed. This can be an antibody, an aptamer, an enzyme, or any other compound that has specificity over the target molecule. Also, the target molecule and the therapeutic agent should have a significant size difference since size is the main factor driving the selective molecular permeability through NPMBs. Other physicochemical features, like electrostatic charge, may also play a role.

Regarding drugs, aptamers represent a promising alternative to antibodies for therapeutic applications within *pseudodelivery* devices. Compared to mAbs, aptamers offer several advantages, higher replicability, and greater control over their properties (high durability, sensitivity, and specificity) and one disadvantage for this including smaller size (278). Other molecules that bind pathogenic proteins also hold potential. For example, human serum albumin (HSA) naturally buffers Aβ. A promising approach to AD prevention involves reducing free Aβ concentrations by enhancing the interaction between HSA and Aβ. This can be achieved by *pseudodelivering* albumin alone (78) or in combination with agents that increase HSA's affinity for Aβ (279). Additionally, computational compounds designed to bind to Aβ have also been developed (280).

Regarding targets, those related to enzymatic dysfunction are another option. One relevant example is switching from the non-amyloidogenic to the amyloidogenic pathway in AD. Compensating for malfunctioning enzymes or using different enzymes (such as Neprilysin and other Aβ-cleaving enzymes (281)) within the *pseudodelivery* device could be an effective approach, given the high CSF throughput. Inflammation is another clear target in neurodegenerative diseases. For instance, perispinal administration of the anti-TNF-α drug etanercept has been reported to improve cognitive function in a case report (282), with similar results in animal studies (283). Infliximab, a chimeric mAb approved for several autoimmune diseases, reduced Aβ plaques and tau phosphorylation in APP/PS1 mice after intracerebroventricular administration (284) and improved cognition in a human case (285). Recent research suggests that TNF-α inhibitors have protective effects on the brain in a transgenic mouse model of tauopathy (286), suggesting IT infliximab could be a potential therapy for AD and other NDs involving TNF-α, such as PD (287) and ALS (288). While systemic TNF-α antagonists carry risks like increased infection risk and rare adverse effects

such as drug-induced lupus and demyelinating diseases (289, 290), IT *pseudodelivery* may offer a safer route of administration. A second-generation TNF-α inhibitor, XPro1595, which specifically targets soluble TNF (291), could be a promising option for this approach.

Other potential therapeutic targets include drugs acting on the complement component C5, CD19 on B cells, and the interleukin-6 (IL-6) receptor. Tocilizumab, a humanized mAb against the IL-6 receptor, has been tested for neurological indications such as neuromyelitis optica (292) and primary CNS vasculitis (293). It has also been tested in ALS (294) and proposed for PD (295) and AD (296). Monoclonal antibodies binding IL-6 directly, such as HZ-0408b, could be administered via IT *pseudodelivery* to target inflammation in neurodegenerative diseases (297). Lastly, a TREM2-activating antibody with a BBB transport vehicle has shown promise in enhancing microglial metabolism in AD model (298). Tau pathology and neurodegeneration are associated with increased CSF sTREM2 (299). However, it remains unclear whether full-length TREM2 or sTREM2 provides protection (300). More research is needed to determine how, when, and in which cases targeting sTREM2 via IT *pseudodelivery* might be beneficial in AD.

Metal ions may contribute to the development of neurodegeneration by triggering or influencing disease progression (301, 302). Iron overload has been associated with several NDs, leading to protein aggregation and harmful pathways contributing to neurodegeneration (303, 304). Iron chelators have been shown to reduce brain Aβ deposition and ameliorate the memory impairment (305, 306). Excess iron in the brain can be exported to CSF or IF (304), making it a potential target for IT *pseudodelivery*. Ferritin, the primary form of iron storage in the brain, with a diameter of approximately 13 nm (307), could be a promising therapeutic agent for this approach.

Theoretically, this strategy provides several advantages and a few disadvantages over systemic immunotherapies. The most obvious disadvantage is the need to use implantable devices, with the risks it implies in terms of complications such as infections, leaks of CSF, obstruction of the system, etcetera.

Among the advantages, the most important one is the expected rate of target clearance, which would be much higher acting directly on the CSF than acting on plasma. As it targets the CSF rather than the periphery, it may be more effective in brain clearance due to the higher permeability of the CSF-brain barrier compared to the BBB (308). Additionally, since in AD the BBB is altered, the efflux of Aβ from the brain through its receptors is reduced (30), reducing the amount of accessible Aβ for clearance by this way. It is important to note that Aβ is also produced in the periphery, with platelets being a major source (309). Its function is not completely understood, but it has been observed to play a role in modulating the immune system response (26), as well as insulin and glucose metabolism (310), accelerating Aβ deposition in the brain. Then, it would explain the positive outcome of plasmapheresis (72-77). However, the concentration of Aβ in CSF is approximately 10 times

higher than in plasma (309), suggesting that removing Aβ from CSF may be more effective in AD treatment. In addition, the fully implantable device provides the benefit of continuous ambulatory treatment, while others such as plasmapheresis or systemically administered immunotherapies need periodic visits to clinical centers for several hours, and the therapeutic effect is intermittent. This would mean higher efficacy and shorter periods of time to achieve significative clearance of deposits. The time it takes for immunotherapies to clear Aβ from the brain in clinical trials varies depending on the specific therapy, stage at treatment onset and the dosage. The results indicated that the first significant reductions in amyloid plaques could be seen in about six months into the treatment, but more relevant reductions took 12-24 months (311). Reducing those times would have a huge impact from several points of view. First, the clinical benefits would be reached sooner. Second, it would mean lower load for clinical centers and professionals. And third, it would reduce the costs notably.

Moreover, the expected frequency of re-dosing is low because this route allows administration of high doses of mAb at a time. Then, the percutaneous and low-frequency route for redosing is an additional advantage because it can be easily performed in outpatient clinics, thus decreasing the workload at hospitals or infusion centers derived from relatively frequent redosing needed for intravenous treatments.

Another important advantage is that several targets can be addressed simultaneously without multiplying safety risks while opening the door to multiple possibilities that can fit the individual needs of each patient, thus advancing towards personalized medicine. Safety is indeed another important advantage because the risks of using implantable devices would be largely compensated by the decrease of frequent and potentially severe reactions from systemic immunotherapies such as allergic reactions and ARIAs, that would be completely avoided because of the *immunoisolation* provided by the membranes.

5. Limitations

The Aβ peptide has been one of the main targets in the search of AD therapies. Most of them have focused on reducing oligomers, fibrils or Aβ plaques, but the role of aggregated Aβ in AD development is under debate, as high Aβ brain load does not always lead to dementia. Some studies even suggest that the low levels of soluble Aβ may be responsible for the development of dementia, as dementia has been linked to decreased soluble Aβ levels (8, 177, 205).

The aim of the IT *pseudodelivery* was to decrease the deposits of Aβ by shifting the equilibrium from insoluble to soluble forms. However, after eight weeks of treatment, only a significant decrease in soluble levels Aβ in the hippocampus was observed, with no change in its biofluids levels to suggest a shift to the CSF- or the peripheral-sink. This limited

effect may be due to pore blockage, highlighting the need to address this issue in future experiments. The fact that soluble Aβ decreases may seem detrimental, based on the hypothesis by Espay et al., since we would be removing an Aβ with physiological function (312). But it is important to note that small soluble aggregates of Aβ can be toxic, appearing even at early stages (313). In fact, it has recently been shown that the level of soluble Aβ peaks before aggregation in early AD stages (34). In our case, therapeutic intervention was performed at an early symptomatic stage, but already with the presence of plaques. Therefore, it is possible that the perfect time-window for this therapeutic strategy is at a pre-symptomatic stage, when therapy can decrease the high Aβ levels characteristic of this stage. In any case, the aim of targeting Aβ in this Thesis was to provide proof-of-concept, whereas IT *pseudodelivery* should be conceived as a platform useful for different combinations of targets and therapeutics.

Additionally, considering the impact of the surgical procedure is crucial, as the complexity and aggressiveness of the procedure may have overshadowed the effects of the IT *pseudodelivery*, overall in the feasibility study.

Another limitation in this study was the restricted number of available alumina NPMBs. These membranes are homemade, with restrictions in size and shape. This is coupled with their fragility, which makes them difficult to use both for assembly in the permeation chambers and in the apheresis modules of the devices. This, along with the complications from Aβ binding to the permeation chambers, prevented *in vitro* testing with Aβ in the donor cell and the antibody in the receptor cell, impeding a better understanding of effective antibody dosing. Additionally, as another consequence, the number of devices was also limited, which hindered *in vivo* studies, with the number of mice still too low to draw clear conclusions for some experiments.

Furthermore, the mouse model limited the analysis of the effect on memory performance, as their reduced mobility impacted the behavioral tests. The original model is in a mixed B6;CH3 background, whereas in our case it is in pure 129Sv background. This may imply both changes in the times of appearance of the behavioral phenotype, onset and disease progression, etc., also losing the ability to compare our results with other studies using the original model. On the other hand, the exploration of other murine AD models with Tau modifications, such as 3xTgAD, could provide further insights into the effects of IT *pseudodelivery* in AD. With all, sufficient evidence for proof-of-principle and proof-of-concept were provided, paving the way for further preclinical development and future clinical studies.

6. Future developments and clinical perspective

The series of studies in this Thesis provide the first proof-of-principle and proof-of-concept for immunoselective nanopheresis and intrathecal *pseudodelivery* respectively, paving the way for further preclinical and clinical developments. The *in vivo* studies were made on a mice model of AD, which brings obvious limitations both from the disease model itself and the size of animals. Size constraints implied using a miniaturized version of what would be a device for humans. Also, we had to access the CSF intraventricularly, while the spinal intrathecal space might be a much more convenient route as it does not imply damage to CNS parenchyma. A prototype for humans using a pumpless system and a spinal intrathecal catheter has been developed to enable a continuous flow of CSF within a subcutaneous tricameral reservoir for enhanced control of therapeutics. However, before a prototype can be tested in humans, it needs to be tested in large animals first. Those studies have already been started beyond the scope of this Thesis, and the first results have recently been published (Figure 53; (314)). Although results are promising, further preclinical studies are needed before this therapy can be moved to clinical research.

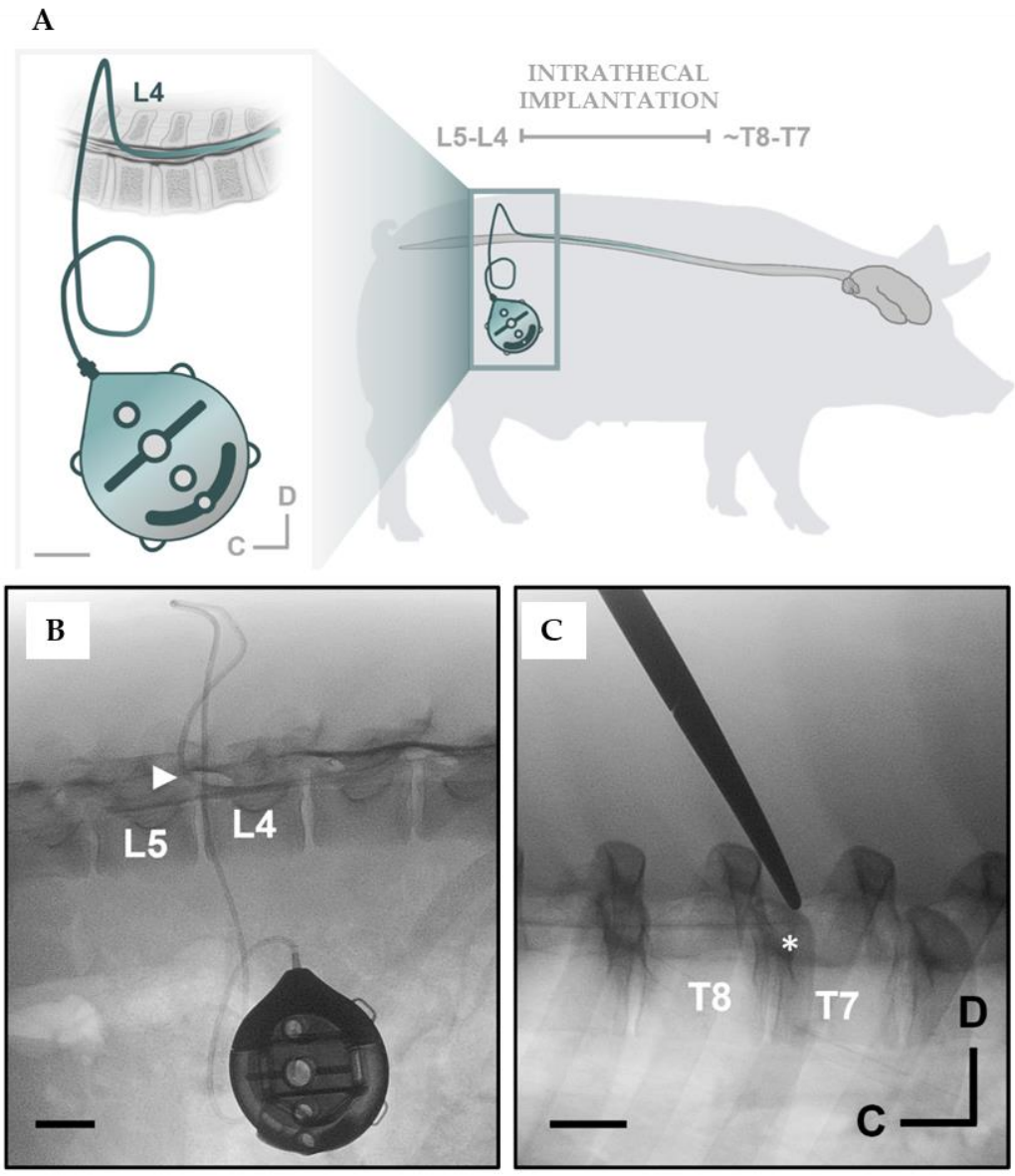

Figure 53. Diagram and phothographs of the implantation of the human prototype of the implantable device in a porcine model. A. Diagram of the localization of the intrathecal implantation in the pig. Scale bar in zoom: 2 cm. **B, C.** Fluoroscopic images of the prototype implanted in the pig. Arrowhead, Catheter entry; *, distal tip of the catheter. Scale bar: 2 cm. These images are courtesy of Neuroscience Innovative Technologies (277).

CONCLUSIONS/*CONCLUSIONES*

1. Immunoselective nanopheresis of fluids can be achieved by means of a combination of nanoporous membranes with tailored pore size and mAbs against smaller molecular targets present in the fluid.
2. IT *pseudodelivery* of drugs is a viable method to achieve the CSF-sink effect *in vivo*.
3. IT *pseudodelivery* of drugs enables long-term therapy by replacing the therapeutic agent percutaneously.
4. IT *pseudodelivery* of anti-Aβ mAb for 8 weeks shows slight improvements in inflammation and proteostasis in an animal model of AD, providing the first proof-of-concept.

1. La nanoféresis inmunoselectiva de fluidos puede lograrse mediante una combinación de membranas nanoporosas con tamaño de poro adaptado y anticuerpos monoclonales contra dianas moleculares más pequeñas presentes en el fluido.
2. La *pseudoliberación* IT de fármacos es un método viable para conseguir el efecto de sumidero de LCR *in vivo*.
3. La *pseudoliberación* IT de fármacos permite una terapia a largo plazo al sustituir el agente terapéutico por vía percutánea.
4. La *pseudoliberación* IT de anticuerpos monoclonales anti-Aβ durante 8 semanas muestra ligeras mejoras en la inflamación y la proteostasis en un modelo animal de EA, proporcionando la primera prueba de concepto.

BIBLIOGRAPHY

1. Erkkinen MG, Kim MO, Geschwind MD. Clinical Neurology and Epidemiology of the Major Neurodegenerative Diseases. Cold Spring Harb Perspect Biol. 2018;10(4).
2. Moda F, Ciullini A, Dellarole IL, Lombardo A, Campanella N, Bufano G, et al. Secondary Protein Aggregates in Neurodegenerative Diseases: Almost the Rule Rather than the Exception. Front Biosci (Landmark Ed). 2023;28(10):255.
3. Lashuel HA. Rethinking protein aggregation and drug discovery in neurodegenerative diseases: Why we need to embrace complexity? Curr Opin Chem Biol. 2021;64:67-75.
4. Bayer TA. Proteinopathies, a core concept for understanding and ultimately treating degenerative disorders? Eur Neuropsychopharmacol. 2015;25(5):713-24.
5. Khanam H, Ali A, Asif M, Shamsuzzaman. Neurodegenerative diseases linked to misfolded proteins and their therapeutic approaches: A review. Eur J Med Chem. 2016;124:1121-41.
6. Boland B, Yu WH, Corti O, Mollereau B, Henriques A, Bezard E, et al. Promoting the clearance of neurotoxic proteins in neurodegenerative disorders of ageing. Nat Rev Drug Discov. 2018;17(9):660-88.
7. Simons M, Levin J, Dichgans M. Tipping points in neurodegeneration. Neuron. 2023;111(19):2954-68.
8. Loeffler T, Schilcher I, Flunkert S, Hutter-Paier B. Neurofilament-Light Chain as Biomarker of Neurodegenerative and Rare Diseases With High Translational Value. Front Neurosci. 2020;14:579.
9. Lopez-Otin C, Blasco MA, Partridge L, Serrano M, Kroemer G. The hallmarks of aging. Cell. 2013;153(6):1194-217.
10. 2022 Alzheimer's disease facts and figures. Alzheimers Dement. 2022;18(4):700-89.
11. Collaborators GBDDF. Estimation of the global prevalence of dementia in 2019 and forecasted prevalence in 2050: an analysis for the Global Burden of Disease Study 2019. Lancet Public Health. 2022;7(2):e105-e25.
12. 2023 Alzheimer's disease facts and figures. Alzheimers Dement. 2023;19(4):1598-695.
13. Alzheimer A. Über eine eigenartige Erkrankung der Hirnrinde. Allgemeine Zeitschrift für Psychiatrie und physisch-gerichtliche Medizin. 1907;64(1):146-8.
14. Alzheimer A, Stelzmann RA, Schnitzlein HN, Murtagh FR. An English translation of Alzheimer's 1907 paper, "Uber eine eigenartige Erkankung der Hirnrinde". Clin Anat. 1995;8(6):429-31.
15. Thal DR, Rub U, Orantes M, Braak H. Phases of A beta-deposition in the human brain and its relevance for the development of AD. Neurology. 2002;58(12):1791-800.
16. Braak H, Braak E. Neuropathological stageing of Alzheimer-related changes. Acta Neuropathol. 1991;82(4):239-59.
17. Kang J, Lemaire HG, Unterbeck A, Salbaum JM, Masters CL, Grzeschik KH, et al. The precursor of Alzheimer's disease amyloid A4 protein resembles a cell-surface receptor. Nature. 1987;325(6106):733-6.
18. Rumble B, Retallack R, Hilbich C, Simms G, Multhaup G, Martins R, et al. Amyloid A4 protein and its precursor in Down's syndrome and Alzheimer's disease. N Engl J Med. 1989;320(22):1446-52.
19. Hardy JA, Higgins GA. Alzheimer's disease: the amyloid cascade hypothesis. Science. 1992;256(5054):184-5.

20. Jonsson T, Atwal JK, Steinberg S, Snaedal J, Jonsson PV, Bjornsson S, et al. A mutation in APP protects against Alzheimer's disease and age-related cognitive decline. Nature. 2012;488(7409):96-9.
21. Li NM, Liu KF, Qiu YJ, Zhang HH, Nakanishi H, Qing H. Mutations of beta-amyloid precursor protein alter the consequence of Alzheimer's disease pathogenesis. Neural Regen Res. 2019;14(4):658-65.
22. Gong CX, Liu F, Iqbal K. Multifactorial Hypothesis and Multi-Targets for Alzheimer's Disease. J Alzheimers Dis. 2018;64(s1):S107-S17.
23. Du X, Wang X, Geng M. Alzheimer's disease hypothesis and related therapies. Transl Neurodegener. 2018;7:2.
24. Mehta RI, Mehta RI. The Vascular-Immune Hypothesis of Alzheimer's Disease. Biomedicines. 2023;11(2).
25. Scheffer S, Hermkens DMA, van der Weerd L, de Vries HE, Daemen M. Vascular Hypothesis of Alzheimer Disease: Topical Review of Mouse Models. Arterioscler Thromb Vasc Biol. 2021;41(4):1265-83.
26. Chen GF, Xu TH, Yan Y, Zhou YR, Jiang Y, Melcher K, et al. Amyloid beta: structure, biology and structure-based therapeutic development. Acta Pharmacol Sin. 2017;38(9):1205-35.
27. Chow VW, Mattson MP, Wong PC, Gleichmann M. An overview of APP processing enzymes and products. Neuromolecular Med. 2010;12(1):1-12.
28. Chen XQ, Mobley WC. Exploring the Pathogenesis of Alzheimer Disease in Basal Forebrain Cholinergic Neurons: Converging Insights From Alternative Hypotheses. Front Neurosci. 2019;13:446.
29. Long JM, Holtzman DM. Alzheimer Disease: An Update on Pathobiology and Treatment Strategies. Cell. 2019;179(2):312-39.
30. Tarasoff-Conway JM, Carare RO, Osorio RS, Glodzik L, Butler T, Fieremans E, et al. Clearance systems in the brain-implications for Alzheimer disease. Nat Rev Neurol. 2015;11(8):457-70.
31. Nordvall G, Lundkvist J, Sandin J. Gamma-secretase modulators: a promising route for the treatment of Alzheimer's disease. Front Mol Neurosci. 2023;16:1279740.
32. Huang YR, Liu RT. The Toxicity and Polymorphism of beta-Amyloid Oligomers. Int J Mol Sci. 2020;21(12).
33. Zhang Y, Chen H, Li R, Sterling K, Song W. Amyloid beta-based therapy for Alzheimer's disease: challenges, successes and future. Signal Transduct Target Ther. 2023;8(1):248.
34. Blomeke L, Rehn F, Kraemer-Schulien V, Kutzsche J, Pils M, Bujnicki T, et al. Abeta oligomers peak in early stages of Alzheimer's disease preceding tau pathology. Alzheimers Dement (Amst). 2024;16(2):e12589.
35. De Strooper B, Karran E. The Cellular Phase of Alzheimer's Disease. Cell. 2016;164(4):603-15.
36. Liu WJ, Ye L, Huang WF, Guo LJ, Xu ZG, Wu HL, et al. p62 links the autophagy pathway and the ubiqutin-proteasome system upon ubiquitinated protein degradation. Cell Mol Biol Lett. 2016;21:29.
37. Liu J, Li L. Targeting Autophagy for the Treatment of Alzheimer's Disease: Challenges and Opportunities. Front Mol Neurosci. 2019;12:203.

38. Scrivo A, Bourdenx M, Pampliega O, Cuervo AM. Selective autophagy as a potential therapeutic target for neurodegenerative disorders. Lancet Neurol. 2018;17(9):802-15.
39. Yuan M, Wang Y, Huang Z, Jing F, Qiao P, Zou Q, et al. Impaired autophagy in amyloid-beta pathology: A traditional review of recent Alzheimer's research. J Biomed Res. 2022;37(1):30-46.
40. Vida C, de Toda IM, Cruces J, Garrido A, Gonzalez-Sanchez M, De la Fuente M. Role of macrophages in age-related oxidative stress and lipofuscin accumulation in mice. Redox Biol. 2017;12:423-37.
41. Song SB, Shim W, Hwang ES. Lipofuscin Granule Accumulation Requires Autophagy Activation. Mol Cells. 2023;46(8):486-95.
42. Villalon-Garcia I, Povea-Cabello S, Alvarez-Cordoba M, Talaveron-Rey M, Suarez-Rivero JM, Suarez-Carrillo A, et al. Vicious cycle of lipid peroxidation and iron accumulation in neurodegeneration. Neural Regen Res. 2023;18(6):1196-202.
43. Nichols MR, St-Pierre MK, Wendeln AC, Makoni NJ, Gouwens LK, Garrad EC, et al. Inflammatory mechanisms in neurodegeneration. J Neurochem. 2019;149(5):562-81.
44. Sarlus H, Heneka MT. Microglia in Alzheimer's disease. J Clin Invest. 2017;127(9):3240-9.
45. Dani M, Wood M, Mizoguchi R, Fan Z, Walker Z, Morgan R, et al. Microglial activation correlates in vivo with both tau and amyloid in Alzheimer's disease. Brain. 2018;141(9):2740-54.
46. Guo S, Wang H, Yin Y. Microglia Polarization From M1 to M2 in Neurodegenerative Diseases. Front Aging Neurosci. 2022;14:815347.
47. Cai Y, Liu J, Wang B, Sun M, Yang H. Microglia in the Neuroinflammatory Pathogenesis of Alzheimer's Disease and Related Therapeutic Targets. Front Immunol. 2022;13:856376.
48. Depp C, Sun T, Sasmita AO, Spieth L, Berghoff SA, Nazarenko T, et al. Myelin dysfunction drives amyloid-beta deposition in models of Alzheimer's disease. Nature. 2023;618(7964):349-57.
49. Shen X, Venero JL, Joseph B, Burguillos MA. Caspases orchestrate microglia instrumental functions. Prog Neurobiol. 2018;171:50-71.
50. Hemonnot-Girard AL, Meersseman C, Pastore M, Garcia V, Linck N, Rey C, et al. Comparative analysis of transcriptome remodeling in plaque-associated and plaque-distant microglia during amyloid-beta pathology progression in mice. J Neuroinflammation. 2022;19(1):234.
51. Wei Y, Li X. Different phenotypes of microglia in animal models of Alzheimer disease. Immun Ageing. 2022;19(1):44.
52. Rachmian N, Medina S, Cherqui U, Akiva H, Deitch D, Edilbi D, et al. Identification of senescent, TREM2-expressing microglia in aging and Alzheimer's disease model mouse brain. Nat Neurosci. 2024.
53. Zhao JF, Ren T, Li XY, Guo TL, Liu CH, Wang X. Research Progress on the Role of Microglia Membrane Proteins or Receptors in Neuroinflammation and Degeneration. Front Cell Neurosci. 2022;16:831977.
54. Tremblay ME. Microglial functional alteration and increased diversity in the challenged brain: Insights into novel targets for intervention. Brain Behav Immun Health. 2021;16:100301.

55. Rodriguez-Giraldo M, Gonzalez-Reyes RE, Ramirez-Guerrero S, Bonilla-Trilleras CE, Guardo-Maya S, Nava-Mesa MO. Astrocytes as a Therapeutic Target in Alzheimer's Disease-Comprehensive Review and Recent Developments. Int J Mol Sci. 2022;23(21).
56. Cai W, Wu T, Chen N. The Amyloid-Beta Clearance: From Molecular Targets to Glial and Neural Cells. Biomolecules. 2023;13(2).
57. Giusti V, Kaur G, Giusto E, Civiero L. Brain clearance of protein aggregates: a close-up on astrocytes. Mol Neurodegener. 2024;19(1):5.
58. Mestre H, Hablitz LM, Xavier AL, Feng W, Zou W, Pu T, et al. Aquaporin-4-dependent glymphatic solute transport in the rodent brain. Elife. 2018;7.
59. Rasmussen MK, Mestre H, Nedergaard M. The glymphatic pathway in neurological disorders. Lancet Neurol. 2018;17(11):1016-24.
60. Hablitz LM, Nedergaard M. The Glymphatic System: A Novel Component of Fundamental Neurobiology. J Neurosci. 2021;41(37):7698-711.
61. Jiang-Xie LF, Drieu A, Bhasiin K, Quintero D, Smirnov I, Kipnis J. Neuronal dynamics direct cerebrospinal fluid perfusion and brain clearance. Nature. 2024;627(8002):157-64.
62. Lohela TJ, Lilius TO, Nedergaard M. The glymphatic system: implications for drugs for central nervous system diseases. Nat Rev Drug Discov. 2022;21(10):763-79.
63. van Dyck CH. Anti-Amyloid-beta Monoclonal Antibodies for Alzheimer's Disease: Pitfalls and Promise. Biol Psychiatry. 2018;83(4):311-9.
64. Miranda A, Montiel E, Ulrich H, Paz C. Selective Secretase Targeting for Alzheimer's Disease Therapy. J Alzheimers Dis. 2021;81(1):1-17.
65. Tortelli R. VA, Gaspar E., Garcia Valdecasas Colell M., Alcaraz F., Yang T., Panton D., Mahil K., Croney R., Vardar T., Squassante L., De Buck S., Muggler T., Klein G., Kulic L., Kerchner G., Gerlach I. A phase IIA study investigating a γ-secretase modulator in individuals at risk for or at the prodromal stage of Alzheimer's disease. ADPD 20242024.
66. Zhang Z, Yang X, Song YQ, Tu J. Autophagy in Alzheimer's disease pathogenesis: Therapeutic potential and future perspectives. Ageing Res Rev. 2021;72:101464.
67. Schmukler E, Pinkas-Kramarski R. Autophagy induction in the treatment of Alzheimer's disease. Drug Dev Res. 2020;81(2):184-93.
68. Liang PZ, Li L, Zhang YN, Shen Y, Zhang LL, Zhou J, et al. Electroacupuncture Improves Clearance of Amyloid-beta through the Glymphatic System in the SAMP8 Mouse Model of Alzheimer's Disease. Neural Plast. 2021;2021:9960304.
69. Salehpour F, Khademi M, Bragin DE, DiDuro JO. Photobiomodulation Therapy and the Glymphatic System: Promising Applications for Augmenting the Brain Lymphatic Drainage System. Int J Mol Sci. 2022;23(6).
70. Wang M, Yan C, Li X, Yang T, Wu S, Liu Q, et al. Non-invasive modulation of meningeal lymphatics ameliorates ageing and Alzheimer's disease-associated pathology and cognition in mice. Nat Commun. 2024;15(1):1453.
71. Zhang Y, Lee DH. Sink hypothesis and therapeutic strategies for attenuating Abeta levels. Neuroscientist. 2011;17(2):163-73.
72. Boada M, Kiprov D, Anaya F, Lopez OL, Nunez L, Olazaran J, et al. Feasibility, safety, and tolerability of two modalities of plasma exchange with albumin replacement to treat elderly patients with Alzheimer's disease in the AMBAR study. J Clin Apher. 2023;38(1):45-54.

73. Boada M, Lopez OL, Olazaran J, Nunez L, Pfeffer M, Puente O, et al. Neuropsychological, neuropsychiatric, and quality-of-life assessments in Alzheimer's disease patients treated with plasma exchange with albumin replacement from the randomized AMBAR study. Alzheimers Dement. 2022;18(7):1314-24.
74. Boada M, Martinez-Lage P, Serrano-Castro P, Costa M, Paez A. Therapeutic plasma exchange with albumin: a new approach to treat Alzheimer's disease. Expert Rev Neurother. 2021;21(8):843-9.
75. Boada M, Lopez OL, Olazaran J, Nunez L, Pfeffer M, Paricio M, et al. A randomized, controlled clinical trial of plasma exchange with albumin replacement for Alzheimer's disease: Primary results of the AMBAR Study. Alzheimers Dement. 2020;16(10):1412-25.
76. Boada M, Lopez O, Nunez L, Szczepiorkowski ZM, Torres M, Grifols C, et al. Plasma exchange for Alzheimer's disease Management by Albumin Replacement (AMBAR) trial: Study design and progress. Alzheimers Dement (N Y). 2019;5:61-9.
77. Boada-Rovira M. [Human Albumin Grifols 5% in plasmapheresis: a new therapy involving beta-amyloid mobilisation in Alzheimer's disease]. Rev Neurol. 2010;50 Suppl 5:S9-18.
78. Menendez-Gonzalez M, Gasparovic C. Albumin Exchange in Alzheimer's Disease: Might CSF Be an Alternative Route to Plasma? Front Neurol. 2019;10:1036.
79. Padmanabhan A, Connelly-Smith L, Aqui N, Balogun RA, Klingel R, Meyer E, et al. Guidelines on the Use of Therapeutic Apheresis in Clinical Practice - Evidence-Based Approach from the Writing Committee of the American Society for Apheresis: The Eighth Special Issue. J Clin Apher. 2019;34(3):171-354.
80. Rohrer L, Yunce M, Montine TJ, Shan H. Plasma Exchange in Alzheimer's Disease. Transfus Med Rev. 2023;37(1):10-5.
81. Jin WS, Shen LL, Bu XL, Zhang WW, Chen SH, Huang ZL, et al. Peritoneal dialysis reduces amyloid-beta plasma levels in humans and attenuates Alzheimer-associated phenotypes in an APP/PS1 mouse model. Acta Neuropathol. 2017;134(2):207-20.
82. Kitaguchi N, Hasegawa M, Ito S, Kawaguchi K, Hiki Y, Nakai S, et al. A prospective study on blood Abeta levels and the cognitive function of patients with hemodialysis: a potential therapeutic strategy for Alzheimer's disease. J Neural Transm (Vienna). 2015;122(11):1593-607.
83. Sakai K, Senda T, Hata R, Kuroda M, Hasegawa M, Kato M, et al. Patients that have Undergone Hemodialysis Exhibit Lower Amyloid Deposition in the Brain: Evidence Supporting a Therapeutic Strategy for Alzheimer's Disease by Removal of Blood Amyloid. J Alzheimers Dis. 2016;51(4):997-1002.
84. Folch J, Ettcheto M, Petrov D, Abad S, Pedros I, Marin M, et al. Review of the advances in treatment for Alzheimer disease: Strategies for combating beta-amyloid protein. Neurologia (Engl Ed). 2018;33(1):47-58.
85. Yadollahikhales G, Rojas JC. Anti-Amyloid Immunotherapies for Alzheimer's Disease: A 2023 Clinical Update. Neurotherapeutics. 2023;20(4):914-31.
86. Billings LM, Oddo S, Green KN, McGaugh JL, LaFerla FM. Intraneuronal Abeta causes the onset of early Alzheimer's disease-related cognitive deficits in transgenic mice. Neuron. 2005;45(5):675-88.
87. Wilcock DM, Munireddy SK, Rosenthal A, Ugen KE, Gordon MN, Morgan D. Microglial activation facilitates Abeta plaque removal following intracranial anti-Abeta antibody administration. Neurobiol Dis. 2004;15(1):11-20.

88. Oddo S, Billings L, Kesslak JP, Cribbs DH, LaFerla FM. Abeta immunotherapy leads to clearance of early, but not late, hyperphosphorylated tau aggregates via the proteasome. Neuron. 2004;43(3):321-32.
89. Tucker SM, Borchelt DR, Troncoso JC. Limited clearance of pre-existing amyloid plaques after intracerebral injection of Abeta antibodies in two mouse models of Alzheimer disease. J Neuropathol Exp Neurol. 2008;67(1):30-40.
90. Seubert P, Barbour R, Khan K, Motter R, Tang P, Kholodenko D, et al. Antibody capture of soluble Abeta does not reduce cortical Abeta amyloidosis in the PDAPP mouse. Neurodegener Dis. 2008;5(2):65-71.
91. Fuller JP, Stavenhagen JB, Christensen S, Kartberg F, Glennie MJ, Teeling JL. Comparing the efficacy and neuroinflammatory potential of three anti-abeta antibodies. Acta Neuropathol. 2015;130(5):699-711.
92. Kamei N, Hashimoto A, Tanaka E, Murata K, Yamaguchi M, Yokoyama N, et al. Therapeutic effects of anti-amyloid beta antibody after intravenous injection and efficient nose-to-brain delivery in Alzheimer's disease mouse model. Drug Deliv Transl Res. 2022;12(11):2667-77.
93. Syvanen S, Hultqvist G, Gustavsson T, Gumucio A, Laudon H, Soderberg L, et al. Efficient clearance of Abeta protofibrils in AbetaPP-transgenic mice treated with a brain-penetrating bifunctional antibody. Alzheimers Res Ther. 2018;10(1):49.
94. Pardridge WM. Treatment of Alzheimer's Disease and Blood-Brain Barrier Drug Delivery. Pharmaceuticals (Basel). 2020;13(11).
95. Loeffler DA. Antibody-Mediated Clearance of Brain Amyloid-beta: Mechanisms of Action, Effects of Natural and Monoclonal Anti-Abeta Antibodies, and Downstream Effects. J Alzheimers Dis Rep. 2023;7(1):873-99.
96. Cummings J, Osse AML, Cammann D, Powell J, Chen J. Anti-Amyloid Monoclonal Antibodies for the Treatment of Alzheimer's Disease. BioDrugs. 2024;38(1):5-22.
97. Jucker M, Walker LC. Alzheimer's disease: From immunotherapy to immunoprevention. Cell. 2023;186(20):4260-70.
98. Cadiz MP, Gibson KA, Todd KT, Nascari DG, Massa N, Lilley MT, et al. Aducanumab anti-amyloid immunotherapy induces sustained microglial and immune alterations. J Exp Med. 2024;221(2).
99. Taylor X, Clark IM, Fitzgerald GJ, Oluoch H, Hole JT, DeMattos RB, et al. Amyloid-beta (Abeta) immunotherapy induced microhemorrhages are associated with activated perivascular macrophages and peripheral monocyte recruitment in Alzheimer's disease mice. Mol Neurodegener. 2023;18(1):59.
100. Barakos J, Purcell D, Suhy J, Chalkias S, Burkett P, Marsica Grassi C, et al. Detection and Management of Amyloid-Related Imaging Abnormalities in Patients with Alzheimer's Disease Treated with Anti-Amyloid Beta Therapy. J Prev Alzheimers Dis. 2022;9(2):211-20.
101. Hampel H, Elhage A, Cho M, Apostolova LG, Nicoll JAR, Atri A. Amyloid-related imaging abnormalities (ARIA): radiological, biological and clinical characteristics. Brain. 2023;146(11):4414-24.
102. Racke MM, Boone LI, Hepburn DL, Parsadainian M, Bryan MT, Ness DK, et al. Exacerbation of cerebral amyloid angiopathy-associated microhemorrhage in amyloid precursor protein transgenic mice by immunotherapy is dependent on antibody recognition of deposited forms of amyloid beta. J Neurosci. 2005;25(3):629-36.

103. Menendez-Gonzalez M, Padilla-Zambrano HS, Alvarez G, Capetillo-Zarate E, Tomas-Zapico C, Costa A. Targeting Beta-Amyloid at the CSF: A New Therapeutic Strategy in Alzheimer's Disease. Front Aging Neurosci. 2018;10:100.
104. Manuel MG, Tamba BI, Leclere M, Mabrouk M, Schreiner TG, Ciobanu R, et al. Intrathecal Pseudodelivery of Drugs in the Therapy of Neurodegenerative Diseases: Rationale, Basis and Potential Applications. Pharmaceutics. 2023;15(3).
105. Rios X, Gomez-Vallejo V, Martin A, Cossio U, Morcillo MA, Alemi M, et al. Radiochemical examination of transthyretin (TTR) brain penetration assisted by iododiflunisal, a TTR tetramer stabilizer and a new candidate drug for AD. Sci Rep. 2019;9(1):13672.
106. Ezra A, Rabinovich-Nikitin I, Rabinovich-Toidman P, Solomon B. Multifunctional Effect of Human Serum Albumin Reduces Alzheimer's Disease Related Pathologies in the 3xTg Mouse Model. J Alzheimers Dis. 2016;50(1):175-88.
107. Ribeiro CA, Oliveira SM, Guido LF, Magalhaes A, Valencia G, Arsequell G, et al. Transthyretin stabilization by iododiflunisal promotes amyloid-beta peptide clearance, decreases its deposition, and ameliorates cognitive deficits in an Alzheimer's disease mouse model. J Alzheimers Dis. 2014;39(2):357-70.
108. Menendez Gonzalez M. Implantable Systems for Continuous Liquorpheresis and CSF Replacement. Cureus. 2017;9(2):e1022.
109. Smilnak GJ, Charalambous LT, Cutshaw D, Premji AM, Giamberardino CD, Ballard CG, et al. Novel Treatment of Cryptococcal Meningitis via Neurapheresis Therapy. J Infect Dis. 2018;218(7):1147-54.
110. Blackburn SL, Grande AW, Swisher CB, Hauck EF, Jagadeesan B, Provencio JJ. Prospective Trial of Cerebrospinal Fluid Filtration After Aneurysmal Subarachnoid Hemorrhage via Lumbar Catheter (PILLAR). Stroke. 2019;50(9):2558-61.
111. Menendez Gonzalez M. Mechanical Dilution of Beta-amyloid Peptide and Phosphorylated Tau Protein in Alzheimer's Disease: Too Simple to be True? Cureus. 2017;9(2):e1062.
112. Gonzalez AS, Vega V, Cuevas AL, Yuso M, Prida VM, Benavente J. Surface Modification of Nanoporous Anodic Alumina during Self-Catalytic Atomic Layer Deposition of Silicon Dioxide from (3-Aminopropyl)Triethoxysilane. Materials (Basel). 2021;14(17).
113. Schreiner TG, Tamba BI, Mihai CT, Lorinczi A, Baibarac M, Ciobanu RC, et al. Nanoporous Membranes for the Filtration of Proteins from Biological Fluids: Biocompatibility Tests on Cell Cultures and Suggested Applications for the Treatment of Alzheimer's Disease. J Clin Med. 2022;11(19).
114. Pike CJ, Burdick D, Walencewicz AJ, Glabe CG, Cotman CW. Neurodegeneration induced by beta-amyloid peptides in vitro: the role of peptide assembly state. J Neurosci. 1993;13(4):1676-87.
115. Krishtal J, Metsla K, Bragina O, Tougu V, Palumaa P. Toxicity of Amyloid-beta Peptides Varies Depending on Differentiation Route of SH-SY5Y Cells. J Alzheimers Dis. 2019;71(3):879-87.
116. Jankowsky JL, Fadale DJ, Anderson J, Xu GM, Gonzales V, Jenkins NA, et al. Mutant presenilins specifically elevate the levels of the 42 residue beta-amyloid peptide in vivo: evidence for augmentation of a 42-specific gamma secretase. Hum Mol Genet. 2004;13(2):159-70.

117. Finnie GS, Gunnarsson R, Manavis J, Blumbergs PC, Mander KA, Edwards S, et al. Characterization of an 'Amyloid Only' Transgenic (B6C3-Tg(APPswe,PSEN1dE9)85Dbo/Mmjax) Mouse Model of Alzheimer's Disease. J Comp Pathol. 2017;156(4):389-99.
118. Smit T, Deshayes NAC, Borchelt DR, Kamphuis W, Middeldorp J, Hol EM. Reactive astrocytes as treatment targets in Alzheimer's disease-Systematic review of studies using the APPswePS1dE9 mouse model. Glia. 2021;69(8):1852-81.
119. Coto-Vilcapoma MA, Castilla-Silgado J, Fernandez-Garcia B, Pinto-Hernandez P, Cipriani R, Capetillo-Zarate E, et al. New, Fully Implantable Device for Selective Clearance of CSF-Target Molecules: Proof of Concept in a Murine Model of Alzheimer's Disease. Int J Mol Sci. 2022;23(16).
120. DeVos SL, Miller TM. Direct intraventricular delivery of drugs to the rodent central nervous system. J Vis Exp. 2013(75):e50326.
121. Liu L, Duff K. A technique for serial collection of cerebrospinal fluid from the cisterna magna in mouse. J Vis Exp. 2008(21).
122. Paxinos G, Franklin KB. The mouse brain in stereotaxic coordinates. Third. Academic Press; 2008.
123. Schneider CA, Rasband WS, Eliceiri KW. NIH Image to ImageJ: 25 years of image analysis. Nat Methods. 2012;9(7):671-5.
124. Trujillo-Estrada L, Davila JC, Sanchez-Mejias E, Sanchez-Varo R, Gomez-Arboledas A, Vizuete M, et al. Early neuronal loss and axonal/presynaptic damage is associated with accelerated amyloid-beta accumulation in AbetaPP/PS1 Alzheimer's disease mice subiculum. J Alzheimers Dis. 2014;42(2):521-41.
125. Perez-Martin E, Coto-Vilcapoma A, Castilla-Silgado J, Rodriguez-Canon M, Prado C, Alvarez G, et al. Refining Stereotaxic Neurosurgery Techniques and Welfare Assessment for Long-Term Intracerebroventricular Device Implantation in Rodents. Animals (Basel). 2023;13(16).
126. Yang S, Zhang S, Tang W, Fang S, Zhang H, Zheng J, et al. Enriched Environment Prevents Surgery-Induced Persistent Neural Inhibition and Cognitive Dysfunction. Front Aging Neurosci. 2021;13:744719.
127. Pham TM, Hagman B, Codita A, Van Loo PL, Strommer L, Baumans V. Housing environment influences the need for pain relief during post-operative recovery in mice. Physiol Behav. 2010;99(5):663-8.
128. Min J, Lai Z, Wang H, Zuo Z. Preoperative environment enrichment preserved neuroligin 1 expression possibly via epigenetic regulation to reduce postoperative cognitive dysfunction in mice. CNS Neurosci Ther. 2022;28(4):619-29.
129. Rufiange M, Leung VS, Simpson K, Pang DS. Prewarming Followed by Active Warming is Superior to Passive Warming in Preventing Hypothermia for Short Procedures in Adult Rats (Rattus norvegicus) Under Isoflurane Anesthesia. J Am Assoc Lab Anim Sci. 2020;59(4):377-83.
130. Kraeuter AK, Guest PC, Sarnyai Z. The Y-Maze for Assessment of Spatial Working and Reference Memory in Mice. Methods Mol Biol. 2019;1916:105-11.
131. Prieur EAK, Jadavji NM. Assessing Spatial Working Memory Using the Spontaneous Alternation Y-maze Test in Aged Male Mice. Bio Protoc. 2019;9(3):e3162.

132. Lewczuk P, Matzen A, Blennow K, Parnetti L, Molinuevo JL, Eusebi P, et al. Cerebrospinal Fluid Abeta42/40 Corresponds Better than Abeta42 to Amyloid PET in Alzheimer's Disease. J Alzheimers Dis. 2017;55(2):813-22.
133. DeMattos RB, Bales KR, Parsadanian M, O'Dell MA, Foss EM, Paul SM, et al. Plaque-associated disruption of CSF and plasma amyloid-beta (Abeta) equilibrium in a mouse model of Alzheimer's disease. J Neurochem. 2002;81(2):229-36.
134. Mengel D, Wellik IG, Schuster KH, Jarrah SI, Wacker M, Ashraf NS, et al. Blood levels of neurofilament light are associated with disease progression in a mouse model of spinocerebellar ataxia type 3. Dis Model Mech. 2023;16(9).
135. Varma VR, An Y, Kac PR, Bilgel M, Moghekar A, Loeffler T, et al. Longitudinal progression of blood biomarkers reveals a key role of astrocyte reactivity in preclinical Alzheimer's disease. medRxiv. 2024.
136. Kumar AV, Mills J, Lapierre LR. Selective Autophagy Receptor p62/SQSTM1, a Pivotal Player in Stress and Aging. Front Cell Dev Biol. 2022;10:793328.
137. Sengupta U, Kayed R. Amyloid beta, Tau, and alpha-Synuclein aggregates in the pathogenesis, prognosis, and therapeutics for neurodegenerative diseases. Prog Neurobiol. 2022;214:102270.
138. Hommen F, Bilican S, Vilchez D. Protein clearance strategies for disease intervention. J Neural Transm (Vienna). 2022;129(2):141-72.
139. Eisele YS, Monteiro C, Fearns C, Encalada SE, Wiseman RL, Powers ET, et al. Targeting protein aggregation for the treatment of degenerative diseases. Nat Rev Drug Discov. 2015;14(11):759-80.
140. Hung DC, Nguyen NC, Uan DK, Son LT. Membrane processes and their potential applications for fresh water provision in Vietnam. Vietnam Journal of Chemistry. 2017;55(5):533.
141. Adiga SP, Jin C, Curtiss LA, Monteiro-Riviere NA, Narayan RJ. Nanoporous membranes for medical and biological applications. Wiley Interdiscip Rev Nanomed Nanobiotechnol. 2009;1(5):568-81.
142. Williams S, Neumann A, Bremer I, Su Y, Drager G, Kasper C, et al. Nanoporous silica nanoparticles as biomaterials: evaluation of different strategies for the functionalization with polysialic acid by step-by-step cytocompatibility testing. J Mater Sci Mater Med. 2015;26(3):125.
143. Domagalski JT, Xifre-Perez E, Marsal LF. Recent Advances in Nanoporous Anodic Alumina: Principles, Engineering, and Applications. Nanomaterials (Basel). 2021;11(2).
144. Ruiz-Clavijo A, Caballero-Calero O, Martin-Gonzalez M. Revisiting anodic alumina templates: from fabrication to applications. Nanoscale. 2021;13(4):2227-65.
145. Stine WB, Jungbauer L, Yu C, LaDu MJ. Preparing synthetic Abeta in different aggregation states. Methods Mol Biol. 2011;670:13-32.
146. Broersen K, Jonckheere W, Rozenski J, Vandersteen A, Pauwels K, Pastore A, et al. A standardized and biocompatible preparation of aggregate-free amyloid beta peptide for biophysical and biological studies of Alzheimer's disease. Protein Eng Des Sel. 2011;24(9):743-50.
147. Strand H, Garabet L, Bjelke B, Sithiravel C, Hardang IM, Moe MK. beta-Amyloid in Cerebrospinal Fluid: How to Keep It Floating (Not Sticking) by Standardization of Preanalytic Processes and Collection Tubes. J Appl Lab Med. 2021;6(5):1155-64.

148. Robinson MK, Caudill SP, Koch DD, Ritchie J, Hortin G, Eckfeldt JH, et al. Albumin adsorption onto surfaces of urine collection and analysis containers. Clin Chim Acta. 2014;431:40-5.
149. Henry M, Dupont-Gillain C, Bertrand P. Conformation Change of Albumin Adsorbed on Polycarbonate Membranes as Revealed by ToF-SIMS. Langmuir. 2003;19(15):6271-6.
150. Ugo P, Marafini P, Meneghello M. Bioanalytical Chemistry: From Biomolecular Recognition to Nanobiosensing: De Gruyter; 2021.
151. Thormann A, Berthold L, Gšring P, Lelonek M, Heilmann A. Nanoporous Aluminum Oxide Membranes for Separation and Biofunctionalization. Procedia Engineering. 2012;44:1107-11.
152. Lee SC, Lueck CJ. Cerebrospinal fluid pressure in adults. J Neuroophthalmol. 2014;34(3):278-83.
153. Li Q, Xu Y, Wei H, Wang X. An electrospun polycarbonate nanofibrous membrane for high efficiency particulate matter filtration. RSC Advances. 2016;6(69):65275-81.
154. Paul J. Wound pruritus: pathophysiology and management. Chronic Wound Care Management and Research. 2015.
155. Sike A, Wengenroth J, Upite J, Bruning T, Eiriz I, Santha P, et al. Improved method for cannula fixation for long-term intracerebral brain infusion. J Neurosci Methods. 2017;290:145-50.
156. Groseclose CH, Draughn RA, Tyor WR, Sallee FR, Middaugh LD. Long-term intracranial cannula stabilization in mice with light cured resin composites. J Neurosci Methods. 1998;79(1):31-6.
157. Ferry B, Gervasoni D. Improving Stereotaxic Neurosurgery Techniques and Procedures Greatly Reduces the Number of Rats Used per Experimental Group-A Practice Report. Animals (Basel). 2021;11(9).
158. Alvarado CG, Franklin CL, Dixon LW. Retrospective Evaluation of Nail Trimming as a Conservative Treatment for Ulcerative Dermatitis in Laboratory Mice. J Am Assoc Lab Anim Sci. 2016;55(4):462-6.
159. Schuler B, Rettich A, Vogel J, Gassmann M, Arras M. Optimized surgical techniques and postoperative care improve survival rates and permit accurate telemetric recording in exercising mice. BMC Vet Res. 2009;5:28.
160. Talbot SR, Biernot S, Bleich A, van Dijk RM, Ernst L, Hager C, et al. Defining body-weight reduction as a humane endpoint: a critical appraisal. Lab Anim. 2020;54(1):99-110.
161. Cnops V, Iyer VR, Parathy N, Wong P, Dawe GS. Test, rinse, repeat: A review of carryover effects in rodent behavioral assays. Neurosci Biobehav Rev. 2022;135:104560.
162. Abramov U, Puussaar T, Raud S, Kurrikoff K, Vasar E. Behavioural differences between C57BL/6 and 129S6/SvEv strains are reinforced by environmental enrichment. Neurosci Lett. 2008;443(3):223-7.
163. Voikar V, Vasar E, Rauvala H. Behavioral alterations induced by repeated testing in C57BL/6J and 129S2/Sv mice: implications for phenotyping screens. Genes Brain Behav. 2004;3(1):27-38.
164. Sik A, van Nieuwehuyzen P, Prickaerts J, Blokland A. Performance of different mouse strains in an object recognition task. Behav Brain Res. 2003;147(1-2):49-54.
165. van Heusden FC, Palacin IBS, Stiedl O, Smit AB, van Kesteren RE. Longitudinal Assessment of Working Memory Performance in the APPswe/PSEN1dE9 Mouse Model of

Alzheimer's Disease Using an Automated Figure-8-Maze. Front Behav Neurosci. 2021;15:655449.
166. Bao J, Liang Z, Gong X, Zhao Y, Wu M, Liu W, et al. Tangeretin Inhibits BACE1 Activity and Attenuates Cognitive Impairments in AD Model Mice. J Agric Food Chem. 2022;70(5):1536-46.
167. Zhang Q, Yang C, Liu T, Liu L, Li F, Cai Y, et al. Citalopram restores short-term memory deficit and non-cognitive behaviors in APP/PS1 mice while halting the advance of Alzheimer's disease-like pathology. Neuropharmacology. 2018;131:475-86.
168. Li XY, Men WW, Zhu H, Lei JF, Zuo FX, Wang ZJ, et al. Age- and Brain Region-Specific Changes of Glucose Metabolic Disorder, Learning, and Memory Dysfunction in Early Alzheimer's Disease Assessed in APP/PS1 Transgenic Mice Using (18)F-FDG-PET. Int J Mol Sci. 2016;17(10).
169. Izco M, Martinez P, Corrales A, Fandos N, Garcia S, Insua D, et al. Changes in the brain and plasma Abeta peptide levels with age and its relationship with cognitive impairment in the APPswe/PS1dE9 mouse model of Alzheimer's disease. Neuroscience. 2014;263:269-79.
170. Lonnemann N, Korte M, Hosseini S. Repeated performance of spatial memory tasks ameliorates cognitive decline in APP/PS1 mice. Behav Brain Res. 2023;438:114218.
171. Volianskis A, Kostner R, Molgaard M, Hass S, Jensen MS. Episodic memory deficits are not related to altered glutamatergic synaptic transmission and plasticity in the CA1 hippocampus of the APPswe/PS1deltaE9-deleted transgenic mice model of ss-amyloidosis. Neurobiol Aging. 2010;31(7):1173-87.
172. Lee S, Kim TK, Choi JE, Choi Y, You M, Ryu J, et al. Dysfunction of striatal MeCP2 is associated with cognitive decline in a mouse model of Alzheimer's disease. Theranostics. 2022;12(3):1404-18.
173. Sharma S, Rakoczy S, Brown-Borg H. Assessment of spatial memory in mice. Life Sci. 2010;87(17-18):521-36.
174. Schimanski LA, Nguyen PV. Multidisciplinary approaches for investigating the mechanisms of hippocampus-dependent memory: a focus on inbred mouse strains. Neurosci Biobehav Rev. 2004;28(5):463-83.
175. Sukoff Rizzo SJ, Silverman JL. Methodological Considerations for Optimizing and Validating Behavioral Assays. Curr Protoc Mouse Biol. 2016;6(4):364-79.
176. Deka H, Sarmah R, Sharma A, Biswas S. Modelling and Characterization of Glial Fibrillary Acidic Protein. Bioinformation. 2015;11(8):393-400.
177. Zhao Y, Arceneaux L, Culicchia F, Lukiw WJ. Neurofilament Light (NF-L) Chain Protein from a Highly Polymerized Structural Component of the Neuronal Cytoskeleton to a Neurodegenerative Disease Biomarker in the Periphery. HSOA J Alzheimers Neurodegener Dis. 2021;7(2).
178. Yuan A, Rao MV, Veeranna, Nixon RA. Neurofilaments at a glance. J Cell Sci. 2012;125(Pt 14):3257-63.
179. Kim B, Kim S, Jin MS. Crystal structure of the human glial fibrillary acidic protein 1B domain. Biochem Biophys Res Commun. 2018;503(4):2899-905.
180. Hillig N, Schumann-Muck F, Hamedy A, Braun PG, Koethe M. Impact of nanoscale silicon dioxide coating of stainless-steel surfaces on Listeria monocytogenes. Folia Microbiol (Praha). 2024;69(1):173-80.

181. Lee J, Ha J-H, Song I-H, Park J-W. Effect of SiO2 coating on alumina microfiltration membranes on flux performance in membrane fouling process. Journal of the Ceramic Society of Japan. 2019;127(1):35-43.
182. Schreiner TG, Menendez-Gonzalez M, Adam M, Popescu BO, Szilagyi A, Stanciu GD, et al. A Nanostructured Protein Filtration Device for Possible Use in the Treatment of Alzheimer's Disease-Concept and Feasibility after In Vivo Tests. Bioengineering (Basel). 2023;10(11).
183. Jesmer AH, Wylie RG. Controlling Experimental Parameters to Improve Characterization of Biomaterial Fouling. Front Chem. 2020;8:604236.
184. Moaness M, El-Sayed SAM, Beherei HH, Mabrouk M. Enhancing the Antifouling Properties of Alumina Nanoporous Membranes by GO/MOF Impregnated Polymer Coatings: In Vitro Studies. J Funct Biomater. 2024;15(3).
185. Zhang X, Brodus D, Hollimon V, Hu H. A brief review of recent developments in the designs that prevent bio-fouling on silicon and silicon-based materials. Chem Cent J. 2017;11:18.
186. He Z, Yang X, Wang N, Mu L, Pan J, Lan X, et al. Anti-Biofouling Polymers with Special Surface Wettability for Biomedical Applications. Front Bioeng Biotechnol. 2021;9:807357.
187. Hampel H, Hardy J, Blennow K, Chen C, Perry G, Kim SH, et al. The Amyloid-beta Pathway in Alzheimer's Disease. Mol Psychiatry. 2021;26(10):5481-503.
188. Han JR, Yang Y, Wu TW, Shi TT, Li W, Zou Y. A Minimally-Invasive Method for Serial Cerebrospinal Fluid Collection and Injection in Rodents with High Survival Rates. Biomedicines. 2023;11(6).
189. Liu L, Herukka SK, Minkeviciene R, van Groen T, Tanila H. Longitudinal observation on CSF Abeta42 levels in young to middle-aged amyloid precursor protein/presenilin-1 doubly transgenic mice. Neurobiol Dis. 2004;17(3):516-23.
190. De Meyer S, Schaeverbeke JM, Verberk IMW, Gille B, De Schaepdryver M, Luckett ES, et al. Comparison of ELISA- and SIMOA-based quantification of plasma Abeta ratios for early detection of cerebral amyloidosis. Alzheimers Res Ther. 2020;12(1):162.
191. Schieb H, Kratzin H, Jahn O, Mobius W, Rabe S, Staufenbiel M, et al. Beta-amyloid peptide variants in brains and cerebrospinal fluid from amyloid precursor protein (APP) transgenic mice: comparison with human Alzheimer amyloid. J Biol Chem. 2011;286(39):33747-58.
192. Cho SM, Lee S, Yang SH, Kim HY, Lee MJ, Kim HV, et al. Age-dependent inverse correlations in CSF and plasma amyloid-beta(1-42) concentrations prior to amyloid plaque deposition in the brain of 3xTg-AD mice. Sci Rep. 2016;6:20185.
193. Andersson E, Schultz N, Saito T, Saido TC, Blennow K, Gouras GK, et al. Cerebral Abeta deposition precedes reduced cerebrospinal fluid and serum Abeta42/Abeta40 ratios in the App(NL-F/NL-F) knock-in mouse model of Alzheimer's disease. Alzheimers Res Ther. 2023;15(1):64.
194. Xiong H, Callaghan D, Wodzinska J, Xu J, Premyslova M, Liu QY, et al. Biochemical and behavioral characterization of the double transgenic mouse model (APPswe/PS1dE9) of Alzheimer's disease. Neurosci Bull. 2011;27(4):221-32.
195. Benedet AL, Mila-Aloma M, Vrillon A, Ashton NJ, Pascoal TA, Lussier F, et al. Differences Between Plasma and Cerebrospinal Fluid Glial Fibrillary Acidic Protein Levels Across the Alzheimer Disease Continuum. JAMA Neurol. 2021;78(12):1471-83.

196. Pereira JB, Janelidze S, Smith R, Mattsson-Carlgren N, Palmqvist S, Teunissen CE, et al. Plasma GFAP is an early marker of amyloid-beta but not tau pathology in Alzheimer's disease. Brain. 2021;144(11):3505-16.
197. Button EB, Cheng WH, Barron C, Cheung H, Bashir A, Cooper J, et al. Development of a novel, sensitive translational immunoassay to detect plasma glial fibrillary acidic protein (GFAP) after murine traumatic brain injury. Alzheimers Res Ther. 2021;13(1):58.
198. Kim KY, Shin KY, Chang KA. GFAP as a Potential Biomarker for Alzheimer's Disease: A Systematic Review and Meta-Analysis. Cells. 2023;12(9).
199. Sanchez-Juan P, Valeriano-Lorenzo E, Ruiz-Gonzalez A, Pastor AB, Rodrigo Lara H, Lopez-Gonzalez F, et al. Serum GFAP levels correlate with astrocyte reactivity, post-mortem brain atrophy and neurofibrillary tangles. Brain. 2024.
200. Janelidze S, Stomrud E, Palmqvist S, Zetterberg H, van Westen D, Jeromin A, et al. Plasma beta-amyloid in Alzheimer's disease and vascular disease. Sci Rep. 2016;6:26801.
201. Shir D, Graff-Radford J, Hofrenning EI, Lesnick TG, Przybelski SA, Lowe VJ, et al. Association of plasma glial fibrillary acidic protein (GFAP) with neuroimaging of Alzheimer's disease and vascular pathology. Alzheimers Dement (Amst). 2022;14(1):e12291.
202. Huss A, Abdelhak A, Mayer B, Tumani H, Muller HP, Althaus K, et al. Association of Serum GFAP with Functional and Neurocognitive Outcome in Sporadic Small Vessel Disease. Biomedicines. 2022;10(8).
203. Janota CS, Brites D, Lemere CA, Brito MA. Glio-vascular changes during ageing in wild-type and Alzheimer's disease-like APP/PS1 mice. Brain Res. 2015;1620:153-68.
204. Abdelhak A, Hottenrott T, Morenas-Rodriguez E, Suarez-Calvet M, Zettl UK, Haass C, et al. Glial Activation Markers in CSF and Serum From Patients With Primary Progressive Multiple Sclerosis: Potential of Serum GFAP as Disease Severity Marker? Front Neurol. 2019;10:280.
205. Giacomucci G, Mazzeo S, Bagnoli S, Ingannato A, Leccese D, Berti V, et al. Plasma neurofilament light chain as a biomarker of Alzheimer's disease in Subjective Cognitive Decline and Mild Cognitive Impairment. J Neurol. 2022;269(8):4270-80.
206. Bacioglu M, Maia LF, Preische O, Schelle J, Apel A, Kaeser SA, et al. Neurofilament Light Chain in Blood and CSF as Marker of Disease Progression in Mouse Models and in Neurodegenerative Diseases. Neuron. 2016;91(1):56-66.
207. Kang MS, Aliaga AA, Shin M, Mathotaarachchi S, Benedet AL, Pascoal TA, et al. Amyloid-beta modulates the association between neurofilament light chain and brain atrophy in Alzheimer's disease. Mol Psychiatry. 2021;26(10):5989-6001.
208. Dittrich A, Ashton NJ, Zetterberg H, Blennow K, Simren J, Geiger F, et al. Plasma and CSF NfL are differentially associated with biomarker evidence of neurodegeneration in a community-based sample of 70-year-olds. Alzheimers Dement (Amst). 2022;14(1):e12295.
209. Kim JH, Jung H, Lee Y, Sohn JH. Surgery Performed Under Propofol Anesthesia Induces Cognitive Impairment and Amyloid Pathology in ApoE4 Knock-In Mouse Model. Front Aging Neurosci. 2021;13:658860.
210. Wan Y, Xu J, Meng F, Bao Y, Ge Y, Lobo N, et al. Cognitive decline following major surgery is associated with gliosis, beta-amyloid accumulation, and tau phosphorylation in old mice. Crit Care Med. 2010;38(11):2190-8.
211. Perucho J, Rubio I, Casarejos MJ, Gomez A, Rodriguez-Navarro JA, Solano RM, et al. Anesthesia with isoflurane increases amyloid pathology in mice models of Alzheimer's disease. J Alzheimers Dis. 2010;19(4):1245-57.

212. Zhang S, Hu X, Guan W, Luan L, Li B, Tang Q, et al. Isoflurane anesthesia promotes cognitive impairment by inducing expression of beta-amyloid protein-related factors in the hippocampus of aged rats. PLoS One. 2017;12(4):e0175654.
213. Belrose JC, Noppens RR. Anesthesiology and cognitive impairment: a narrative review of current clinical literature. BMC Anesthesiol. 2019;19(1):241.
214. Kundovic SA, Rasic D, Popovic L, Peraica M, Crnjar K. Oxidative stress under general intravenous and inhalation anaesthesia. Arh Hig Rada Toksikol. 2020;71(3):169-77.
215. Tamagno E, Guglielmotto M, Monteleone D, Tabaton M. Amyloid-beta production: major link between oxidative stress and BACE1. Neurotox Res. 2012;22(3):208-19.
216. Su D, Zhao Y, Xu H, Wang B, Chen X, Chen J, et al. Isoflurane exposure during mid-adulthood attenuates age-related spatial memory impairment in APP/PS1 transgenic mice. PLoS One. 2012;7(11):e50172.
217. Kozai TD, Jaquins-Gerstl AS, Vazquez AL, Michael AC, Cui XT. Brain tissue responses to neural implants impact signal sensitivity and intervention strategies. ACS Chem Neurosci. 2015;6(1):48-67.
218. Wellman SM, Coyne OA, Douglas MM, Kozai TDY. Aberrant accumulation of age- and disease-associated factors following neural probe implantation in a mouse model of Alzheimer's disease. J Neural Eng. 2023;20(4).
219. Zou J, Wang M, Uchiumi O, Shui Y, Ishigaki Y, Liu X, et al. Learning impairment by minimal cortical injury in a mouse model of Alzheimer's disease. Brain Res. 2016;1637:56-63.
220. Wu Y, Wu H, Zeng J, Pluimer B, Dong S, Xie X, et al. Mild traumatic brain injury induces microvascular injury and accelerates Alzheimer-like pathogenesis in mice. Acta Neuropathol Commun. 2021;9(1):74.
221. Collins JM, King AE, Woodhouse A, Kirkcaldie MT, Vickers JC. The effect of focal brain injury on beta-amyloid plaque deposition, inflammation and synapses in the APP/PS1 mouse model of Alzheimer's disease. Exp Neurol. 2015;267:219-29.
222. Collins JM, King AE, Woodhouse A, Kirkcaldie MTK, Vickers JC. Age Moderates the Effects of Traumatic Brain Injury on Beta-Amyloid Plaque Load in APP/PS1 Mice. J Neurotrauma. 2019;36(11):1876-89.
223. Kagusa H, Yamaguchi I, Shono K, Mizobuchi Y, Shikata E, Matsuda T, et al. Differences in amyloid-beta and tau/p-tau deposition in blood-injected mouse brains using micro-syringe to mimic traumatic brain microhemorrhages. J Chem Neuroanat. 2023;130:102258.
224. Youmans KL, Tai LM, Kanekiyo T, Stine WB, Jr., Michon SC, Nwabuisi-Heath E, et al. Intraneuronal Abeta detection in 5xFAD mice by a new Abeta-specific antibody. Mol Neurodegener. 2012;7:8.
225. Goni F, Marta-Ariza M, Herline K, Peyser D, Boutajangout A, Mehta P, et al. Anti-beta-sheet conformation monoclonal antibody reduces tau and Abeta oligomer pathology in an Alzheimer's disease model. Alzheimers Res Ther. 2018;10(1):10.
226. Henderson SJ, Andersson C, Narwal R, Janson J, Goldschmidt TJ, Appelkvist P, et al. Sustained peripheral depletion of amyloid-beta with a novel form of neprilysin does not affect central levels of amyloid-beta. Brain. 2014;137(Pt 2):553-64.
227. Xie H, Guo C. Albumin Alters the Conformational Ensemble of Amyloid-beta by Promiscuous Interactions: Implications for Amyloid Inhibition. Front Mol Biosci. 2020;7:629520.

228. Campos HC, Ribeiro DE, Hashiguchi D, Glaser T, Milanis MDS, Gimenes C, et al. Neuroprotective effects of resistance physical exercise on the APP/PS1 mouse model of Alzheimer's disease. Front Neurosci. 2023;17:1132825.
229. Nixon RA. Autophagy, amyloidogenesis and Alzheimer disease. J Cell Sci. 2007;120(Pt 23):4081-91.
230. Krishnan S, Shrestha Y, Jayatunga DPW, Rea S, Martins R, Bharadwaj P. Activate or Inhibit? Implications of Autophagy Modulation as a Therapeutic Strategy for Alzheimer's Disease. Int J Mol Sci. 2020;21(18).
231. Bjorkoy G, Lamark T, Pankiv S, Overvatn A, Brech A, Johansen T. Monitoring autophagic degradation of p62/SQSTM1. Methods Enzymol. 2009;452:181-97.
232. Luo G, Wang X, Cui Y, Cao Y, Zhao Z, Zhang J. Metabolic reprogramming mediates hippocampal microglial M1 polarization in response to surgical trauma causing perioperative neurocognitive disorders. J Neuroinflammation. 2021;18(1):267.
233. Yu G, Zhang Y, Ning B. Reactive Astrocytes in Central Nervous System Injury: Subgroup and Potential Therapy. Front Cell Neurosci. 2021;15:792764.
234. Pekny M, Nilsson M. Astrocyte activation and reactive gliosis. Glia. 2005;50(4):427-34.
235. Brahmachari S, Fung YK, Pahan K. Induction of glial fibrillary acidic protein expression in astrocytes by nitric oxide. J Neurosci. 2006;26(18):4930-9.
236. von Saucken VE, Jay TR, Landreth GE. The effect of amyloid on microglia-neuron interactions before plaque onset occurs independently of TREM2 in a mouse model of Alzheimer's disease. Neurobiol Dis. 2020;145:105072.
237. Jung CK, Keppler K, Steinbach S, Blazquez-Llorca L, Herms J. Fibrillar amyloid plaque formation precedes microglial activation. PLoS One. 2015;10(3):e0119768.
238. Mun BR, Park SB, Choi WS. The Oligomeric Form of Amyloid Beta Triggers Astrocyte Activation, Independent of Neurons. Chonnam Med J. 2024;60(1):27-31.
239. Rivera-Escalera F, Pinney JJ, Owlett L, Ahmed H, Thakar J, Olschowka JA, et al. IL-1beta-driven amyloid plaque clearance is associated with an expansion of transcriptionally reprogrammed microglia. J Neuroinflammation. 2019;16(1):261.
240. Koffie RM, Meyer-Luehmann M, Hashimoto T, Adams KW, Mielke ML, Garcia-Alloza M, et al. Oligomeric amyloid beta associates with postsynaptic densities and correlates with excitatory synapse loss near senile plaques. Proc Natl Acad Sci U S A. 2009;106(10):4012-7.
241. Querol-Vilaseca M, Colom-Cadena M, Pegueroles J, Nunez-Llaves R, Luque-Cabecerans J, Munoz-Llahuna L, et al. Nanoscale structure of amyloid-beta plaques in Alzheimer's disease. Sci Rep. 2019;9(1):5181.
242. Sanchez-Varo R, Sanchez-Mejias E, Fernandez-Valenzuela JJ, De Castro V, Mejias-Ortega M, Gomez-Arboledas A, et al. Plaque-Associated Oligomeric Amyloid-Beta Drives Early Synaptotoxicity in APP/PS1 Mice Hippocampus: Ultrastructural Pathology Analysis. Front Neurosci. 2021;15:752594.
243. Trujillo-Estrada L, Jimenez S, De Castro V, Torres M, Baglietto-Vargas D, Moreno-Gonzalez I, et al. In vivo modification of Abeta plaque toxicity as a novel neuroprotective lithium-mediated therapy for Alzheimer's disease pathology. Acta Neuropathol Commun. 2013;1:73.

244. Bolmont T, Haiss F, Eicke D, Radde R, Mathis CA, Klunk WE, et al. Dynamics of the microglial/amyloid interaction indicate a role in plaque maintenance. J Neurosci. 2008;28(16):4283-92.
245. Wang S, Mustafa M, Yuede CM, Salazar SV, Kong P, Long H, et al. Anti-human TREM2 induces microglia proliferation and reduces pathology in an Alzheimer's disease model. J Exp Med. 2020;217(9).
246. Luo R, Su LY, Li G, Yang J, Liu Q, Yang LX, et al. Activation of PPARA-mediated autophagy reduces Alzheimer disease-like pathology and cognitive decline in a murine model. Autophagy. 2020;16(1):52-69.
247. Serrano-Pozo A, Muzikansky A, Gomez-Isla T, Growdon JH, Betensky RA, Frosch MP, et al. Differential relationships of reactive astrocytes and microglia to fibrillar amyloid deposits in Alzheimer disease. J Neuropathol Exp Neurol. 2013;72(6):462-71.
248. Nagele RG, D'Andrea MR, Lee H, Venkataraman V, Wang HY. Astrocytes accumulate A beta 42 and give rise to astrocytic amyloid plaques in Alzheimer disease brains. Brain Res. 2003;971(2):197-209.
249. Kraft AW, Hu X, Yoon H, Yan P, Xiao Q, Wang Y, et al. Attenuating astrocyte activation accelerates plaque pathogenesis in APP/PS1 mice. FASEB J. 2013;27(1):187-98.
250. Andrade MK, Souza LC, Azevedo EM, Bail EL, Zanata SM, Andreatini R, et al. Melatonin reduces beta-amyloid accumulation and improves short-term memory in streptozotocin-induced sporadic Alzheimer's disease model. IBRO Neurosci Rep. 2023;14:264-72.
251. Yang J, Zhang R, Shi C, Mao C, Yang Z, Suo Z, et al. AQP4 Association with Amyloid Deposition and Astrocyte Pathology in the Tg-ArcSwe Mouse Model of Alzheimer's Disease. J Alzheimers Dis. 2017;57(1):157-69.
252. Kecheliev V, Boss L, Maheshwari U, Konietzko U, Keller A, Razansky D, et al. Aquaporin 4 is differentially increased and dislocated in association with tau and amyloid-beta. Life Sci. 2023;321:121593.
253. Yang W, Wu Q, Yuan C, Gao J, Xiao M, Gu M, et al. Aquaporin-4 mediates astrocyte response to beta-amyloid. Mol Cell Neurosci. 2012;49(4):406-14.
254. Peng S, Liu J, Liang C, Yang L, Wang G. Aquaporin-4 in glymphatic system, and its implication for central nervous system disorders. Neurobiol Dis. 2023;179:106035.
255. Zhang J, Zhan Z, Li X, Xing A, Jiang C, Chen Y, et al. Intermittent Fasting Protects against Alzheimer's Disease Possible through Restoring Aquaporin-4 Polarity. Front Mol Neurosci. 2017;10:395.
256. Fukuda AM, Badaut J. Aquaporin 4: a player in cerebral edema and neuroinflammation. J Neuroinflammation. 2012;9:279.
257. Smith AJ, Duan T, Verkman AS. Aquaporin-4 reduces neuropathology in a mouse model of Alzheimer's disease by remodeling peri-plaque astrocyte structure. Acta Neuropathol Commun. 2019;7(1):74.
258. Lan YL, Zhao J, Ma T, Li S. The Potential Roles of Aquaporin 4 in Alzheimer's Disease. Mol Neurobiol. 2016;53(8):5300-9.
259. Chandra A, Farrell C, Wilson H, Dervenoulas G, De Natale ER, Politis M, et al. Aquaporin-4 polymorphisms predict amyloid burden and clinical outcome in the Alzheimer's disease spectrum. Neurobiol Aging. 2021;97:1-9.

260. Hoshi A, Yamamoto T, Shimizu K, Ugawa Y, Nishizawa M, Takahashi H, et al. Characteristics of aquaporin expression surrounding senile plaques and cerebral amyloid angiopathy in Alzheimer disease. J Neuropathol Exp Neurol. 2012;71(8):750-9.
261. Delle C, Cankar N, Digebjerg Holgersson C, Hvorup Knudsen H, Schioler Nielsen E, Kjaerby C, et al. Long-term high-fat diet increases glymphatic activity in the hypothalamus in mice. Sci Rep. 2023;13(1):4137.
262. Monai H, Wang X, Yahagi K, Lou N, Mestre H, Xu Q, et al. Adrenergic receptor antagonism induces neuroprotection and facilitates recovery from acute ischemic stroke. Proc Natl Acad Sci U S A. 2019;116(22):11010-9.
263. Hablitz LM, Pla V, Giannetto M, Vinitsky HS, Staeger FF, Metcalfe T, et al. Circadian control of brain glymphatic and lymphatic fluid flow. Nat Commun. 2020;11(1):4411.
264. Feng S, Wu C, Zou P, Deng Q, Chen Z, Li M, et al. High-intensity interval training ameliorates Alzheimer's disease-like pathology by regulating astrocyte phenotype-associated AQP4 polarization. Theranostics. 2023;13(10):3434-50.
265. Neumaier F, Zlatopolskiy BD, Neumaier B. Drug Penetration into the Central Nervous System: Pharmacokinetic Concepts and In Vitro Model Systems. Pharmaceutics. 2021;13(10).
266. Pardridge WM. A Historical Review of Brain Drug Delivery. Pharmaceutics. 2022;14(6).
267. Meng Y, Reilly RM, Pezo RC, Trudeau M, Sahgal A, Singnurkar A, et al. MR-guided focused ultrasound enhances delivery of trastuzumab to Her2-positive brain metastases. Sci Transl Med. 2021;13(615):eabj4011.
268. Chu C, Jablonska A, Lesniak WG, Thomas AM, Lan X, Linville RM, et al. Optimization of osmotic blood-brain barrier opening to enable intravital microscopy studies on drug delivery in mouse cortex. J Control Release. 2020;317:312-21.
269. Solar P, Zamani A, Kubickova L, Dubovy P, Joukal M. Choroid plexus and the blood-cerebrospinal fluid barrier in disease. Fluids Barriers CNS. 2020;17(1):35.
270. Pinheiro RGR, Coutinho AJ, Pinheiro M, Neves AR. Nanoparticles for Targeted Brain Drug Delivery: What Do We Know? Int J Mol Sci. 2021;22(21).
271. Poudel P, Park S. Recent Advances in the Treatment of Alzheimer's Disease Using Nanoparticle-Based Drug Delivery Systems. Pharmaceutics. 2022;14(4).
272. Cano A, Munoz-Morales A, Sanchez-Lopez E, Ettcheto M, Souto EB, Camins A, et al. Exosomes-Based Nanomedicine for Neurodegenerative Diseases: Current Insights and Future Challenges. Pharmaceutics. 2023;15(1).
273. Capozza MA, Triarico S, Mastrangelo S, Attina G, Maurizi P, Ruggiero A. Narrative review of intrathecal drug delivery (IDD): indications, devices and potential complications. Ann Transl Med. 2021;9(2):186.
274. Partridge B, Eardley A, Morales BE, Campelo SN, Lorenzo MF, Mehta JN, et al. Advancements in drug delivery methods for the treatment of brain disease. Front Vet Sci. 2022;9:1039745.
275. Ajeeb R, Clegg JR. Intrathecal delivery of Macromolecules: Clinical status and emerging technologies. Adv Drug Deliv Rev. 2023;199:114949.
276. Khang M, Bindra RS, Mark Saltzman W. Intrathecal delivery and its applications in leptomeningeal disease. Adv Drug Deliv Rev. 2022;186:114338.

277. Huwait EA, Baghallab IM, Glabe CG, Abulnaja KO, Kumosani TA, Moselhy SS. Identification of amyloid antibodies for Alzheimer disease - immunotherapy. Arch Physiol Biochem. 2022;128(5):1275-82.
278. Thiviyanathan V, Gorenstein DG. Aptamers and the next generation of diagnostic reagents. Proteomics Clin Appl. 2012;6(11-12):563-73.
279. Loktyushov EV, Litus EA, Deryusheva EI. Systematic search for peptide and protein ligands of human serum albumin capable of affecting its interaction with amyloid β peptide. Acta Biomedica Scientifica. 2022;7(5-1):19-26.
280. Grayson JD, Baumgartner MP, Santos Souza CD, Dawes SJ, El Idrissi IG, Louth JC, et al. Amyloid binding and beyond: a new approach for Alzheimer's disease drug discovery targeting Abetao-PrP(C) binding and downstream pathways. Chem Sci. 2021;12(10):3768-85.
281. Kato D, Takahashi Y, Iwata H, Hatakawa Y, Lee SH, Oe T. Comparative studies for amyloid beta degradation: "Neprilysin vs insulysin", "monomeric vs aggregate", and "whole Abeta(40) vs its peptide fragments". Biochem Biophys Rep. 2022;30:101268.
282. Tobinick EL, Gross H. Rapid cognitive improvement in Alzheimer's disease following perispinal etanercept administration. J Neuroinflammation. 2008;5:2.
283. Chang R, Yee KL, Sumbria RK. Tumor necrosis factor alpha Inhibition for Alzheimer's Disease. J Cent Nerv Syst Dis. 2017;9:1179573517709278.
284. Shi JQ, Shen W, Chen J, Wang BR, Zhong LL, Zhu YW, et al. Anti-TNF-alpha reduces amyloid plaques and tau phosphorylation and induces CD11c-positive dendritic-like cell in the APP/PS1 transgenic mouse brains. Brain Res. 2011;1368:239-47.
285. Shi JQ, Wang BR, Jiang WW, Chen J, Zhu YW, Zhong LL, et al. Cognitive improvement with intrathecal administration of infliximab in a woman with Alzheimer's disease. J Am Geriatr Soc. 2011;59(6):1142-4.
286. Ou W, Yang J, Simanauskaite J, Choi M, Castellanos DM, Chang R, et al. Biologic TNF-alpha inhibitors reduce microgliosis, neuronal loss, and tau phosphorylation in a transgenic mouse model of tauopathy. J Neuroinflammation. 2021;18(1):312.
287. El-Kattan MM, Rashed LA, Shazly SR, Ismail RS. Relation of serum level of tumor necrosis factor-alpha to cognitive functions in patients with Parkinson's disease. The Egyptian Journal of Neurology, Psychiatry and Neurosurgery. 2022;58(1):25.
288. Wood H. TNF - a potential therapeutic target for ALS. Nat Rev Neurol. 2022;18(6):317.
289. Hu Y, Huang Z, Yang S, Chen X, Su W, Liang D. Effectiveness and Safety of Anti-Tumor Necrosis Factor-Alpha Agents Treatment in Behcets' Disease-Associated Uveitis: A Systematic Review and Meta-Analysis. Front Pharmacol. 2020;11:941.
290. Khanna D, McMahon M, Furst DE. Safety of tumour necrosis factor-alpha antagonists. Drug Saf. 2004;27(5):307-24.
291. Liu P, Wang Y, Sun Y, Peng G. Neuroinflammation as a Potential Therapeutic Target in Alzheimer's Disease. Clin Interv Aging. 2022;17:665-74.
292. Carreon Guarnizo E, Hernandez Clares R, Castillo Trivino T, Meca Lallana V, Arocas Casan V, Iniesta Martinez F, et al. Experience with tocilizumab in patients with neuromyelitis optica spectrum disorders. Neurologia (Engl Ed). 2022;37(3):178-83.
293. Cabreira V, Dias L, Fernandes B, Aires A, Guimaraes J, Abreu P, et al. Tocilizumab for severe refractory primary central nervous system vasculitis: A center experience. Acta Neurol Scand. 2022;145(4):479-83.

294. Milligan C, Atassi N, Babu S, Barohn RJ, Caress JB, Cudkowicz ME, et al. Tocilizumab is safe and tolerable and reduces C-reactive protein concentrations in the plasma and cerebrospinal fluid of ALS patients. Muscle Nerve. 2021;64(3):309-20.
295. Pons-Espinal M, Blasco-Agell L, Fernandez-Carasa I, di Domenico A, Richaud Y, Mosquera JL, et al. Immunosuppressive tocilizumab prevents astrocyte induced neurotoxicity in hiPSC-LRRK2 Parkinson's disease by targeting receptor interleukin-6. bioRxiv. 2022:2022.08.23.504918.
296. Elcioglu HK, Aslan E, Ahmad S, Alan S, Salva E, Elcioglu OH, et al. Tocilizumab's effect on cognitive deficits induced by intracerebroventricular administration of streptozotocin in Alzheimer's model. Mol Cell Biochem. 2016;420(1-2):21-8.
297. Liu X, Li L, Wang Q, Jiang F, Zhang P, Guo F, et al. A Novel Humanized Anti-Interleukin-6 Antibody HZ0408b With Anti-Rheumatoid Arthritis Therapeutic Potential. Front Immunol. 2021;12:816646.
298. van Lengerich B, Zhan L, Xia D, Chan D, Joy D, Park JI, et al. A TREM2-activating antibody with a blood-brain barrier transport vehicle enhances microglial metabolism in Alzheimer's disease models. Nat Neurosci. 2023;26(3):416-29.
299. Ma LZ, Tan L, Bi YL, Shen XN, Xu W, Ma YH, et al. Dynamic changes of CSF sTREM2 in preclinical Alzheimer's disease: the CABLE study. Mol Neurodegener. 2020;15(1):25.
300. Brown GC, St George-Hyslop P. Does Soluble TREM2 Protect Against Alzheimer's Disease? Front Aging Neurosci. 2021;13:834697.
301. Bolognin S, Messori L, Zatta P. Metal ion physiopathology in neurodegenerative disorders. Neuromolecular Med. 2009;11(4):223-38.
302. Lee S, Martinez-Valbuena I, Lang AE, Kovacs GG. Cellular iron deposition patterns predict clinical subtypes of multiple system atrophy. Neurobiol Dis. 2024;197:106535.
303. Levi S, Ripamonti M, Moro AS, Cozzi A. Iron imbalance in neurodegeneration. Mol Psychiatry. 2024.
304. Gao G, You L, Zhang J, Chang YZ, Yu P. Brain Iron Metabolism, Redox Balance and Neurological Diseases. Antioxidants (Basel). 2023;12(6).
305. Wang F, Wang J, Shen Y, Li H, Rausch WD, Huang X. Iron Dyshomeostasis and Ferroptosis: A New Alzheimer's Disease Hypothesis? Front Aging Neurosci. 2022;14:830569.
306. Wang J, Fu J, Zhao Y, Liu Q, Yan X, Su J. Iron and Targeted Iron Therapy in Alzheimer's Disease. Int J Mol Sci. 2023;24(22).
307. Everett J, Brooks J, Lermyte F, O'Connor PB, Sadler PJ, Dobson J, et al. Iron stored in ferritin is chemically reduced in the presence of aggregating Abeta(1-42). Sci Rep. 2020;10(1):10332.
308. Pardridge WM. CSF, blood-brain barrier, and brain drug delivery. Expert Opin Drug Deliv. 2016;13(7):963-75.
309. Ullah R, Park TJ, Huang X, Kim MO. Abnormal amyloid beta metabolism in systemic abnormalities and Alzheimer's pathology: Insights and therapeutic approaches from periphery. Ageing Res Rev. 2021;71:101451.
310. Shigemori K, Nomura S, Umeda T, Takeda S, Tomiyama T. Peripheral Abeta acts as a negative modulator of insulin secretion. Proc Natl Acad Sci U S A. 2022;119(12):e2117723119.
311. Leisher S, Bohorquez A, Gay M, Garcia V, Jones R, Baldaranov D, et al. Amyloid-Lowering Monoclonal Antibodies for the Treatment of Early Alzheimer's Disease. CNS Drugs. 2023;37(8):671-7.

312. Espay AJ, Herrup K, Kepp KP, Daly T. The proteinopenia hypothesis: Loss of Abeta(42) and the onset of Alzheimer's Disease. Ageing Res Rev. 2023;92:102112.
313. Sideris DI, Danial JSH, Emin D, Ruggeri FS, Xia Z, Zhang YP, et al. Soluble amyloid beta-containing aggregates are present throughout the brain at early stages of Alzheimer's disease. Brain Commun. 2021;3(3):fcab147.
314. Pérez-Martín E R-CM, Roces-Llorián C, Álvarez G, Prado C, Tomás-Zapico C, Menéndez-González M. Intrathecal Pseudodelivery of mAb to Clear Target Molecules from the CNS: Testing a Human Prototype in a Porcine Model. European Academy of Neurology Congress2024.